Development of Optical Fiber-Based Sensing Devices Using Laser Microfabrication Methods

by

Seyed Hamidreza Alemohammad

A thesis
presented to the University of Waterloo
in fulfillment of the
thesis requirement for the degree of
Doctor of Philosophy
in
Mechanical Engineering

Waterloo, Ontario, Canada, 2010

I hereby declare that I am the sole author of this thesis. This is a true copy of the thesis, including any required final revisions, as accepted by my examiners.

I understand that my thesis may be made electronically available to the public.

Abstract

The focus of this thesis is on the development of sensing devices based on optical fiber sensors, specifically optical Fiber Bragg Gratings (FBG), using laser microfabrication methods. FBG is a type of optical fibers whose spectral response is affected by applied strain and temperature. As a result, it can be calibrated for the measurement of physical parameters manifesting themselves in the changes of strain or temperature. The unique features of optical fiber sensors such as FBGs have encouraged the widespread use of the sensor and the development of optical fiber-based sensing devices for structural measurements, failure diagnostics, thermal measurements, pressure monitoring, etc. These features include light weight, small size, long-term durability, robustness to electromagnetic disturbances, and resistance to corrosion. Despite the encouraging features, there are some limitations and challenges associated with FBGs and their applications. One of the challenges associated with FBGs is the coupling of the effects of strain and temperature in the optical response of the sensors which affects the reliability and accuracy of the measurements. Another limitation of FBGs is insensitivity to the index of refraction of their surrounding medium. In liquids, the index of refraction is a function of concentration. Making FBGs sensitive to the index of refraction and keeping their thermal sensitivity intact enable optical sensors with the capability of the simultaneous measurement of concentration and temperature in liquids. Considering the unique features of FBGs, embedding of the sensors in metal parts for in-situ load monitoring is a cutting-edge research topic. Several industries such as machining tools, aerospace, and automotive industries can benefit from this technology. The metal embedding process is a challenging task, as the thermal decay of UV-written gratings can starts at a temperature of ~200 ^{o}C and accelerates at higher temperatures. As a result, the embedding process needs to be performed at low temperatures.

The objective of the current thesis is to move forward the existing research front in the area of optical fiber sensors by finding effective solutions to the aforementioned limitations. The approaches consist of modeling, design, and fabrication of new FBG-based sensing devices. State-of-the-art laser microfabrication methods are proposed and implemented for the fabrication of the devices. Two approaches are adopted for the development of the FBG-based sensing devices: the additive method and the subtractive method. In both methods, laser direct microfabrication techniques are utilized. The additive method deals with the

deposition of on-fiber metal thin films, and the subtractive method is based on the selective removal of materials from the periphery of optical fibers.

To design the sensing devices and analyze the performance of the sensors, an opto-mechanical model of FBGs for thermal and structural monitoring is developed. The model is derived from the photo-elastic and thermo-optic properties of optical fibers. The developed model can be applied to predict the optical responses of a FBG exposed to structural loads and temperature variations with uniform and non-uniform distributions. The model is also extended to obtain optical responses of superstructure FBGs in which a secondary periodicity is induced in the index of refraction along the optical fiber.

To address the temperature-strain coupling in FBGs, Superstructure FBGs (SFBG) with on-fiber metal thin films are designed and fabricated. It is shown that SFBGs have the capability of measuring strain and temperature simultaneously. The design of the sensor with on-fiber thin films is performed by using the developed opto-mechanical model of FBGs. The performance of the sensor in concurrent measurement of strain and temperature is investigated by using a customized test rig.

A laser-based Direct Write (DW) method, called Laser-Assisted Maskless Microdeposition (LAMM), is implemented to selectively deposit silver thin films on optical fibers and fabricate the superstructure FBGs. To attain thin films with premium quality, a characterization scheme is designed to study the geometrical, mechanical, and microstructural properties of the thin films in terms of the LAMM process parameters.

A FBG, capable of measuring concentration and temperature of liquids is developed, and its performance is tested. Femtosecond laser micromachining is successfully implemented as a subtractive method for the sensor fabrication. For this purpose, periodic micro-grooves are inscribed in the cladding of regular FBGs so as to increase their sensitivity to the concentration of their surrounding liquid while keeping their thermal sensitivity intact. This type of sensors has the potential for applications in biomedical research, in which the in-situ measurement of the properties of biological analytes is required.

Another accomplishment of this thesis is the development of FBG sensors embedded in metal parts for structural health monitoring using low temperature embedding processes. In this regard, the opto-mechanical model is extended to predict the optical response of the embedded FBGs. The embedding process involves low temperature casting, on-fiber thin film deposition, and electroplating methods. The performance of the embedded sensors is evaluated in structural loading and thermal cycling.

Acknowledgements

I would like to express my gratitude to my supervisor, Dr. Ehsan Toyserkani, for his support, advice, and encouragement during the last four years. I hereby acknowledge my thesis examining committee members, Dr. Peter Herman from the University of Toronto, Dr. Walter W. Duley, Dr. Amir Khajepour, and Dr. Patricia Nieva, from the University of Waterloo, for reviewing my thesis and giving useful comments. I would also like to thank Dr. Shahrzad Esmaeili for her comments and guidance. I also thank Dr. John B. Medley and Dr. William W. Melek for their support and encouragement.

I want to acknowledge my colleagues at the Laser Processing Research Centre of the University of Manchester, UK, Dr. Andrew J. Pinkerton, Dr. Amin Abdolvand, and Dr. David Whitehead for their guidance and support.

I am pleased to thank my former supervisors at Sharif University of Technology: Dr. Mohammad Durali, Dr. Ali Meghdari, and Dr. Aria Alasty.

I would like to acknowledge the Government of Ontario for Ontario Graduate Scholarship (OGS), University of Waterloo for President's Graduate Scholarship, International Doctoral Student Award, and UW Graduate Scholarships, and the financial support from Natural Resources and Engineering Research Council (NSERC) of Canada, Canada Foundation for Innovation (CFI), and Ontario Centres of Excellence (OCE).

I would like to thank my colleagues at Rapid Prototyping Laboratory of the University of Waterloo: Dr. Masoud Alimardani, Yaser Shanjani, Negar Rasti, Saman Mohammadi, Hanieh Aghighi, Mihaela Vlasea, Ash Charles, and Hajar Sharif. I want to thank my friends with whom I had memorable experience: Dr. Naser Lashgarian, Dr. Alireza Fathi, Alireza Kasaaizadeh, Arash Tajik, Pedram Hassanzadeh, Mohsen Shahini, Omid Aminfar, Panthea Sepehrband, Mehrdad Iravani, Kian Aladdini, Ehsan Fathi, Amir H. Goldan, Dr. Saeed Bagheri, Dr. Reza H. Khiabani, Hadi Tavkoli Nia, Saeid Rostami Bookani, Reza Afzali, and Pouria Haddadi.

I would like to express my deepest gratitude and appreciation to my beloved parents, Ahmad and Manijeh, and my brother, Hamed, for their great support and encouragement.

To my parents

who taught me to learn

Contents

Appendices

List of Figures

List of Tables

Nomenclature

Symbol	Description
α	Coefficient of thermal expansion
α_c	Coefficient of thermal expansion of coating
α_f	Coefficient of thermal expansion of optical fiber
α_{silica}	Coefficient of thermal expansion of silica
α_{silver}	Coefficient of thermal expansion of silver
α^*	Correction factor in Oliver-Pharr model of nanoindentation
β	Propagation constant
β_i	Propagation constant of the i^{th} mode
$[\varepsilon]$	Dielectric tensor
ε	Electric permittivity
ε_0	Electric permittivity of vacuum
ε_i	Components of the dielectric permittivity tensor
λ	wavelength
λ_B	Bragg wavelength
λ_{k^+}	Upper Sideband wavelength is superstructure FBG
λ_{k^-}	Lower sideband wavelength in superstructure FBG
μ	Magnetic permeability
ν_c	Poisson's ration of coating
ν_f	Fringe visibility in gratings, Poisson's ratio of film
$\sigma^c_{zz}, \sigma^c_{rr}, \sigma^c_{\theta\theta}$	Stress components of coating in cylindrical coordinates

$\sigma_{zz}^{f}, \sigma_{rr}^{f}, \sigma_{\theta\theta}^{f}$	Stress components of fiber in cylindrical coordinates
ω	Light frequency
Γ	Superstructure FBG secondary period
Λ	Grating period
$\Phi(z)$	Grating chirp
e_{j}	Elements of strain tensor
$e_{zz}, e_{rr}, e_{\theta\theta}$	Strain components in cylindrical coordinates
$e_{zz}^{c}, e_{rr}^{c}, e_{\theta\theta}^{c}$	Strain components of coating in cylindrical coordinates
$e_{zz}^{f}, e_{rr}^{f}, e_{\theta\theta}^{f}$	Strain components of fiber in cylindrical coordinates
$[e]$	Strain tensor
k	Light propagation constant
n_{core}	Index of refraction of core
n_{clad}	Index of refraction of cladding
n_{clad}^{i}	i^{th} cladding effective mode index of refraction
n_{eff}	Effective mode index of refraction
n_{i}	Elements of index of refraction tensor
n_{x}, n_{y}, n_{z}	Index of refraction in the x, y, and z directions
$\hat{\mathbf{n}}_1, \hat{\mathbf{n}}_2$	Surface unit normal vectors
$\overline{\Delta n}$	Average of the modulation of the index of refraction in grating
$[n]$	Index of refraction tensor
$\frac{\partial n}{\partial T}$	Constant parameter describing the variations of the index of refraction with temperature in dielectric materials
p_{ij}	Elements of Pockel's constant matrix
$[p]$	Pockel's constant
$r(\lambda)$	Reflectivity as a function of wavelength
r_{c}	Radius of coating

r_f	Radius of fiber
t	Thickness
u	Displacement in the r direction (cylindrical coordinates)
v	Displacement component in the θ direction (cylindrical coordinates)
w	Displacement in the z direction (cylindrical coordinates)
A	Area
A_l	Amplitude of the l^{th} propagating mode
$\mathbf{B}$	Magnetic induction
B_i	Elements of dielectric impermeability tensor
$[B]$	Dielectric impermeability tensor
$\mathbf{D}$	Electric displacement
$\mathbf{E}$	Electric field
$\mathbf{E}^*$	Conjugate of electric field
E	Magnitude of electric field, Modulus of elasticity
E^*	Reduced modulus of elasticity
E_x, E_y, E_z	Components of electric field in Cartesian coordinates
E_{x_i}, E_{y_i}	Nodal values of electric filed components
E_l	Magnitude of electric filed for the l^{th} propagating mode
E_f	Modulus of elasticity of film/optical fiber
E_{fiber}	Modulus of elasticity of optical fiber
E_c	Modulus of elasticity of coating
E_{in}	Modulus of elasticity of indenter
E_{silica}	Modulus of elasticity of silica
F	Force
$\mathbf{H}$	Magnetic field
H	Hardness
K_{ml}	Coupling coefficient between the l^{th} and m^{th} propagating modes

K_{AC}	Coupling coefficient
K_{dc}	Coupling coefficient
L	Grating length
$\{N\}$	Shape function
P_m	Maximum load in nanoindentation experiment
R	Amplitude of forward propagating mode in FBG
S	Amplitude of backward propagating mode in FBG/Slope of relaxation curve in nanoindentation experiment
T	Temperature

The whole of science is nothing more than a refinement of everyday thinking.

Albert Einstein

Chapter 1

Introduction

Photonics technology is one of the primary research areas in the 21st century, called the "photon century". In this regard, optical fibers have attracted researchers to develop new generations of optical fiber-based sensing devices. According to the "Fiber Optic Sensors" report from BCC Research in 2008 (Report Code: IAS002D), the optical fiber sensors market in the USA is estimated to reach $1.6 billion by the year of 2014 from $235 million in 2007, indicating a huge boost in the applications of optical fibers in the coming years [1].

In addition to telecommunication applications, optical fibers are widely used for monitoring physical parameters such as strain, stress, force, pressure, temperature, index of refraction, and liquid concentration [2]. Fiber grating is a type of optical fibers that is widely utilized for sensing the physical parameters such as strain and temperature. Fiber gratings are periodic modulations of the index of refraction in optical fibers [2]. Optical fibers, made of amorphous silica, have a core with a diameter of 8 to 10 μm in single-mode fibers and 50 or 62.5 μm in multimode optical fibers with a cladding diameter of 125 μm. The modulation of the index of refraction, called grating, is inscribed in optical fibers by UV or femtosecond laser radiation [2]. In short period fiber gratings (with a period of ~500 nm), called Fiber Bragg Gratings (FBG), the gratings are inscribed in the core of single-mode optical fibers. When FBG is exposed to a broadband spectrum of light, due to the coupling of the contra-directional core modes, the light at a specific wavelength, called the Bragg wavelength, with a specific bandwidth is reflected back [3]. The sensing characteristics of FBGs arise from

photo-elastic and thermo-optic properties of optical fibers [4, 5]. The index of refraction of silica is related to the applied strain and temperature variations. At no-load conditions, silica is optically isotropic, that is, the index of refraction components in all directions are equal. When an optical fiber is exposed to strain distributions and temperature variations, the components of the index of refraction are not necessarily equal in all directions, and the material becomes optically anisotropic. This optical anisotropy affects the propagation of the light and the core-mode coupling. The period of the grating is also affected by the applied strain and temperature. These effects manifest themselves in the spectral response of the FBG. The shift in the Bragg wavelength and the modification of the reflection spectrum are the effects seen in loaded FBGs. The optical response is calibrated based on the parameter that is intended to be measured.

The distinctive features of FBGs encourage the development of embedded sensors in metal parts for in-situ load measurements, structural health monitoring, and failure diagnostics. Promising applications can be sought for FBGs in various industrial sectors including, but not limited to, aerospace, petroleum, nuclear, and automotive industries. For instance, embedded FBG sensors in machining tools enable the in-situ monitoring of structural and thermal loads applied on the tools during the manufacturing process. Compared with conventional electric and electromagnetic sensing devices such as MEMS pressure and temperature sensors, optical fiber sensors are significantly advantageous. They are known for their light weight, small size, long-term durability, and long-range linearity. Moreover, they are robust to external electromagnetic noises and disturbances and are corrosion-resistant. In addition, arrays of sensors can be produced on a single strand of optical fiber to capture the measurement data at multiple points. As a result, masses of wires which are typically observed in thin film transducers are not required. When it comes to remote sensing, optical fibers can transfer the data at long distances with very low losses as opposed to electric sensors which are prone to Ohmic losses. The attenuation of standard single-mode optical fibers (Corning SMF-28) used for telecommunication applications is less than 0.22 db/km [6]. One of the limitations that can impede the extensive application of optical fiber sensing is the cost of the measurement devices. The light sources and spectrum analyzers can cost thousands of dollars.

1.1 State-of-the-Art FBG Sensors Technology

The aforementioned features of optical fiber sensors encourage the development of innovative technologies for the production of FBG-based sensing devices. One of the promising applications of FBGs is structural health monitoring and failure diagnostics. Surface mounted or embedded FBG sensors can replace strain gauges. According to the literature, several methods have been proposed to embed FBGs in composite materials, concrete, and metals [7-10]. Compared with electrical and electromagnetic sensors, such as thin film thermocouples, strain gauges, and MEMS transducers, optical fibers are electrically insulated. As a result, metal-embedding process does not require the inclusion of insulators [11, 12]. In addition, arraying of the FBG sensors on optical fibers enable in-situ load measurement at multiple points in the metal structures using only one strand of optical fiber. Casting, electroplating, brazing, and ultrasonic consolidation are the methods that have been used to embed FBGs in metal parts [13-16].

In addition to temperature and strain measurements, FBGs can also be used for the monitoring of the concentration of liquids. Surface modifications need to be performed to convert FBGs to concentration sensors. To do so, the cladding layer is etched with Hydrofluoric acid (HF). In this way, the propagation of the light in the cladding-etched optical fiber is affected by the index of refraction of the liquid surrounding the optical fiber. Since the index of refraction in liquids can be correlated to the concentration of liquids, the optical response of the FBG can be calibrated for the measurement of concentration. [17-21].

1.2 Limitations and Challenges in the Applications of FBGs

Despite the numerous applications of FBGs and their extensive usage for structural health monitoring, the FBG technology involves limitations and challenges. The effects of strain and temperature are coupled in the reflection spectrum of FBGs. As a result, they can barely be efficient in environments in which both parameters are fluctuating. This limitation necessitates the development of methods to compensate for the effect of one parameter or enable the simultaneous measurement of both parameters. Several methods have been proposed to compensate for the effect of temperature or enable FBGs to measure strain and temperature simultaneously. The approaches are based on multiple FBGs, use of bi-material,

combined FBG Fabry-Perot Cavity, surface mounted FBGs on beams, and UV written superstructure FBGs [22-30].

Although the proposed methods can effectively resolve the strain-temperature coupling in FBGs, there are some limitations with their applications. Using additional materials and structures makes the size of the sensors large which hinders the miniaturization of the sensor. Moreover, the use of a secondary sensor and optical cavity such as Fabry-Perot increases the volume of the captured data for analysis.

Another limitation associated with the application of FBGs is related to the insensitivity of the sensor to the index of refraction of the surrounding environment. The index of refraction does not affect the core-cladding mode coupling in the reflection spectrum of FBGs. In liquids, the index of refraction is a function of concentration. If FBGs become sensitive to the index of refraction of their surrounding medium, while retaining their thermal sensitivity, they can be utilized for the simultaneous measurement of temperature and concentration in liquids, which has numerous applications in biomedical research. As mentioned before, HF etching is the most common method to make FBGs sensitive to the concentration of liquids. However, the HF-etched sensor cannot be used for the simultaneous measurement of temperature and concentration in liquids, and a secondary FBG sensor is used to measure the temperature separately [20]. In addition, the mechanical strength of the HF-etched optical fibers degrades due to the diametric reduction of the optical fiber.

Another challenge associated with the applications of FBGs is related to metal-embedded optical fiber sensors. The unique characteristics of FBG sensors, which were discussed in the previous section, encourage the development of FBG-based sensing devices for in-situ load monitoring in metal structures. The challenge arises from the sensitivity of FBGs to high temperatures. The UV-written gratings in FBGs can start to degrade at a temperature of ~200 ^{o}C and the decay speed increases with temperature [2, 31]. In addition, the optical fiber can structurally been damaged at very high temperatures. The glass transition temperature for fused silica is around 1200 ^{o}C [32].

As mentioned in the previous section, low temperature casting, electroplating, brazing, and ultrasonic consolidation have been proposed for the metal-embedding process. Although casting and brazing can be performed at temperatures below the decay temperature of the gratings, they can cause the formation of residual stress on the optical fiber and the metal surrounding the glass fiber. The residual stress can cause material delamination and crack formation. Electroplating is a low temperature process that can be used for this purpose.

However, optical fibers are electrically non-conductive and they cannot be plated directly with metals. As a result, on-fiber metal interlayer is needed for the electroplating process [10].

1.3 Thesis Objective

The main objective of the thesis is to move the research front in the area of optical fiber sensors by implementing novel solutions for the aforementioned limitations associated with the applications of FBGs. For this purpose, different approaches including superstructure FBGs, laser surface micromachining of FBGs, and low temperature processes for embedding FBGs in metal parts are explored.

1.4 Superstructure FBGs for Strain and Temperature Measurements: Modeling, Design, and Fabrication

In this thesis, a superstructure FBG is developed by the selective deposition of on-fiber silver films. The superstructure FBG has the capability of measuring strain and temperature simultaneously. The superstructure FBG is produced by the deposition of periodic metal thin films on regular FBGs. The applied strain and temperature on the FBG not only shifts the Bragg wavelength but also forms equally spaced side bands in the reflection spectrum. The reflectivity of the side bands is tuned by the applied strain and temperature. The Bragg wavelength combined with the reflectivity measurements are used for the simultaneous measurement of strain and temperature. For the design of the sensor, an opto-mechanical model is developed to study the effects of the geometrical features of on-fiber thin films on the optical response of FBGs. The model is based on the photo-elastic and thermo-optic properties of optical fibers. The state of stress and strain in an optical fiber selectively coated with metal films and exposed to temperature variations and/or structural loading is obtained. The strain components are used in the photo-elastic and thermo-optic formulations to obtain the distribution of modified index of refraction in the optical fiber, as well as the modified grating pitch. The results are combined with Coupled-Mode Theory (CMT) to obtain the spectral response of the metal-coated FBG.

1.5 Metal-Embedded FBG Sensors for Structural Health Monitoring

In this thesis, FBGs are embedded in metal structures by using two low temperature processes: (1) casting with a low melting point metal, (2) metal thin-film deposition followed by electroplating. The deposited thin film acts as conductive interlayer for the electroplating process. To realize smart machining tools, the embedding process is followed by Laser Solid Freeform Fabrication (LSFF) of tungsten carbide reinforced in cobalt (WC-Co) on the surface of the part with embedded FBG sensor.

To have an efficient embedding process, an opto-mechanical model is required not only to design the embedded sensor but also to gain insight into the quality of the embedding process by comparing the experimental and modeling results. As a result, a model is developed, based on both the structural analysis of the metal part and the optical model of FBGs.

1.6 On-Fiber Metal Thin Films

The superstructure FBGs for strain and temperature measurements and the metal embedding process require the deposition of on-fiber metal thin films. The coating of optical fibers with metal thin films has been reported in the literature for various applications such as dispersion compensation in Bragg gratings, tunable Bragg gratings, and sensitivity enhancement at cryogenic temperatures. The conventional methods available for the deposition of thin films on optical fibers are electrowinning, sputtering, electron beam evaporation, and electroplating [33-36]. These methods lose their efficiency in selective and customized coating of optical fibers. They increase the time and cost by incorporating masks for addition and removal of materials. In addition, some of these methods such as sputtering have low deposition rate making them inefficient for micro-scale coatings. Direct Write (DW) methods have superior advantages to the conventional methods for patterning and selective thin-film deposition. In this regard, one of the contributions of this thesis is to deploy a laser-based direct deposition process for the selective deposition of on-fiber thin films.

1.7 Laser-Assisted Deposition of On-Fiber Metal Thin Films

The technique that is adopted for on-fiber thin-film deposition in this research is Laser-Assisted Maskless Microdeposition (LAMM). In the LAMM technology, which is categorized as a Laser Direct Write (LDW) process, the deposited material is in the form of nanoparticles suspended in a liquid. The nanoparticles suspension is atomized to an aerosol form. The aerosol is carried to a deposition head and ejected toward a moving substrate. The substrate is programmed to move beneath the deposition head for the production of different patterns. After deposition, the deposited material is radiated by a laser beam to evaporate the suspension liquid, heat the deposited material, and sinter the nanoparticles. The LAMM process is maskless which makes it less expensive and more flexible than the conventional methods. Moreover, by incorporating the laser beam as a heat source for local post-heating, the deposition process becomes faster and more efficient than bulk heating in a furnace or hot plate. Compared with other direct write technologies such as inkjet printing, LAMM has the capability of depositing conformal patterns on non-planar surfaces and three-dimensional substrates. This makes the LAMM process suitable for on-fiber thin film deposition.

In this technology, the quality of the deposited materials including electrical conductivity, mechanical bonding, and surface morphology depends significantly on the process parameters. The parameters associated with the deposition and laser sintering processes need to be optimized to achieve films with the desired quality. Since the laser interacts directly with the deposited material, the laser processing parameters, which are laser power and laser scanning velocity, have significant effects on the final quality of the deposited films. One of the contributions of this thesis is to develop a characterization procedure to tune the process parameters for the selective deposition of conformal patterns on optical fiber gratings with the desired geometrical features and mechanical properties.

1.8 Femtosecond Laser Micromachining of FBGs: Simultaneous Measurement of Temperature and Concentration

As mentioned before, the index of refraction of the surrounding medium can barely affect the reflection spectra of FBGs. As a result, FBGs in their original shape are not capable of monitoring the index of refraction which is an indication of liquid concentration. It is

demonstrated in this thesis that the selective inscription of micro-grooves on the outer surface of optical fibers makes FBGs sensitive to the index of refraction and the concentration of the surrounding medium. Laser direct micromachining is chosen for the inscription of micro-grooves. Ultrashort laser pulses in the range of femtosecond (10^{-15} s) enable the fabrication of features with submicron precision in a large group of materials, specifically transparent dielectrics such as silica. Due to the non-linear phenomena occurring in the interactions of ultrashort pulse lasers with dielectric materials, these lasers can effectively be used for micromachining and structural modifications of transparent materials, such as silica. In this regard, micromachining of optical fiber sensors can be performed with femtosecond lasers. In this thesis, a femtosecond pulse laser is utilized to micromachine FBGs to enhance their performance for multi-parameter sensing, that is, simultaneous measurement of temperature and concentration.

1.9 Thesis Contributions

Following the assigned objectives of this research work, the main contribution of the thesis is

> *Design, modeling, and fabrication of optical fiber-based sensing devices with enhanced sensing capabilities.*

To realize the aforementioned contribution, the following tasks are conducted:

1. Opto-mechanical modeling of optical fiber gratings coated with periodic metal thin films and/or embedded in metallic structures,
2. Characterization of the LAMM process for metal thin-film deposition on the non-planar surface of optical fibers,
3. Design and fabrication of superstructure FBGs for simultaneous measurement of force and temperature by the deposition of periodic on-fiber silver thin films,
4. Development of FBG sensors for the simultaneous measurement of temperature and concentration by femtosecond laser micromachining of FBGs,
5. Characterization of the femtosecond laser micromachining process for the inscription of periodic micro-grooves on FBGs,
6. Development of low temperature processes to embed optical fibers in metal parts for structural health monitoring.

1.10 Thesis Outline

The present thesis consists of eight chapters. The problem definition and the statement of objectives and contributions are provided in Chapter 1. Chapter 2 is concerned with the background and the literature review of fiber grating sensors. In this chapter, FBGs and their characteristics for sensing physical parameters are introduced. The opto-mechanical modeling of FBGs is described in Chapter 3. In Chapter 4, laser microfabrication methods for the development of optical fiber-based sensing device are addressed. The chapter includes the characterizations of the LAMM and femtosecond laser micromachining processes. Chapter 5 addresses the modeling, design, and fabrication of superstructure FBGs with on-fiber silver thin films for the simultaneous measurement of strain and temperature. Chapter 7 covers the experimental results for the development of FBG sensors for the simultaneous measurement of temperature and concentration by employing femtosecond laser micromachining. Chapter 6 consists of the implementation of low temperature methods for embedding FBGs in metal structures for health monitoring and structural diagnostics. The thesis ends with Chapter 8 containing conclusions and future work.

Chapter 2

Background and Literature Review

In this chapter, the principles of optical fiber gratings, applications for sensing physical parameters, sensing limitations, and the existing literature are reviewed.

2.1 Fiber Gratings

Fiber gratings are permanent modulations of the index of refraction in optical fibers. Fiber gratings are classified into two groups according to their grating pitch length (Λ):

- Fiber Bragg Grating (FBG), also known as short period or reflection grating
- Long Period Grating (LPG), also known as transmission grating

Figure 2-1 depicts a FBG with gratings inscribed in the core of an optical fiber. An optical fiber is a cylindrical optical waveguide, made of fused silica, with a central core surrounded by a cladding layer. In single-mode optical fibers, the core has a diameter of 8 to 10 μm, and the cladding outside diameter is 125 μm [37]. The core has dopants such as germanium to increase the index of refraction (n_{core}). The index of refraction of the core is slightly higher than that of cladding (n_{clad}). In Corning SMF-28^{TM} single-mode optical fibers, which are standardized optical fibers for telecommunication applications, the difference between the indices of refraction of core and cladding is 0.36%. Accordingly, the

numerical aperture, defined as $N.A. = \sqrt{n_{core}^2 - n_{cladding}^2}$, is 0.14 for SMF-28 optical fiber in vacuum [6]. To protect optical fibers against physical damage, they are covered by a polymer coating of polyimide or acrylate, during the fiber production process (Figure 2-2). The working wavelengths for optical fibers are typically 1310 nm and 1550 nm in which the hydroxyl absorption loss is minimum.

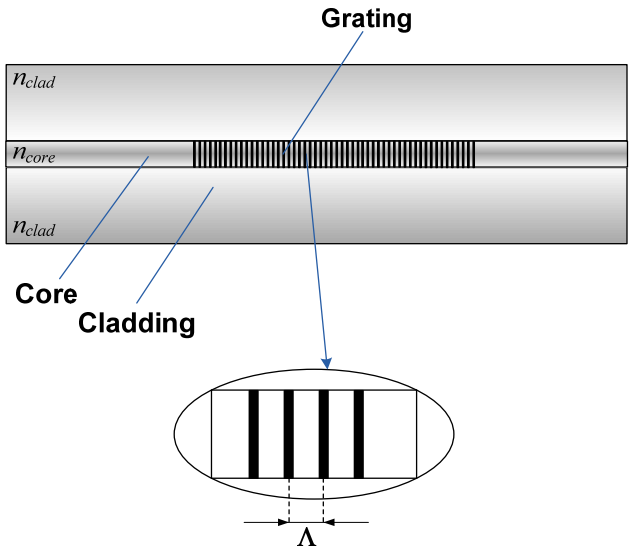

Figure 2-1: FBG with periodic modulation of the index of refraction in the core of optical fiber

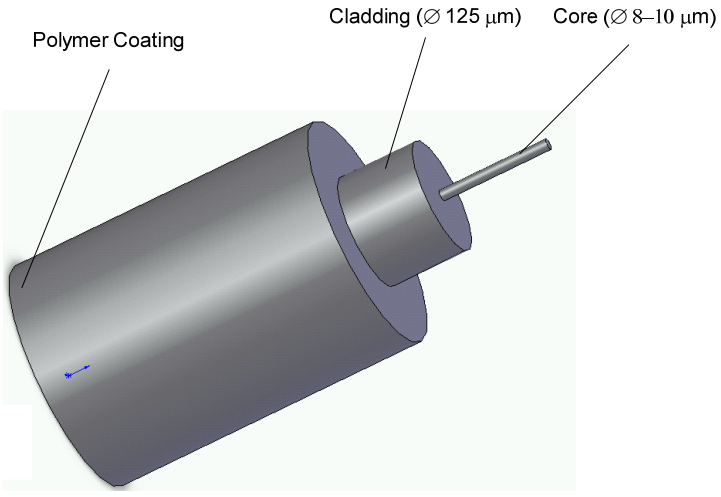

Figure 2-2: Structure of a single-mode optical fiber

A fiber Bragg grating, with a sub-micron periodic modulation of the index of refraction, functions as the filter. When a Bragg grating is exposed to a broadband spectrum of light, the guided light wave, propagating along the optical fiber, is scattered by each grating plane. As a result, parts of the spectrum at specific wavelengths are reflected back. The coupling between the forward and backward propagating modes results in a resonance condition. The resonance occurs at a specific wavelength called the Bragg wavelength (λ_B). Wavelengths not coincident with the Bragg condition degenerate progressively with weak reflections, whereas wavelengths close to the resonance wavelength determined by the Bragg condition (2.1), undergo strong reflections. Figure 2-3 shows the spectral response of a uniform Bragg grating. The Bragg wavelength is related to the effective propagating mode index of refraction (n_{eff}) and the grating parameters, as defined in the Bragg condition [2, 38]

$$\lambda_B = 2n_{eff}\Lambda \tag{2.1}$$

where Λ is the grating pitch length.

Typically, the modulation of the index of refraction ($\Delta n(z)$) along the fiber axis is expressed as [3]

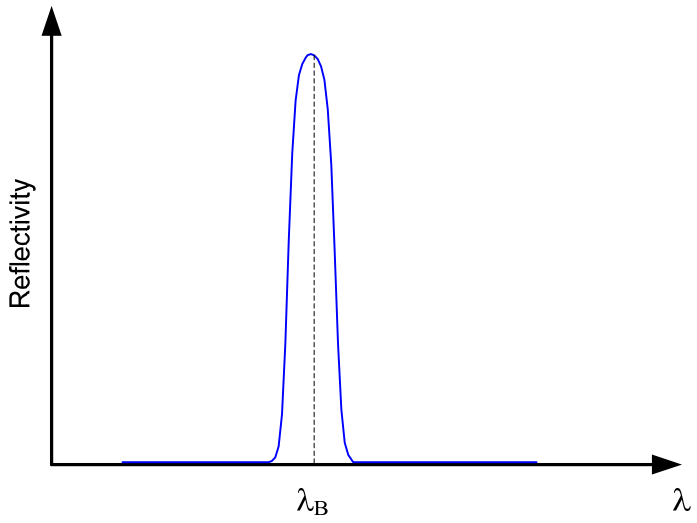

Figure 2-3: Spectral response of a uniform fiber Bragg grating

$$\Delta n(z) = \overline{\Delta n}(z)\left[1 + \nu_f \cos\left(\frac{2\pi}{\Lambda} z + \Phi(z)\right)\right] \tag{2.2}$$

where $\overline{\Delta n}(z)$ is the spatially averaged index change along the fiber, ν_f is fringe visibility, $\Phi(z)$ is the grating chirp determining the variations of the grating pitch length along the fiber, and the z direction is coincident with the fiber axis.

LPGs have longer periods of modulation than FBGs (typically larger than 100 μm) [39]. There is no reflection propagation mode in LPGs. However, the coupling between the propagating core mode and the cladding modes leads to a resonance condition in the transmitted spectrum. The transmitted spectrum of LPG contains a series of attenuation bands at specific wavelengths, as shown in Figure 2-4. Each attenuation band corresponds to the coupling with a cladding mode [39]. The wavelengths of the attenuation bands are obtained from

$$\lambda_i = (n_{eff} - n^i_{clad})\Lambda \tag{2.3}$$

where n^i_{clad} is the index of refraction of the i^{th} cladding mode, and Λ is the grating pitch.

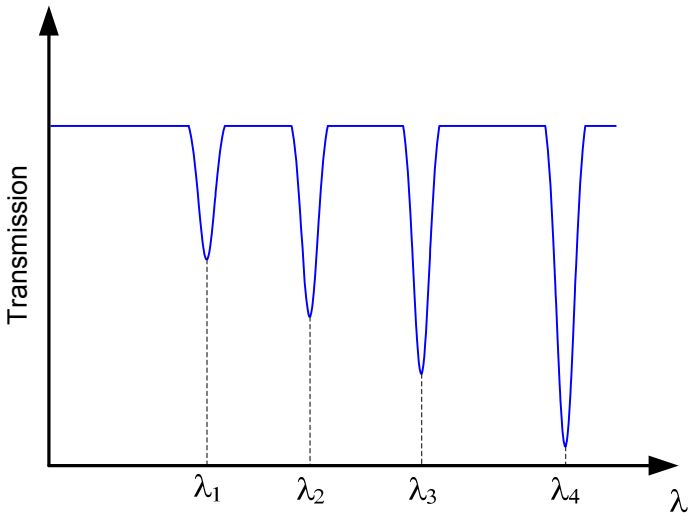

Figure 2-4: Spectral response of LPGs

2.2 Types of Fiber Bragg Gratings

FBGs are categorized into different groups in terms of the grating modulation function [38] as follows:

- **Common Bragg Reflector**

This is the simplest and the most popular type of FBG. The grating pitch is uniform along the fiber, and the grating planes are normal to the axis of the fiber (Figure 2-5a).

- **Blazed Bragg Grating**

In this type of FBGs, the gratings are tilted at an angle to the fiber axis (Figure 2-5b). They are used in erbium-doped fiber amplifiers for telecommunication applications.

- **Chirped Bragg Grating**

In chirped Bragg grating, the grating pitch length is not constant and varies along the fiber axis (Figure 2-5c). In this type, the reflected spectrum bandwidth is large because of the varying pitch length.

- **Apodized Grating**

To eliminate side lobes in the reflection spectrum of FBGs, gratings with non-uniform distribution of the modulations of the index of refraction, known as apodized gratings, are written in optical fibers. In apodized gratings, the amplitude of the average index change $(\overline{\Delta n})$ varies along the fiber axis [3]. The average index modulations for two common types of apodization are depicted in Figure 2-6. In Gaussian apodization, $\overline{\Delta n}$ is described as [3]

$$\overline{\Delta n}(z) = \overline{\Delta n}\, e^{\left(-\frac{36\ln 2}{L^2}z^2\right)} \tag{2.4}$$

and the raised-cosine apodization profile is obtained from [3]

$$\overline{\Delta n}(z) = \overline{\Delta n}\frac{1}{2}\left(1+\cos\left(\frac{\pi}{L}z\right)\right) \tag{2.5}$$

where L is the grating length.

The reflection spectra of a uniform and a Gaussian apodized FBG are plotted in Figure 2-7. It is evident that the reflection spectrum of apodized gratings does not have side lobes appeared in the reflection spectra of uniform gratings.

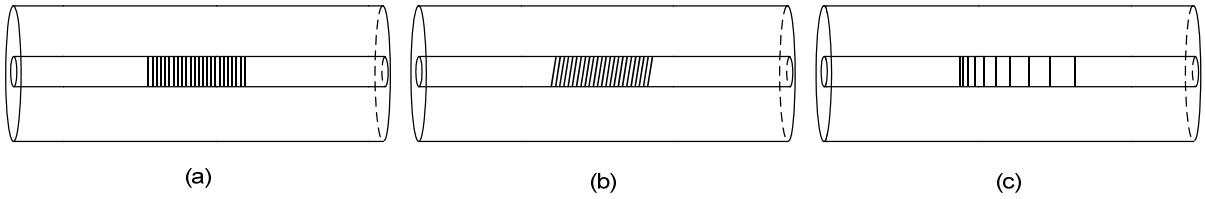

Figure 2-5: (a) Common Bragg reflector, (b) blazed Bragg grating, and (c) chirped Bragg grating

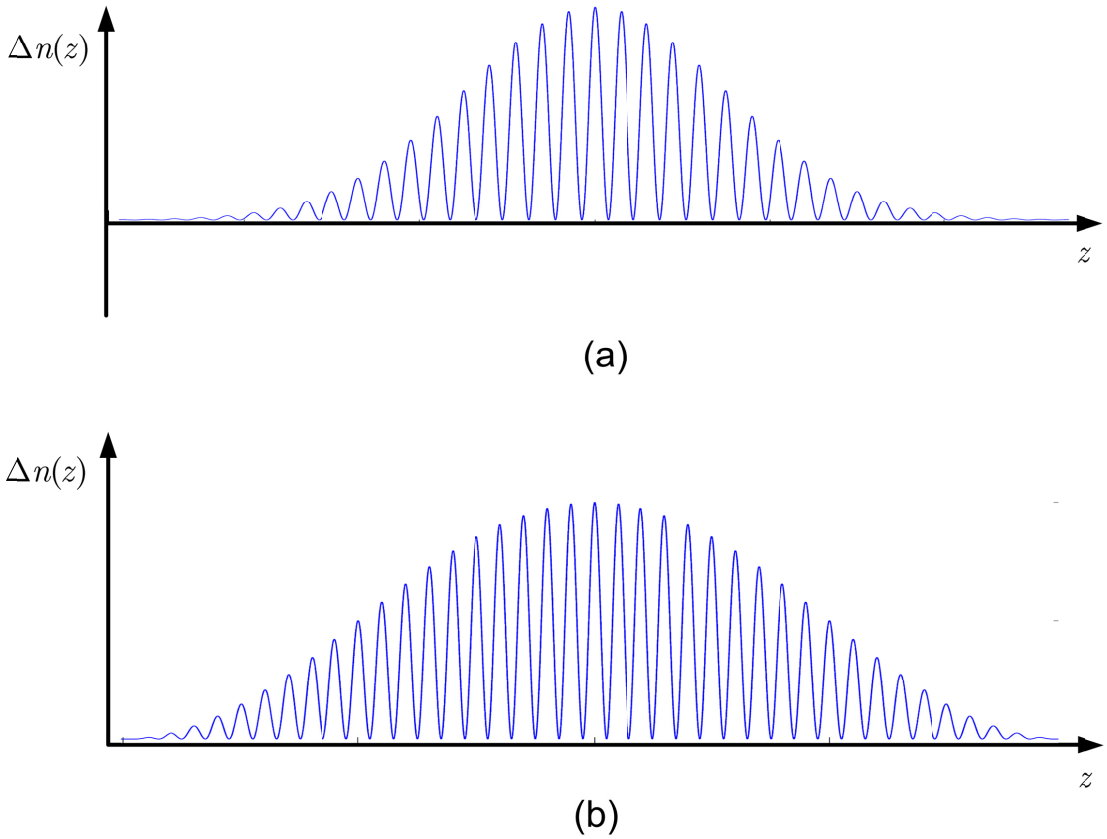

Figure 2-6: Apodized grating profiles (a) Gaussian apodization and (b) raised-cosine apodization

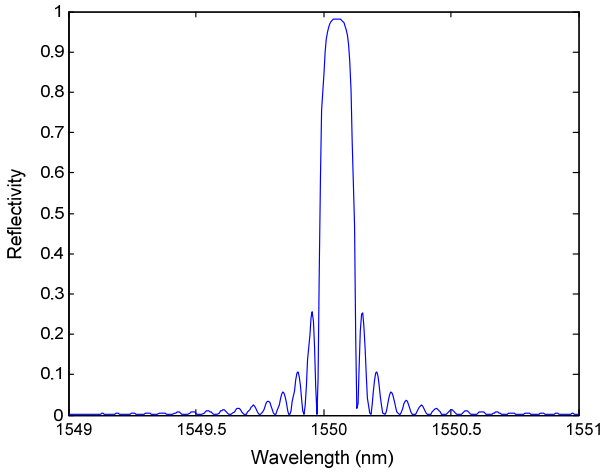

Figure 2-7: Reflection spectra of (a) uniform grating, $\overline{\Delta n} = 5\times10^{-5}$, $\nu_f = 1.9$, L=14 mm and (b) Gaussian apodized, $\overline{\Delta n} = 1\times10^{-5}$, $\nu_f = 25$, L=14 mm

2.3 Materials and Fabrication Techniques for Fiber Bragg Gratings

2.3.1 Photosensitivity of Optical Fibers: UV Exposure

Photosensitivity results in permanent changes in the index of refraction on exposure of optical fibers to radiation. The conventional method of grating inscription in optical fibers is UV radiation to create periodic index changes in the core of optical fibers. The photosensitivity of optical fibers arises from defects in the glass structure. The core of

optical fibers is doped with germanium which manifests itself as germanium oxides (GeO_n n=1 to 4) and forms defect bonds (Si-Ge/Ge-Ge) in the amorphous structure of silica glass. The defect bonds are absorbent to UV radiation and break upon exposure, and form GeE' color centers leading to the changes in the index of refraction [2].

The photosensitivity in germanosilicate fibers is increased by hydrogen loading. Hydrogen reacts with germanium to form G-H bonds. On UV exposure, due to bond breakages, Si-OH and/or Ge-OH, and Ge oxygen deficient centers form, resulting in the changes of the index of refraction [2].

2.3.2 Femtosecond Laser Induced Index Change

Femtosecond laser pulses can also be used for the inscription of gratings in optical fibers. High intensity laser pulses, bursting at ultrashort time steps in the range of femtosecond, result in structural changes such as the changes in the index of refraction of dielectric materials, due to the nonlinear phenomenon of multi-photon ionization [40-43].

2.3.3 Methods for Grating Inscription

Gratings are inscribed in optical fibers either by UV radiation or femtosecond laser micromachining. Despite the differences in the design and implementation, the methods have one common component, a laser as the radiation source. The methods for the grating inscription are as follow:

- **Interferometric Writing**

This method is based on the recombination of waves passing at different distances and producing interferometric fringe patterns. By changing the fringe patterns, different types of gratings are written into the fiber [38].

- **Phase Mask Writing**

Phase mask is a groove-shape grating etched in silica. The principles of the operation are based on the diffraction of the UV or IR femtosecond laser beams, passing through the phase mask to form a fringe pattern. The fringe pattern is focused on the optical fiber for the grating inscription [38, 40].

- **Point-by-Point Writing**

In this method, the laser beam passes through an ultra narrow slit, and a lens projects the image of the slit on the fiber, or the beam is focused by a lens in the case of femtosecond laser. With this method, the index of refraction is changed locally [38, 43].

2.4 Fiber Grating Sensors

One of the pertinent applications of fiber gratings is to sense physical parameters. In FBGs, the index of refraction and the grating pitch are functions of temperature and strain applied on the optical fiber. Consequently, the Bragg condition in FBGs and the attenuation bands wavelengths in LPGs are altered, when the fiber is subject to strain or temperature variations. By calibrating the spectral response of fiber gratings, they can be incorporated in the measurement of stress, strain, force, pressure, and temperature. The change in the Bragg wavelength ($\Delta\lambda_B$), in terms of the variations of n_{eff} and Λ under uniform elongation and temperature variations, is expressed as [38]

$$\Delta\lambda_B = 2(\Lambda\frac{\partial n_{eff}}{\partial l} + n_{eff}\frac{\partial\Lambda}{\partial l})\Delta l + 2(\Lambda\frac{\partial n_{eff}}{\partial T} + n_{eff}\frac{\partial\Lambda}{\partial T})\Delta T \tag{2.6}$$

Similarly, the shift in the attenuation band wavelengths in LPGs ($\Delta\lambda_i$) is obtained by

$$\begin{aligned}\Delta\lambda_i = &\left(\Lambda(\frac{\partial n_{eff}}{\partial l} - \frac{\partial n^i_{clad}}{\partial l}) + (n_{eff} - n^i_{clad})\frac{\partial\Lambda}{\partial l}\right)\Delta l \\ &+ \left(\Lambda(\frac{\partial n_{eff}}{\partial T} - \frac{\partial n^i_{clad}}{\partial T}) + (n_{eff} - n^i_{clad})\frac{\partial\Lambda}{\partial T}\right)\Delta T\end{aligned} \tag{2.7}$$

Non-uniform elongation and temperature distribution along FBGs results in the non-uniform variations of n_{eff} and Λ which changes the shape of the reflection spectrum . In this case, numerical methods should be incorporated to solve coupled-mode equations [3] to obtain the actual reflection spectrum. Figure 2-8 depicts the reflection spectra of a FBG at no-load conditions and a FBG with a linear distribution of axial strain along the optical fiber. The details of the coupled-mode equations to obtain the reflection spectrum of FBGs are discussed in Chapter 3.

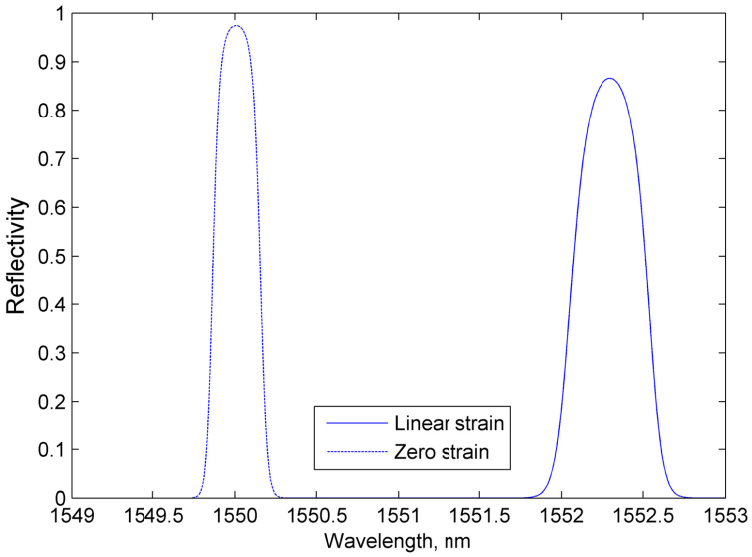

Figure 2-8: Reflection spectra of a FBG with zero strain and with linear strain variations along the grating expressed as $e_z = 0.002 + 0.004\left(z/L\right)$

2.5 Birefringence and Transverse Loading

In addition to axial strain, transverse strain components modify the spectral response of optical fiber sensors. Unequal diametric loads in FBGs result in birefringence in optical fibers. Birefringence is the difference in the index of refraction in two orthogonal directions. Birefringence divides the propagating modes into two orthogonal modes with different propagation constants. This splits the reflection peak into two peaks. The optical responses of FBGs with equal and unequal transverse strain components are plotted in Figure 2-9.

Strain induced birefringence in optical fiber sensors was a research topic in the past years. Bosia et al. [44] characterized the spectral response of single-mode FBGs subject to combined transverse and axial loadings. The authors studied bare and embedded-in-epoxy, low-birefringence and polarization-maintaining fibers. The experimental results were compared with the results obtained from finite element modeling. Gafsi *et al.* [45] analyzed the birefringence induced by transverse static loads on FBG sensors in plane stress and plane strain conditions. Wagreich *et al.* [46] studied FBGs with birefringence induced by diametric loads. Lawrence *et al.* [47] developed a FBG sensor for the independent measurements of diametric load components on the fiber. They inscribed Bragg gratings in

the core of high birefringence and polarization-maintaining optical fibers. The authors also developed a finite element model to obtain a scheme for the sensor calibration. Silva-Lopez *et al.* [48] investigated the influence of transverse loading on the peak splitting in the reflection spectrum of multi-core FBGs.

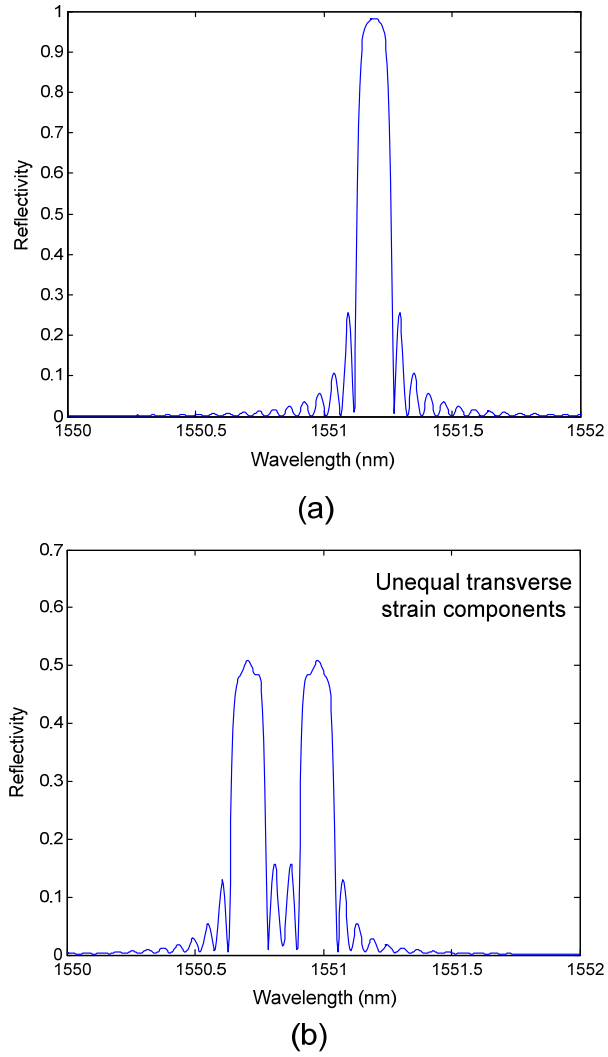

Figure 2-9: Reflection spectra of a uniform FBG with (a) equal transverse strain components and (b) unequal transverse strain components causing birefringence

2.6 Structural-Thermal Coupling in Fiber Grating Sensors

According to (2.6), a linear coupling exists between the effects of temperature and strain on the shifts in the Bragg wavelength. When it comes to sensing, the structural-thermal

coupling can cause inaccuracies in monitoring one parameter, while the other parameter is changing. For instance, structural sensing in environments with temperature fluctuations such as power plant generators is not possible with only one sensor. In other words, the influence of temperature and strain cannot be determined by reading the Bragg wavelength shifts.

2.7 Multi-Parameter FBG Sensors for Structural-Thermal Sensing

As mentioned in the previous section, one of the limitations of FBGs is the linear coupling of the effects of temperature and strain. If the sensor is subject to the simultaneous variations of strain and temperature, their effects cannot be discriminated in the spectral response. FBG strain gauge rosettes, which are temperature independent, have been developed for multi-parameter measurements. In the design of such strain gauges, more than one FBG is used so that one of them can be used for the temperature compensation [22, 23]. By inscribing a chirped grating in a tapered optical fiber, Xu *et al.* [49] developed a temperature independent FBG. It was shown that the bandwidth of the reflected spectrum was only the function of strain. Hsu *et al.* [24] developed a temperature compensated pressure sensor with a FBG. A bi-material was used to compensate for the effect of temperature. Yoffe *et al.* [25] proposed a technique for the temperature compensation of FBGs by using two materials with different thermal expansions. The FBG was mounted in a passive mechanism under tension. For the simultaneous measurement of strain and measurement, Du et al.[50] designed a combined FBG and Fabry-Perot, called Grating Fabry-Perot Cavity (GFPC). James *et al.* [26] devised a FBG sensor for the simultaneous measurement of temperature and strain by inscribing gratings in two fibers with different diameters and splicing them as a single sensor. Yu *et al.* [51] developed a FBG sensor for the simultaneous measurement of displacement and temperature. The FBG was mounted on the surface of a triangular cantilever beam. The deflection of the beam causes non-uniform grating pitch, whereas the temperature variations result in the Bragg wavelength shift. Zhang *et al.* [52] used a FBG mounted on a bilateral beam to measure force/displacement and temperature simultaneously. Dong *et al.* [27] presented a displacement sensor, based on FBGs that were mounted on a slanted cantilever beam. It was found that the bandwidth of the reflection spectrum was insensitive to temperature. To reduce the temperature dependence of FBGs, Iwashima *et al.* [28] developed a technique by packaging FBGs in

liquid crystalline polymer tubes with negative coefficient of thermal expansion. Tanaka *et al.* [53] studied FBGs embedded in a carbon fiber reinforced plastic. They proposed two methods, namely, the hybrid sensor and laminate sensor, to eliminate the effect of temperature. The use of UV-written superstructure FBGs has also been proposed for the simultaneous measurement of strain/pressure and temperature [29, 30]

2.8 FBGs for Structural Health Monitoring

Optical fibers exhibit promising features, distinguishing them from other types of electric and electromagnetic sensors. These characteristics are classified as light weight, small size, long-term durability, long-range linearity, immunity to electromagnetic noises and disturbances, and resistance to corrosion. These features encourage the development of methods and systems for structural health monitoring with FBGs. They can be used as embedded sensors for structural diagnostics. Furthermore, some embedding methods can be devised to enhance the performance of the sensor and eliminate some inherent limitations.

Recently, embedding optical fiber gratings in composite laminates for the delamination diagnostics and the structural sensing has been reported. Guemes *et al.* [7] studied embedded FBGs in composite laminates. They investigated the effect of transverse and longitudinal stresses in a composite laminate on the spectral response of the embedded FBG. Kuang *et al.* [54] reported embedding of FBGs in a fiber-metal laminate composite during the fabrication process to monitor the residual strains after processing. Lau *et al.* [8]used embedded FBGs in composite-strengthened concrete structures for structural health monitoring. Ling et al.[16, 55, 56] studied the feasibility of embedding FBGs in composite laminates for non-uniform strain sensing, delamination diagnostics, and dynamic strain measurements.

Metal-embedded optical fibers have also been reported in the literature. Embedding optical fibers in metal parts is a challenging process. Optical fibers are susceptible to high temperatures which can degrade the gratings or damage the fiber permanently. Gratings thermal degradation begins at temperatures as low as 200 ^{o}C, depending on the fiber dopants. Therefore, any embedding process involving high temperatures cannot be directly used for the embedding process. In addition, high temperature processes can cause failure by forming large residual stresses in the optical fiber. Some techniques have been proposed for embedding optical fibers in metals. Casting, which is a high temperature process, can be

used for embedding optical fibers in metal elements with low melting points. Seo *et al.* [57] proposed a numerical model to analyze optical fibers coated with molten tin. Lee *et al.* [58] studied the performance of fiber optic Fabry-Perots embedded in aluminium by casting in graphite moulds. Lin *et al.* [59] demonstrated that the thermal sensitivity increases for FBG sensors coated with solder. Lupi *et al.* [13] coated FBGs with zinc and copper. They used electrowinning for the deposition of the metal layer preceded by pre-coating the optical fiber with aluminium.

Another recognized embedding methodology is electrodeposition. In this method, a protective layer is fabricated around the fiber prior to further steps that might involve high temperature processes. Li *et al.* [9, 60] investigated the embedding of FBGs in nickel and steel using electrodeposition, followed by Shape Deposition Manufacturing (SDM). Electrodeposition was used for the fabrication of a protective layer around the fiber. Since fibers are not conductive, the electrodeposition cannot be used directly to grow metal coatings on fibers. A thin layer of titanium was deposited on the fiber prior to the nickel electrodeposition. Afterwards, SDM, involving laser material processing with powder injection, was employed for the final embedding step. Sandlin *et al.* [14] proposed a method of coating FBGs using electroplating and brazing. Prior to electroplating, the optical fiber was coated with a thin silver interlayer by the reduction of silver ammonium complex ($[Ag(NH_3)_2]^+$) with glucose in strongly alkaline conditions. Then, electroplating was used to deposit a nickel layer on the optical fiber. The nickel-coated fiber was embedded in a substrate of Inconel by vacuum brazing technique. Another low temperature method for embedding optical fibers is ultrasonic consolidation. Kong *et al.* [15] chose this process to embed optical fibers in aluminium parts.

Embedding optical fibers in materials such as rubber and epoxy for the fabrication of customized sensors has also been reported. Tjin *et al.* [61] developed a shear test sensor based on FBGs. The FBG was embedded in a rubber part placed between two plates of carbon composite material. The shear stress applied to the plates changes the period of the grating and the reflection spectrum. Peters *et al.* [62] investigated the response of FBGs embedded in epoxy under non-homogeneous strain fields.

Since the coefficient of thermal expansion of silica is small at cryogenic temperatures, its sensitivity is reduced for very low temperature measurements. The optical fiber sensor can be embedded in or attached to a part made of a material with a larger cryogenic coefficient of thermal expansion to increase the sensitivity of the measurements. Gupta *et al.* [63]

developed an embedded FBG for sensing temperatures as low as 80 K. Mizunami *et al.* [64] studied the performance of FBGs mounted on a Teflon substrate at temperatures as low as 77 K. Teflon has a large coefficient of thermal expansion at low temperatures relative to optical fibers.

In addition to the fabrication of parts with embedded optical fiber sensors, the modeling of the embedded sensor is of primary importance for design optimization and sensor calibration. Using an embedded fiber optic Fabry-Perot, Kim *et al.* explored the measurement of strain and temperature changes [4]. They developed a model of embedded fiber optic Fabry-Perot sensors to relate the changes in strain and temperature to the sensor's spectral response. They used the linear photo-elastic and thermo-optic models of optical waveguides. Prabhugoud *et al.* [65] developed a finite element model for the analysis of the spectral response of embedded FBG sensors.

2.9 FBGs with On-Fiber Thin Films

Some research studies have been conducted to deposit metal thin films on FBGs for dispersion compensation, tunable Bragg gratings, and sensitivity enhancement at cryogenic temperatures. On-fiber thin films have also been deposited conductive interlayer for embedding optical fibers in metallic structures. Electrowinning, sputtering, electron beam evaporation, and electroplating techniques are conventional methods that have been employed for the deposition of on-fiber Ti, Ag, Au, Pt, Zn, Pd, and Cu films [13, 33-36]. Figure 2-10 shows a FBG coated with Zn by using electrowinning. The Zn layer was deposited on a pre-coated layer of Al.

Li *et al.* studied the thermal response of tunable FBGs coated with Ti, Pt, and Ni both analytically and experimentally [33]. Fox *et al.* developed on-fiber resistive and piezoelectric thin films for the fabrication of tunable FBGs using sputtering [35]. Ahuja *et al.* [66] devised a tunable FBG by depositing metal thin films on optical fibers. By joule heating, the index of refraction of the coated fiber at the deposition locations was modified due to the thermo-optic effect. They showed that by the periodic deposition of metal thin films with different thicknesses, superstructure FBGs with tunable sideband reflectivities can be produced. Eggleton *et al.* [67] deposited gold layers on FBGs with variable thickness along the fiber for dispersion compensation in FBGs. When the coating is heated, a chirp pattern is generated in the grating because of the non-uniform distribution of temperature along the fiber. Rogers

et al. [68] coated FBGs with two independent metal layers, separated by an electric insulator layer. By controlling the electric current in the metal coatings, the Bragg wavelength is changed and a chirp is induced in the grating.

Despite the advantages of the aforementioned methods, they lose their functionality and efficiency for selective deposition of thin films and on-fiber thin-film patterning. They require material removal and the use of a mask which makes the process slow and expensive.

Figure 2-10: FBG coated with Zn on a pre-coated layer of Al [13]

2.10 Fiber Gratings for Monitoring Liquid Concentration

In FBGs written in single-mode optical fibers, the dominant mode (LP_{01}) is confined in the core, and the core-cladding mode coupling does not manifest itself in the reflection spectrum. As a result, the reflection spectrum is not influenced by the index of refraction of the surrounding medium. The changes in the chemical composition of fluids lead to changes in their index of refraction. Making the optical fiber sensitive to the index of refraction produces a chemical sensor.

Etching of the cladding of FBGs using Hydrofluoric (HF) acid has been proposed to increase the sensitivity of FBGs to the index of refraction of the surrounding liquid [17-21]. HF is an etchant for silicon dioxide and extremely hazardous. The HF-etched FBGs can be used to measure the concentration of the surrounding liquid via the measurement of the index of refraction. A specific length of the fiber with inscribed gratings is placed in a

solution of HF acid, to reduce the diameter of the optical fiber. Etching rates of 1.8 mm/min in 52% HF solution [17], 80 nm/min in buffered oxide etch (BOE) [18], and 650 nm/min in 24% buffered HF solution [19] have been reported in the literature. Figure 2-11 shows an etch-eroded optical fiber with a diameter reduced to 6 μm.

Although HF etching increases the sensitivity of the FBG to the refractive index of the surrounding liquid, the fabrication process is slow, and the diameter reduction reduces the mechanical strength of optical fibers, which increases the risk of fiber breakage during the measurements. When it comes to selective removal and patterning, a mask is needed for the etching process. In addition, the HF etching process is isotropic and non-directional, which creates undercuts.

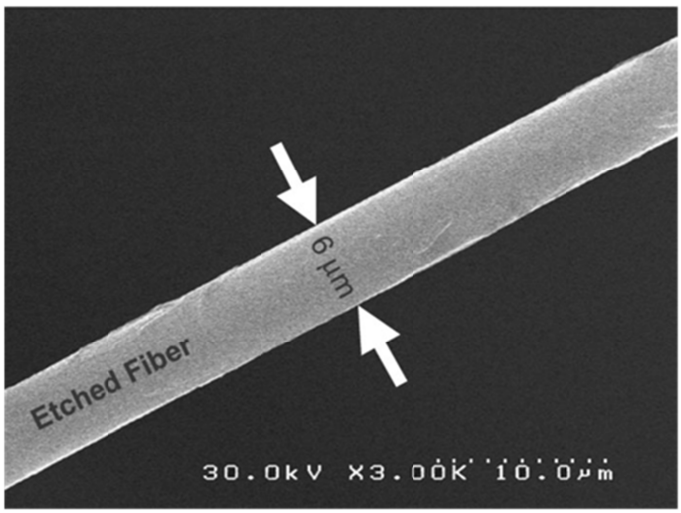

Figure 2-11: Scanning electron microscopy image of a FBG etched to 6 μm [17]

2.11 Signal Interrogation

In FBG sensing applications, it is essential to analyze the spectral response of the sensor in order to interrogate the physical parameters. Several research papers have been published for the reconstruction of strain and temperature fields sensed by optical fiber gratings. The procedure for the identification of measured parameters is based on solving an inverse problem in optics; that is, finding the grating parameters and physical temperature and strain fields by using the reflection spectrum of FBGs. Huang *et al.* [69] developed a technique for the interrogation of FBGs based on the measurement of the phase spectrum.

They also presented a method to interrogate the reflection spectrum of FBGs for distributed strain sensing with a spatial resolution of 1 mm [70]. Skaar *et al.* [71] suggested a method based on the combination the Runge-Kutta method and a genetic algorithm for the synthesis of FBGs. Cormier *et al.* [72] developed a decoding method using genetic algorithm for parameter synthesis. The method can be used for designing fiber gratings and reconstructing the measured parameters. For the reconstruction of FBG parameters, Azana *et al.* [73] used time-frequency signal analysis. Casagrande *et al.* [74] proposed an interrogation method for the distributed uni-axial strain sensing by applying genetic algorithm. Gill *et al.* [75] developed a genetic algorithm to reconstruct the axial strain applied to the fiber.

2.12 Thin-Film Fabrication Processes: Laser Direct Write Methods

Ever increasing requirements for inexpensive and rapidly produced thin films have prompted the development of novel direct fabrication technologies. Over the past decades, the conventional methods such as photolithography and screen-printing have been extensively used for the fabrication of thin films in the microelectronics industry. When it comes to surface patterning, the conventional methods involve the addition and removal of materials incorporating masks, which makes the deposition process slow and expensive. Furthermore, most of the available techniques involve high temperature processes. This limits the selection range of substrate materials and creates thermally induced residual stresses which can result in delamination and materials failure. Although, photolithography techniques are efficient for the fabrication of thin films with nano-scale feature sizes, these techniques lose their efficacy in large sizes (10-100 μm), as the material waste increases due to the material removal. Furthermore, the requirement for temperature/pressure controlled chambers in some thin-film fabrication processes increases the cost and production time.

To address the issues related to conventional thin-film fabrication processes, direct fabrication techniques have been considered as alternatives. Despite different names for direct writing technologies, all of them share a common feature: selective and layer-by-layer deposition without the use of masks. In this regard, with the recent advances in laser material processing, the laser beam has also been incorporated in a variety of direct write technologies. The characteristics of the laser beam, i.e. coherence and monochromaticity,

provide the potential for the development of micro-scale laser-assisted additive manufacturing technologies.

Considering their advantages, direct write technologies can be alternatively incorporated for on-fiber thin-film deposition. In the following, various laser-assisted direct thin-film writing processes are reviewed.

2.12.1 Laser Chemical Vapor Deposition

Laser Chemical Vapor Deposition (LCVD) is a type of Chemical Vapor Deposition (CVD) process for the localized deposition of thin films. The LCVD equipment consists of a chamber with inlets for reagent gases. In the chamber, the reagent gases are decomposed by the heat generated from a focused laser beam to form metal and ceramic depositions on a substrate. The laser heating is performed locally. As a result, patterning and direct writing are achievable by moving the focused laser beam relative to the substrate. The deposition rate in the CVD process is dependent on the diffusion of gases into and out of the process zone. Since, in LCVD, the diffusion paths are distributed in a three-dimensional semispherical region above the focused laser spot on the substrate rather than one-dimensional diffusion paths in CVD, the deposition rate in LCVD is much higher than CVD [76].

2.12.2 Laser Induced Forward Transfer

Laser Induced Forward Transfer (LIFT) was introduced by Bohandy in 1986 [77]. In this technology, the deposited material is pre-coated with a thickness less than a few hundreds of nanometers on one side of a transparent support, called target or donor. The substrate, or the receptor, is mounted in a very small standoff length (25-75 μm) from the donor in such a way that the thin film faces the substrate. The transparent support is radiated by a focused pulse laser beam from the back side, causing the laser energy to be absorbed by the pre-coated material [78]. The generated heat ablates the film from the support, and in an ideal case, the ablated material is transferred to the substrate. Typical laser pulse durations for the ablation and transfer process are in the range of nanosecond to femtosecond [79]. Patterning can be performed by moving the laser beam, relative to the substrate. The thickness of the deposited patterns is controlled by the repetition of the laser radiation process.

The LIFT process has been incorporated for the deposition of various metals, oxides, polymers, semiconductors, and biological materials. Dielectric inks [80], Au/Sn [79], Au for contact masks [81], Ni [82], InO_x active optical structures [83] have been deposited using LIFT. LIFT has also been used for semiconductor die transfer [84].

2.12.3 Matrix-Assisted Pulse Laser Evaporation Direct Write

Matrix-Assisted Pulse Laser Evaporation Direct Write (MAPLE DW) is similar to LIFT in terms of the application of laser to radiate a transparent support to induce material transfer. However, the materials for the deposition are solved in a matrix solvent and pre-coated on a support forming a ribbon. The incident focused laser beam evaporates or decomposes the solvent, causing its loss of adhesion to the support. The solute is separated from the support, and the vapor pressure of the solvent pushes it toward the substrate. The solvent vapor is pumped away by the flow of a gas to hinder the formation of residues.

This process has been employed for the conformal direct deposition of GPS antennas on a spherical substrate. For this application, the substrate is rotated under the deposition head in addition to its linear movements [85].

2.12.4 Laser Induced Thermal Imaging

Laser Induced Thermal Imaging (LITI) is a surface patterning process with specific applications in organic electronics [86, 87]. In LITI, the material that is deposited is pre-coated on a donor film, vacuumed to the substrate or the receptor. The donor is selectively exposed to a laser radiation. The donor has a light-to-heat conversion layer, an ejection layer, and the final layer which is the material for the deposition. The generated heat decomposes the organic material layer to gas, which expands and propels the final layer to the substrate [86]. A writing accuracy of 2-5 um is achieved in this technology.

2.12.5 Drop-on-Demand (DOD) Inkjet Printing and Laser Curing of Nanoparticles

Inkjet printing assisted by laser curing has been used to deposit metal nanoparticles, e.g. gold and silver nanoparticles. In inkjet printing, electric pulses at a specific frequency are applied to a piezoelectric actuator, surrounding a tube connected to a reservoir or connected to a membrane at one side of the reservoir. The reservoir is filled with conductive inks such as nanoparticle suspensions. The pressure impulse, generated from the piezo actuator in the

reservoir creates droplets, with a diameter of 60-100 um which exit through an orifice.. The droplets contain the solvent and the nanoparticles [88]. To reach an optimum viscosity of the liquid, the reservoir is maintained at a constant temperature. By applying electric pulses to the piezo actuator, droplets are continuously deposited on a moving substrate. To improve the deposition quality, the substrate can be heated.

The deposited material contains the suspension liquid and nanoparticles. To produce conductive patterns, the nanoparticles should agglomerate and make clusters. After the deposition, a laser beam is used to cure the as-deposited material, evaporate the solvent, and sinter the nanoparticles.

2.12.6 Aerosol Jet Deposition

Aerosol Jet deposition is a flow-based direct write process for the deposition of thin coatings of various materials, including metals, resistors, dielectrics, organic semiconductors, and carbon nanotubes [89-94]. When it comes to the deposition of metal films, the process incorporates laser for the post-annealing of the deposited materials.

Aerosol Jet deposition technology has been introduced by Optomec Inc. Laser-Assisted Maskless Mirodeposition (LAMM) is a version of Aerosol Jet deposition technology at the University of Waterloo. The LAMM workstation has a Continuous Wave (CW) erbium-doped fiber laser at a wavelength of 1550 nm for post-sintering of deposited metal nanoparticles.

The deposition of metal thin films by using LAMM is conducted in two steps: (1) micro-deposition, in which metal nano-particles suspended in liquid are atomized to aerosols and injected from the deposition head toward a moving substrate, (2) laser post-processing, in which the laser beam is directed for post-heating and sintering of the as-deposited material. The micro-deposition and sintering processes can be conducted at room temperature. Figure 2-12 shows the flow mixing mechanism in the deposition head of LAMM and the aerosol flow exiting from the deposition tip. LAMM has the capability of depositing conformal patterns on non-planar surfaces and three-dimensional objects.

The LAMM process is superior to the conventional thin film deposition technologies such as physical vapor deposition methods in different aspects. LAMM is a maskless and direct write process which eliminates the addition and removal of materials. This can reduce the production time and cost significantly. Thicknesses in the range of 500 nm to tens of micro-

meters can be controlled by the layer-by-layer deposition fashion. The process can be performed at atmospheric pressure and does not need clean room facilities. Compared with other direct write methods such as inkjet printing, the gap between the deposition head and the substrate varies from 2 to 5 mm which enables conformal deposition patterns on non-planar surfaces. For the sintering of the nanoparticles, the substrates with the deposited patterns can be heated by a furnace or hot plate. However, the laser spot heating provides a faster sintering process by creating local heating zones and preventing the entire substrate from being exposed to high temperatures.

These features makes the LAMM process a suitable candidate for the deposition of thin films on optical fibers. In this thesis, the LAMM process is successfully implemented for the deposition of on-fiber silver films in order to develop sensing devices based on FBGs such as superstructure FBGs and metal-embedded FBGs.

Figure 2-13a shows silver pads deposited on a planar silica substrate with a width of about 20 μm. A typical non-planar deposition of silver film is also illustrated in Figure 2-13b.

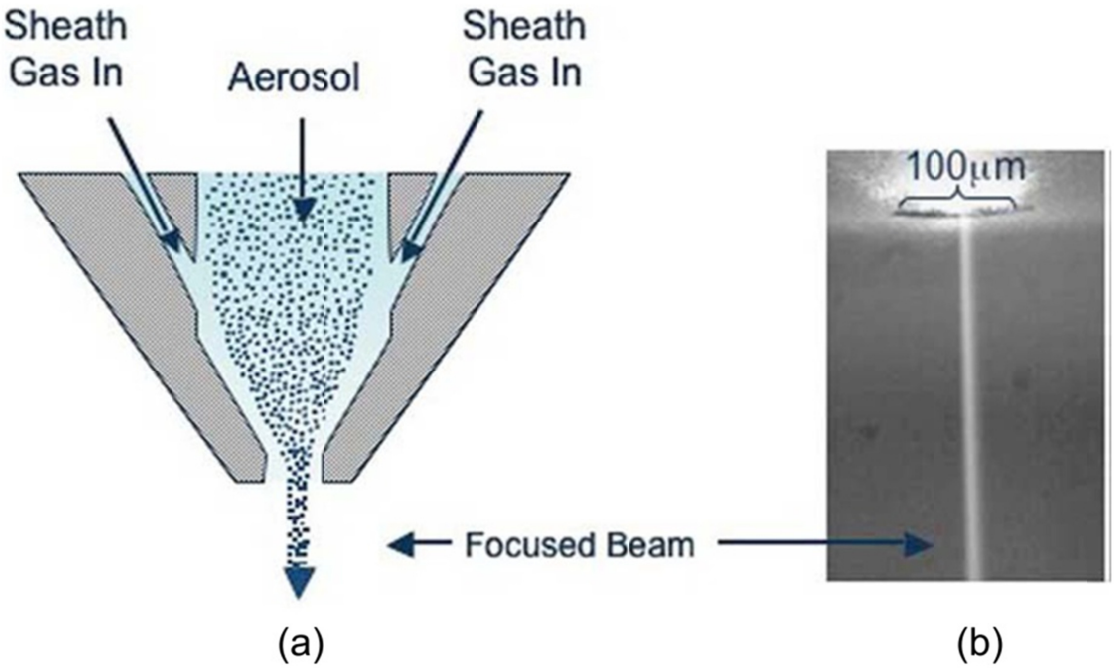

Figure 2-12: (a) Flow mixing mechanism in the deposition head of LAMM and (b) aerosol flow from the deposition head of LAMM (Courtesy of Optomec Inc., USA)

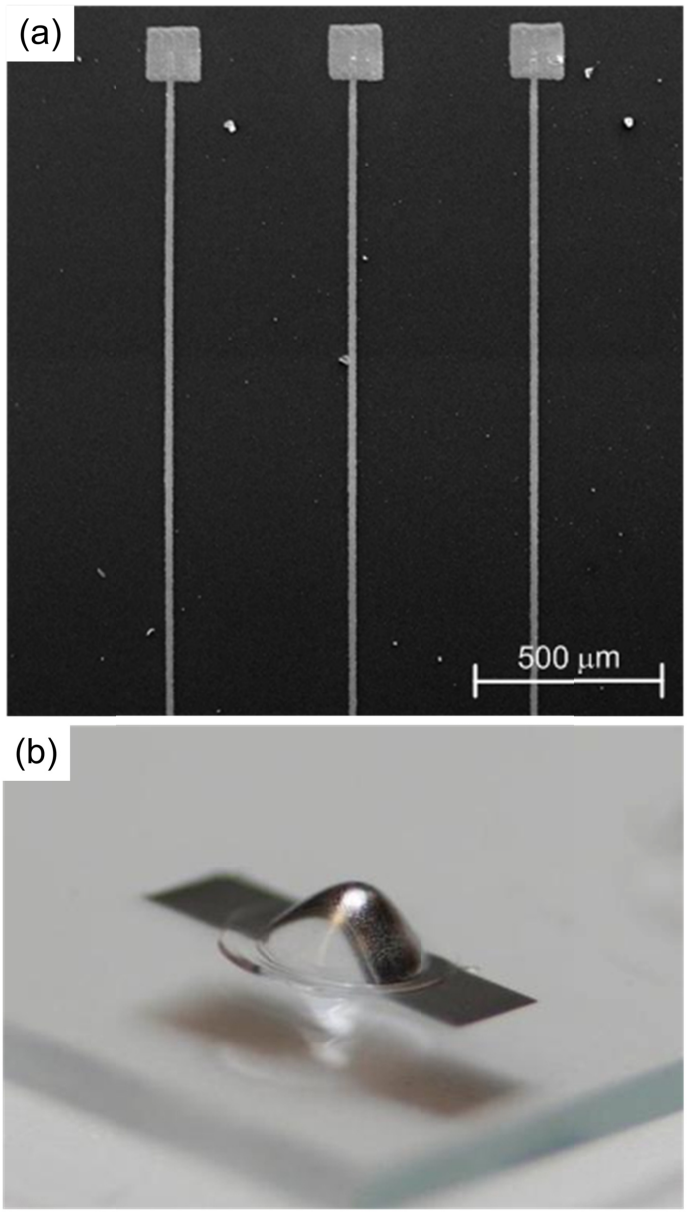

Figure 2-13: Typical silver patterns deposited by LAMM (a) planar substrate and (b) non-planar surface

2.13 Summary

In this chapter, the literature related to optical fiber sensors technology was reviewed. The literature review revealed the lack of contributions to several areas related to optical fiber sensors, especially FBGs. The technologies and methods, which have been proposed for

multi-parameter sensing with FBGs, are so complex for real-world applications. Most of the methods require additional mechanisms to compensate for the effect of temperature, which compromises the miniaturization of the sensing modules.

In addition, research on embedded FBG sensors for structural health monitoring in metallic structures has not matured yet. New manufacturing methods need to be devised and implemented to develop such sensors. In addition, opto-mechanical models should be developed for the design and optimization of embedded optical fiber sensors.

To the best knowledge of the author, there is no record of design and modeling of superstructure FBGs with on-fiber films for multi-parameter sensing. The optimized design of such sensors necessitates the development of a comprehensive model with the capability of predicting the spectral response of the sensor at various loading conditions, i.e. structural and thermal loading.

According to the literature, there is no record of on-fiber thin-film fabrication using direct write methods. Given the particular features and advantages of direct write methods, development of new generations of optical fiber-based sensors can be facilitated by the selective deposition of on-fiber thin films. The process for on-fiber thin-film deposition requires process characterization to determine the films morphological features and mechanical properties in terms of the process parameters.

According to the reviewed literature, HF etching of optical fibers is the only method for the enhancement of the sensitivity of FBGs to the concentration of their surrounding medium. Laser micromachining with ultrashort pulse lasers has not been reported for this application. Given the advantages of ultrashort pulse lasers in micromachining dielectric materials such as glass, the development of FBG-based concentration sensors can be facilitated by ultrashort pulse laser micromachining. Laser micromachining enables selective patterning and material removal from the outer surface of optical fibers. This makes them sensitive to the concentration of liquids.

Chapter 3

FBG Theory and Opto-Mechanical Modeling

This chapter covers the theory and opto-mechanical modeling of FBGs. The chapter includes the opto-mechanical properties of optical fibers, induced optical anisotropy in optical fibers caused by temperature and structural loading, light propagation in optically anisotropic optical fibers, and the coupled mode-theory to obtain the spectral response of FBGs. In addition, the theory of superstructure FBGs is elaborated at the end of this chapter.

3.1 Opto-Mechanical Properties of Optical Fibers

The index of refraction in silica which is a dielectric material is a function of the applied strain and temperature. Due to photo-elastic and thermo-optic effects, strain and temperature induce changes in the index of refraction [95].

Figure 3-1 shows a dielectric medium (Ω) exposed to temperature and strain distributions, $T(x,y,z)$ and $e_i(x,y,z)$ respectively, in the xyz coordinates. The index of refraction tensor in dielectric materials in the Cartesian coordinates is given by

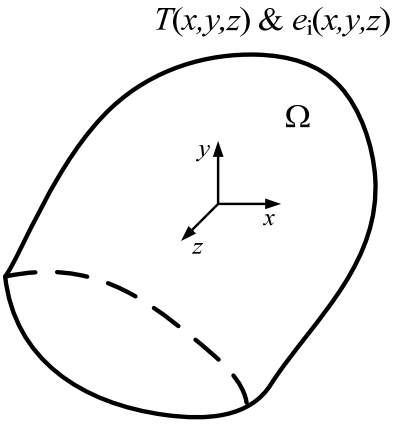

Figure 3-1: Dielectric material under temperature and strain distributions

$$[n] = \begin{bmatrix} n_{xx} & n_{xy} & n_{xz} \\ n_{yx} & n_{yy} & n_{yz} \\ n_{zx} & n_{zy} & n_{zz} \end{bmatrix} \tag{3.1}$$

Since the tensor is symmetric, it is represented by six elements as follows:

$$[n] = \begin{bmatrix} n_1 & n_6 & n_5 \\ n_6 & n_2 & n_4 \\ n_5 & n_4 & n_3 \end{bmatrix} \tag{3.2}$$

The photo-elastic and thermo-optic effects are defined by introducing dielectric impermeability tensor ($[B]$) [95], where

$$\begin{aligned} B_i &= \frac{1}{n_i^2} \qquad i = 1,2,3 \\ B_i &= 0 \qquad\quad i = 4,5,6 \end{aligned} \tag{3.3}$$

By neglecting the second-order terms, the change in the impermeability tensor (ΔB_i), due to the applied strain (photo-elastic effect) and temperature (thermo-optic effect), is obtained by [4, 5]

$$\Delta B_i = Q_i \Delta T + p_{ij} e_j \qquad i,j = 1...6 \tag{3.4}$$

where $[p]$ is the strain-optic tensor, called Pockel's photo-elastic constant. For an isotropic material, $[p]$ is expressed as

$$[p] = \begin{bmatrix} p_{11} & p_{12} & p_{12} & 0 & 0 & 0 \\ p_{12} & p_{11} & p_{12} & 0 & 0 & 0 \\ p_{12} & p_{12} & p_{11} & 0 & 0 & 0 \\ 0 & 0 & 0 & \frac{(p_{11}-p_{12})}{2} & 0 & 0 \\ 0 & 0 & 0 & 0 & \frac{(p_{11}-p_{12})}{2} & 0 \\ 0 & 0 & 0 & 0 & 0 & \frac{(p_{11}-p_{12})}{2} \end{bmatrix} \tag{3.5}$$

e_j's are the elements of the strain tensor,

$$[e] = \begin{bmatrix} e_1 & e_6 & e_5 \\ e_6 & e_2 & e_4 \\ e_5 & e_4 & e_3 \end{bmatrix} \tag{3.6}$$

and Q_i is defined as

$$Q_i = Q_i' - p_{ij}\alpha_j \tag{3.7}$$

where

$$Q_i' = \left(\frac{\partial \left(\frac{1}{n_i^2} \right)}{\partial T} \right)_{\text{Constant Stress}} \qquad i = 1...6 \tag{3.8}$$

For an optically isotropic material,

$$\begin{aligned} Q_i' &= \frac{\partial}{\partial T}\left(\frac{1}{n_i^2}\right) = -\frac{2}{n_i^3}\left(\frac{\partial n_i}{\partial T}\right) = -\frac{2}{n_i^3}\left(\frac{\partial n}{\partial T}\right) \qquad i = 1,2,3 \\ Q_i' &= 0 \qquad\qquad i = 4,5,6 \end{aligned} \tag{3.9}$$

where $\partial n \,/\, \partial T$ is constant, and α_j's are the coefficient of thermal expansion of the dielectric material. For isotropic materials

$$\begin{aligned} \alpha_i &= \alpha \qquad i = 1,2,3 \\ \alpha_i &= 0 \qquad i = 4,5,6 \end{aligned} \tag{3.10}$$

The substitution of (3.9) and (3.10) in (3.4) leads to

$$\begin{aligned} \Delta B_1 &= p_{11}e_1 + p_{12}(e_2 + e_3) - \frac{2}{n_1^3}(\frac{\partial n}{\partial T})\Delta T - (p_{11} + 2p_{12})\alpha\Delta T \\ \Delta B_2 &= p_{11}e_2 + p_{12}(e_1 + e_3) - \frac{2}{n_2^3}(\frac{\partial n}{\partial T})\Delta T - (p_{11} + 2p_{12})\alpha\Delta T \\ \Delta B_3 &= p_{11}e_3 + p_{12}(e_1 + e_2) - \frac{2}{n_3^3}(\frac{\partial n}{\partial T})\Delta T - (p_{11} + 2p_{12})\alpha\Delta T \\ \Delta B_4 &= \frac{(p_{11} - p_{12})}{4}e_4 \\ \Delta B_5 &= \frac{(p_{11} - p_{12})}{4}e_5 \\ \Delta B_6 &= \frac{(p_{11} - p_{12})}{4}e_6 \end{aligned} \tag{3.11}$$

By linear approximation, $\Delta B_i = \Delta(1 \,/\, n_i^2) \approx -2\Delta n_i \,/\, n_i^3$, (3.11) is written as

$$\begin{aligned} \Delta n_1 &= -\frac{n_1^3}{2}(p_{11}e_1 + p_{12}(e_2 + e_3)) + (\frac{\partial n}{\partial T})\Delta T + \frac{n_1^3}{2}(p_{11} + 2p_{12})\alpha\Delta T \\ \Delta n_2 &= -\frac{n_2^3}{2}(p_{11}e_2 + p_{12}(e_1 + e_3)) + (\frac{\partial n}{\partial T})\Delta T + \frac{n_2^3}{2}(p_{11} + 2p_{12})\alpha\Delta T \\ \Delta n_3 &= -\frac{n_3^3}{2}(p_{11}e_3 + p_{12}(e_1 + e_2)) + (\frac{\partial n}{\partial T})\Delta T + \frac{n_3^3}{2}(p_{11} + 2p_{12})\alpha\Delta T \\ \Delta n_4 &= -n_4^3\frac{(p_{11} - p_{12})}{4}e_4 \\ \Delta n_5 &= -n_5^3\frac{(p_{11} - p_{12})}{4}e_5 \\ \Delta n_6 &= -n_6^3\frac{(p_{11} - p_{12})}{4}e_6 \end{aligned} \tag{3.12}$$

Equations (3.11) and (3.12) show that structural loads and temperature variations, applied to the optical fibers, induce optical anisotropy changing the index of refraction. Since the dielectric constant is a function of the index of refraction, the strain/temperature

induced optical anisotropy affects the propagation of the light wave in the dielectric material (Section 3.3).

3.2 FBGs with Structurally and Thermally Induced Index Changes

Optical anisotropy induced by the external loads and temperature variations cause changes in the spectral response of FBGs. Assume that a FBG is subject to a uniform temperature change (ΔT) and a strain field with principal components e_1, e_2, e_3, where e_1 is in the direction of the grating vector, and e_2 and e_2 are the transverse strain components, as shown in Figure 3-2. Accordingly, the non-zero components of the index of refraction along the principle axes are n_1, n_2, and n_3.

In FBGs, the gratings are inscribed in single-mode optical fibers which are weakly guided ($n_{clad} \approx n_{core}$). For guided modes, the effective mode index of refraction (n_{eff}) satisfies $n_{clad} < n_{eff} < n_{core}$. Therefore, the modified effective mode index of refraction for the optical fiber exposed to strain components or temperature variations can be approximated as $n_{eff} \approx n_2$ or $n_{eff} \approx n_3$, where n_2 and n_3 are the transverse components of the index of refraction in the optical fiber. If $e_2 \neq e_3$, there exist two orthogonal guided modes with two effective indices of refraction (n_{eff_1} and n_{eff_2}). By substituting n_2 and n_3 with n_{eff_1} and n_{eff_2} in (3.12), the changes in the effective modes index of refraction are given by

$$\begin{aligned} \Delta n_{eff_1} &= -\frac{n_{eff_1}^3}{2}(p_{11}e_2 + p_{12}(e_1 + e_3)) + (\frac{\partial n}{\partial T})\Delta T + \frac{n_{eff_1}^3}{2}(p_{11} + 2p_{12})\alpha\Delta T \\ \Delta n_{eff_2} &= -\frac{n_{eff_2}^3}{2}(p_{11}e_3 + p_{12}(e_1 + e_2)) + (\frac{\partial n}{\partial T})\Delta T + \frac{n_{eff_2}^3}{2}(p_{11} + 2p_{12})\alpha\Delta T \end{aligned} \tag{3.13}$$

Equation (2.6) can be rewritten as

$$\Delta\lambda_B = 2\Big(\Lambda\Delta n_{eff} + n_{eff}\Delta\Lambda\Big)_{\Delta T=0} + 2\Big(\Lambda\Delta n_{eff} + n_{eff}\Delta\Lambda\Big)_{e_i=0} \tag{3.14}$$

where $\Delta\Lambda = e_1\Lambda$. By substituting (3.13) in (3.14),

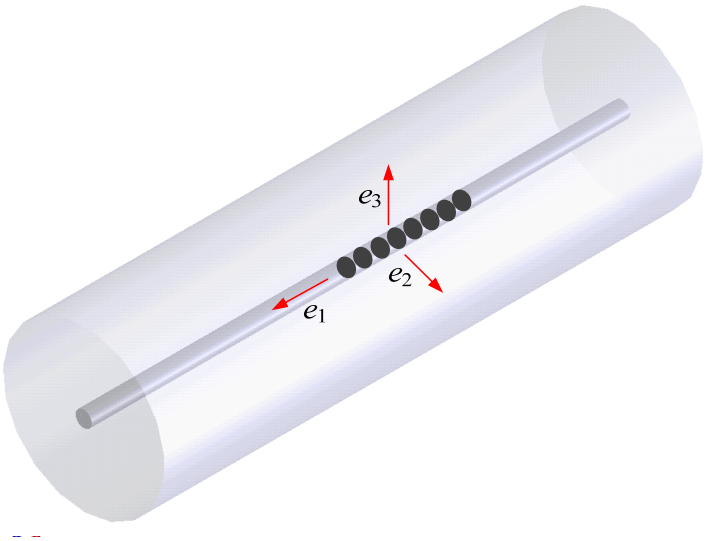

Figure 3-2: FBG subject to strain field

$$\frac{\Delta\lambda_{B_1}}{\lambda_B} = e_1 - \frac{n_{eff_1}^2}{2}(p_{12}e_1 + p_{11}e_2 + p_{12}e_3) + \frac{1}{n_{eff_1}}(\frac{\partial n}{\partial T})\Delta T + \frac{n_{eff_1}^2}{2}(p_{11} + 2p_{12})\alpha\Delta T$$
$$\frac{\Delta\lambda_{B_2}}{\lambda_B} = e_1 - \frac{n_{eff_2}^2}{2}(p_{12}e_1 + p_{12}e_2 + p_{11}e_3) + \frac{1}{n_{eff_2}}(\frac{\partial n}{\partial T})\Delta T + \frac{n_{eff_2}^2}{2}(p_{11} + 2p_{12})\alpha\Delta T \quad (3.15)$$

The splitting of the reflectivity spectrum of FBGs into two peaks with Bragg wavelengths λ_{B_1} and λ_{B_2} is called birefringence, as shown in Figure 3-3a. Since it is caused by external loads, it is also known as stress induced birefringence. If the transverse components are equal ($e_2 = e_3$), there is no peak splitting (Figure 3-3b), and (3.15) is reduced to

$$\frac{\Delta\lambda_B}{\lambda_B} = e_1 - \frac{n_{eff}^2}{2}[(p_{11} + p_{12})e_2 + p_{12}e_1] + \frac{1}{n_{eff}}(\frac{\partial n}{\partial T})\Delta T + \frac{n_{eff}^2}{2}(p_{11} + 2p_{12})\alpha\Delta T \quad (3.16)$$

3.3 Light Propagation in Optical Fibers with Induced Optical Anisotropy

The general form of light propagation in a dielectric material is obtained from Maxwell's equations as follows [37]

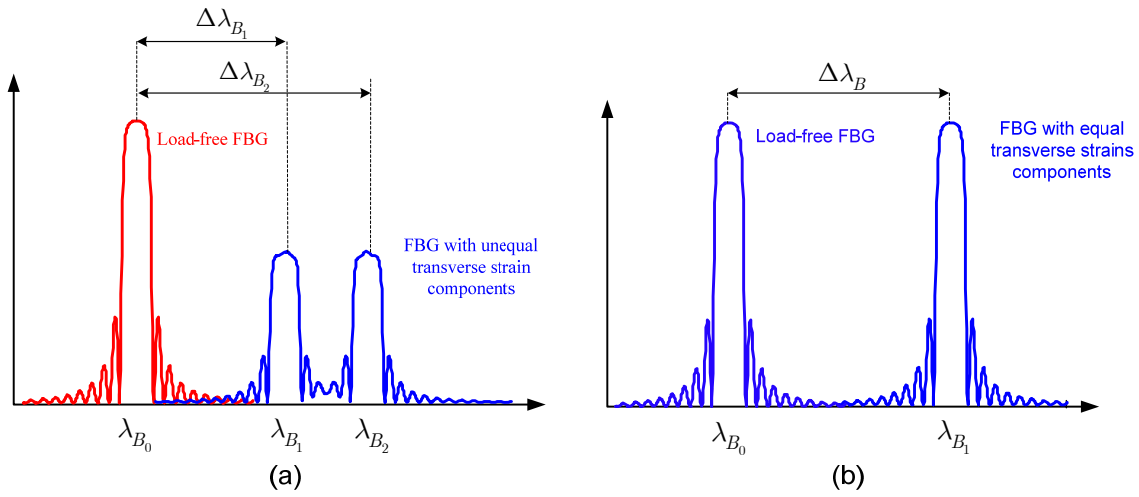

Figure 3-3: FBG reflectivity and The Bragg wavelength shift (a) unequal transverse strain components causing birefringence and (b) equal transverse strain components

$$\begin{aligned} \nabla \times \mathbf{E} &= -\frac{\partial \mathbf{B}}{\partial t} \\ \nabla \times \mathbf{H} &= \frac{\partial \mathbf{D}}{\partial t} \\ \nabla \cdot \mathbf{D} &= 0 \\ \nabla \cdot \mathbf{B} &= 0 \end{aligned} \tag{3.17}$$

Considering a time-harmonic solution, Maxwell's equations can be reformulated as

$$\begin{aligned} \nabla \times \mathbf{E} &= -i\omega\mu\mathbf{H} \\ \nabla \times \mathbf{H} &= i\omega\varepsilon\mathbf{E} \\ \nabla \cdot \mathbf{D} &= 0 \\ \nabla \cdot \mathbf{B} &= 0 \end{aligned} \tag{3.18}$$

where $\mathbf{E}$, $\mathbf{D}$, $\mathbf{H}$, and $\mathbf{B}$ are electric field, electric displacement, magnetic field, and magnetic induction, respectively. ε and μ are electric permittivity and magnetic permeability of the dielectric material. Through this study, it is assumed that the material is only electrically anisotropic; the anisotropy is caused by only the index of refraction, and the magnetic permeability of the medium (μ) is constant and equal to that of free space. In the general form, the dielectric tensor $[\varepsilon]$ is written as

$$\varepsilon_i(x,y,z) = \varepsilon_0 n_i^2 \qquad i = 1,...,6 \tag{3.19}$$

where ε_0 is the free space electric permittivity. The considered Cartesian coordinates xyz are shown in Figure 3-4.

By taking the curl of the first equation in (3.17) and substituting from the second Maxwell's equation,

$$\nabla \times \nabla \times \mathbf{E} = \omega^2 \mu \mathbf{E} \tag{3.20}$$

By expanding (3.20),

$$\begin{bmatrix} -\frac{\partial^2}{\partial y^2} - \frac{\partial^2}{\partial z^2} & \frac{\partial^2}{\partial x \partial y} & \frac{\partial^2}{\partial x \partial z} \\ \frac{\partial^2}{\partial x \partial y} & -\frac{\partial^2}{\partial x^2} - \frac{\partial^2}{\partial z^2} & \frac{\partial^2}{\partial y \partial z} \\ \frac{\partial^2}{\partial x \partial z} & \frac{\partial^2}{\partial y \partial z} & -\frac{\partial^2}{\partial x^2} - \frac{\partial^2}{\partial y^2} \end{bmatrix} \mathbf{E}(x,y,z) = \mu \varepsilon \omega^2 \mathbf{E}(x,y,z) j \tag{3.21}$$

The solution is written as

$$\mathbf{E}(x,y,z) = \mathbf{E}(x,y) e^{-i\beta} \tag{3.22}$$

where β is the propagation constant. By substituting (3.22) into (3.21)

$$\begin{bmatrix} -\frac{\partial^2}{\partial y^2} & -\frac{\partial^2}{\partial x \partial y} & -i\beta \frac{\partial}{\partial x} \\ -\frac{\partial^2}{\partial x \partial y} & -\frac{\partial^2}{\partial y^2} & -i\beta \frac{\partial}{\partial y} \\ -i\beta \frac{\partial}{\partial x} & -i\beta \frac{\partial}{\partial y} & -\frac{\partial^2}{\partial x^2} - \frac{\partial^2}{\partial y^2} \end{bmatrix} \mathbf{E}(x,y) = (\mu \varepsilon \omega^2 - \tilde{\beta}^2) \mathbf{E}(x,y) \tag{3.23}$$

where

$$\tilde{\beta}^2 = \beta^2 \begin{bmatrix} 1 & 0 & 0 \\ 0 & 1 & 0 \\ 0 & 0 & 0 \end{bmatrix} \tag{3.24}$$

The dielectric tensor in an anisotropic material is expressed as

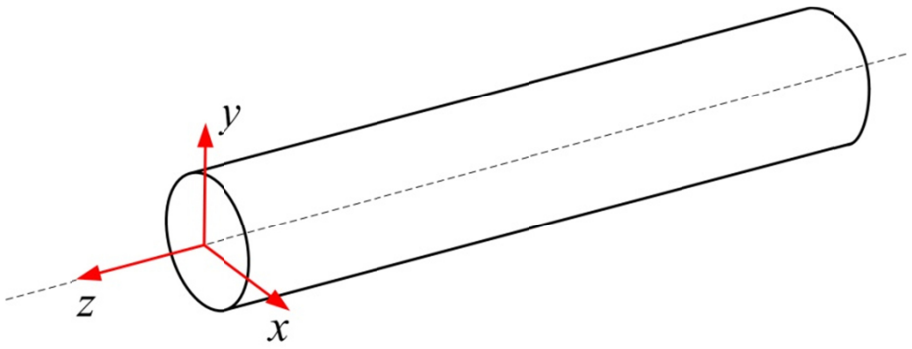

Figure 3-4: Cartesian coordinates for an optical fiber

$$[\varepsilon] = \varepsilon_0 \begin{bmatrix} n_1^2 & n_6^2 & n_5^2 \\ n_6^2 & n_2^2 & n_4^2 \\ n_5^2 & n_4^2 & n_3^2 \end{bmatrix} \tag{3.25}$$

Three principal axes can be found in such a way that the dielectric tensor becomes diagonal as follows:

$$[\varepsilon] = \varepsilon_0 \begin{bmatrix} n_x^2 & 0 & 0 \\ 0 & n_y^2 & 0 \\ 0 & 0 & n_z^2 \end{bmatrix} \tag{3.26}$$

where n_x, n_y, and n_z are the indices of refraction in the direction of the principal axes, assuming that x, y, and z are the principal directions.

By substituting $\mathbf{D} = \varepsilon\mathbf{E}$ in the third Maxwell's equation,

$$\frac{\partial}{\partial x}\Big[n_x^2 E_x(x,y)\Big] + \frac{\partial}{\partial y}\Big[n_y^2 E_y(x,y)\Big] - i\beta n_z^2 E_z(x,y) = 0 \tag{3.27}$$

and

$$E_z(x,y) = -\frac{i}{\beta n_z^2}\left\{\frac{\partial}{\partial x}\Big[n_x^2 E_x(x,y)\Big] + \frac{\partial}{\partial y}\Big[n_y^2 E_y(x,y)\Big]\right\} \tag{3.28}$$

Substitution of (3.27) in (3.23) returns

$$-\frac{\partial^2 E_x(x,y)}{\partial y^2}-\frac{\partial}{\partial x}\left[\frac{1}{n_z^2}\frac{\partial}{\partial x}(n_x^2 E_x(x,y))\right] +\frac{\partial^2 E_y(x,y)}{\partial x\partial y}-\frac{\partial}{\partial x}\left[\frac{1}{n_z^2}\frac{\partial}{\partial y}(n_y^2 E_y(x,y))\right]=(kn_x^2-\beta^2)E_x(x,y) \tag{3.29}$$

$$-\frac{\partial^2 E_y(x,y)}{\partial x^2}-\frac{\partial}{\partial y}\left[\frac{1}{n_z^2}\frac{\partial}{\partial x}(n_x^2 E_x(x,y))\right] +\frac{\partial^2 E_x(x,y)}{\partial x\partial y}-\frac{\partial}{\partial y}\left[\frac{1}{n_z^2}\frac{\partial}{\partial y}(n_y^2 E_y(x,y))\right]=(kn_y^2-\beta^2)E_y(x,y) \tag{3.30}$$

where

$$k=\mu\varepsilon_0\omega^2 \tag{3.31}$$

Equations (3.29) and (3.30) are eigenvalue problems that are solved to find the propagation constants β_i, which are the solutions of the eigenvalue problem. The effective mode index of refraction for the i^{th} propagation mode (n_{eff}^{i}) is defined by

$$n_{eff}^{i}=\frac{\beta_i}{k} \tag{3.32}$$

Equations (3.29) and (3.30) are planar PDEs, and should be solved in the cross section (xy plane) of the optical fiber. A given length of fiber (L) is divided into small longitudinal segments with length Δz, as shown in Figure 3-5. The solution of the light propagation PDE results in the effective mode index of refraction at each wavelength along the fiber ($n_{eff}(\lambda,z)$).

The length of the subsections (Δz) should be chosen appropriately. Smaller values of Δz yield more precise results. However, the selection depends on the desired resolution and strain or temperature gradients along the fiber. If the variations of strain and temperature along the fiber are large, smaller values of Δz should be selected.

The boundary conditions for (3.29) and (3.30) are

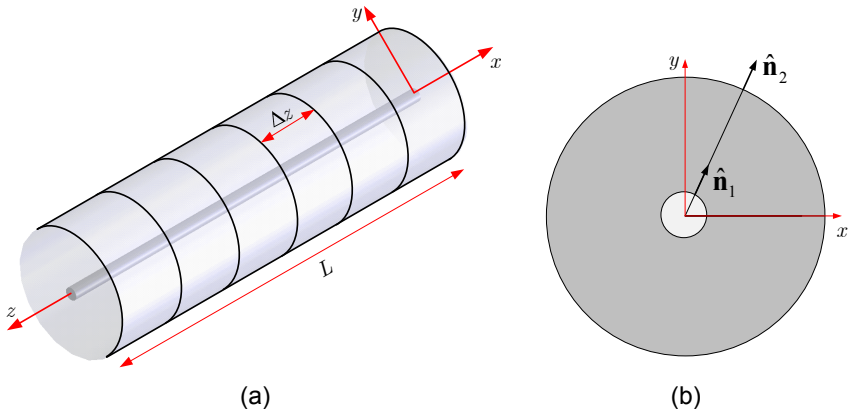

Figure 3-5: (a) Optical fiber divided into longitudinal segments for (b) surface normal unit vectors

$$\begin{aligned} \hat{\mathbf{n}}_1 \times (\mathbf{E}_{core} - \mathbf{E}_{clad}) &= 0 \qquad & r = r_{core} \\ \hat{\mathbf{n}}_1 \bullet (n_{core}^2 \mathbf{E}_{core} - n_{clad}^2 \mathbf{E}_{clad}) &= 0 \qquad & r = r_{core} \end{aligned} \tag{3.33}$$

which implies that at the core-cladding interface, the tangential components of the electric fields and the normal components of the displacement fields are continuous. At the periphery of the optical fiber, the boundary condition is

$$\hat{\mathbf{n}}_2 \times \mathbf{E}_{clad} = 0 \qquad r = r_{clad} \tag{3.34}$$

where $\hat{\mathbf{n}}_1$ and $\hat{\mathbf{n}}_2$ are the surface normal unit vector.

There is no analytical solution for anisotropic optical fibers, and numerical methods such as finite element method can be used to solve the partial differential equations. However, a closed form analytical solution can be derived for a load-free optical fiber which is optically isotropic. Appendix A contains the details of closed form solution for load-free isotropic fibers. The FEM formulation to find the effective mode index of refraction is available in Appendix B.

3.4 Coupled-Mode Theory

The coupled-mode theory is a useful tool for the quantitative analysis of the spectral response of FBGs. Considering a dielectric medium with a dielectric tensor perturbation $\Delta\varepsilon$, the optical waves propagate in an infinite number of modes. According to the coupled-mode

theory (Appendix C), the infinitesimal variation of amplitude A_m of the m^{th} mode, denoted by dA_m, due to the coupling with the l^{th} mode in the region between z and $z + dz$ is

$$dA_m(z) = -i\frac{|\beta_m|}{\beta_m}\sum_l A_l(z)K_{ml}e^{i(\beta_m-\beta_l)z} \tag{3.35}$$

where K_{ml} is the coupling coefficient between the l^{th} and the m^{th} modes, defined by

$$K_{ml} = \frac{\omega}{4}\int_S \mathbf{E}_m^*(x,y)\Delta\varepsilon(x,y,z)\mathbf{E}_l(x,y)dxdy \tag{3.36}$$

Equation (3.35) is a set of coupled differential equations describing the coupling between an infinite number of modes in the light propagation.

Based on the direction of the propagating mode, the coupling can be co-directional, where the modes propagate in the same direction, or contra-directional, where the modes propagate in opposite directions.

3.5 Derivation of Coupled-Mode Theory for FBGs with Uniform Grating

In FBGs, the mode coupling occurs between two contradirectional core modes, as shown in Figure 3-6 [3].

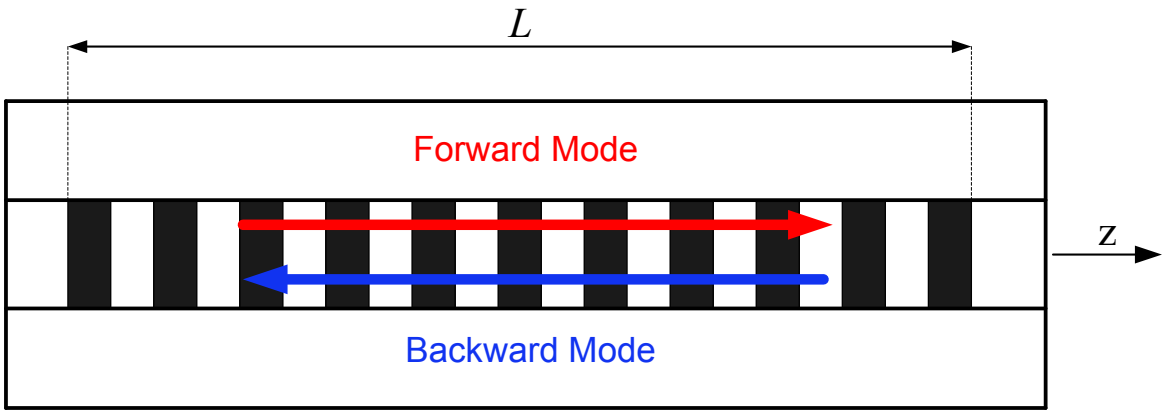

Figure 3-6: Forward and backward modes in FBG

As a result, the coupled-mode equation (3.35) can be simplified to

$$\frac{dA_1(z)}{dz} = -iK_{11}A_1(z) - iK_{12}A_2(z)e^{i(\beta_1-\beta_2)z} \tag{3.37}$$

$$\frac{dA_2(z)}{dz} = iK_{21}A_1(z)e^{i(\beta_2-\beta_1)z} + iK_{22}A_2(z) \tag{3.38}$$

where $A_1(z)$ and $A_2(z)$ are the amplitudes of the forward and backward propagating modes, respectively. Since FBG is a periodic modulation in the index of refraction, the perturbation in the dielectric tensor ($\Delta\varepsilon$) is written as

$$\Delta\varepsilon(z) = \varepsilon_0\Delta n^2(z) \tag{3.39}$$

By assuming small variations of the index of refraction,

$$\Delta\varepsilon \approx 2\varepsilon_0 n\Delta n \tag{3.40}$$

where Δn is described by

$$\Delta n(z) = \overline{\Delta n}(z)\left[1 + \nu\cos\left(\frac{2\pi}{\Lambda}z + \Phi(z)\right)\right] \tag{3.41}$$

In a uniform grating $\overline{\Delta n}(z)$ is constant and can be replaced by $\overline{\Delta n}$. Δn can also be expressed as

$$\Delta n(z) = \overline{\Delta n}\left[1 + \frac{\nu}{2}\left(e^{i\left(\frac{2\pi}{\Lambda}z+\Phi(z)\right)} + e^{-i\left(\frac{2\pi}{\Lambda}z+\Phi(z)\right)}\right)\right] \tag{3.42}$$

By substituting (3.42) into (3.36), K_{ml} is rewritten as

$$K_{ml} = \frac{\omega\varepsilon_0}{2}\left[1 + \frac{\nu}{2}\left(e^{i\left(\frac{2\pi}{\Lambda}z+\Phi(z)\right)} + e^{-i\left(\frac{2\pi}{\Lambda}z+\Phi(z)\right)}\right)\right]\int_S n\overline{\Delta n}\mathbf{E}_m^*(x,y)\mathbf{E}_l^*(x,y)dxdy \qquad m,l=1,2 \tag{3.43}$$

For two contra-directional modes with propagation constants β_1 and β_2 in FBG,

$$\begin{aligned} &\beta_1 = -\beta_2 = \beta > 0 \\ &\mathbf{E}_1(x,y) = \mathbf{E}_2(x,y) \end{aligned} \tag{3.44}$$

Equation (3.43) is used to obtain K_{11}, K_{12}, K_{21}, and K_{22}. By substituting them in (3.37),

$$\begin{aligned} \frac{dA_1(z)}{dz} = &-i\frac{\omega\varepsilon_0 n\overline{\Delta n}}{2}A_1(z)\int_S \mathbf{E}_1^*(x,y)\mathbf{E}_1(x,y)dxdy \\ &- i\frac{\omega\varepsilon_0 \nu n\overline{\Delta n}}{4}A_1(z)\left(e^{i\left(\frac{2\pi}{\Lambda}z+\Phi(z)\right)} + e^{-i\left(\frac{2\pi}{\Lambda}z+\Phi(z)\right)}\right)\int_S \mathbf{E}_1^*(x,y)\mathbf{E}_1(x,y)dxdy \\ &- i\frac{\omega\varepsilon_0 n\overline{\Delta n}}{2}A_2(z)e^{2\beta zi}\int_S \mathbf{E}_1^*(x,y)\mathbf{E}_1(x,y)dxdy \\ &- i\frac{\omega\varepsilon_0 \nu n\overline{\Delta n}}{4}A_2(z)\left(e^{i\left(2\beta z+\frac{2\pi}{\Lambda}z+\Phi(z)\right)} + e^{i\left(2\beta z-\frac{2\pi}{\Lambda}z-\Phi(z)\right)}\right)\int_S \mathbf{E}_1^*(x,y)\mathbf{E}_1(x,y)dxdy \end{aligned} \tag{3.45}$$

From the orthogonality of the propagating modes [96],

$$\int_S \mathbf{E}_1^*(x,y)\mathbf{E}_1(x,y)dxdy = \frac{2\omega\mu}{\beta} \tag{3.46}$$

By substituting (3.46) into (3.45),

$$\begin{aligned} \frac{dA_1(z)}{dz} = &-iK_{dc}A_1(z) - iK_{AC}A_1(z)e^{i\left(\frac{2\pi}{\Lambda}z+\Phi(z)\right)} - iK_{AC}A_1(z)e^{-i\left(\frac{2\pi}{\Lambda}z+\Phi(z)\right)} \\ &- iK_{dc}A_2(z)e^{i\beta zi} - iK_{AC}A_2(z)e^{i\left(2\beta z+\frac{2\pi}{\Lambda}z+\Phi(z)\right)} - iK_{AC}A_2(z)e^{i\left(2\beta z-\frac{2\pi}{\Lambda}z-\Phi(z)\right)} \end{aligned} \tag{3.47}$$

where

$$K_{dc} = \frac{\omega^2\mu\varepsilon_0 n\overline{\Delta n}}{\beta} = \frac{2\pi}{\lambda}\frac{n}{n_{eff}}\overline{\Delta n} \tag{3.48}$$

and

$$K_{AC} = \frac{\nu}{2} K_{dc} \tag{3.49}$$

In apodized gratings $\overline{\Delta n}$ is not constant along the fiber and can vary according to (2.4) or (2.5). As a result, the coupling coefficients K_{dc} and K_{AC} are not constant along the grating.

The net variation of amplitude $\Delta A_1(z)$ over a distance L, which is much larger than the grating period and much smaller than the variation scale of the amplitude, is

$$\begin{aligned}\Delta A_1(z) = &-iK_{dc}\int_z^{z+L} A_1(z)dz - iK_{AC}A_1(z)\int_z^{z+L} e^{i\left(\frac{2\pi}{\Lambda}z+\Phi(z)\right)}dz - iK_{AC}A_1(z)\int_z^{z+L} e^{-i\left(\frac{2\pi}{\Lambda}z+\Phi(z)\right)}dz \\ &- iK_{dc}A_2(z)\int_z^{z+L} e^{i\beta zi}dz - iK_{AC}A_2(z)\int_z^{z+L} e^{i\left(2\beta z+\frac{2\pi}{\Lambda}z+\Phi(z)\right)}dz \\ &- iK_{AC}A_2(z)\int_z^{z+L} e^{i\left(2\beta z-\frac{2\pi}{\Lambda}z-\Phi(z)\right)}dz\end{aligned} \tag{3.50}$$

According to (3.50), for the integral of the exponential terms to be non-vanishing, at least one of the exponents must be zero. For uniform gratings ($\Phi(z) = 0$), it is evident that $2\pi / \Lambda \neq 0$ and $\beta \neq 0$. Thus, one of the following conditions should be satisfied:

$$2\beta + \frac{2\pi}{\Lambda} = 0 \tag{3.51}$$

$$2\beta - \frac{2\pi}{\Lambda} = 0 \tag{3.52}$$

Since β is a positive number, (3.51) cannot be satisfied; therefore, the only condition is (3.52). Equation (3.52) is called the "phase matching" condition, describing the resonance in the coupling of the propagating modes [96]. The Bragg condition in FBG is obtained directly from (3.52).

$$\beta = \frac{\pi}{\Lambda} \tag{3.53}$$

Substitution of $\beta = kn_{eff}$ in (3.53) results in the Bragg condition

$$\lambda_B = 2n_{eff}\Lambda \tag{3.54}$$

Eliminating the vanishing terms from (3.47) results in

$$\frac{dA_1(z)}{dz} = -iK_{dc}A_1(z) - iK_{AC}A_2(z)e^{i\left(2\beta z - \frac{2\pi}{\Lambda} - \Phi(z)\right)} \tag{3.55}$$

In the same way, (3.38) can be simplified to

$$\frac{dA_2(z)}{dz} = -iK_{dc}A_2(z) + iK_{AC}A_1(z)e^{i\left(2\beta z - \frac{2\pi}{\Lambda} - \Phi(z)\right)} \tag{3.56}$$

Equations (3.86) and (3.87) are further simplified by assuming that

$$A_1(z) = R(z)e^{i\psi_1(z)} \tag{3.57}$$

$$A_2(z) = S(z)e^{i\psi_2(z)} \tag{3.58}$$

where

$$\psi_1(z) = -\psi_2(z) \tag{3.59}$$

The substitution of (3.57) and (3.58) in (3.55) and (3.56) gives

$$\begin{aligned} \psi_1(z) &= \beta z - \frac{\pi}{\Lambda}z - \frac{\Phi(z)}{2} \\ \psi_2(z) &= -\beta z + \frac{\pi}{\Lambda}z + \frac{\Phi(z)}{2} \end{aligned} \tag{3.60}$$

and

$$\begin{aligned}\frac{dR(z)}{dz} &= i\left(-\beta + \frac{\pi}{\Lambda} + \frac{1}{2}\frac{d\Phi}{dz} - K_{dc}\right)R(z) - iK_{AC}S(z)\\ \frac{dS(z)}{dz} &= i\left(\beta - \frac{\pi}{\Lambda} - \frac{1}{2}\frac{d\Phi}{dz} + K_{dc}\right)S(z) + iK_{AC}R(z)\end{aligned} \tag{3.61}$$

Equation (3.61) can be rewritten as:

$$\begin{aligned}\frac{dR(z)}{dz} &= -i\left(\frac{2\pi n_{eff}}{\lambda} - \frac{\pi}{\Lambda} - \frac{1}{2}\frac{d\Phi}{dz} + K_{dc}\right)R(z) - iK_{AC}S(z)\\ \frac{dS(z)}{dz} &= i\left(\frac{2\pi n_{eff}}{\lambda} - \frac{\pi}{\Lambda} - \frac{1}{2}\frac{d\Phi}{dz} + K_{dc}\right)S(z) + iK_{AC}R(z)\end{aligned} \tag{3.62}$$

Equation (3.61) is a set of first order differential equations describing the spectral response of FBGs. To find the reflectivity of FBG, (3.61) is solved with specific boundary conditions. For a FBG with length L, (3.61) can be integrated from $L/2$ to $-L/2$ with the following boundary conditions [3]

$$\begin{aligned}R(-L/2) &= 1\\ S(L/2) &= 0\end{aligned} \tag{3.63}$$

After integration, the reflectivity of the FBG at each wavelength ($r(\lambda)$) is

$$r(\lambda) = \left|\frac{S(-L/2)}{R(-L/2)}\right|^2 \tag{3.64}$$

3.6 Coupled-Mode Theory for Superstructure FBGs

Following the procedures described for the development of the coupled-mode theory for regular FBGs (in which $\overline{\Delta n}(z)$ is constant), the coupled mode equation for superstructure FBGs is formulated. In superstructure FBGs, the average index of refraction ($\overline{\Delta n}(z)$) varies periodically along the optical fiber with a period of Γ which is larger than the UV written gratings, as shown in Figure 3-7. In superstructure FBGs Γ ranges from a few micron to a few millimeters. The secondary periodic variations of $\overline{\Delta n}(z)$ can be induced in the grating during the writing process or by the deposition of on-fiber thin films with periodic

geometrical features, i.e. the periodic variation of the thickness along the grating. If the FBG with periodic on-fiber thin films is exposed to the variations of temperature or structural loadings, periodic strain components are formed along the grating. This leads to the periodic variations of the index of refraction due to the photo-elastic and thermo-optic effects in dielectric materials (3.4).

The secondary periodic variations of $\overline{\Delta n}(z)$ in FBGs with uniform grating profiles can be described by a Fourier series as follows:

$$\overline{\Delta n}(z) = \frac{1}{2}a_0 + \frac{1}{2}\sum_{k=1}^{\infty} a_k \left(e^{i\left(2k\pi z/\Gamma\right)} + e^{-i\left(2k\pi z/\Gamma\right)} \right) \tag{3.65}$$

where a_k's are constants. In apodized gratings the periodicity is applied on the initial Gaussian or cosine grating profile.

By substituting (3.65) in (3.48), (3.49), and (3.50) the procedures for non-vanishing exponential terms in Section 3.6 can be followed to obtain the "phase matching" conditions for superstructure FBGs. The exponential components for superstructure FBGs are

$$\begin{aligned}
1: &\quad \frac{2\pi}{\Lambda} + \frac{2k\pi z}{\Gamma} \\
2: &\quad \frac{2\pi}{\Lambda} - \frac{2k\pi}{\Gamma} \\
3: &\quad 2\beta + \frac{2\pi}{\Lambda} + \frac{2k\pi}{\Gamma} \\
4: &\quad 2\beta - \frac{2\pi}{\Lambda} - \frac{2k\pi}{\Gamma} \\
5: &\quad 2\beta + \frac{2\pi}{\Lambda} - \frac{2k\pi}{\Gamma} \\
6: &\quad 2\beta - \frac{2\pi}{\Lambda} + \frac{2k\pi}{\Gamma}
\end{aligned} \tag{3.66}$$

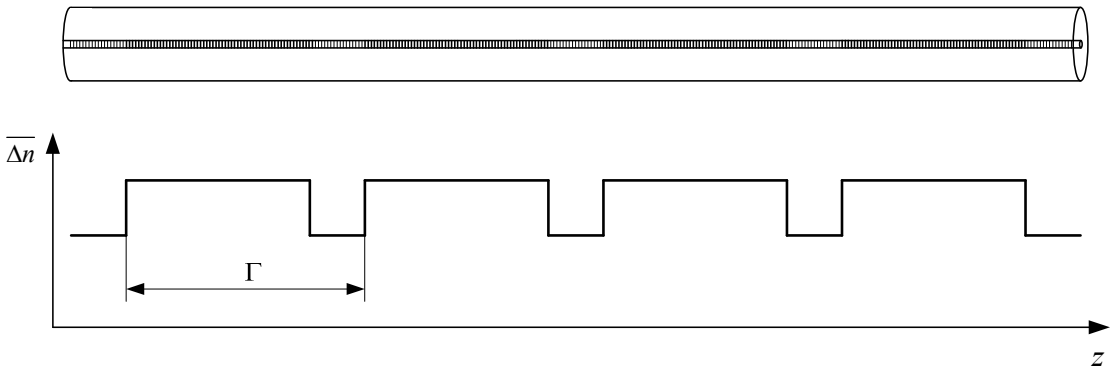

Figure 3-7: SFBG with periodic variation of $\overline{\Delta n}$ along the fiber for a uniform grating

By considering $\beta > 0$ and $\Gamma \geq \Lambda$, conditions 1, 3, and 5 cannot be satisfied. As a result, the phase matching conditions are:

$$2\beta - \frac{2\pi}{\Lambda} = 0 \tag{3.67}$$

$$2\beta - (\frac{2\pi}{\Lambda} + \frac{2k\pi}{\Gamma}) = 0 \qquad k = 1,2,... \tag{3.68}$$

$$2\beta - (\frac{2\pi}{\Lambda} - \frac{2k\pi}{\Gamma}) = 0 \qquad k = 1,2,... \tag{3.69}$$

where (3.67) is the same as the Bragg condition and (3.68) and (3.69) are the new conditions. Accordingly, the resonance wavelengths are obtained as follows

$$\begin{aligned} \lambda_0 &= \lambda_B = 2n_{eff}\Lambda \\ \lambda_{k^-} &= \frac{2n_{eff}\Gamma\Lambda}{\Gamma + k\Lambda} \qquad k = 1,2,... \\ \lambda_{k^+} &= \frac{2n_{eff}\Gamma\Lambda}{\Gamma - k\Lambda} \qquad k = 1,2,... \end{aligned} \tag{3.70}$$

According to (3.70), the resonances occur on the sides of the main Bragg wavelength (λ_B). The wavelength spacing of resonances $((\lambda_{k^+} - \lambda_0)$ or $(\lambda_0 - \lambda_{k^-}))$ is equal to

$$\lambda_{k^+} - \lambda_0 = \frac{2kn_{eff}\Lambda^2}{\Gamma - k\Lambda}$$
$$\lambda_0 - \lambda_{k^-} = \frac{2kn_{eff}\Lambda^2}{\Gamma + k\Lambda} \tag{3.71}$$

By considering $\Gamma \gg k\Lambda$, and using $\lambda_0 = 2n_{eff}\Lambda$, (3.71) can be written as

$$\lambda_{k^+} - \lambda_0 = \lambda_0 - \lambda_{k^-} = \frac{k\lambda_0^2}{2n_{eff}\Gamma} \tag{3.72}$$

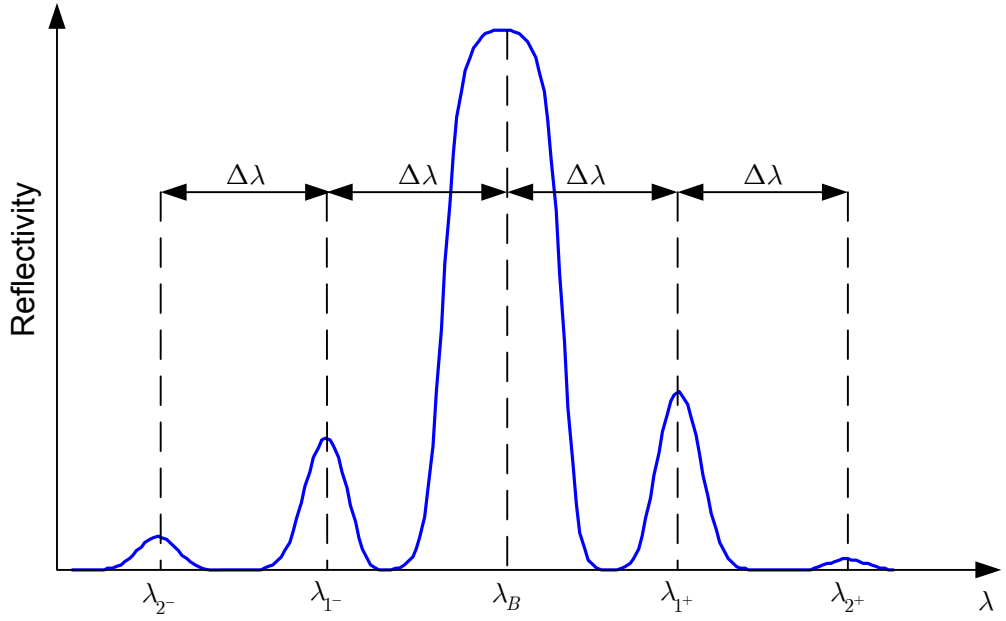

Figure 3-8: Reflection spectrum of SFBG, the equally spaced side bands are located at wavelengths λ_{k^+} and λ_{k^-}.

As a result, the wavelength spacing of the resonance peaks ($\Delta\lambda$) in a superstructure FBG is expressed as:

$$\Delta\lambda = \frac{\lambda_0^2}{2n_{eff}\Gamma} \tag{3.73}$$

In the reflection spectrum of SFBGs, in addition to the main Bragg resonance, equally spaced resonance peaks or sidebands, occur at wavelengths λ_{k^+} and λ_{k^-}. A typical reflection spectrum of a SFBG is plotted in Figure 3-8. The reflectivity of the sidebands is obtained by solving the coupled mode equations for superstructure FBGs. The solution of the coupled-mode equations for SFBGs is described in Chapter 5.

3.7 Summary

Modeling of FBGs for thermal and structural sensing was elaborated in this chapter. The modeling was based on the photo-elastic and thermo-optic properties of dielectric materials resulting in anisotropic index of refraction in optical fibers exposed to strain and temperature changes. The propagation of the light in temperature and strain induced anisotropic optical fibers was studied and the general form of the light propagation PDE for optically anisotropic FBGs was obtained. It was shown that the optical anisotropy affects the light propagation constants (β_i) of the guided mode in FBGs. The general form of the coupled-mode theory for FBGs was obtained. The coupled-mode equations are first-order ordinary differential equations that are solved in the grating segments of the optical fiber to calculate and analyze the reflection spectrum of FBGs. Furthermore, the procedures for the development of coupled-mode theory for uniform FBGs were extended to obtain the equations and the resonance conditions for superstructure FBGs.

Chapter 4

Laser Microfabrication Processes for Modification of FBGs

This chapter addresses the laser microfabrication processes implemented in this thesis for the development of the FBG-based sensors. Two laser-based approaches, including additive and subtractive methods, are considered through the course of this research to increase FBGs' sensitivity and develop new sensors. In the additive method, thin films with specific patterns are fabricated on the outer surface of FBGs. In subtractive methods, sections of the FBG cladding layer are selectively removed. Laser direct microfabrication methods, including laser-assisted maskless microdeposition and femtosecond laser micromachining are used for additive and subtractive methods, respectively. The chapter contains the process development and characterization of each method.

4.1 Laser-Assisted Fabrication of Thin Films

As a part this research, on-fiber metal thin films were required for the production of superstructure FBGs, as well as conductive interlayer for further embedding processes. Various methods have been proposed for the fabrication of metal films on optical fibers.

As discussed in Chapter 2, conventional deposition methods have been utilized for on-fiber thin-film fabrication. Another group of technologies that can be considered for the fabrication of on-fiber coatings is the Direct Write (DW) methods. In the DW methods, categorized as layered manufacturing technologies, the materials are selectively deposited in a layer-by-layer fashion at specific locations on substrates. Compared with conventional coating methods, the DW methods do not involve masks, and they are fast and inexpensive. Patterning with conventional thin-film deposition methods requires the addition and removal of materials which makes the use of masks inevitable.

The DW method that has been proposed and implemented in this research is Laser-Assisted Maskless Microdeposition (LAMM). As mentioned in Section 2.12.6, in addition to the characteristics of the DW methods, LAMM has some distinguishing features enabling the deposition of thin films on optical fibers. The key feature of the LAMM process is conformal deposition on non-planar surfaces. Compared with other DW methods such as ink-jet printing in which the gap between the depositing head and the substrates is less than a few tens of microns, the gap in LAMM is around 1-5 mm. This enables the conformal and selective deposition on non-planar surfaces and three-dimensional substrates. In the following, the details of the LAMM process are explained.

4.1.1 LAMM Process

The LAMM equipment consists of four major components:

1. Atomizers (ultrasonic and pneumatic),
2. Deposition unit (including processing head, nozzles, shutter, sheath gas, atomizer gas, and tubing),
3. Laser and optical head (including a CW Erbium fiber laser with the wavelength of 1550 nm),
4. Positioning stage.

Thin-film fabrication using the LAMM process is performed in two steps: (1) micro deposition, in which metal nanoparticles suspended in a liquid are atomized to aerosols, injected from the deposition head and impinge on a moving substrate and (2) laser post-processing, in which the laser beam is used for post-heating and sintering of the as-deposited material.

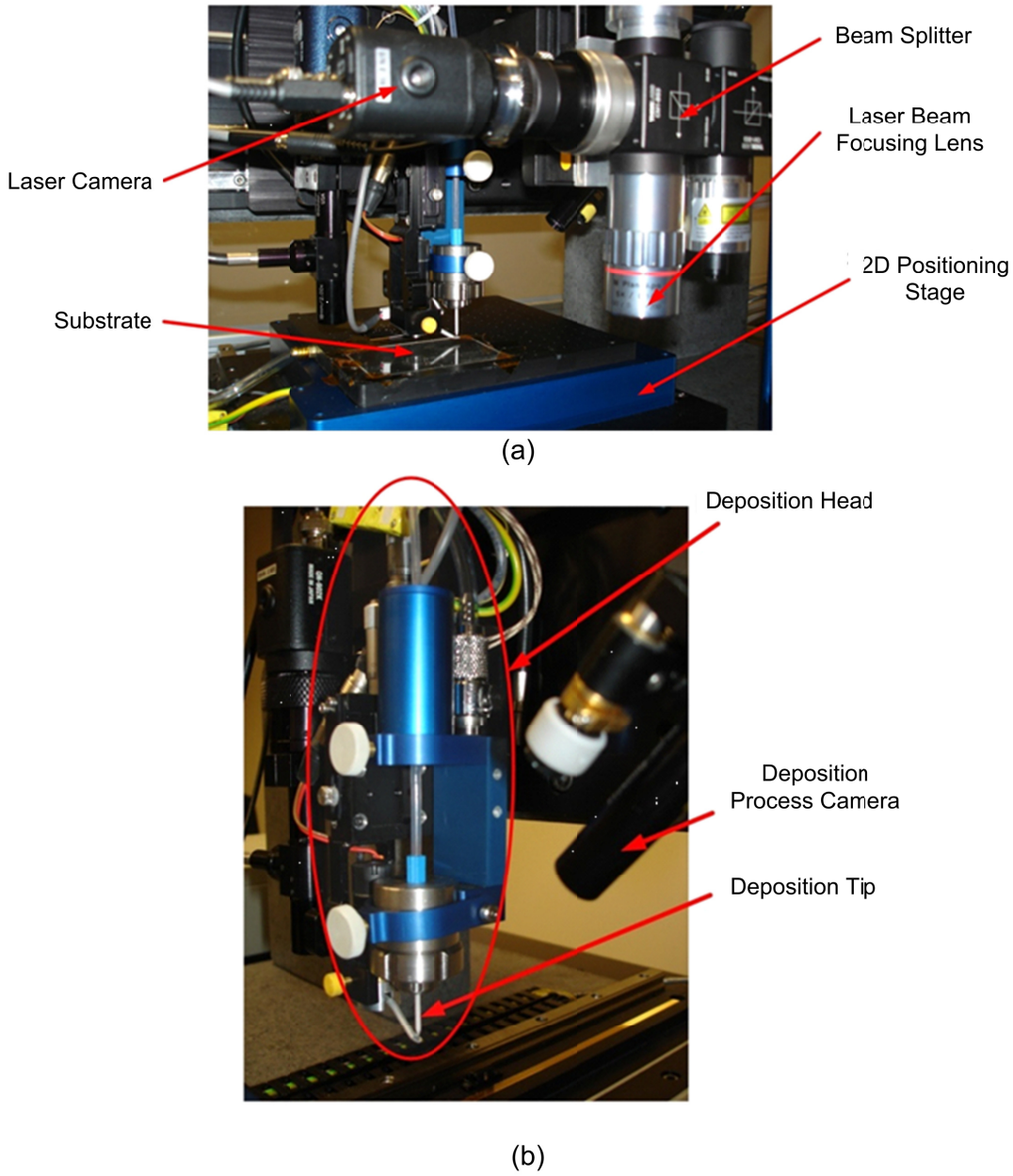

Figure 4-1: LAMM workstation setup (a) laser processing and deposition heads and (b) deposition head

The complete setup of LAMM is illustrated in Figure 4-1. The atomizers and positioning stage have been manufactured by Optomec Inc. The deposited materials are in the form of nanoparticles suspended in liquid, called nano-ink. The nano-ink is placed in one of the atomizer systems. The ultrasonic atomizer generates ultrasonic waves that are transferred to

the nanoparticle solution. When the solution is exposed to the ultrasonic waves, minuscule droplets of the liquid are ejected at the gas-liquid interface and form a dense mist in the surrounding gas. This phenomenon is well described by cavitation and capillary wave hypotheses [97, 98].

In the pneumatic atomizer, a high velocity gas stream is used to shear a liquid stream into droplets. The liquid stream is generated through the Bernoulli effect which creates the flow of nanoparticle suspension from the reservoir. The atomizer systems have the capability to generate mist with droplet sizes of 1-5 microns. For the best performance, the values of viscosities of the liquid in the atomizers should be 0.7-10 cP for the ultrasonic atomizer and 1-2500 cP for the pneumatic atomizer.

The gas flow from the ultrasonic atomizer is directed to the deposition head. However the gas flow rate in the pneumatic atomizer is high for the deposition head. The aerosol generated in the pneumatic atomizer passes through Virtual Impactor module, where the excess gas is removed by a vacuum pump, and the aerosol and the remaining gas are carried to the deposition head.

The aerosol is carried to the deposition head by the flow of nitrogen gas. At the deposition head, the aerosol stream is mixed with a secondary gas stream of nitrogen, called sheath gas flow, and passes through a co-axial nozzle. This causes the aerodynamic focusing of the aerosol stream which then passes through a deposition tip with a diameter of 100 to 250 μm. The sheath flow focuses the main stream down to 10% of the size of the deposition tip, as demonstrated in Figure 4-2.

The substrate is mounted on a two-degree-of-freedom moving stage, controlled by a motion control module. By moving the substrate relative to the deposition head, the desired patterns are produced in a layer-by-layer fashion. An electric heater, embedded in the stage, can heat the substrate up to 200 °C.

For the deposition on optical fibers, an in-house rotational stage was designed and manufactured to equip LAMM with one additional degree of freedom. As illustrated in Figure 4-3, the connectorized and stripped optical fiber is mounted at each end of the concentric rotational holders. The entire setup is mounted on the translational stage of the LAMM workstation.

For the laser post-processing, a CW single-mode erbium fiber laser with a wavelength of 1550 nm along with the associated optics was added to the LAMM workstation, as shown in

Figure 4-1a. The focused laser beam has a diameter of 30 μm and delivers powers of 0.5 W to 3.5 W to the process zone. After the deposition, the laser beam irradiates the as-deposited materials and causes the agglomeration of the nanoparticles.

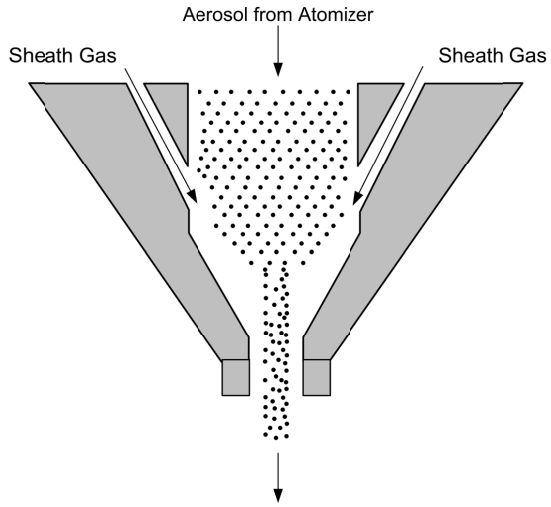

Figure 4-2: Flow mixing mechanism for focusing the aerosol stream in the LAMM deposition head

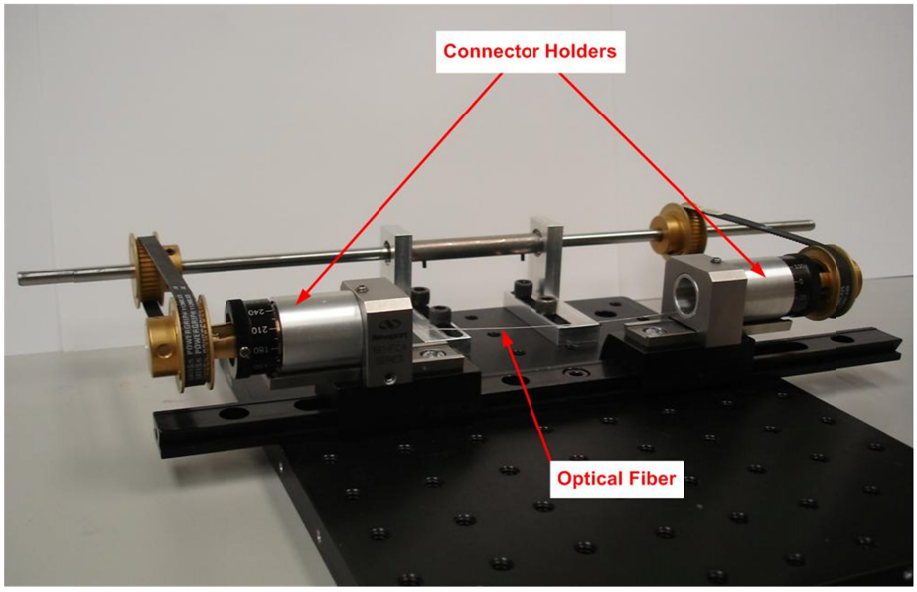

Figure 4-3: Rotational stage for the installation of optical fibers in the LAMM workstation

4.1.2 Laser-Assisted Sintering of Nanoparticles

The laser sintering mechanism of nanoparticles is shown in Figure 4-4. When the nanoparticles solution is radiated by the laser beam, the solvent evaporates and the particles agglomerate to form solid structures. As shown in Figure 4-4, the agglomerated particles produce "neck-shape" structures [99-101]. Agglomeration, which leads to the reduction of surface energy, occurs as a result of the atomic diffusion between the nanoparticles. Different diffusion mechanisms can occur in the laser sintering process: surface diffusion, grain boundary diffusion, and lattice diffusion. In the laser sintering of nanoparticles, the dominance of a diffusion mechanism depends on the size of nanoparticles. In the early stages of the sintering process, surface diffusion and grain boundary diffusion, with lower activation energies than lattice diffusion, are dominant. Applying the laser energy to the process increases the density of the deposited films, resulting in an increased electrical conductivity [102]. The laser sintering of nanoparticle solutions involve liquid evaporation and densification. As a result, weight loss and the formation of residual stress are prevalent in this process.

4.1.3 LAMM Process Parameters

The parameters involved in the LAMM process fall into two groups of deposition and laser sintering, and are provided in Table 4-1.

Table 4-1: LAMM process parameters

Deposition Process Parameters	**Laser Sintering Process Parameters**
Pneumatic Atomizer	Laser power (W)
Atomizer gas flow rate (cm^3/min)	Laser scanning speed (mm/s)
Sheath gas flow rate (cm^3/min)	Focused laser beam diameter (μm)
Virtual impactor gas flow rate (cm^3/min)	
Deposition speed (mm/s)	
Deposition tip diameter (μm)	
Ultrasonic Atomizer	
Atomizer gas flow rate (cm^3/min)	
Sheath gas flow rate (cm^3/min)	
Atomizer voltage (V)	
Deposition speed (mm/s)	
Deposition tip diameter (μm)	

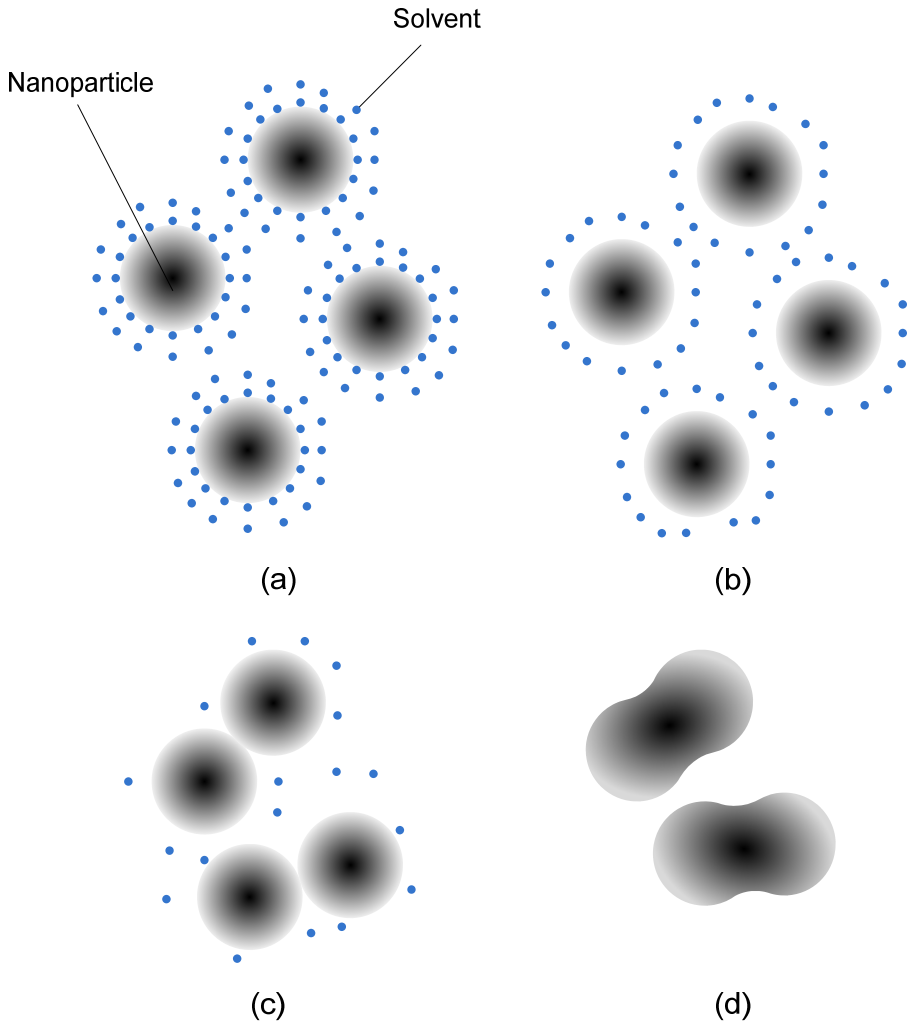

Figure 4-4: Laser sintering mechanism of nanoparticles (a) before sintering, (b) liquid evaporation, (c) start of agglomeration, and (d) end of agglomeration

4.1.4 LAMM Process Characterizations

As listed in Table 4-1, the LAMM process involves various parameters. To attain films with desired geometrical features and mechanical and microstructural properties, and investigate the effects of the process parameters on the final quality and characteristics of the deposited films, the process needs to be characterized. In the LAMM process, the deposition parameters primarily affect the geometrical features such as the thickness and width of the films. For the analysis of the microstructural and mechanical properties, the effects of the laser processing parameters should be investigated. The final goal is the

deposition on the non-planar surface of optical fibers. However, in the current characterization scheme, the optimum parameters are obtained for planar substrates. Then, the parameters are further tuned for the deposition on the non-planar surface of optical fibers.

4.1.5 Experimental Procedures

Silver nanoparticles suspended in ethylene glycol ($C_2H_4(OH)_2$) were used in the experiments. The suspension contained 50 wt. % of silver nanoparticles with an average particle size of 50 nm, supplied by Nano-Size Ltd.

The deposition, followed by laser sintering, was performed on planar silica (SiO_2) substrates at different process parameters. After the deposition and laser sintering, the samples were examined by optical microscope and scanning electron microscope (SEM) to study the microstructure of the deposited tracks. A BH2-UMA model Olympus microscope and a LEO 1530 Field Emission Scanning Electron Microscope (FE-SEM) were used for this purpose. In addition, white light interferometry using optical profilometery (WYKO NT 1100 optical profiling system, Veeco, Plainview, NY, USA) was utilized to study the geometrical features of the deposited films. The laser power at the process zone was measured by a power meter (L30A Thermal Head, OPHIR, Logan, UT, USA). The crystalline structure of the thin films was examined with X-ray Diffraction (XRD) by using a micro X-ray diffraction machine with Cu-K_α radiation. To obtain the effect of laser parameters on the mechanical properties of the deposited thin films, nano-indentation tests were performed. For these tests, Hysitron TI 900 TriboIndenter (Hysitron, Inc., Minneapolis, MN, USA) was utilized.

4.1.6 Optimized Process Parameters for the Deposition of Silver Films

A Design of Experiments (DOE), based on the Taguchi method, was developed to optimize the process parameters and gain insight into the effects of the process parameters on the properties of the films. The optimization of the process parameters was based on the width and the thickness of the deposited films. The details of the DOE method are available in Appendix D. The optimized process parameters for the deposition with pneumatic atomizer and ultrasonic atomizer are listed in Table 4-2 and Table 4-3. These process parameters result in fine-edge films with thicknesses of about 1 μm and widths of 20-50 μm.

Table 4-2: Deposition process parameters for pneumatic atomizer

Parameter	Value
Atomizer flow rate (cm^3/min)	740-750
Sheath gas flow rate (cm^3/min)	100-110
Virtual impactor gas flow rate (cm^3/min)	700
Deposition velocity (mm/s)	3-5
Deposition tip diameter (μm)	200

Table 4-3: Deposition process parameters for ultrasonic atomizer

Parameter	Value
Atomizer flow rate (cm^3/min)	7-12
Sheath gas flow rate (cm^3/min)	40-55
Atomizer voltage (V)	35-40
Deposition velocity (mm/s)	0.5-10
Deposition tip diameter (μm)	150

4.1.7 Deposition on Planar Surfaces

Trials were conducted to deposit silver on planar fused silica substrates. Figure 4-5 presents spiral and straight line patterns. The topography images of the samples taken by the optical profiling system are illustrated in Figure 4-6.

4.1.8 Microstructure Analysis

Samples were fabricated with different laser powers at a laser speed of 0.25 mm/s. Laser powers of 1.35 W, 2.41 W, and 3.28 W at the process zone with a beam spot diameter of 200 μm were used in the experiments. Figure 4-7 and Figure 4-8 depict the microstructure of the samples taken by FE-SEM at magnifications of 20 kX and 35 kX. The figures show the changes in the microstructure during laser sintering. As seen, at the laser power of 1.35 W, the nanoparticles have been slightly sintered, and neck-shape formation is rarely seen in this sample. As the laser power increases, the agglomeration and neck-shape formation are observed in the nanoparticles. At the power of 3.28 W, which is the maximum achievable power in the LAMM system, close-packed sintered particles are observed.

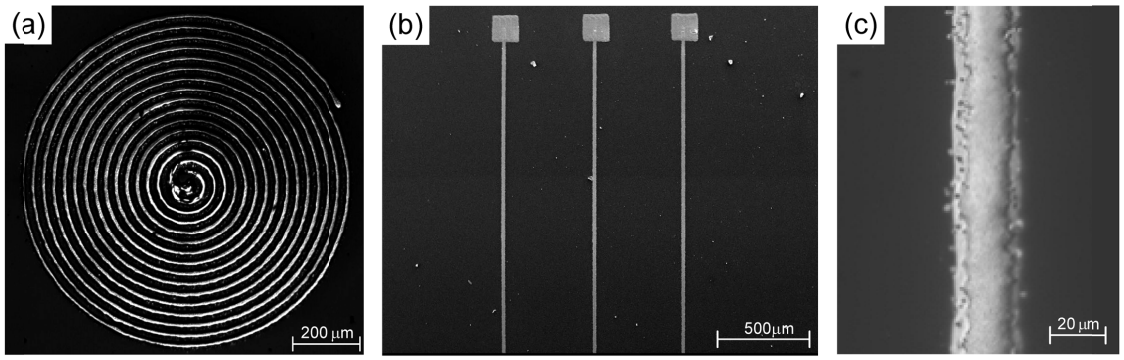

Figure 4-5: Typical deposition patterns on a planar silica substrate, (a) spiral pattern, (b) conductive lines with pads at the ends, and (c) magnified images of the conductive lines in (b). Atomizer gas flow rate: 12 cm^3/min, sheath gas flow rate: 50 cm^3/min, deposition velocity: 0.5 mm/s, laser power: 0.8 W, laser scanning speed: 0.25 mm/s for the lines and 1 mm/s for the spiral pattern

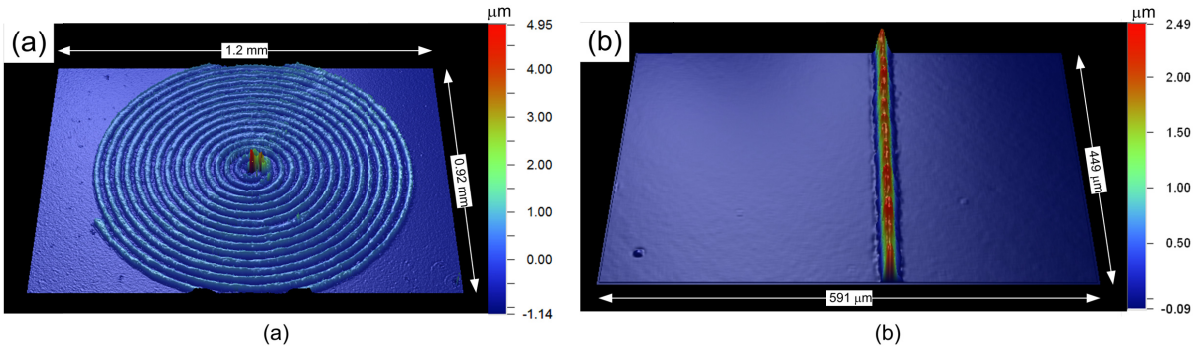

Figure 4-6: Topography images of the deposition patterns in Figure 4-5 taken by optical profiling system (a) spiral pattern and (b) lines

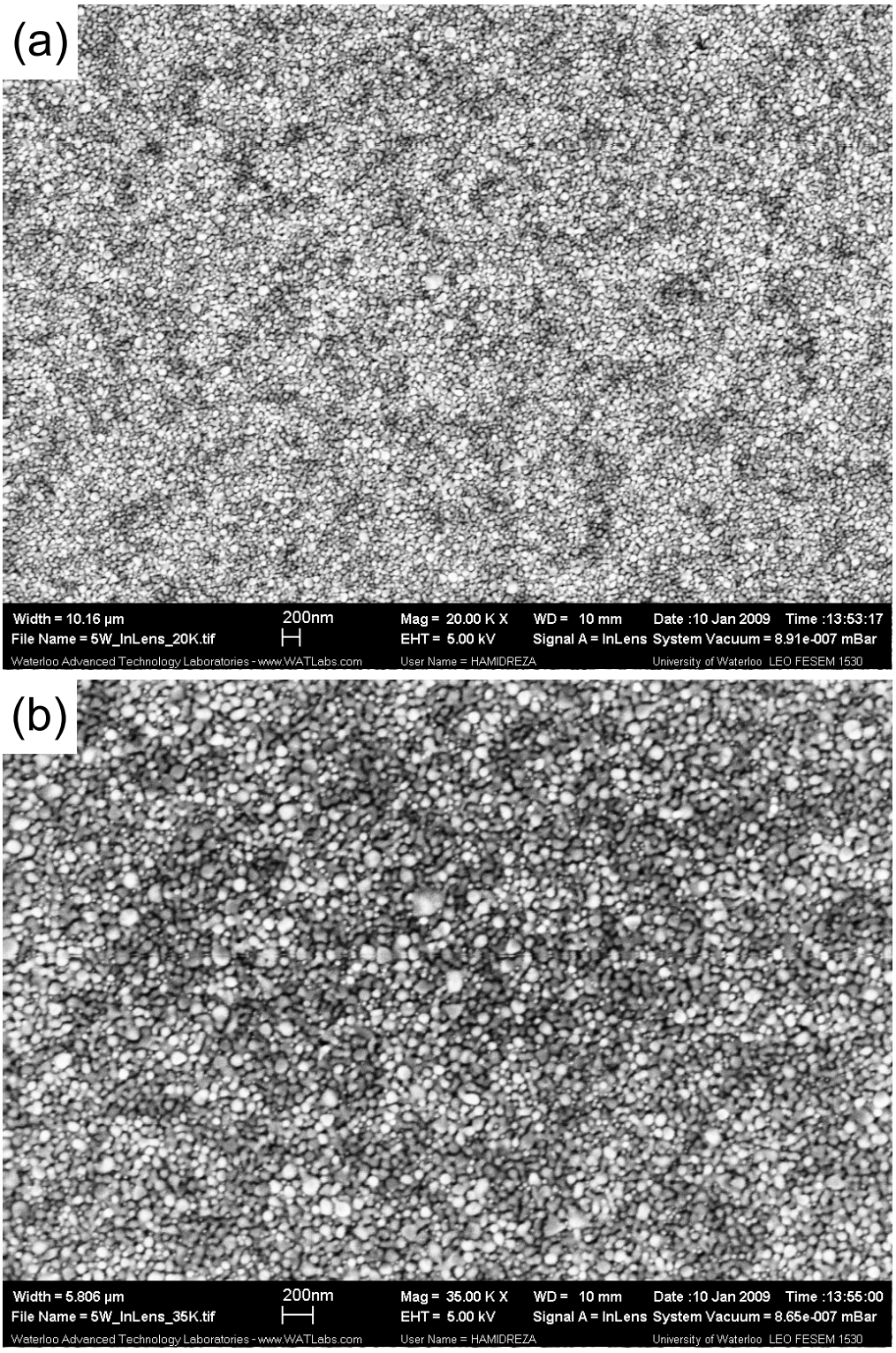

Figure 4-7: In-lens images of the microstructure of the silver thin films sintered at 1.35 W taken at magnifications of (a) 20 kX and (b) 35 kX

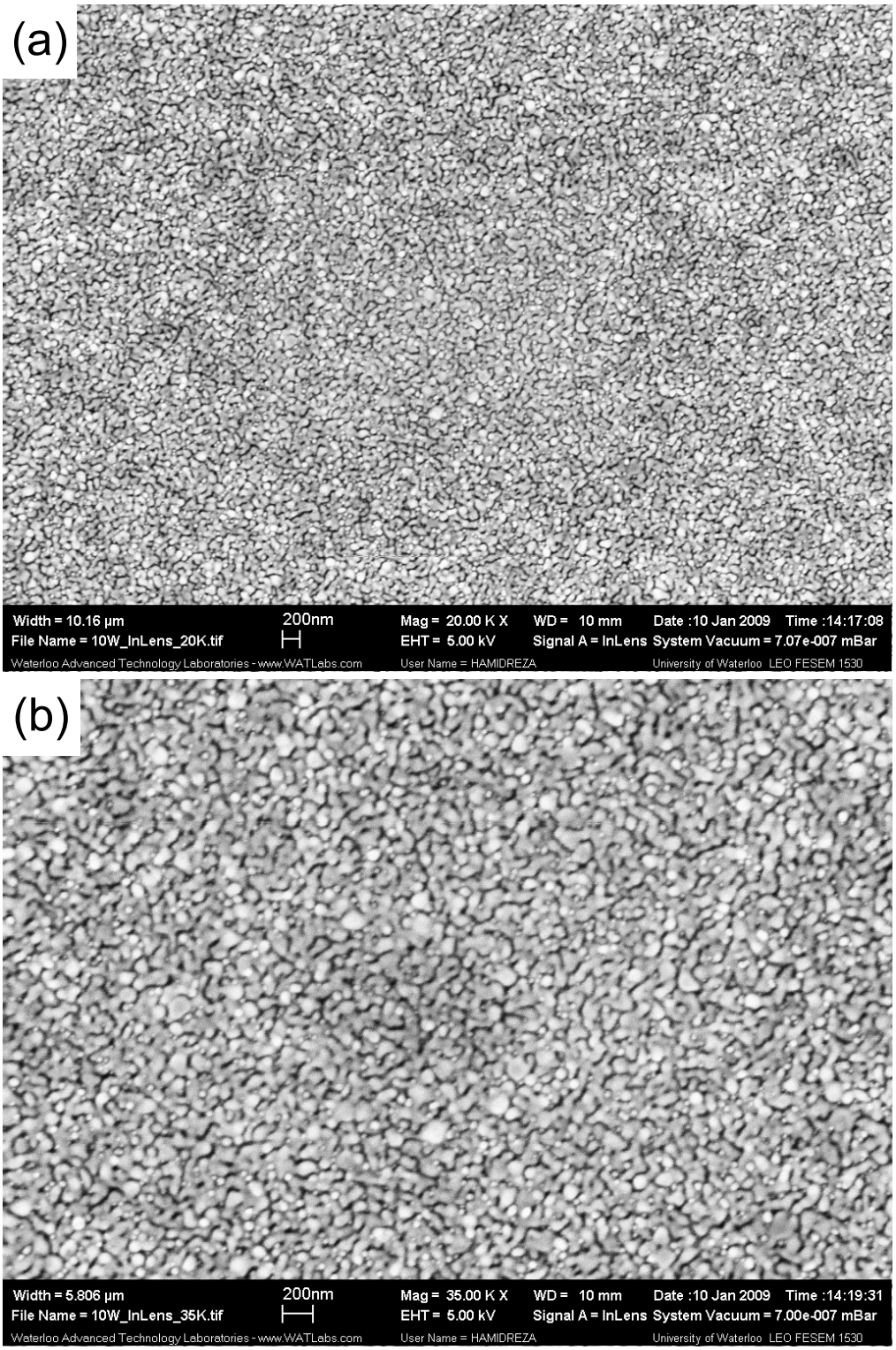

Figure 4-8: In-lens images of the microstructure of the silver thin films sintered at 3.28 W at magnifications of (a) 20 kX and (b) 35 kX

4.1.9 Crystal Structure

In the characterization of the process, the crystal structure of silver films was also investigated. Figure 4-9 shows the XRD spectra of unsintered films and the films sintered at laser powers of 2.41 W and 3.28 W. The existence of multiple peaks in the XRD spectra implies that the silver nanoparticles are polycrystalline. The magnified peaks at 44° associated with (200) planes are also shown in Figure 4-10. According to the magnified image, the peak of the untreated sample is broader than that of laser-sintered samples. The Full-Width-at-Half-Maximum (FWHM) of the unsintered sample, and the samples sintered at 2.41 W and 3.28 W are is 0.77°, 0.65°, and 0.63°, respectively. The increase of the FWHM in the X-ray diffraction is related to the crystallite structure [103]. As the laser power increases, the particles agglomerate and the level of periodic arrangement in the crystals increases. This results in sharper peaks when the X-ray beam is diffracted.

4.1.10 Mechanical Properties

Another part of the characterization process was to investigate the mechanical properties including modulus of elasticity and hardness of the silver films by using nanoindentation tests. For the nanoindentation tests, an image of each sample was obtained by the nanoindenter tip, and six locations which were 10 μm apart were located. A maximum load of 1000 μN was applied at each location, and the load-displacement curves were obtained. Figure 4-11 shows the indentation profiles of six locations in a sample taken by the nanoindenter tip.

Figure 4-12 shows the load-displacement curves for each sample at five indentation locations of Figure 4-11. According to the Oliver-Pharr method [104], the indentation hardness (H) is obtained from

$$H = \frac{P_m}{A} \tag{4.1}$$

where P_m is the maximum applied load and A is the contact area between the indenter and the silver layer.

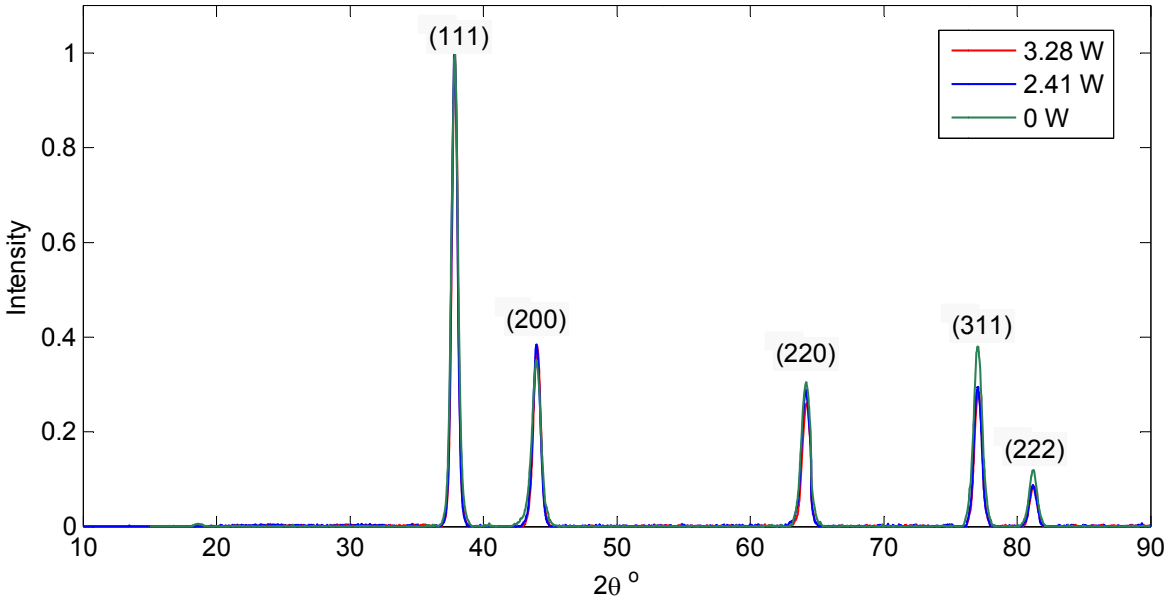

Figure 4-9: XRD spectra of the silver thin films sintered at different laser powers

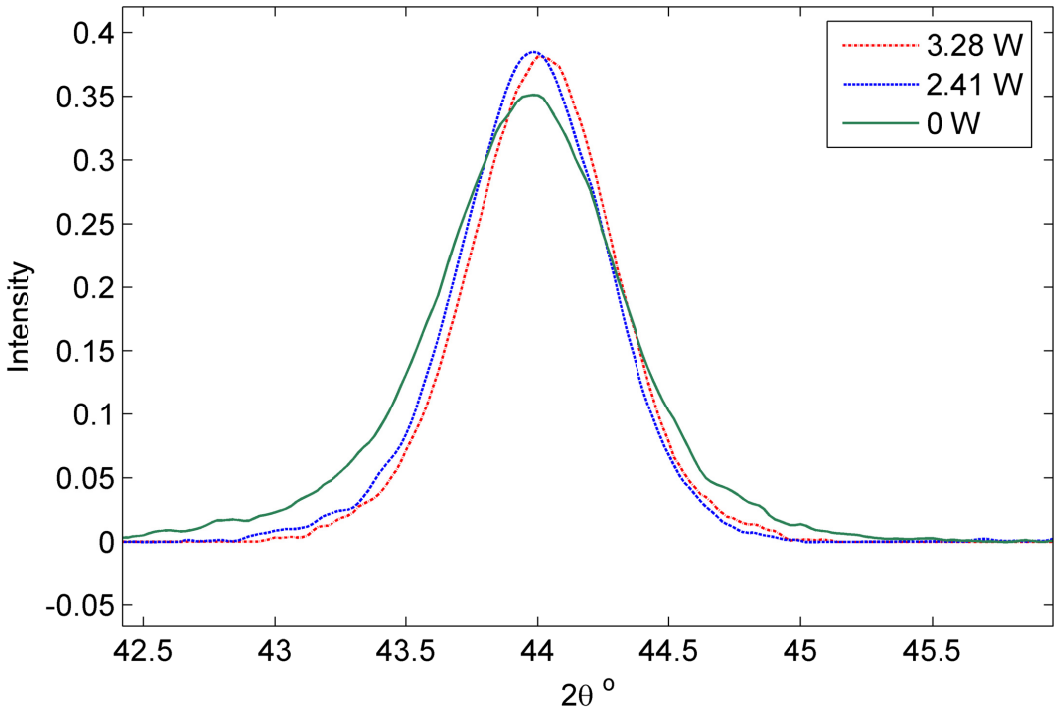

Figure 4-10: XRD peaks for (200) planes at different laser powers

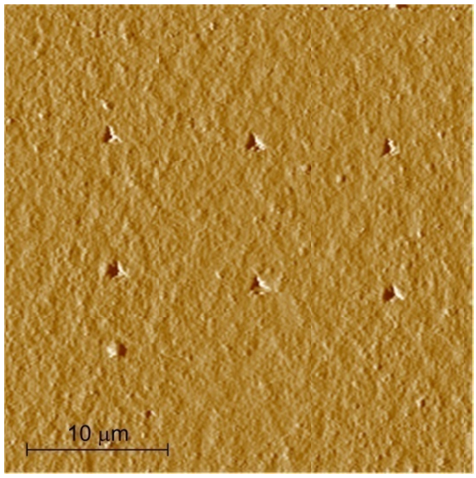

Figure 4-11: Nanoindentation profiles at six locations on a silver thin film

In addition, the nanoindentation test results were employed to obtain the modulus of elasticity of the deposited silver layers. The modulus of elasticity is related to the initial slope of the relaxation curve in the force-displacement graph as follows [105]:

$$S = \frac{2\alpha^{*} E^{*} A^{1/2}}{\sqrt{\pi}} \tag{4.2}$$

where S is the initial slope of the relaxation curve, α^{*} is a correction factor for the shape of the indenter, and E^{*} is the reduced modulus of elasticity which is related to the modulus of elasticity of the film and the indenter, as follows:

$$E^{*} = \left(\frac{1-\nu_f^2}{E_f} + \frac{1-\nu_{in}^2}{E_{in}} \right)^{-1} \tag{4.3}$$

where ν is the Poisson's ratio, and subscripts f and in denote the film and the indenter properties. The modulus of elasticity of the deposited silver films can be obtained by using (4.2) and (4.3). The mechanical properties of the indenter were $E_{in} = 1140$ GPa and $\nu_{in} = 0.07$, and $\nu_f = 0.37$ was used for silver.

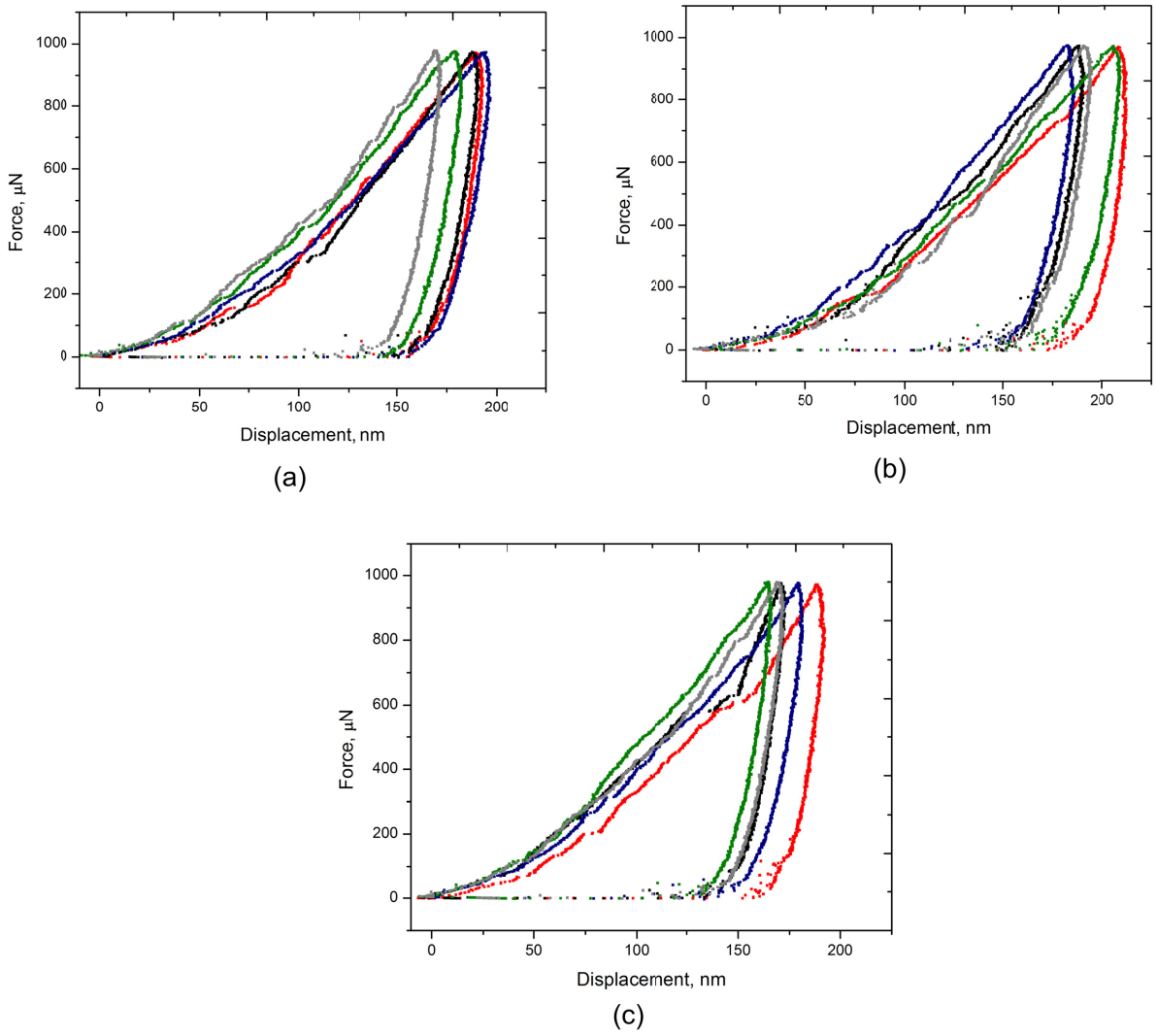

Figure 4-12: Load displacement curves obtained from the nanoindentation test at five locations of the silver thin films sintered at (a) 1.35 W, (b) 2.41 W, and (c) 3.28 W

The hardness and modulus of elasticity, obtained from the nanoindentation test results, are plotted in Figure 4-13 and Figure 4-14. It is clear that hardness and modulus of elasticity increase by increasing the laser power. This is the result of the agglomeration and sintering of nanoparticles. Close values of hardness have been reported for silver thin films [106, 107]. In these experiments, the maximum obtained value for modulus of elasticity is 65 GPa, which is 21% less than that of bulk silver (83 GPa). This can be caused by the differences in the samples microstructure, affected by the type of the fabrication process [106]. In addition, the agglomeration of the nanoparticles might not be complete and contain porosity. The surface morphology such as the roughness of the deposited silver layers can also cause the discrepancies.

4.2 LAMM for On-Fiber Film Deposition

4.2.1 Materials

Silver was selected as the coating material for FBGs. Among the precious materials that are available as nanoink, silver has a good adhesion with silica. In addition, the coefficient of thermal expansion of silver is high ($\alpha_{silver} = 18.9\times10^{-6}\ ^{o}C^{-1}$), compared with that of silica ($\alpha_{silica} = 0.55\times10^{-6}\ ^{o}C^{-1}$), which increases the thermal sensitivity of the FBG sensor.

A FBG with a Bragg wavelength of 1550 nm and grating length of 14 mm (O/E LAND Inc., Quebec, QC, Canada) was selected. The optical fiber was coated with a polymeric layer to protect it during shipping and handling. The polymer coating was chemically stripped by immersing the fiber in acetone for 15 min.

4.2.2 Path Planning and Process Parameters

During the deposition process, the FBG was mounted on the rotational stage in Figure 4-3 and fixed at the ends to keep it straight under the deposition head. The films were deposited on the optical fiber by moving it in a programmed path relative to the deposition head. To coat a desired length of the fiber, silver tracks were deposited adjacent to each other with a distance of 20 to 25 μm. Figure 4-15 shows the relative path followed by the deposition head.

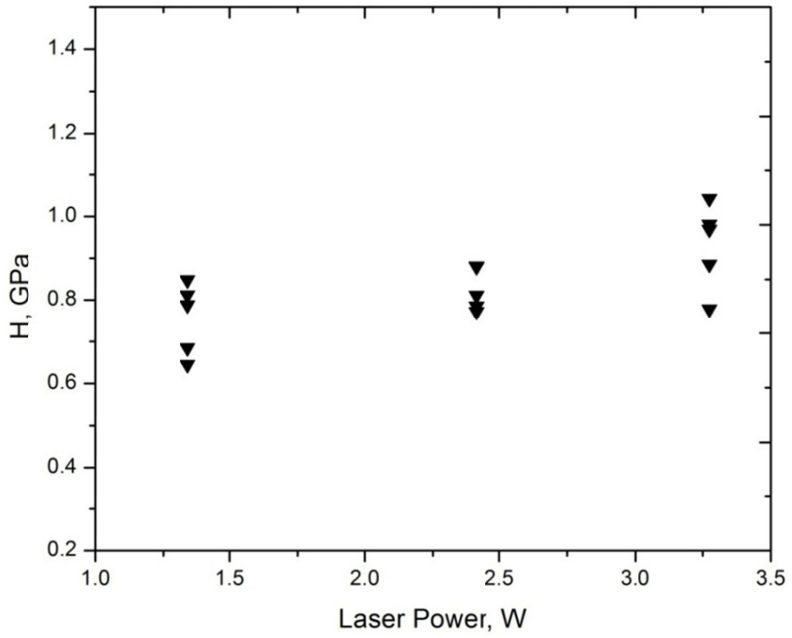

Figure 4-13: Hardness of silver thin films as a function of incident laser power obtained from nanoindentation tests

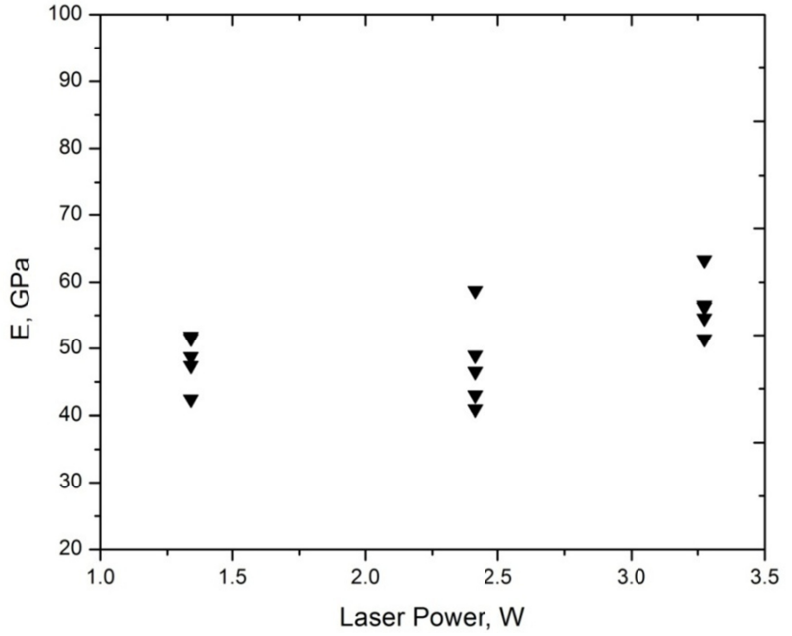

Figure 4-14: Modulus of elasticity of silver thin films as a function of incident laser power obtained from nanoindentation tests

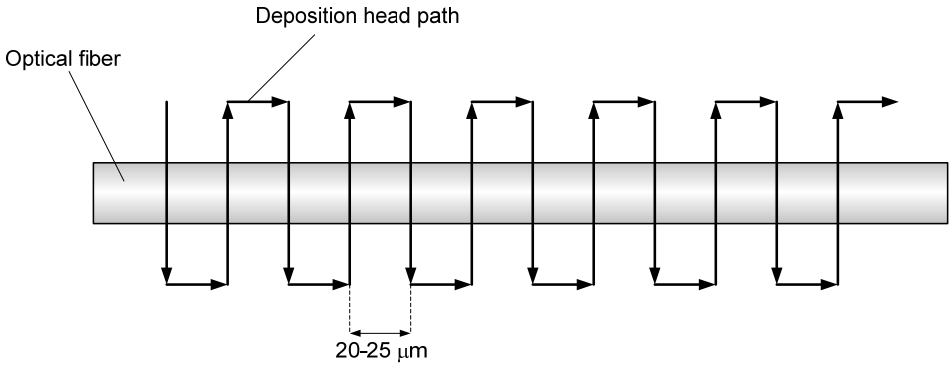

Figure 4-15: Path followed by the deposition head of LAMM relative to the optical fiber for the deposition of on-fiber silver thin films

During the deposition process, only one side of the optical fiber was exposed to the aerosol of silver nanoparticles. This causes non-uniformity in the thickness of the films around the fibers. To get a uniform coating thickness, the optical fiber was rotated by 90° in each round of depositions, as displayed in Figure 4-16. The process parameters used for the deposition of on-fiber silver films are listed in Table 4-4.

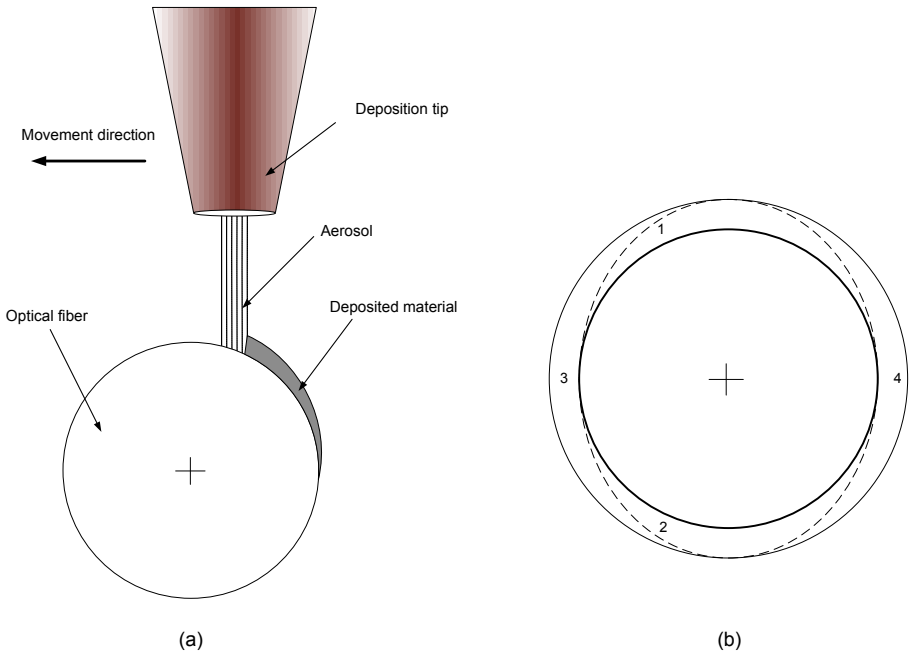

Figure 4-16: (a) Schematic diagram of the LAMM deposition tip and the optical fiber and (b) for each set of depositions the fiber is rotated by 90°.

4.2.3 Results

Figure 4-17 and Figure 4-18 display the periodic silver coatings deposited on an optical fiber to create a superstructure FBG. Films were deposited with a period of 2 mm, duty cycle of 3/4, and thickness of 9 µm. Totally, seven coating segments with a length of 1.5 mm were fabricated. The optical fiber has a diameter of 125 µm, and the average diameter of the coatings is 143 µm. Figure 4-19 illustrates the measured values of the film thickness at different angles around the fiber. As observed, the film is uniformly distributed around the optical fiber.

Table 4-4: LAMM process parameters for the deposition of silver films on optical fibers

Parameter	**Value**
Aerosol flow rate (cm^3/min)	45-50
Deposition velocity (mm/s)	3
Laser power at the process zone (W)	3.3
Laser scanning speed (mm/s)	0.25
Laser spot size at the core of optical fiber (µm)	200
Deposition tip inside diameter (µm)	200

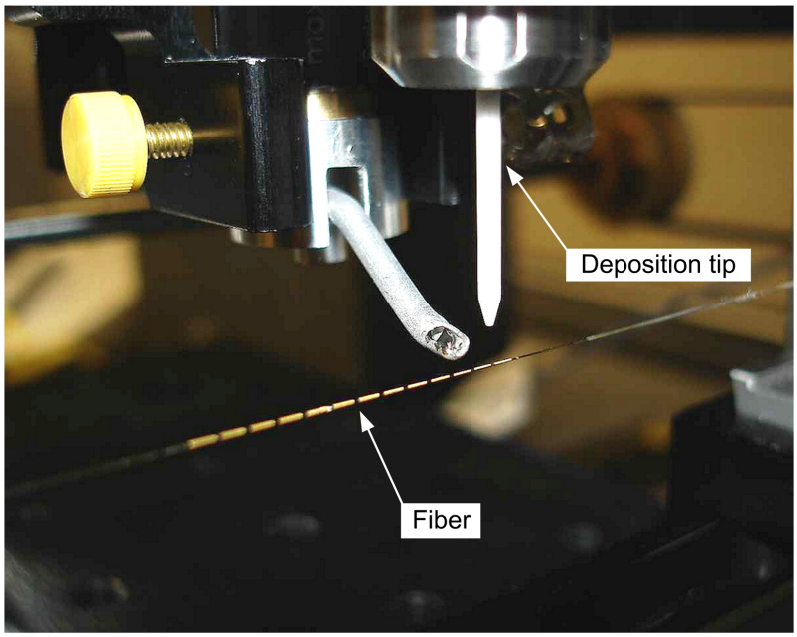

Figure 4-17: LAMM deposition tip and the optical fiber during the deposition of on-fiber silver thin films

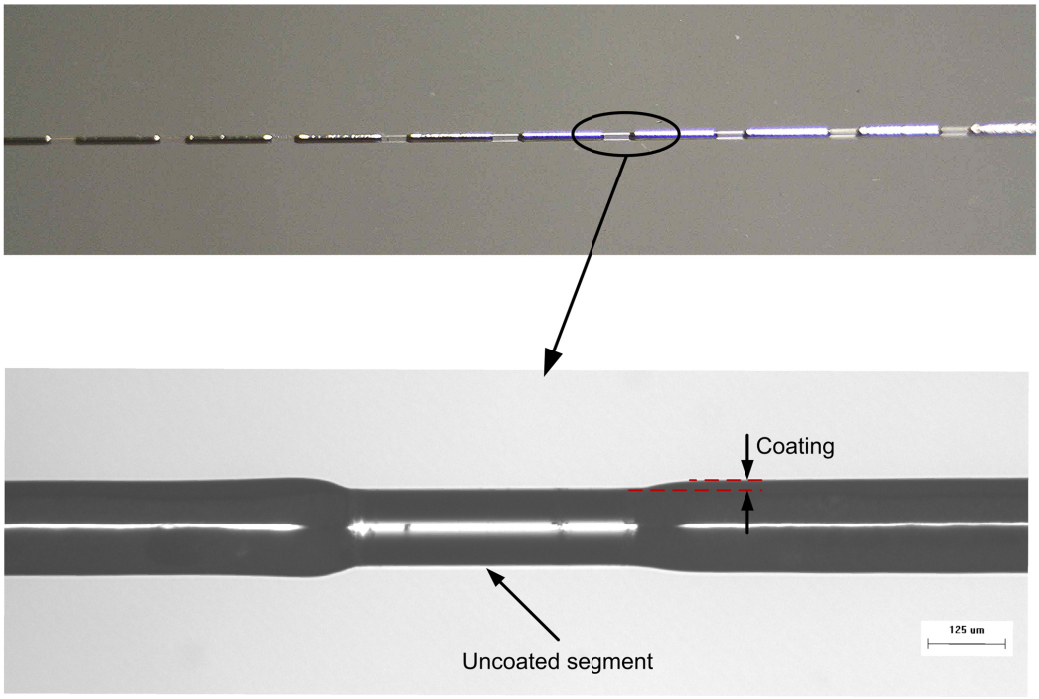

Figure 4-18: Periodic silver thin films with a thickness of 9 μm deposited on an optical fiber

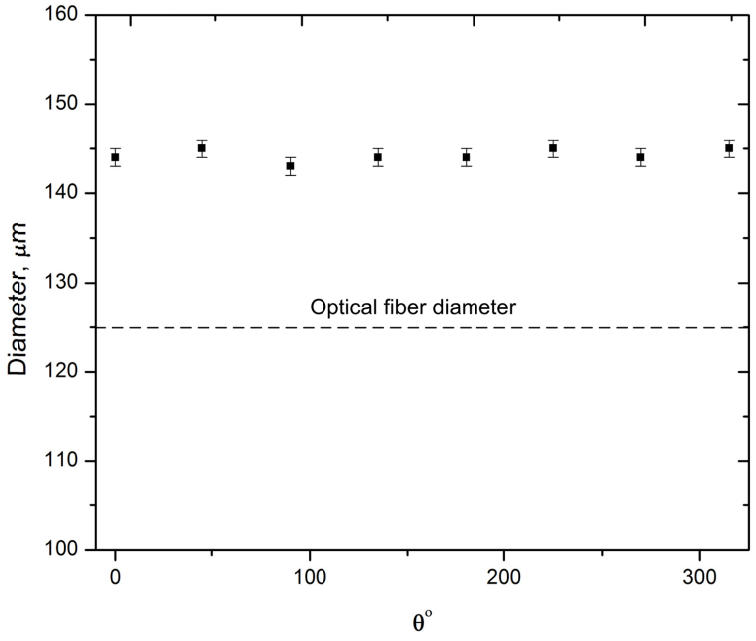

Figure 4-19: Distribution of the thickness of silver thin films deposited around the optical fiber

4.3 Femtosecond Laser Micromachining of Optical Fibers

One of the approaches of this research is to increase the sensitivity of FBGs to the concentration of the surrounding media while retaining its thermal sensitivity intact. The new developed sensor is utilized for the simultaneous measurement of concentration and temperature in liquids. Reduction of the diameter of FBGs is a method that is used to make them sensitive to the index of refraction and concentration [17-21]. HF etching is typically used for the material removal and the reduction of the diameter of optical fibers. The etching rate is slow and the process is isotropic and non-directional. Etching rates of 1.8 μm/min with 52% HF solution [17], 80 nm/min in buffered oxide etch (BOE) [18], and 650 nm/min in 24% buffered HF solution [19] have been reported for the reduction of the cladding diameter of FBGs.

In this thesis, the selective micromachining of the outer surface of FBGs using femtosecond laser pulses is proposed to remove the materials from the cladding. Compared with HF etching, the femtosecond laser micromachining process is faster and can be easily controlled for patterning on optical fibers. The optical fiber, made of silica, is transparent to the visible and Near-Infrared (NIR) electromagnetic radiation. Long pulse lasers (pulse durations of 10 ps and larger) cannot be absorbed by silica for micromachining. However, ultrashort laser pulses (tenth of picoseconds or femtosecond) in the NIR range enable both surface and bulk micromachining of silica.

4.3.1 Interaction of Femtosecond Laser Pulses with Silica

The interaction of femtosecond laser pulses with dielectric materials such as silica was a research topic in the past years [108-111]. The interaction of ultra-short laser pulses with materials differs completely from that of long pulse lasers. In the interaction of long pulse lasers (pulse durations larger than 10 ps) with materials, the laser energy absorption mechanism is electronic excitation due to the absorption of electromagnetic radiation and the electron-lattice interaction to convert the energy to heat [112].

The interaction of femtosecond laser pulses with dielectrics such as silica involves some fundamental processes. When silica is irradiated by intense femtosecond laser pulses, the index of refraction of the material becomes intensity dependent. The energy of a single photon is not sufficient to excite the electrons in the valence band and transfer them to the conduction band. As a result, in the interaction of high density laser pulses, the electrons in

the valence band are excited through the absorption of multiple photons which is called multi-photon ionization. The rate of the multi-photon ionization is a function of the laser intensity. The electrons in the conduction band can absorb more laser energy through free-carrier absorption. If the energy of the conduction electrons increases by an amount higher than that of the band gap, the conduction electrons can ionize more valence electrons through impact ionization. This process continues as long as the laser energy is available, and results in increase of the plasma density, which is known as avalanche ionization. [112]. After the formation of the plasma, various mechanisms can cause damage in the dielectric material. The transfer of energy from the high density plasma results in melting, vaporization, and ablation of the material. The transfer of energy from the high density plasma to the lattice occurs in a time scale much smaller than the thermal diffusion time, which reduces the heat affected zone. [109, 110, 113]. The damage can also result from the defects originated from the creation and relaxation of Self-Trapped Excitons (STE). The generated defects in silica are oxygen vacancy (E' center), peroxy radical/linkage, and Non-Bridging Oxygen Hole Center (NBOHC) [114].

In addition to surface micromachining and material removal, structural modifications, including changes in the index of refraction and stress induction, can be achieved in the interaction of femtosecond laser pulses with silica [115-117]. Femtosecond lasers have been used for the induction of birefringence in optical fibers by exposing the cladding to the laser radiation [42] and for direct writing of Bragg gratings in the core of optical fibers for sensing and fiber laser applications [40, 41, 43, 118]. The fabrication of intracore Bragg gratings by the lateral illumination of optical fibers using phase mask scanning technique has been reported to enhance the sensing performance of FBGs [118]. Femtosecond lasers have been used for the inscription of high-temperature stable Bragg gratings in Polarization Maintaining (PM) optical fibers. The photo-enhanced birefringence, caused by the femtosecond pulses, resulted in FBG sensors with a dual-parameter sensing capability in a wide range [41]. Bragg gratings have also been inscribed in the core of the Yb-doped optical fibers used in fiber lasers [119].

4.3.2 Femtosecond Laser Micromachining Setup

Figure 4-20 shows the workstation setup of the femtosecond laser facility, used for this research work at the Laser Processing Research Centre (LPRC) of the University of

Manchester, UK. Figure 4-21 is the schematic diagram of the femtosecond laser setup, and the position of the optical fiber relative to the laser beam. The Libra-S laser system, a diode-pumped Ti:Sapphire femtosecond laser (Coherent Inc., Santa Clara, CA, USA) was used for the experiments. The laser produces light of 800 nm wavelength in 100 fs pulses with a repetition rate of 1 kHz. The maximum pulse energy is 1 mJ which was attenuated to 20-40 μJ for the experiments. A 15X lens (N.A.=0.28) was chosen to focus the beam on the process zone. The FBGs were installed on a high precision three-dimensional motion system, with a precision of ±10 nm (Aerotech, Inc., Pittsburgh, PA, USA), and moved across the laser beam to inscribe micro-grooves along the fiber. The beam focal point parameters were small relative to the cladding diameter. However, in the experiments, the laser beam was defocused on the fiber cladding surface to create larger features. The circular shape of the optical fiber gives a non-circular intensity distribution at the process zone. In this case, the beam diameter along the optical fiber axis (z axis) is smaller than that in the direction perpendicular to the optical fiber axis (x axis).

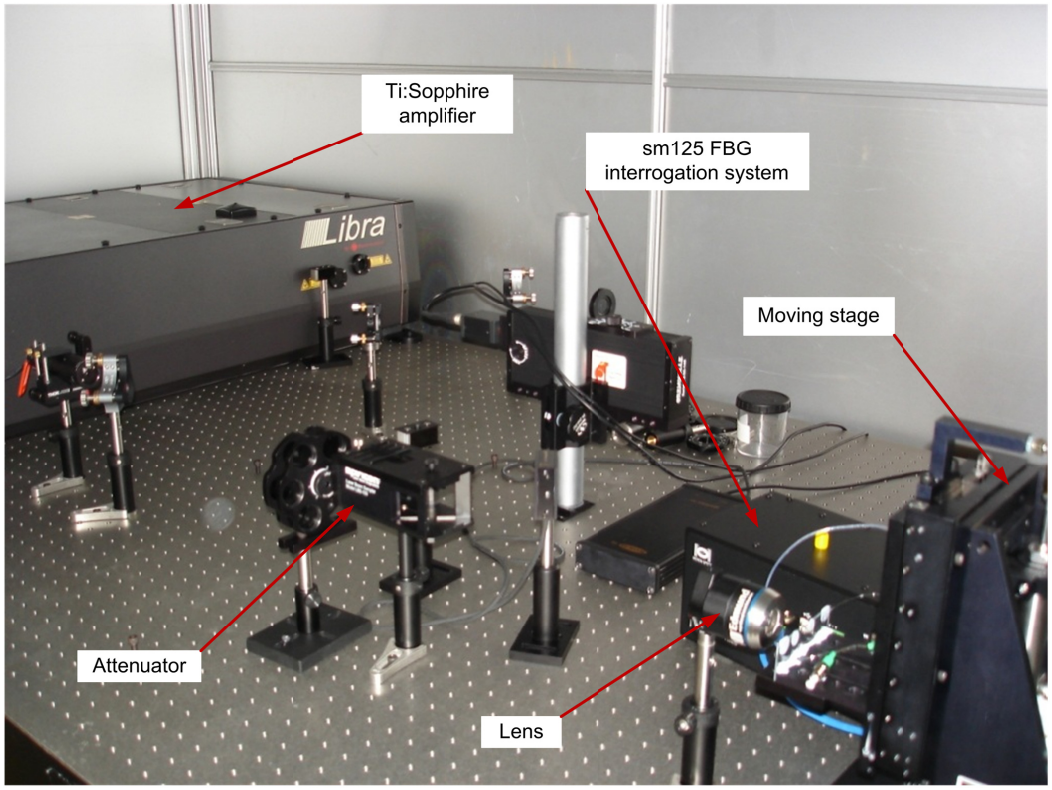

Figure 4-20: Femtosecond laser workstation setup at LPRC, the University of Manchester, UK

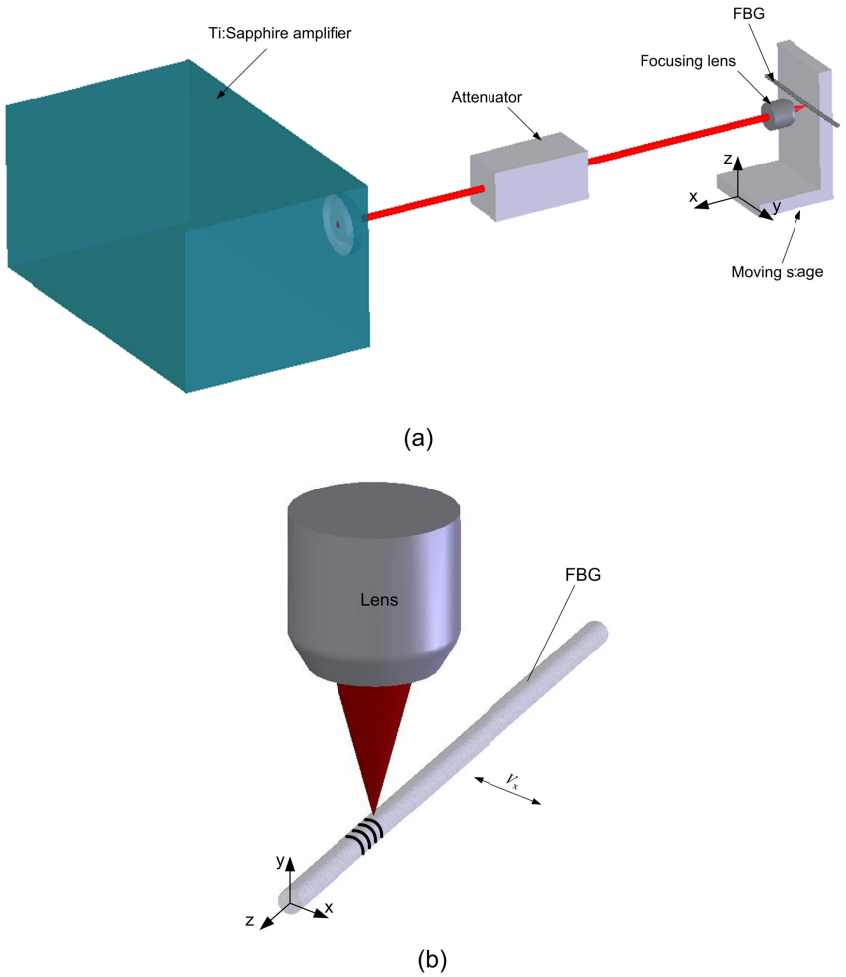

Figure 4-21: (a) Schematic diagram of the femtosecond laser workstation setup and (b) femtosecond laser beam and FBG

4.3.3 Micromachining Results

The femtosecond micromachining process was initially characterized by the fabrication of micro-grooves on planar silica substrates. To do so, micro-grooves at various laser average powers were inscribed. Figure 4-22 illustrates the variations of the grooves' width as functions of the laser power and a laser scanning speed of 5 μm/s. The widths of micro-groves increase by increasing laser power. A micro-groove width of less than 20 μm is achievable at laser powers of less than 50 mW. In the experiment, it was observed that the roughness of the micro-groove edges increases by increasing the laser scanning speed. This can be attributed to the number of pulses per spot.

For the inscription of micro-grooves on optical fibers, the fibers were mounted on the three-dimensional moving stage and irradiated by the laser beam. The stage was programmed to move the optical fiber across the laser beam to inscribe micro-grooves.

Figure 4-23 shows micro-grooves inscribed on the surface of an optical fiber at a laser average power of 41 mW and laser scanning speeds of 100 μm/s and 500 μm/s. For these two cases the numbers of pulses per spot are 175 and 33 on the center line, respectively. It is observed that lower scanning speeds form smoother groove edges due to the increased number of pulses per spot and less temporal separation between the pulses.

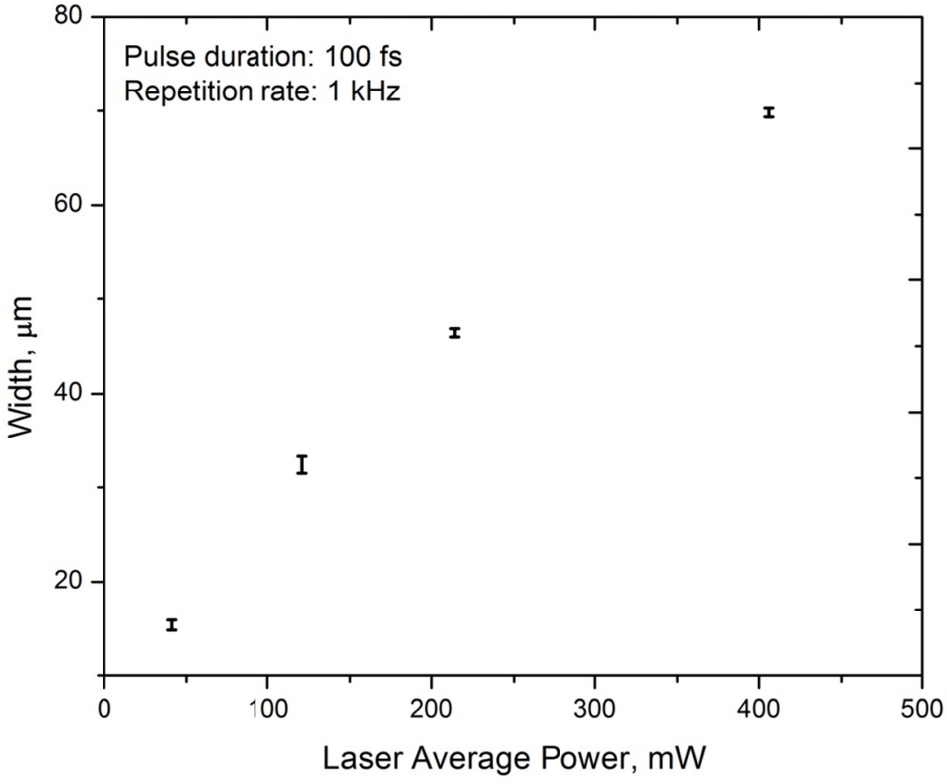

Figure 4-22: Micro-grooves width as a function of laser average power for laser scanning speed of 5 μm/s, inscribed on a planar silica substrate

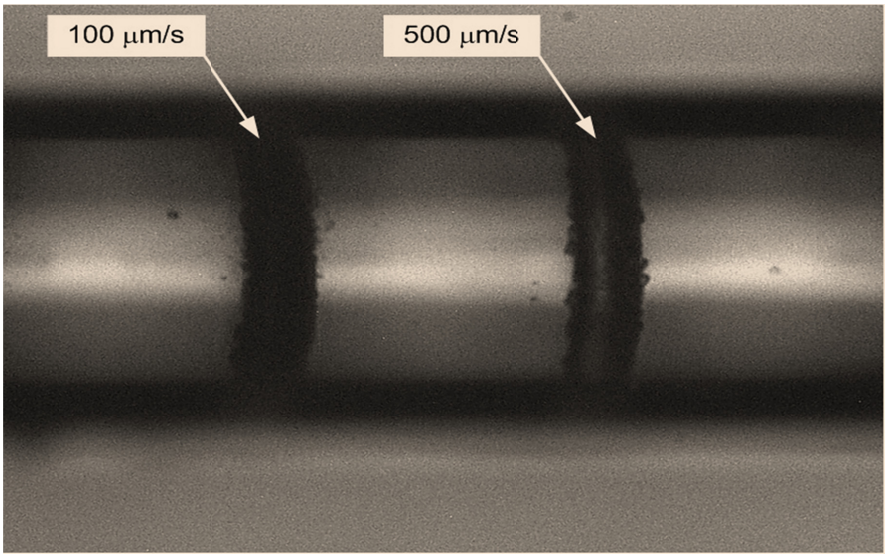

Figure 4-23: Effect of laser scanning speed on the surface quality of micromachined grooves on an optical fiber

4.4 Summary

The characterizations of laser-assisted direct microfabrication processes were explored in this chapter. The goal was the implementation of the additive and subtractive laser-based processes for the modification of FBGs. In the additive method, the LAMM process was successfully characterized to selectively deposit silver thin films on optical fibers. Several methods were employed to study the geometrical features, microstructure, crystal structure, and mechanical properties of the deposited films. These properties were related to the deposition process parameters. In the subtractive method, femtosecond laser micromachining was implemented for the inscription of micro-grooves in the cladding of optical fibers. The effects of the laser average power and laser scanning speed on the geometrical features of the micro-machined grooves were investigated in this study.

Chapter 5

Superstructure FBGs for Multi-Parameter Sensing

In this chapter the modeling, design, and fabrication of Superstructure FBGs (SFBG) are addressed for the simultaneous measurement of temperature and strain. The procedures for the development of a structural model, along with the opto-mechanical model of FBGs are presented. The modeling simulation results are also provided. The chapter ends with the experimental results consisting of the optical response of SFBG exposed to structural loading and temperature variations, and also, the simultaneous measurement of strain and temperature.

5.1 Superstructure FBGs with Periodic On-Fiber Films

In SFBGs, the modulations of the index of refraction vary periodically along the fiber axis with a longer period (typically larger than 100 μm) than that of the grating . The long-period variations of the index of refraction cause the formation of equally spaced sidebands in the reflection spectrum of FBG, as described in Chapter 3 (Figure 3-8).

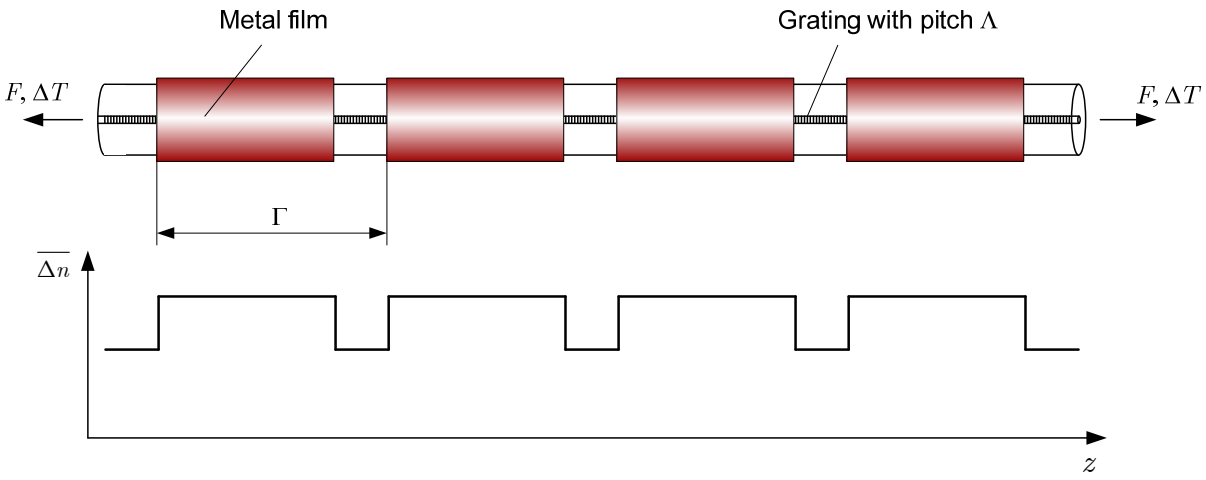

Figure 5-1: Periodic films on FBG and their effects on the average index of refraction ($\overline{\Delta n}$) when the optical fiber is exposed to axial tensile force and/or temperature variations

The concept of SFBG can also be realized by the deposition of periodic metal films on FBGs, as shown in Figure 5-1. In a SFBG with periodically deposited on-fiber films, a periodic distribution of strain is induced along the grating, when the fiber is exposed to axial force (F) or thermal heating/cooling (ΔT). This is due to the differences in the geometries and the thermal expansions of the films and the optical fiber. The periodic distribution of the strain components along the grating causes the periodic variations of the average index of refraction ($\overline{\Delta n}$) due to photo-elastic effect. In addition to the index of refraction, the grating pitch (Λ) varies periodically along the fiber. The sideband spacing in a FBG, coated with metal films with period of Γ is derived from the phase matching condition (3.73) as described in Chapter 3:

$$\Delta\lambda = \frac{\lambda_B^2}{2n_{eff}\Gamma} \tag{5.1}$$

The periodically spaced sidebands in the reflection spectrum of SFBG have a broad range of applications in fiber lasers and tunable filters [66]. In contrast to the superstructure FBGs fabricated by UV exposure, the reflectivity of the sidebands in SFBGs with on-fiber films can be tuned by changing temperature and force. The concept of tunable SFBG by the fabrication of metal films on optical fibers has been elaborated on in the paper of Ahuja *et al.* [66]. They proposed tunable SFBGs for wavelength-division multiplexing, optical sensing,

and fiber lasers. In their work, thin films of gold with periodic variable diameters were deposited on a pre-deposited on-fiber titanium thin film by using electron beam evaporation. They showed that joule heating causes a periodic distribution of temperature along the fiber. This creates sidebands whose reflectivities are tuned by electric current.

From the sensing point of view, SFBGs with periodic metal coatings can be used for simultaneous parameter measurements, which eliminates the inherent limitations of FBGs in the thermal and structural measurements. The intensity of the sidebands generated in SFBGs is regulated by the applied temperature and force on the optical fiber. The intensity of the sidebands combined with the Bragg wavelength shift can be used to discriminate the coupled effects of temperature and strain. To the best knowledge of the author, there is no report on the implementation of SFBGs with on-fiber films for the concurrent measurement of temperature and strain. UV induced SFBGs have been used for multi-parameter sensing. In the work of Guan [29] *et al.* the transmission spectrum of a UV-exposed SFBG was used for the simultaneous measurement of strain and temperature. The measurements were based on the analysis of the attenuation bands generated by cladding mode couplings.

In this thesis, the LAMM process was adopted for the fabrication of on-fiber thin films, which was explained in Chapter 4. The rest of this chapter elaborates on the modeling, design, and test of SFBG sensors with on-fiber thin films.

5.2 Opto-mechanical Modeling

To design the SFBGs with multi-parameter sensing capabilities, an opto-mechanical model is developed. The model consists of two components: (1) structural model of SFBGs to find the state of stress and strain in optical fibers, and (2) opto-mechanical model consisting of the photo-elastic and thermo-optic effects to find the reflection spectrum of SFBGs.

5.2.1 Structural Modeling of SFBGs Exposed to Force and Temperature Variations

For the structural modeling, it is assumed that the optical fiber is uniformly heated by ΔT and is exposed to an axial tensile force of F. The approach is similar to the modeling of thick-wall cylinders under structural loading and temperature variations [120]. Figure 5-2 demonstrates the coated segment of the optical fiber in cylindrical coordinates (r, θ, z). It is

assumed that the optical fiber with a diameter of r_f is coated with a layer with a thickness of $t = r_c - r_f$.

The displacement component in θ direction (v) is neglected, because of the symmetry, and the dependency of the radial and axial displacements (u , w) on z is considered to be small at the points far from the ends. At these points, the shear components are also zero because of the symmetry. The strain-displacement relations are written as [120]

$$\begin{aligned} e_{rr} &= \frac{du}{dr} \\ e_{\theta\theta} &= \frac{u}{r} \end{aligned} \tag{5.2}$$

As a result, e_{rr} and $e_{\theta\theta}$ are interrelated as

$$\frac{d}{dr}(re_{\theta\theta}) = e_{rr} \tag{5.3}$$

From the equilibrium conditions, the radial and tangential stress components, σ_{rr} and $\sigma_{\theta\theta}$, are related as

$$r\frac{d\sigma_{rr}}{dr} = \sigma_{\theta\theta} - \sigma_{rr} \tag{5.4}$$

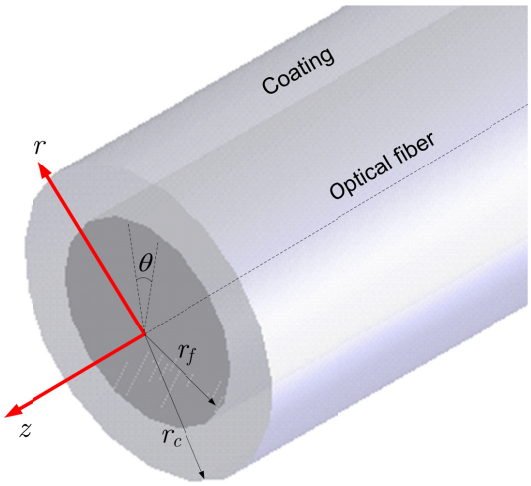

Figure 5-2: Coated segment of an optical fiber in cylindrical coordinates

which yields

$$\frac{d}{dr}(r\sigma_{rr}) = \sigma_{\theta\theta} \tag{5.5}$$

The stress-strain-temperature relations are written as

$$\begin{bmatrix} e_{rr} \\ e_{\theta\theta} \\ e_{zz} \end{bmatrix} = \frac{1}{E}\begin{bmatrix} 1 & -\nu & -\nu \\ -\nu & 1 & -\nu \\ -\nu & -\nu & 1 \end{bmatrix}\begin{bmatrix} \sigma_{rr} \\ \sigma_{\theta\theta} \\ \sigma_{zz} \end{bmatrix} + \alpha\Delta T \tag{5.6}$$

where ν is the Poisson's ratio, E is the modulus of elasticity, and α is the coefficient of thermal expansion. By integrating (5.3) and (5.5) and using (5.6), the stress components in the optical fiber and the coating are obtained as follows:

$$\begin{aligned} \sigma^f_{rr} &= \frac{-\alpha_f E_f}{2(1-\nu_f)}\Delta T + C^f_1 \\ \sigma^f_{\theta\theta} &= \frac{-\alpha_f E_f}{2(1-\nu_f)}\Delta T + C^f_1 \\ \sigma^c_{rr} &= \frac{-\alpha_c E_c}{2(1-\nu_c)}\Delta T + C^c_1(1-\frac{r_f^2}{r^2}) + \frac{C^c_2}{r^2} \\ \sigma^c_{\theta\theta} &= \frac{-\alpha_c E_c}{2(1-\nu_c)}\Delta T - C^c_1(1-\frac{r_f^2}{r^2}) - \frac{C^c_2}{r^2} \end{aligned} \tag{5.7}$$

where C^c_1, C^f_1, and C^c_2 are integration constants and the superscripts f and c are associated with the optical fiber and the coating, respectively. Considering the following boundary conditions,

$$\begin{aligned} & e^f_{zz} = e^c_{zz} \\ & \sigma^f_{zz}A_f + \sigma^c_{zz}A_c = F \\ & \sigma^c_{rr}(r_c) = 0 \\ & e^f_{\theta\theta}(r_f) = e^c_{\theta\theta}(r_f) \\ & \int_{r_f}^{r_c} \sigma^c_{\theta\theta}dr = \int_0^{r_f} \sigma^f_{\theta\theta}dr \end{aligned} \tag{5.8}$$

σ_{zz}^{f}, σ_{zz}^{c}, C_1^c, C_1^f, and C_2^c are obtained, which are substituted in (5.7) and (5.6) to find the strain components.

5.2.2 Opto-mechanical Modeling of SFBG with Periodic On-Fiber Films

The results of the structural modeling are used in the opto-mechanical model to find the anisotropic index of refraction by using (3.12), and the modified effective mode index of refraction by using (3.13) in the coated and uncoated segments of the optical fiber. Afterwards, the coupled-mode equations (3.62) are solved to obtain the spectral response of SFBG. By defining,

$$\rho(z) = \frac{S(z)}{R(z)} \tag{5.9}$$

and taking the derivative of (5.9),

$$\frac{d\rho(z)}{dz} = \frac{1}{R(z)}\frac{dS(z)}{dz} - \frac{\rho(z)}{R(z)}\frac{dR(z)}{dz} \tag{5.10}$$

Substitution of $R(z)$ and $S(z)$ from (3.62) in (5.10), results in a new form of the coupled-mode equations as follows:

$$\frac{d\rho(z)}{dz} = iK_{AC}\rho^2 + 2i\left(\frac{2\pi n_{eff}}{\lambda} - \frac{\pi}{\Lambda} - \frac{1}{2}\frac{d\Phi}{dz} + K_{dc}\right)\rho + iK_{AC} \tag{5.11}$$

which is in the form of the Riccati equation. Accordingly, $r(\lambda)$ in (3.64) is written as

$$r(\lambda) = \left|\rho\left(-L\,/\,2\right)\right|^2 \tag{5.12}$$

The boundary condition is

$$\rho(L\,/\,2) = 0 \tag{5.13}$$

The Riccati ODE (5.11) can be solved by direct integration. A 4^{th}-order Runge-Kutta algorithm was developed for this purpose in MATLAB, which is available in Appendix E.

5.3 Simulation Results

In this section, the simulation results are presented to investigate the effects of different parameters on the optical response of the SFBG sensor. The optical constants for the simulations are listed in Table 4-4. The values are obtained for the FBGs supplied from external suppliers.

The coefficient $\hat{K} = 2\pi n_{eff} / \lambda - \pi / \Lambda - d\Phi / 2dz + K_{dc}$ in (5.11) is plotted along a FBG at different forces and temperatures at the wavelength of 1550 nm in Figure 5-3 and Figure 5-4. It is assumed that the original grating is Gaussian apodized. The graphs are obtained for the periodically spaced on-fiber silver coatings with a thickness of 9 μm and a period of 2 mm (Figure 4-18 and Figure 5-5). There exists seven silver films on a 14 mm long grating, and the length of coated segments is 1.5 mm.

As shown in Figure 5-3 and Figure 5-4, $\hat{K}$ changes with the same period as the thin films, and its amplitude increases as force and temperature increase.

When FBG is under tensile force F, $\hat{K}$ in the coated segments of the optical fiber is less than that in the uncoated segments due to the larger strain in the uncoated segments.

As a result of the temperature increase, $\hat{K}$ in the coated segments is larger than that of the uncoated segments. This is attributed to larger strain components in the coated segments of the fiber due to the differences in the coefficients of thermal expansions.

Table 5-1: Modeling constants

Parameter	**Value**
E_{silica}	73 GPa
E_{fiber}	83 GPa
n_{eff} (initial)	1.44405
p_{11}	0.113
p_{12}	0.252
$\overline{\Delta n}$	1×10^{-5}
ν_f	25
Λ(nm)	537
$\partial n / \partial T$	1.2×10^{-5}
L(mm)	14

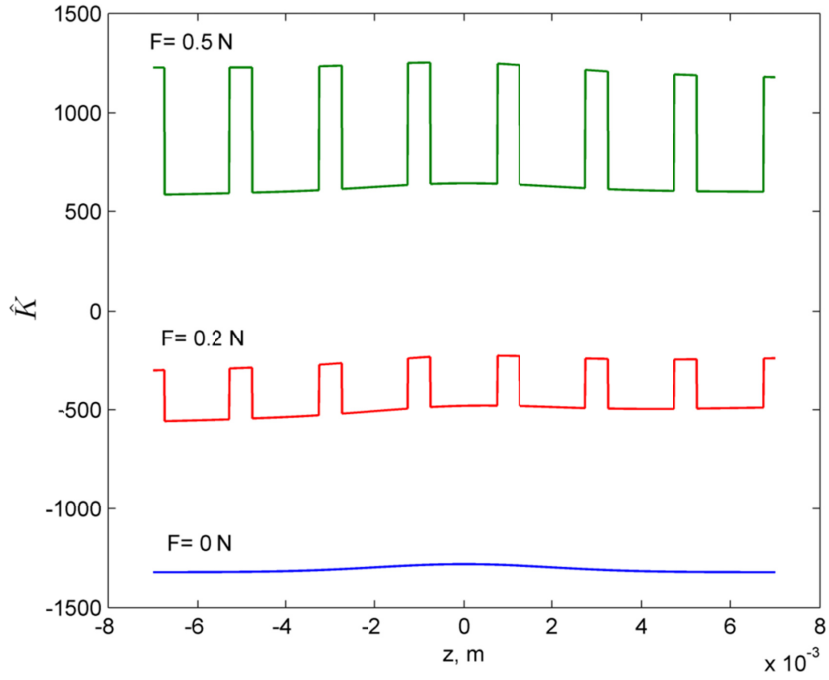

Figure 5-3: $\hat{K}$ at the wavelength of 1550 nm along SFBG with a grating length of 14 mm at different tensile forces and $\Delta T = 0$

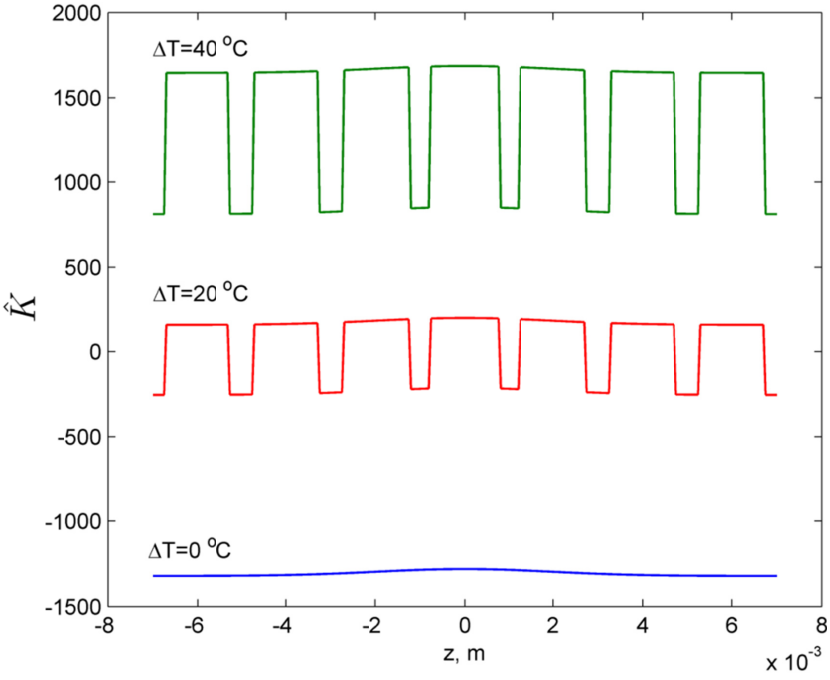

Figure 5-4: $\hat{K}$ at the wavelength of 1550 nm along SFBG with the grating length of 14 mm at different temperatures and $F = 0$

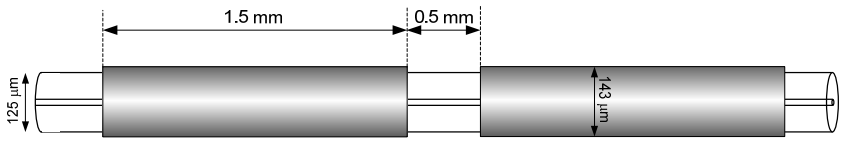

Figure 5-5: Geometrical dimensions of periodic silver films deposited on FBG

Figure 5-6 shows the reflection spectra of the SFBG as a function applied axial loads for 5, 7, and 9 µm silver film thicknesses. The simulations were run for the SFBG design shown in Figure 5-5. The silver films are 1.5 mm long with a period of 2 mm. Figure 5-7 and Figure 5-8 show the reflectivity of the first upper sideband and the Bragg wavelength of SFBG as functions of the applied axial force at different film thicknesses. Table 5-2 contains the Bragg wavelength sensitivity to axial load for different film thicknesses. As seen the sensitivity of the Bragg wavelength to the applied axial load decreases with increasing the film thickness. At the film thickness of 1 µm the sensitivity is 1.32 nm/N and is reduced to 1.05 nm/N at the thickness of 15 µm. Increasing the film thickness results in the reduction of the average strain along the grating which leads to the reduction of the sensitivity of the Bragg wavelength. The sensitivity of the sidebands reflectivity increases with thicker films; however, the trend of the variations of reflectivity with axial force is not linear. The film thickness manifests itself in the amplitude of the periodic variation of strain along the grating.

Table 5-2: Bragg wavelength sensitivity to axial force for different film thicknesses

Film Thickness (µm)	**Bragg Wavelength Sensitivity (nm/N)**
1	1.32
5	1.23
7	1.17
9	1.10
15	1.05

The reflection spectra at various temperatures are plotted in Figure 5-9. The Bragg wavelength vs. temperature and reflectivity vs. temperature graphs are plotted in Figure 5-10 and Figure 5-11. Table 5-3 summarizes the Bragg wavelength sensitivity to temperature for different film thicknesses. The thermal sensitivity of the Bragg wavelength to temperature increases from 14.2 pm/°C at a film thickness of 1 µm to 18.8 pm/°C at a

film thickness of 15 μm. In addition, the sensitivity of the sidebands reflectivity increases in thicker films.

Table 5-3: Bragg wavelength sensitivity to temperature for different film thicknesses

Film Thickness (μm)	**Bragg Wavelength Sensitivity (pm/** °C)
1	14.3
5	16.0
7	16.8
9	18.2
15	18.8

It is evident that the tensile force and temperature can change the reflectivity of the sidebands as well as the Bragg wavelength. The sensitivity of the reflectivity of the sidebands to temperature and axial force is determined by the geometrical features of the periodic films. Thicker coatings increase the amplitude of the periodic variations of the index of refraction along the fiber which leads to higher sensitivities.

As it will be explained in the experimental results, after the deposition and laser sintering of silver nanoparticles, residual stresses are generated in the coatings and the coated segments of the fiber. This changes the spectral response of the coated fiber at no-load conditions. In the current simulations, the residual stresses are ignored.

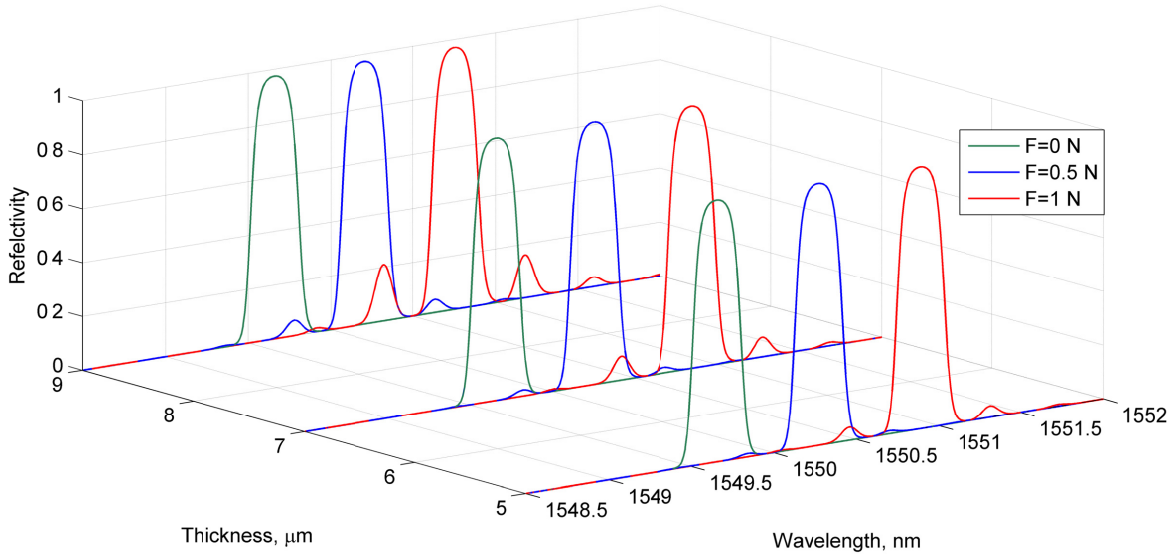

Figure 5-6: Reflection spectra as a function of applied tensile force for SFBG with silver film thicknesses of 5 μm, 7 μm, and 9 μm

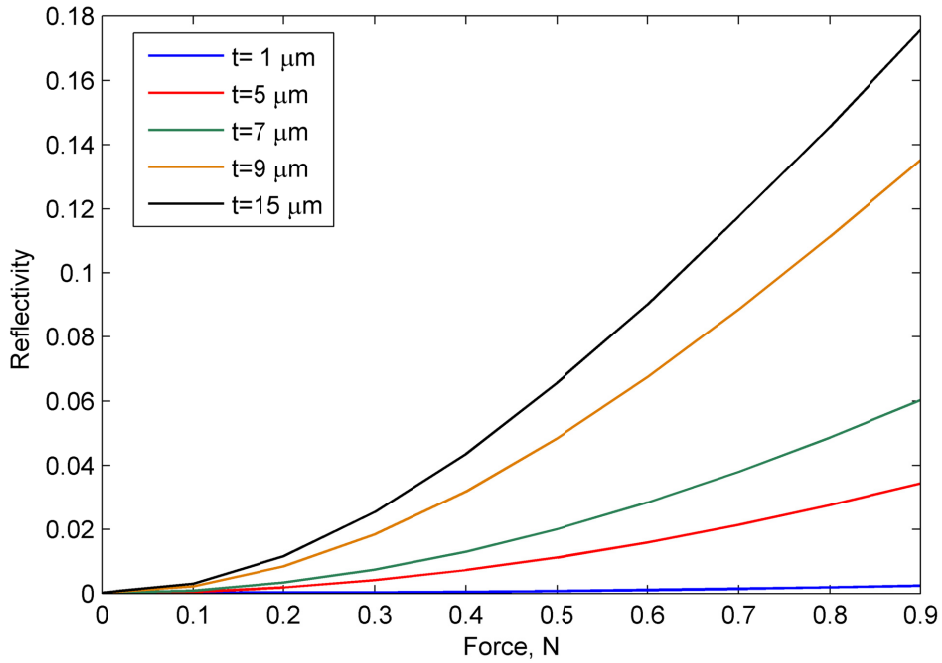

Figure 5-7: Reflectivity of the first upper sideband as a function of applied tensile force on SFBG with different film thicknesses

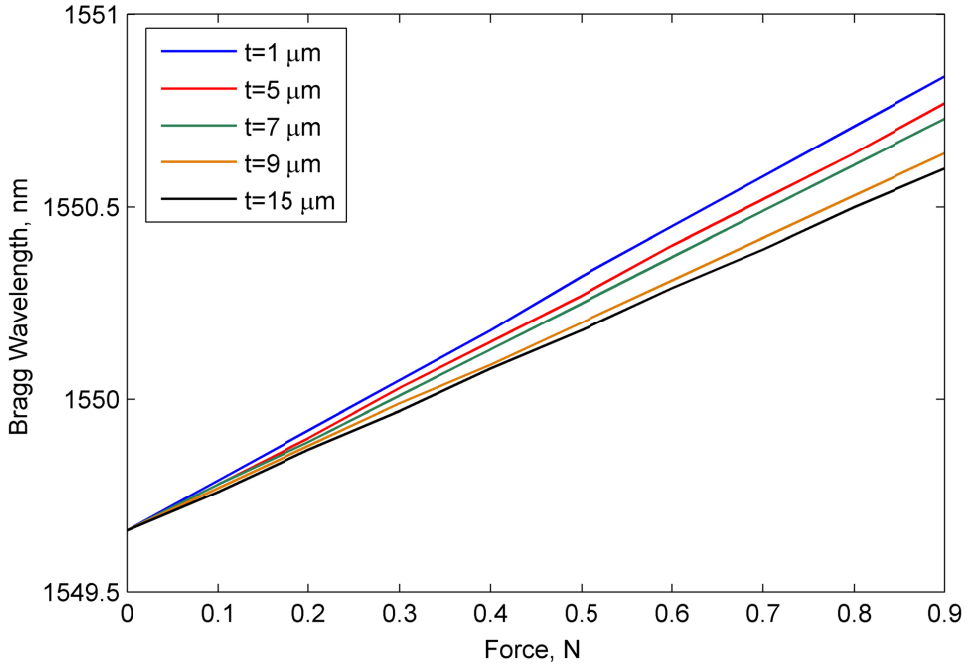

Figure 5-8: Bragg wavelength shift as a function of applied tensile force on SFBG with different film thicknesses

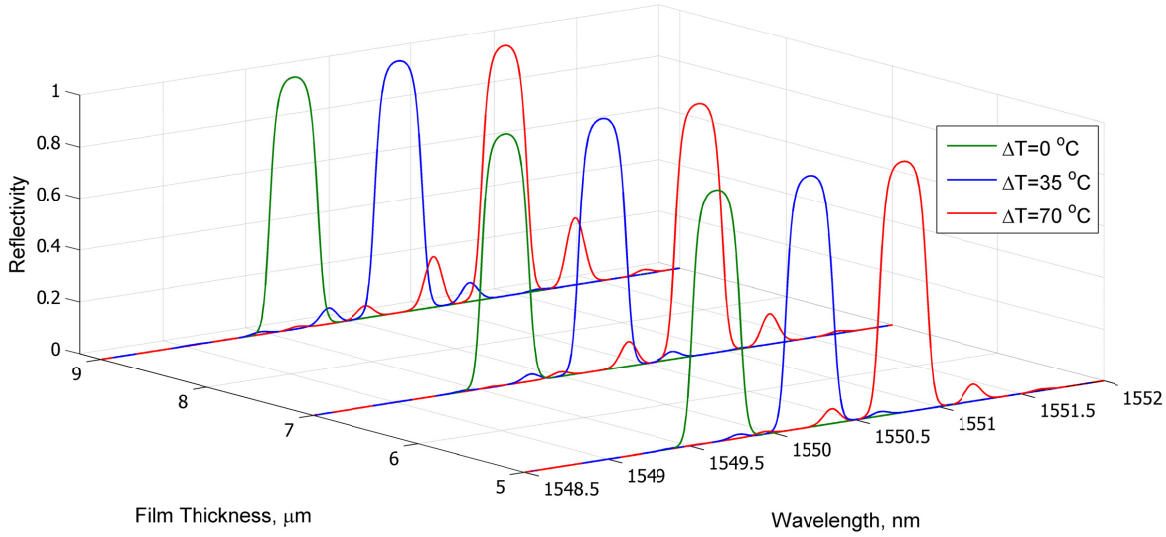

Figure 5-9: Reflection spectra as a function of temperature for SFBG with silver film thicknesses of 5 μm, 7 μm, and 9 μm

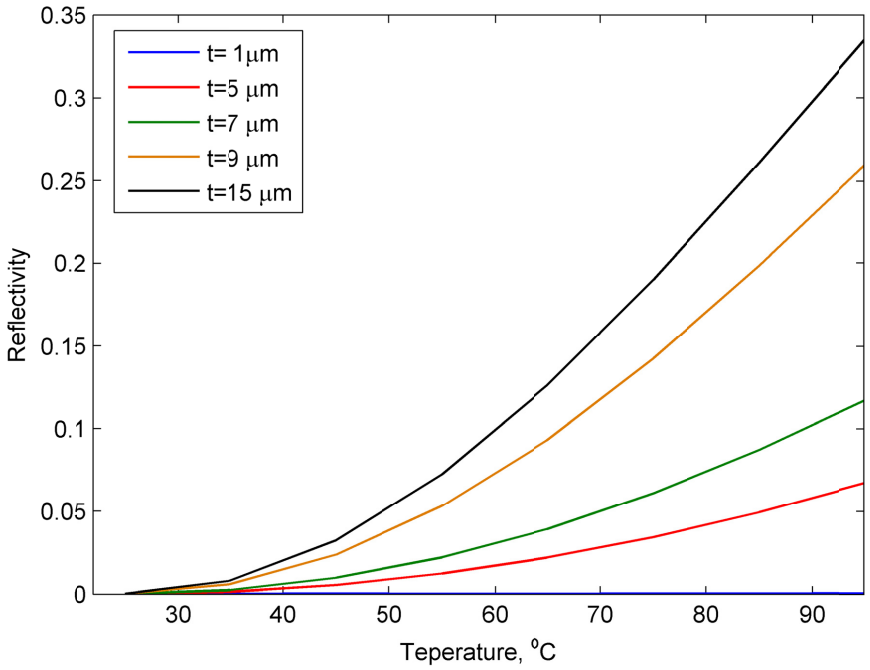

Figure 5-10: Reflectivity of the first upper sideband as a function of temperature for SFBG with different film thicknesses

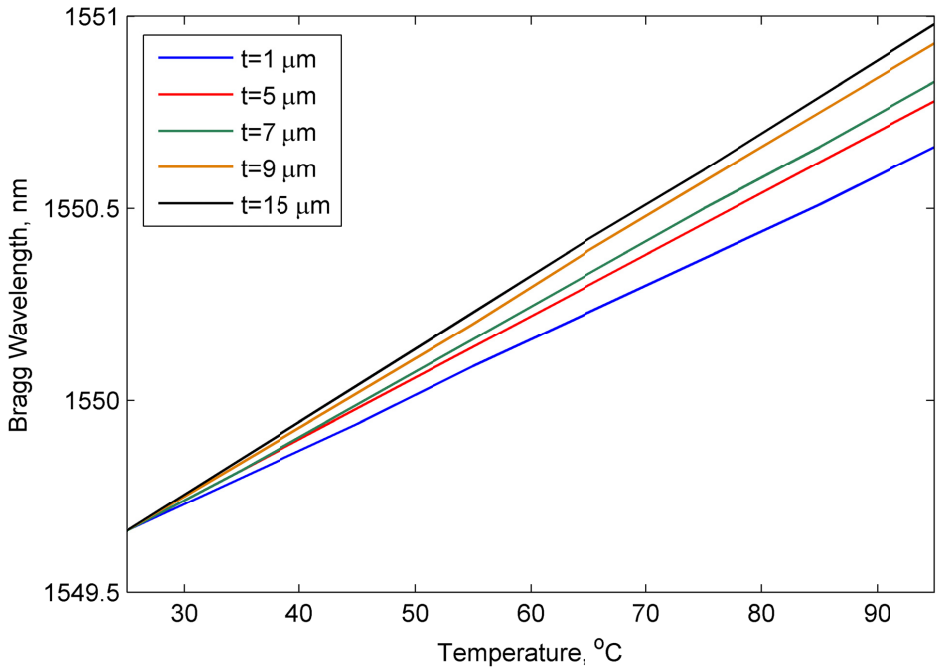

Figure 5-11: Bragg wavelength shift as a function of temperature for SFBG with different film thicknesses

5.4 Geometrical Features of fabricated SFBGs with On-Fiber Films

A SFBG was fabricated by depositing silver coatings on the outer surface of regular FBGs. The details of the deposition process using LAMM and the geometrical and the microstructural features of the silver films were elaborated on in Chapter 4. A FBG with a grating length of 14 mm was selected for the experiments, on which seven silver films with a duty cycle of 3/4 were fabricated with the geometrical features depicted in Figure 5-5.

5.5 Measurement Test Rig

For the analysis of the spectral response, the SFBG was loaded axially at different temperatures to study the effects of force and temperature simultaneously. For the axial loading, the rotational stage, in which the optical fiber was mounted during the fabrication process (as described in Chapter 4), was connected to a motorized positioning stage, with a precision of 1 µm, and a load cell, as shown in Figure 5-12. The grating segment of the FBG was placed in the proximity of a thermoelectric module in a chamber to control its temperature, measured by a thermocouple.

The reflection spectra of the FBGs were taken by sm125 FBG interrogation system (Micron Optics Inc., Atlanta, GA, USA).

5.6 Optical Response Analysis

The reflection spectra of the SFBG before and after the fabrication of the silver films are exhibited in Figure 5-13. A comparison of the two graphs signifies the presence of sidebands in the reflectivity after the deposition of the silver films. This is attributed to the formation of residual stresses in the optical fiber after the agglomeration and sintering of the nanoparticles. Sintering of nanoparticles involves solvent evaporation and thickness reduction, which lead to stress formation in the film and the optical fiber. In addition, after sintering and on cooling, due to the difference between the Coefficients of Thermal Expansions (CTE) of silver and silica ($\alpha_{silver} = 18.9\times10^{-6}$ $^{o}C^{-1}$ and $\alpha_{silica} = 0.55\times10^{-6}$ $^{o}C^{-1}$), tensile/compressive stresses build up in the silver films/optical fiber. In Figure 5-13, the wavelength spacing of the reflectivity peaks is ~400 pm which is consistent with the results obtained from (5.1) with $\Gamma = 2$ mm. The Bragg wavelength shift to lower wavelengths is the result of compressive stress in the coated segments of the fiber. The graph obtained from the modeling is also plotted in the figure showing that the modeling results and the experimental results are in good agreement.

5.6.1 SFBG under Temperature Variations

Figure 5-14 shows the reflectivity of the upper sideband as a function of the Bragg wavelength in a thermal cycle ranging from 45 ^{o}C to 85 ^{o}C. It was observed that the response of the reflectivity curve has a hysteresis behavior at temperatures lower than 45 ^{o}C. This can be attributed to the existence of micro-porosity within the silver films. At temperatures higher than 45 ^{o}C, the reflectivity reduces monotonically from 20% to 3% as temperature rises.

Figure 5-15 depicts the Bragg wavelength shift as a linear function of temperature with a sensitivity of 17.3 pm/^{o}C. In addition, the results obtained from modeling are plotted in Figure 5-14 and Figure 5-15, showing agreement between the modeling and the experimental results with a deviation of 5%. The variations of the reflectivity with temperature are the results of the changes in the amplitude of the strain components along the fiber. As

mentioned before, the deposition and laser sintering of silver films cause the formation of residual stress in the coated segments of the optical fiber. This leads to a periodic distribution of strain, and as a result, the periodic variations of n_{eff} and Λ along the optical fiber. On heating, the state of stress in the silver films changes from tensile to compressive, whereas the reverse occurs in the optical fiber. In the uncoated segments of the optical fiber, the strain components are generated because of thermal expansions that are equal to $\alpha_{silica}\Delta T$. The strain components in the coated and uncoated segments of the FBG are schematically plotted in Figure 5-16. As shown, the difference between the strain components reduces with temperature, which causes the reduction of the amplitude of n_{eff} and Λ and as a result the coefficient $\hat{K}$ in (5.11).

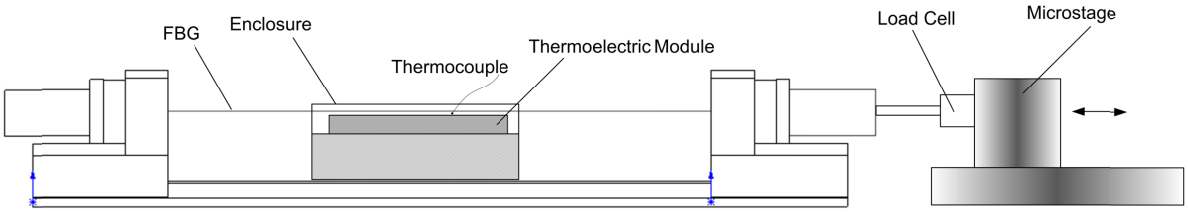

Figure 5-12: Test setup for axial loading of SFBG at different temperatures

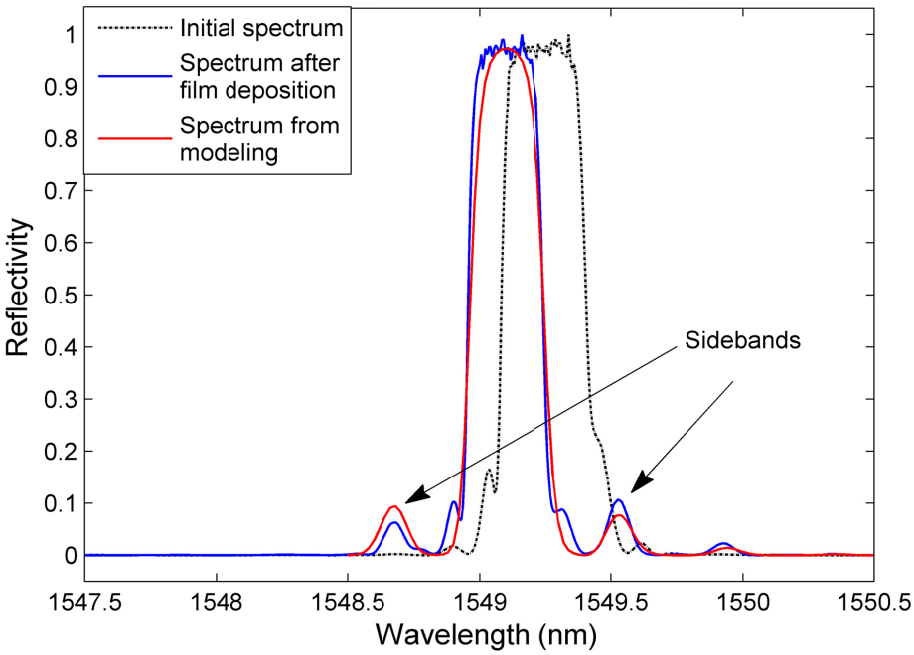

Figure 5-13: Reflection spectra of FBG before and after the deposition of the on-fiber silver films showing the effects of residual stress

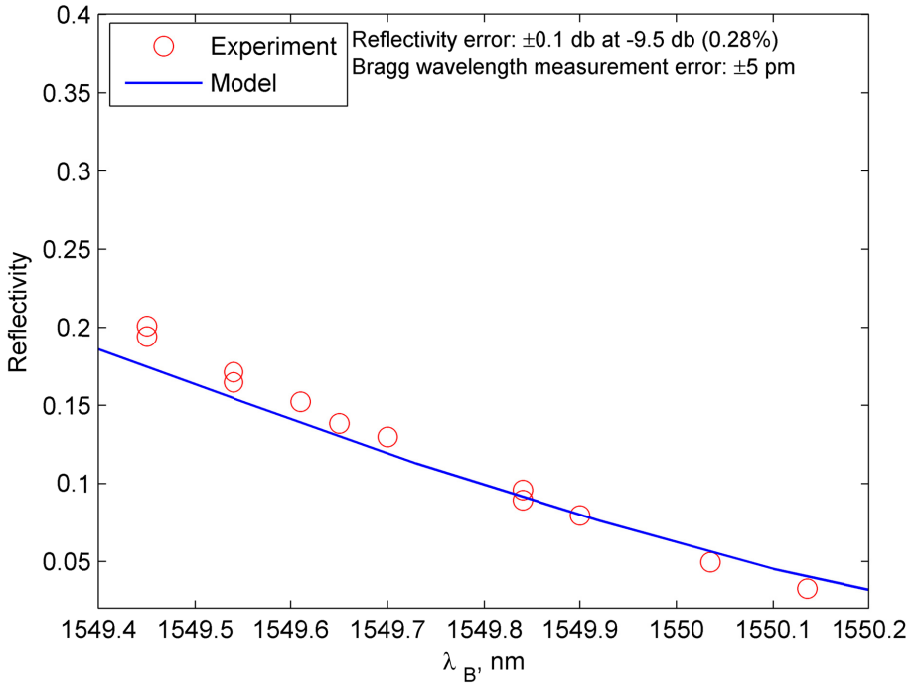

Figure 5-14: Reflectivity of the first upper sideband as a function of the Bragg wavelength in a thermal cycle

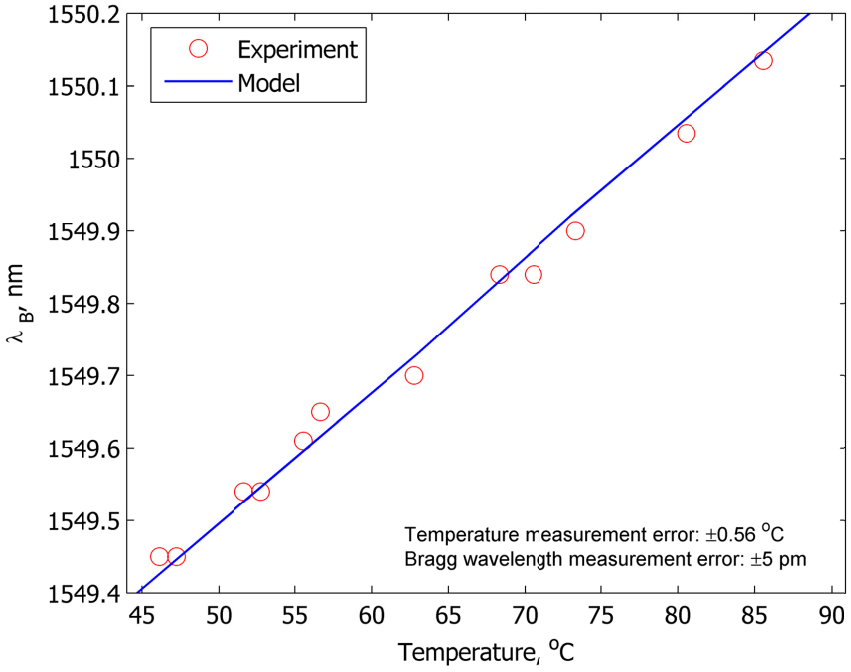

Figure 5-15: Bragg wavelength as a function of temperature

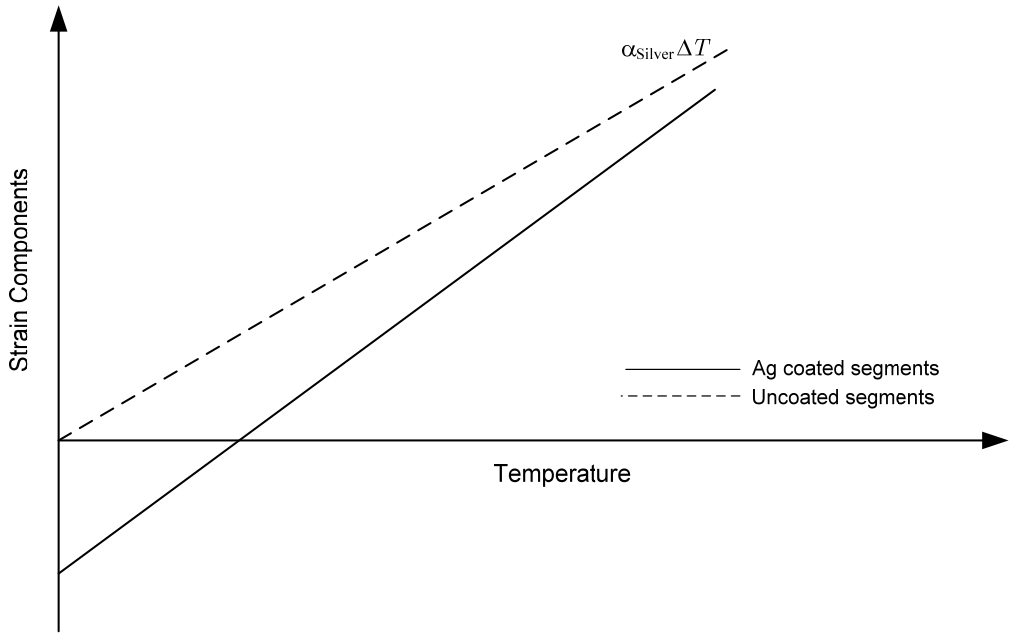

Figure 5-16: Strain components in the coated and uncoated segments of the optical fiber

5.6.2 Structural Loading

The structural parameter that is measured by FBGs is strain. To induce strain, an axial load is applied on the optical fiber. For axial loading, the SFBG was installed on the test rig and tensile loads of 0-0.9 N were applied to the fiber. Figure 5-17 shows the reflectivity of the first upper sideband as a function of the Bragg wavelength at a temperature of 45 °C during the tensile loading. According to this figure, the reflectivity increases to 32% by applying a tensile load of 0.9 N. Due to the existence of periodic films, tensile forces acting on the optical fiber produce the periodic strain distribution along the grating. The tensile force increases the amplitude of the strain distribution and that of n_{eff} and Λ, which amplifies the sidebands reflectivity. The results, obtained from the opto-mechanical modeling in the figure are in agreement with the experimental data.

Figure 5-18 shows the corresponding Bragg wavelength shift as a function of the axial force. The shift of the Bragg wavelength has a sensitivity of 1.2 nm/N deviating from the modeling results by 9%. The linear behavior of the Bragg wavelength variations implies that the silver films are in elastic region, and there is no crack or delamination in the silver films and between the films and the optical fiber.

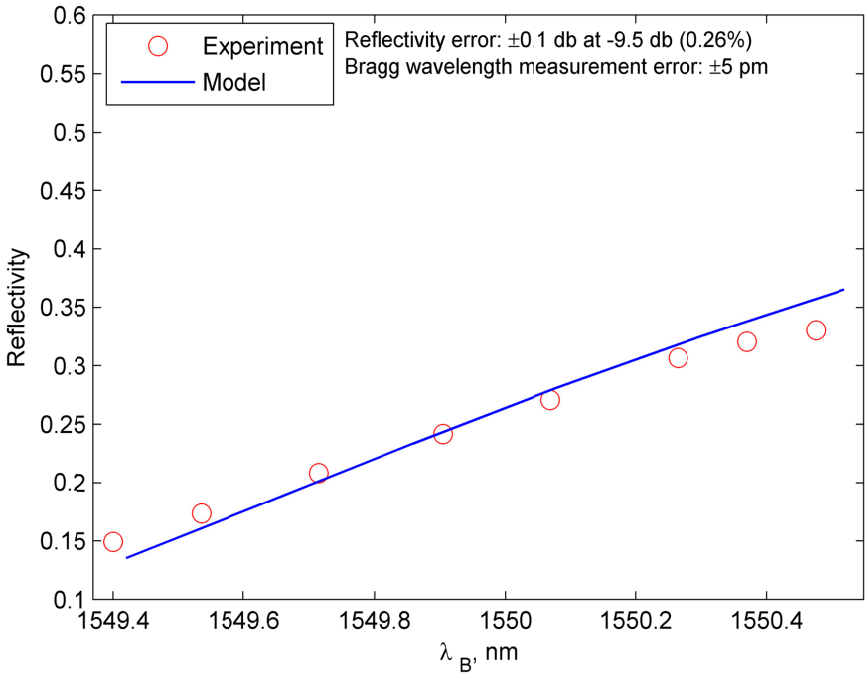

Figure 5-17: Reflectivity of the first upper sideband as a function of the Bragg wavelength in tensile loading

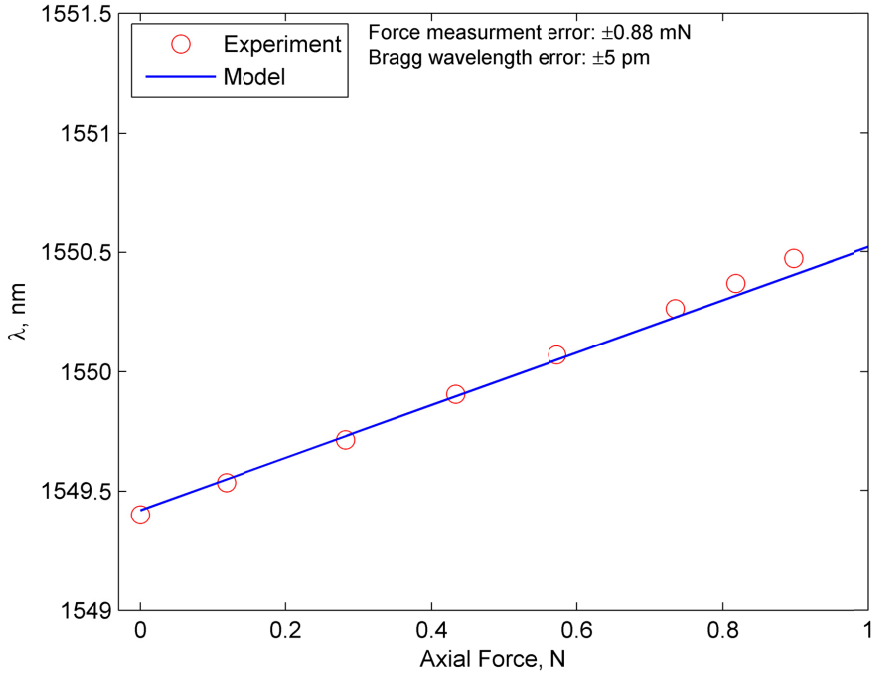

Figure 5-18: Bragg wavelength as a function of tensile force

It should be noted that the behavior of the modeling graphs is dependent on the initial residual stress formed in the coated segments of the optical fiber. In the analyses performed in this research, the model was tuned to fit the experimental data. The tuning was done by finding the initial residual stress for the best fit. In spite of this tuning, the model predicts the gradient and tendency of the results. Obtaining accurate values for the residual stress components requires microstructural analysis of the films.

5.6.3 Simultaneous Measurement of Strain and Temperature

The capabilities of the developed SFBG sensor for the simultaneous measurement of strain and temperature were investigated. The experimental results are displayed in Figure 5-19 to Figure 5-21. Figure 5-19 provides the spectra of SFBG at different temperatures and tensile forces. It is apparent from the figures that both structural loading and temperature shift the Bragg wavelength. As discussed in the previous sections, structural load, inducing strain on the optical fiber, increases the reflectivity of the sidebands; however, temperature inversely affects the reflectivity. This feature enables the simultaneous measurement of strain and temperature using a single FBG. Figure 5-20 contains the reflectivity vs. Bragg wavelength graphs for SFBG in multi-parameter sensing. The graphs are obtained by measuring the reflectivity and the Bragg wavelength in thermal cycles while the sensor is under tensile force.

When the sensor is exposed to tensile force and temperature variations, the strain can be directly obtained from Figure 5-20 by locating the corresponding force graph from the Bragg wavelength and the reflectivity readings. The strain on the optical fiber is related to the applied force. Temperature is obtained by using the Bragg wavelength vs. temperature curves in Figure 5-21.

For each sensor, a set of characteristic curves should be obtained to enable multi-parameter measurements. The characteristic curves are in the form of reflectivity vs. Bragg wavelength and Bragg wavelength vs. temperature. The characteristic curves are schematically plotted in Figure 5-22. The plots consist of a series of constant-strain curves. Strain can be measured by using the reflectivity vs. Bragg wavelength graph. To obtain temperature, the corresponding constant strain curve is located in Bragg wavelength vs. temperature graph in Figure 5-22b.

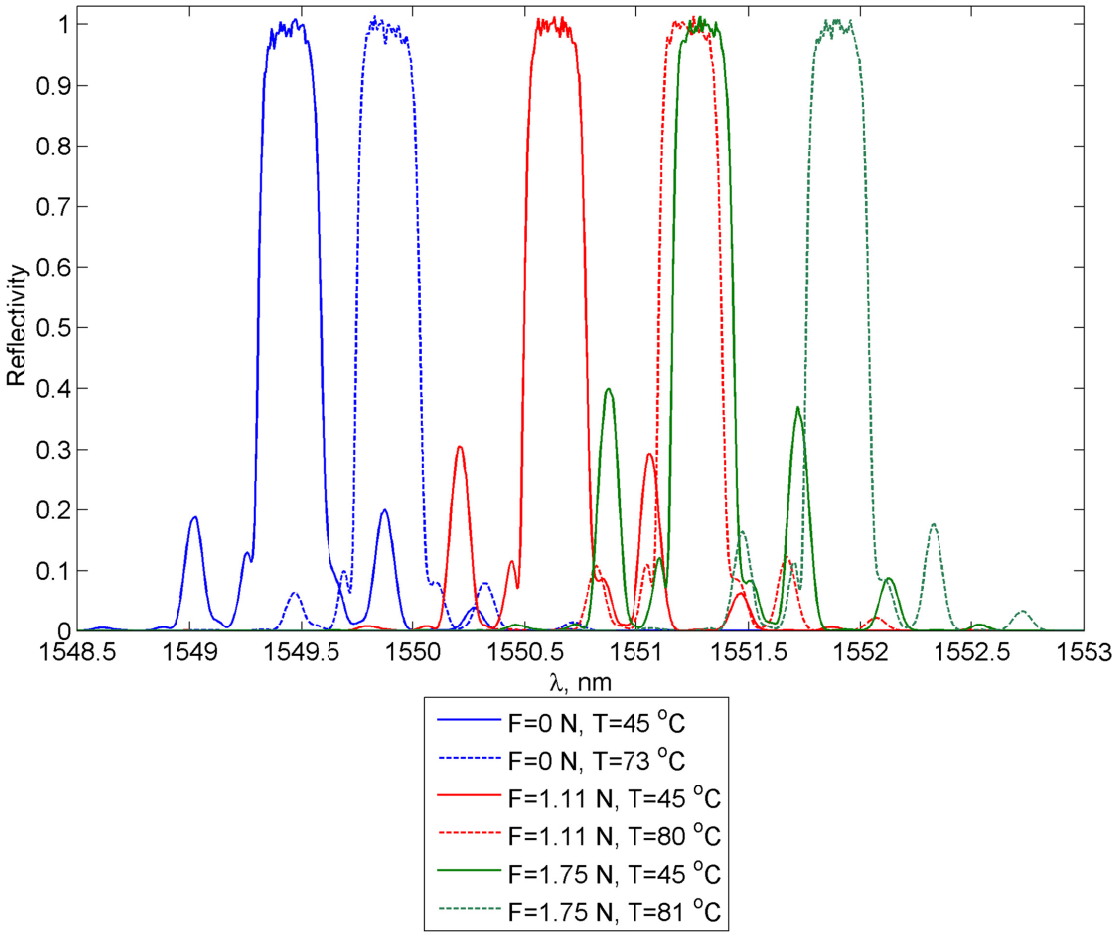

Figure 5-19: Reflection spectra of SFBG exposed to axial tensile force and temperature variations

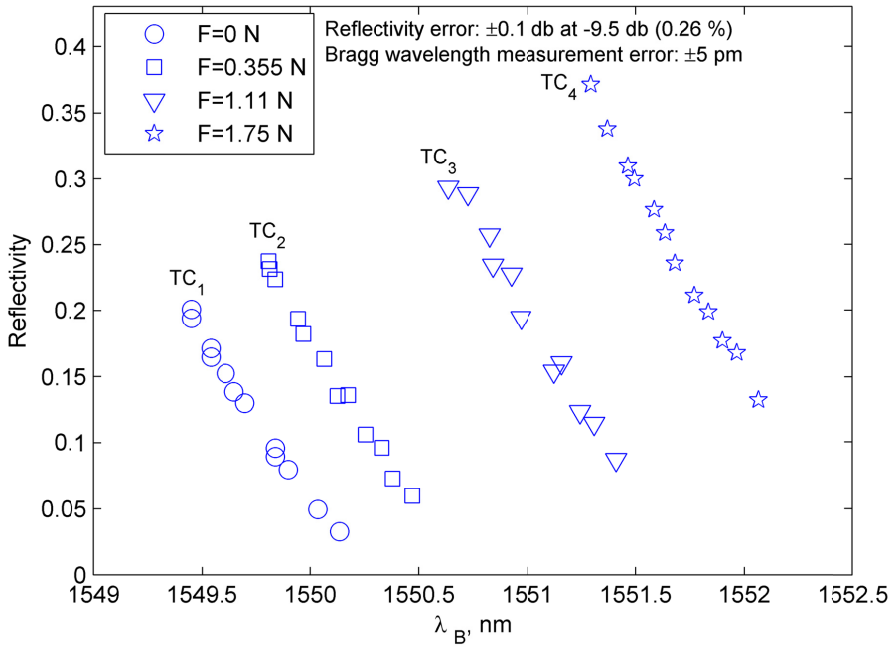

Figure 5-20: Reflectivity of the first upper sideband as a function of the Bragg wavelength for the SFBG exposed to axial tensile force at four thermal cycles (TC_1 to TC_4)

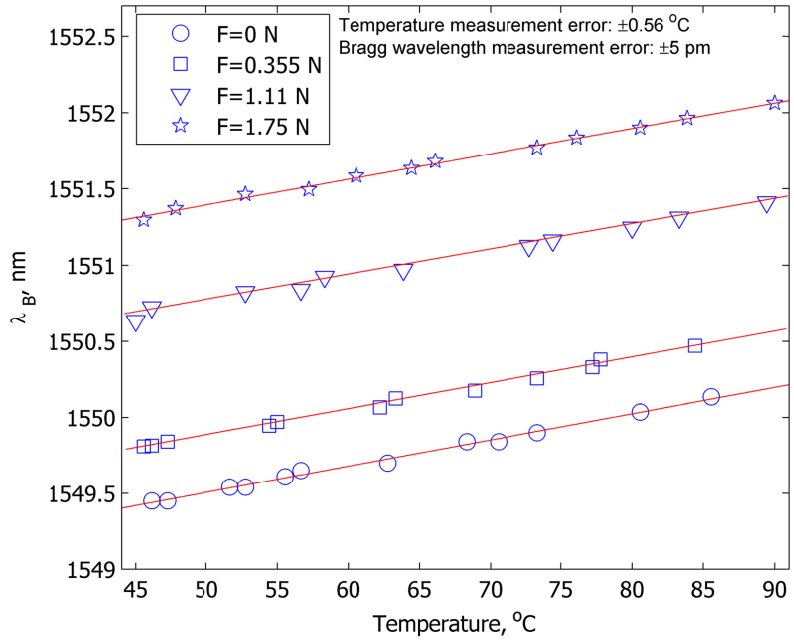

Figure 5-21: Bragg wavelength as a function of temperature for SFBG exposed to tensile force at four thermal cycles (TC_1 to TC_4)

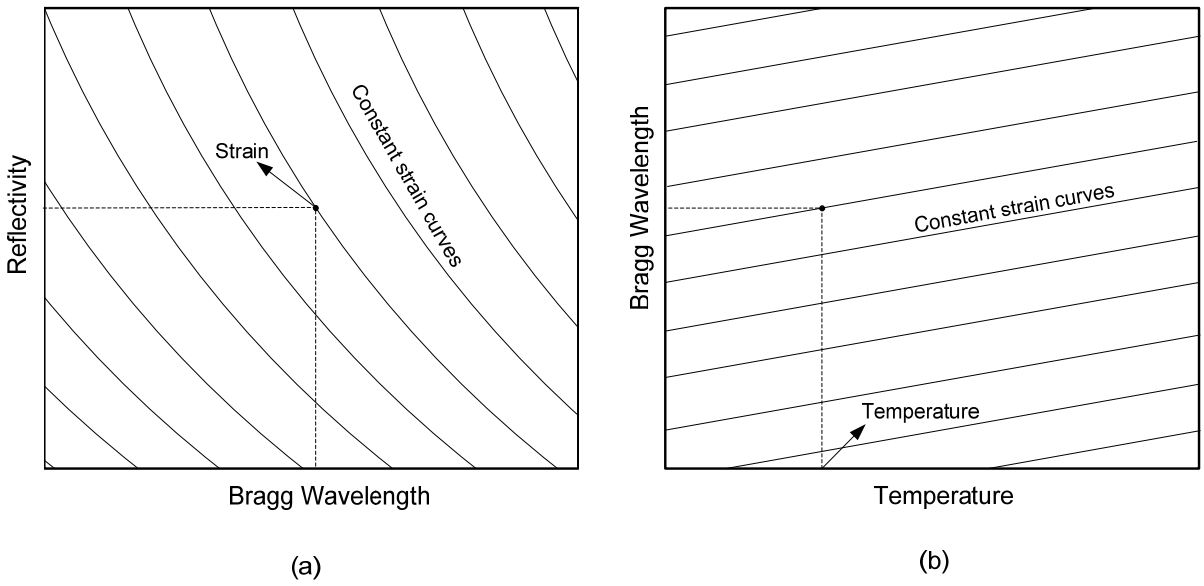

Figure 5-22: Characteristic curves for SFBG with periodic on-fiber thin films (a) reflectivity as a function of Bragg wavelength and (b) Bragg wavelength as a function of temperature

5.7 Comparison with State-of-the-Art Technology

The experimental results of this chapter showed that the developed SFBG can simultaneously monitor temperature and strain in a temperature range of 45 °C to 90 °C and an axial force range of 0 N to 1.75 N. Compared with the state-of-the-art technology for the simultaneous measurement of strain and temperature and the compensation of the effect of temperature using FBGs, the developed SFBG sensor has some distinguished characteristics. One of the features of the developed sensor is the measurement of two parameters using a single reflection spectrum of FBG. As a result, the new sensor does not increase the volume of the captured data, as opposed to the methods proposing the use of multiple sensors such as two FBGs or combined FBG-Fabry Perot cavity [22, 23, 50]. Compared with the methods that have been proposed only for temperature compensation in such a way that the actual value of temperature is not monitored [49], the developed SFBG can be utilized for the simultaneous measurement of strain and temperature in addition to temperature compensation.

When it comes to packaging, the size of the sensor is not increased significantly from the original FBG; only a few micron thin-film coating is added to the optical fiber. This facilitates the miniaturization of the sensing packages. Consequently, there is no need for the

development of new packaging technologies to accommodate this type of sensor. The methods that have been proposed using bi-materials [24] make the sensing device bulky and are not applicable in miniaturized packages.

As discussed before, the thin-film fabrication process induces residual stress in the thin films and the optical fiber resulting in the formation of residual sidebands in the reflection spectrum. To have a systematic calibration procedure, the values of the residual stresses need to be known. The residual stresses can be predicted by using the sintering model of nanoparticles and also by the analysis of the crystal structure of the thin films. A characterization scheme can be developed to correlate the magnitude of the residual stress in the thin films to the geometrical features and the process parameters.

5.8 Summary

In this chapter, the modeling and design of SFBGs with periodically spaced on-fiber silver thin films were described. The LAMM process was successfully utilized for the deposition of on-fiber silver thin films with a thickness of 9 μm. The developed SFBG was successfully tested for the simultaneous measurement of strain and temperature. To analyze the sensitivity of the developed sensor to strain, the SFBG sensor was loaded axially in a test rig. The temperature sensitivity was investigated by heating the optical fiber. The reflection spectrum of the SFBG has equally spaced sidebands whose intensities are tunable with temperature and strain. It was shown that by concurrent reading of the sidebands reflectivities and the Bragg wavelength shift, the effects of temperature and strain can be separated in the reflection spectrum. A series of characteristic curves can be obtained for the calibration of the SFBG sensor. The characteristic curves consist of sideband reflectivity vs. Bragg wavelength and Bragg wavelength vs. temperature curves.

Chapter 6

Multi-Parameter FBG for Temperature and Concentration Measurement in Liquids

This chapter is concerned with the modifications of as-fabricated FBGs by using laser micromachining. Femtosecond laser micromachining is implemented to modify the optical performance of FBG sensors through surface ablation and on-fiber micro-groove inscription. The sensing performance of the modified FBGs is investigated for the simultaneous monitoring of the temperature and concentration of liquids.

6.1 FBGs Radiated by Femtosecond Laser Pulses

As mentioned in Chapter 3, the effective mode index of refraction (n_{eff}) in FBGs is a function of the indices of refraction of the core and cladding. If the index of refraction at a segment of the grating is changed, the Bragg reflection peak is split into two reflection peaks at λ_{B_1} and λ_{B_2}, as shown in Figure 6-1. As discussed in Chapter 3, the temporary changes of n_{eff} can be caused by structural loading and/or temperature variations due to photo-elastic

and thermo-optic effects. However, femtosecond laser pulses can cause permanent changes in the effective mode index of refraction. This results from the structural changes such as change of the index of refraction in silica imposed by femtosecond laser pulses as described in Section 4.3.1.

In a FBG, if a segment of the grating length is radiated with femtosecond laser pulses, the Bragg wavelength peak splits into two peaks. The resonance wavelengths spacing (Υ) is obtained by

$$\Upsilon = \lambda_{B_2} - \lambda_{B_1} = 2\Delta n_{eff}\Lambda \tag{7.1}$$

However, if the wavelength spacing is small enough, the individual peaks are combined to form one single resonance peak with a larger bandwidth. If the entire length of the grating is radiated by femtosecond laser pulses, Υ is zero, and only a permanent red shift in the Bragg wavelength is observed.

In addition to structural changes such as the modifications of the index of refraction, femtosecond laser pulses can cause material ablation from the surface of optical fibers, as described in Chapter 4.

Since there is no coupling between the cladding and core modes of regular FBGs in the reflection spectrum, FBGs are not sensitive to the changes in the index of refraction of their surrounding medium. If a FBG which has had the cladding selectively removed by the laser micromachining process is moved from one medium to another with a different refractive index, the effective mode index of refraction and as a result the Bragg wavelength are altered. Since the index of refraction of a liquid is an indication of its concentration, monitoring and analyzing the reflection spectra allows the measurement of concentration. In this regard, the modified FBGs can be employed effectively as chemical and biological sensors. Since the FBGs are electrically isolated, the sensors are suitable for the measurements in environments in which the use of electricity is hazardous.

As discussed in Chapter 2, HF etching is a common method for the reduction of the diameter of FBGs and removal of cladding to make the sensors sensitive to the index of refraction. However, the HF-etching process has some limitations including very low etch rate, non-directional etching, and mask requirements for selective etching. Femtosecond laser micromachining is an alternative fabrication method for the material removal from the surface of optical fibers. The details of the micromachining of silica using femtosecond laser

were discussed in Chapter 4. In the following, the details of the fabrication procedures for the development of temperature/concentration FBG sensors using femtosecond laser micromachining are discussed.

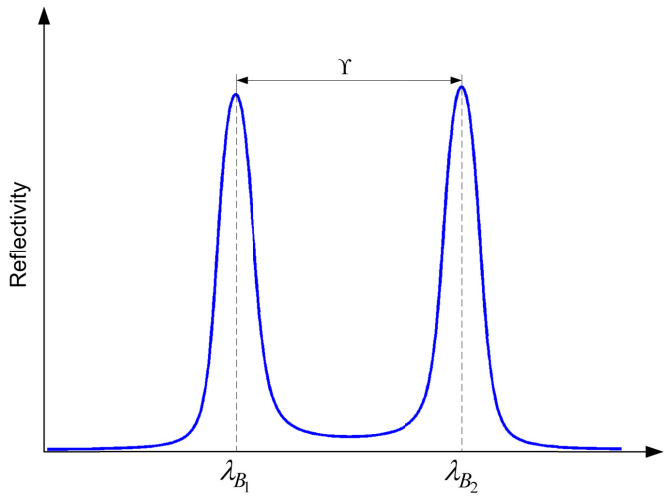

Figure 6-1: Reflection spectrum of a modified FBG using femtosecond laser radiation with dual resonance wavelengths (λ_{B_1} and λ_{B_2}) and resonance wavelengths spacing of $\Upsilon = \lambda_{B_2} - \lambda_{B_1}$

6.2 Experimental Procedures

For the micromachining of FBGs, the femtosecond laser was used as described in Chapter 4. The details of laser micromachining workstation setup are available in Section 4.3.2.

FBGs with a central wavelength of around 1550 nm and a grating length of 10 mm were selected for the experiments. The FBGs were supplied by O/E Land Inc. (O/E Land, Quebec, QC, Canada), and according to the data sheets they were apodized and fabricated by UV radiation.

The optical fibers were coated with a polymer layer to protect them during shipping and handling. Since the layer can modify the laser beam characteristics during the beam exposure, the layer was removed by a chemical stripping process. The FBGs were immersed in acetone for 10-15 minutes to dissolve the polymer coating. In the micromachining experiments, the optical fibers were moved continuously at a constant speed with a pre-specified pitch relative to the focused laser beam to periodically irradiate the optical fiber, as shown in Figure 6-2.

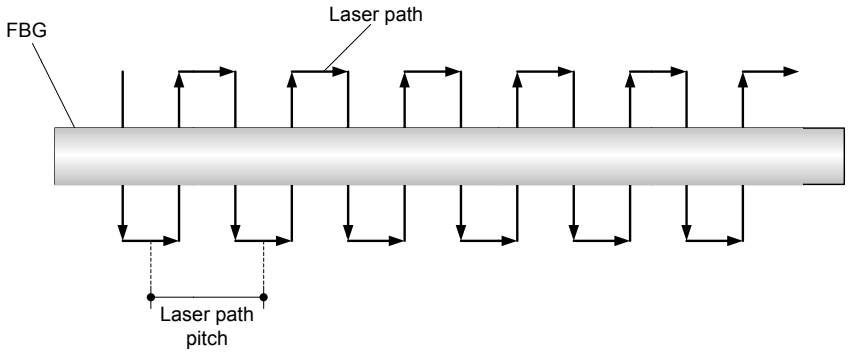

Figure 6-2: The path followed by FBGs relative to the laser beam

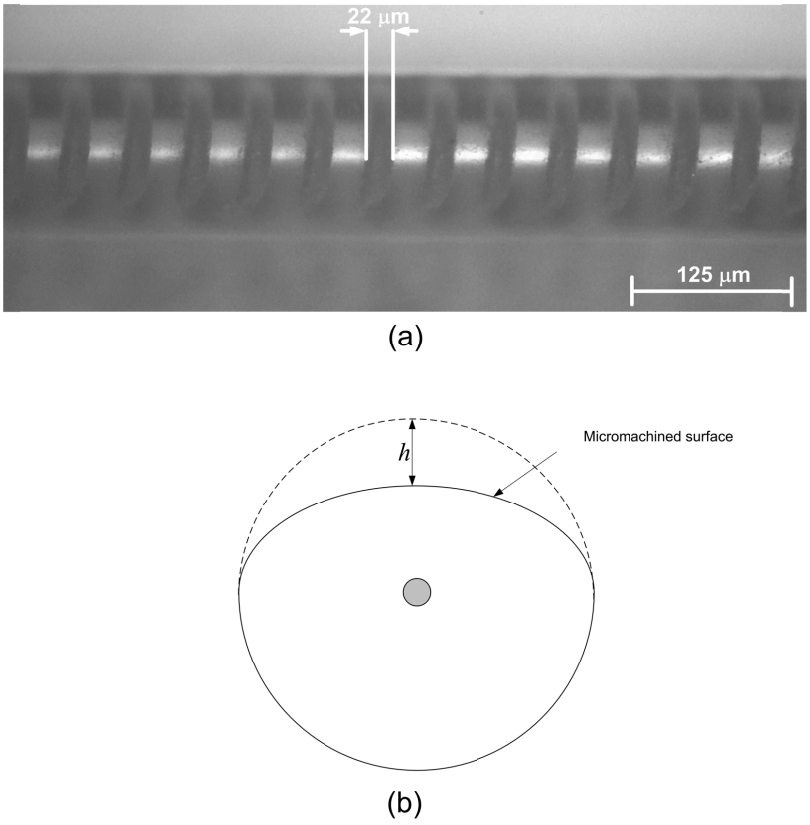

Figure 6-3: (a) Corrugated structures fabricated on an optical fiber using Ti:Sapphire femtosecond laser with an average power of 40 mW, repetition rate of 100 kHz (pulse energy of 40 μJ), and laser scanning speed of 100 μm/s and (b) schematic diagram of the optical fiber cross section before and after laser micromachining

Figure 6-3a displays corrugated structures with a pitch of 50 μm, inscribed on an optical fiber using Ti:Sapphire femtosecond laser with an average power of 40 mW (corresponding to a laser pulse energy of 40 μJ at a repetition rate of 100 kHz) and laser scanning speed of 100 μm/s. Figure 6-3b is the schematic diagram of the optical fiber cross section before and after micromachining. The width (w) and the depth (h) of the structures, obtained by white light interferometry (WYKO NT1100 optical profiling system, Veeco Metrology Inc., Tucson, AZ, USA), are 22 μm and 32 μm, respectively. The number of pulses per spot is 220 on the center line at the laser scanning speed of 100 μm/s.

6.3 Optical Responses of FBGs Micromachined by Femtosecond Lasers

In this section the reflection spectrum of FBGs micromachined by femtosecond laser are provided and compared to the reflection spectrum of the as-received FBGs. Different cases including the permanent shift of the Bragg wavelength, split of the Bragg peak into two peaks, and increase in the bandwidth are observed.

6.3.1 Shift of the Bragg Wavelength

In the first experiment, the laser beam was attenuated to an average power of 40 mW (equal to 40 μJ pulse energy), and the F BG was moved continuously with a pitch of 50 μm and a scanning speed of 100 μm/s. Laser micromachining was performed on the full length of the grating (10 mm). The laser-fiber distance was set in such a way that the exposure area on the optical fiber was 20 μm. This was obtained by measuring the trace width of the irradiated regions. As a result, the pulse intensity was 3.2×10^{13} W/cm^2. The initial and final reflection spectra of the FBG and the schematic diagram of the micromachined optical fiber are plotted in Figure 6-4. As observed, the central wavelength of the FBG is shifted by $\Delta\lambda_B = 465$ pm. The red shift in the Bragg wavelength is attributed to the change in the index of refraction of the optical fiber. The effective mode index of refraction at the locations exposed to the femtosecond laser pulses increases, resulting in the changes in the reflection spectrum. The change in the effective mode index of refraction at the points of laser exposure obtained from $\Delta n_{eff} = \Delta\lambda_B / 2\Lambda$ is $\Delta n_{eff} \approx 4\times10^{-4}$.

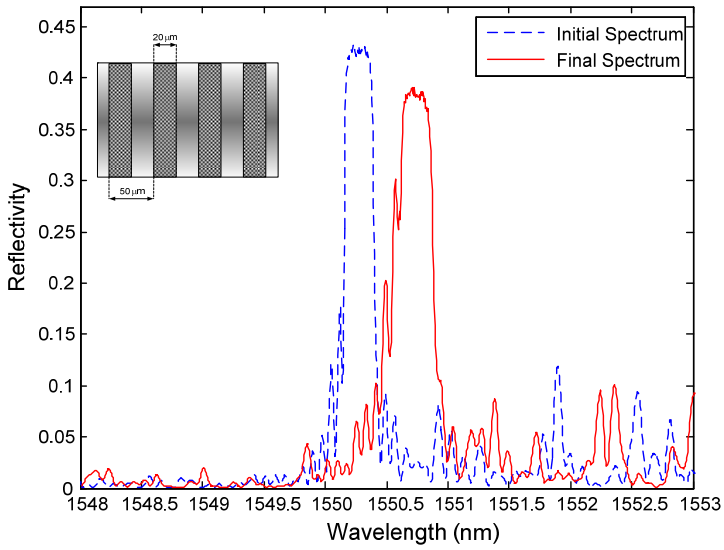

Figure 6-4: Initial and micromachined FBGs reflection spectra, laser pulse intensity: 3.2×10^{13} W/cm^2

6.3.2 Dual Peak Reflection Spectrum

In another experiment, the laser beam was attenuated to a power of 17.5 mW (equal to a pulse energy of 17.5 μJ). The exposure area on the optical fiber was 10 μm, resulting in a pulse intensity of 5.57×10^{13} W/cm^2. The optical fiber was moved continuously with a pitch of 10 μm and a scanning speed of 100 μm/s to radiate half of the length of the grating (5 mm). The reflectivity spectra and the schematic diagram of the micromachined optical fiber are shown in Figure 6-5. Two resonance wavelengths are generated in the reflection spectrum of the FBG at 1550.33 nm and 1550.99 nm ($\Delta\lambda_B = 660$ pm). Accordingly, the change in the effective index of refraction is $\Delta n_{eff} \approx 6\times10^{-4}$.

6.3.3 Bandwidth Increase

Figure 6-6 demonstrates the results of an experiment in which the FBG was moved periodically with a pitch of 50 μm, and half of the length of the grating (5 mm) was micromachined with a laser power of 40 mW and a laser scanning speed of 100 μm/s. The

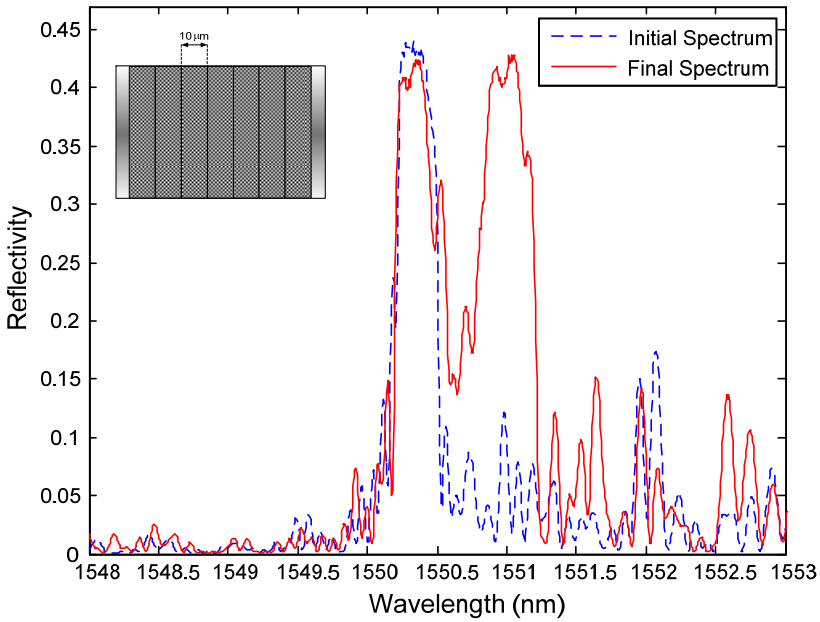

Figure 6-5: Initial and micromachined FBGs reflection spectra, laser pulse intensity: $5.57\times10^{13}\,\mathrm{W/cm^2}$

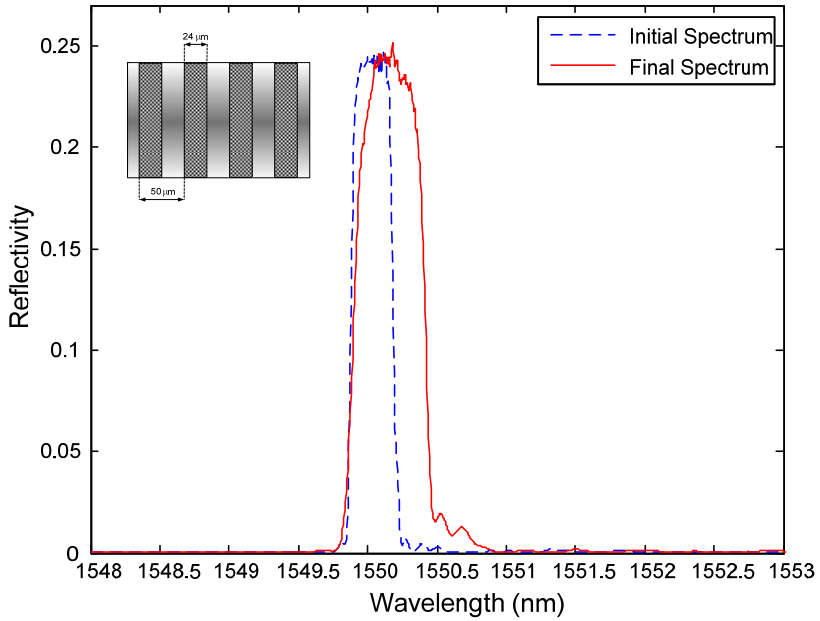

Figure 6-6: Initial and micromachined FBGs reflection spectra, laser pulse intensity: $2.21\times10^{13}\,\mathrm{W/cm^2}$

exposure area was 24 μm, resulting in a pulse intensity of 2.21×10^{13} W/cm^2. In this experiment, the bandwidth of the reflectivity signal was increased. The Full-Width-at-Half-Maximum (FWHM) for the initial and final spectra are 304 pm and 510 pm, respectively.

6.3.4 Discussion on Optical Responses of Micromachined FBGs

According to the experimental results, three different cases occurred in the interaction of femtosecond laser pulses with FBGs. The modifications are attributed to the change in the index of refraction of the FBGs and the geometrical changes induced by laser ablation..In the interaction of femtosecond pulses with silica, the index of refraction is increased in the exposed areas [116]. The change in the index of refraction is a function of the pulse intensity; higher pulse intensities result in larger index changes. In Figure 6-4, the Bragg wavelength has permanently shifted to a higher wavelength, because the entire length of the grating is exposed to laser pulses. However, in Figure 6-5, the micromachining was conducted on half of the length of the grating. This resulted in two resonance peaks. In Figure 6-6, there exist two resonance peaks. However, due to the lower laser pulse intensity, the Bragg peaks spacing is small, and they are combined as a single peak with a larger bandwidth. Another factor that has an opposite effect on the permanent changes of the Bragg wavelength is related to the stress release in the micromachined segments of the optical fiber. During the fabrication of optical fibers, residual stress forms in the fiber which can be released by the inscription of grooves. The release of stress can cause a blue shift in the Bragg wavelength in Figure 6-4. However, the effect of the femtosecond laser pulses in changing the index of refraction is more dominant. As a result, a red shift is observed in the reflection spectrum. Due to the inscription of periodic micro-grooves on the FBGs, a superstructure behavior, that is equally spaced sidebands, is expected to be observed in the spectral response. According to(3.73), the wavelength spacing for a period of 50 μm is ~15.6 nm which is not observed in the captured wavelength range shown in Figure 6-4.

In addition to the aforementioned modifications of the spectral response, the reduction of the sharpness (observed in Figure 6-4, Figure 6-5, and Figure 6-6), increase of the out-of-band background level (observed in Figure 6-5 and Figure 6-6), and grating strength reduction (observed in Figure 6-4) are observed.

The modifications of the index of refraction obtained in these experiments are comparable with the results reported in the literature [117, 121]. The experiments indicate

that by tuning the laser parameters and characterizing the process, the optical performance of the FBGs can be selectively customized.

6.4 Sensing Performance of Micromachined FBGs

6.4.1 Dual Parameter Sensor

The sensing performance of the micromachined FBGs was assessed by placing them in solutions of Polyvinyl Butyral (PVB) in ethanol. Figure 6-7 illustrates the changes in the reflection spectrum of a micromachined FBG sensor with a single resonance peak at different temperatures in ethanol and 4.8% solution of PVB in ethanol. Increasing the liquid concentration at a constant temperature results in a red shift in the Bragg wavelength. Figure 6-8 presents the Bragg wavelength shift in terms of temperature for the micromachined FBG in ethanol and a solution of 4.8% PVB in ethanol. According to this figure, the average change in the Bragg wavelength from ethanol to 4.8% solutions of PVB in ethanol is 9%. It is clear that by increasing the temperature or concentration the Bragg wavelength increases accordingly. According to these graphs, the sensitivity of the FBG sensors to temperature is around 10 pm/^{o}C which is comparable to the previously reported results [21]. To compare the results with those of an unmachined FBG, the thermal responses of an unmachined FBG in ethanol and 4.8% solution of PVB in ethanol are plotted in Figure 6-9. The slope of both curves is 10.9 pm/^{o}C indicating that the unmachined FBG is not sensitive to the concentration of the surrounding medium. However, the capabilities of the FBG for the measurement of the concentration, as well as the temperature have been increased by the inscription of micro-grooves.

The variations of the Bragg wavelength as a function of concentration at temperatures of 40 ^{o}C, 50 ^{o}C, 55 ^{o}C, 60 ^{o}C are plotted in Figure 6-10. As shown, both temperature and concentration affect the Bragg wavelength. Increasing the concentration results in a red shift in the Bragg wavelength. For the measurement of each parameter (concentration or temperature) the sensor needs to be calibrated separately.

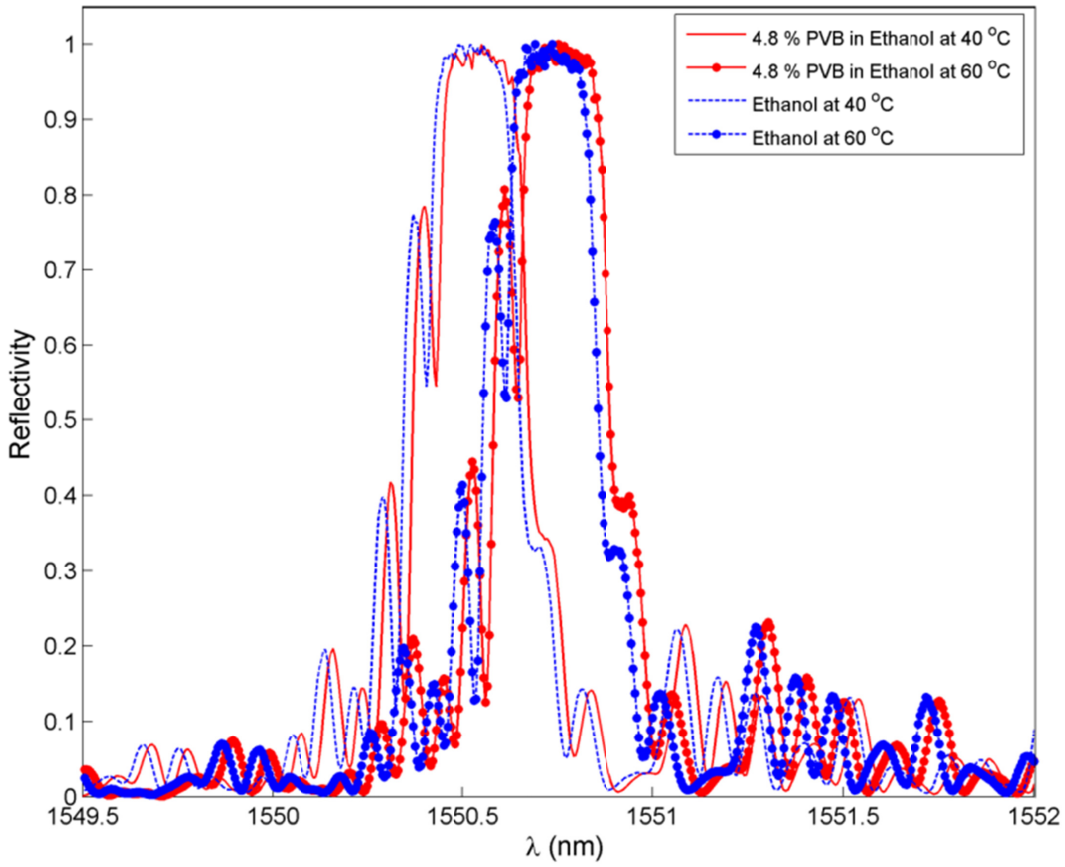

Figure 6-7: Reflection spectra of the micromachined FBG with single Bragg wavelength peak at different temperatures and concentrations

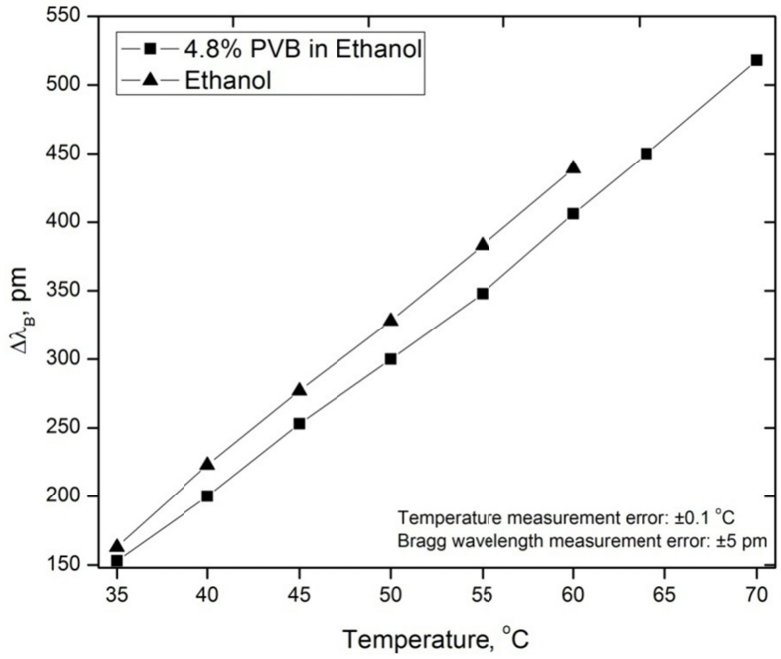

Figure 6-8: Bragg wavelength shift ($\Delta\lambda_B$) in terms of temperature for the micromachined FBG with single resonance peak placed in ethanol and 4.8% solution of PVB in ethanol.

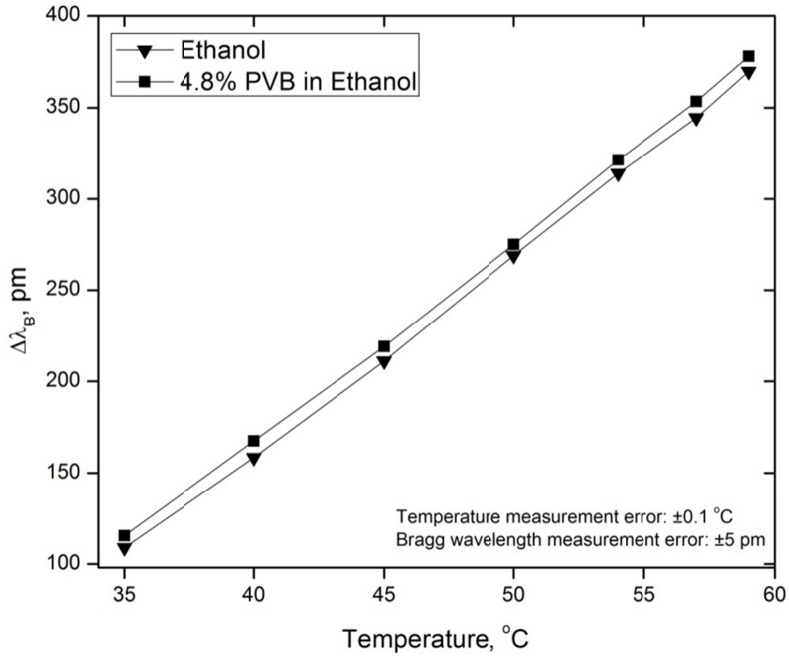

Figure 6-9: Bragg wavelength shift ($\Delta\lambda_B$) in terms of temperature for an unmachined FBG in ethanol and 4.8% solution of PVB in ethanol

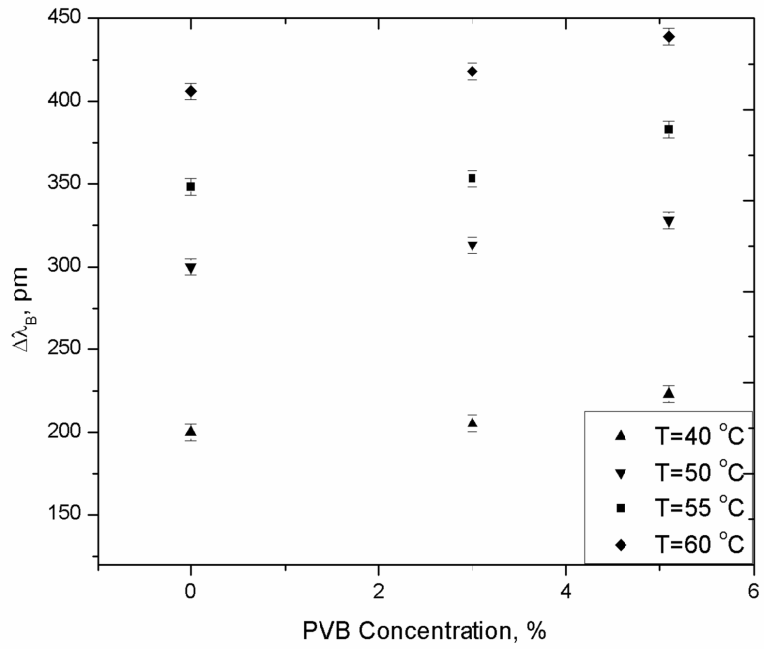

Figure 6-10: Bragg wavelength shift ($\Delta\lambda_B$) as a function of PVB concentration at different temperature

6.4.2 Simultaneous Measurement of Temperature and Concentration

The micromachined FBG with double resonance peaks was placed in PVB solutions with different concentrations, and the corresponding optical responses were obtained. Figure 6-11 shows the reflection spectra of the FBG at different temperatures in ethanol and a 2.6% solution of PVB in ethanol. The thermal response of the micromachined FBG depends on the concentration of surrounding liquid. Increasing the concentration causes the red shift in the Bragg wavelength. According to this figure, the Bragg wavelength spacing ($\Upsilon = \lambda_{B_2} - \lambda_{B_1}$) is a function of concentration. Figure 6-12 shows the reflection spectra for liquids with different indices of refraction at room temperature. According to the figure, Υ for water, epoxy resin, and silver nanoparticle suspension in ethylene glycol is 355 pm, 375 pm, and 320 pm, respectively. The different values of Υ are related to the differences in the index of refraction of liquids. The index of refraction of epoxy resin is higher than water which results in smaller Υ. The index of refraction of ethylene glycol is larger than that of water, but Υ is smaller for water. This can be attributed to the existence of silver

nanoaprticles with complex dielectric constant causing changes in the index of refraction of the nanoparticles solution.

Figure 6-13 shows the change in the Bragg wavelengths ($\Delta\lambda_{B_1}$ and $\Delta\lambda_{B_2}$) as a result of temperature increase, when the sensor is immersed in ethanol and in the PVB solution in ethanol. In Figure 6-13, the slope of the linear trend in wavelength shift increases by 10% from ethanol to the PVB solution in ethanol. The wavelength spacing as a function of PVB concentration is plotted in Figure 6-14. The figure clearly shows the reduction of Υ with increasing concentration. However, a linear trend is not observed in the measurement data.

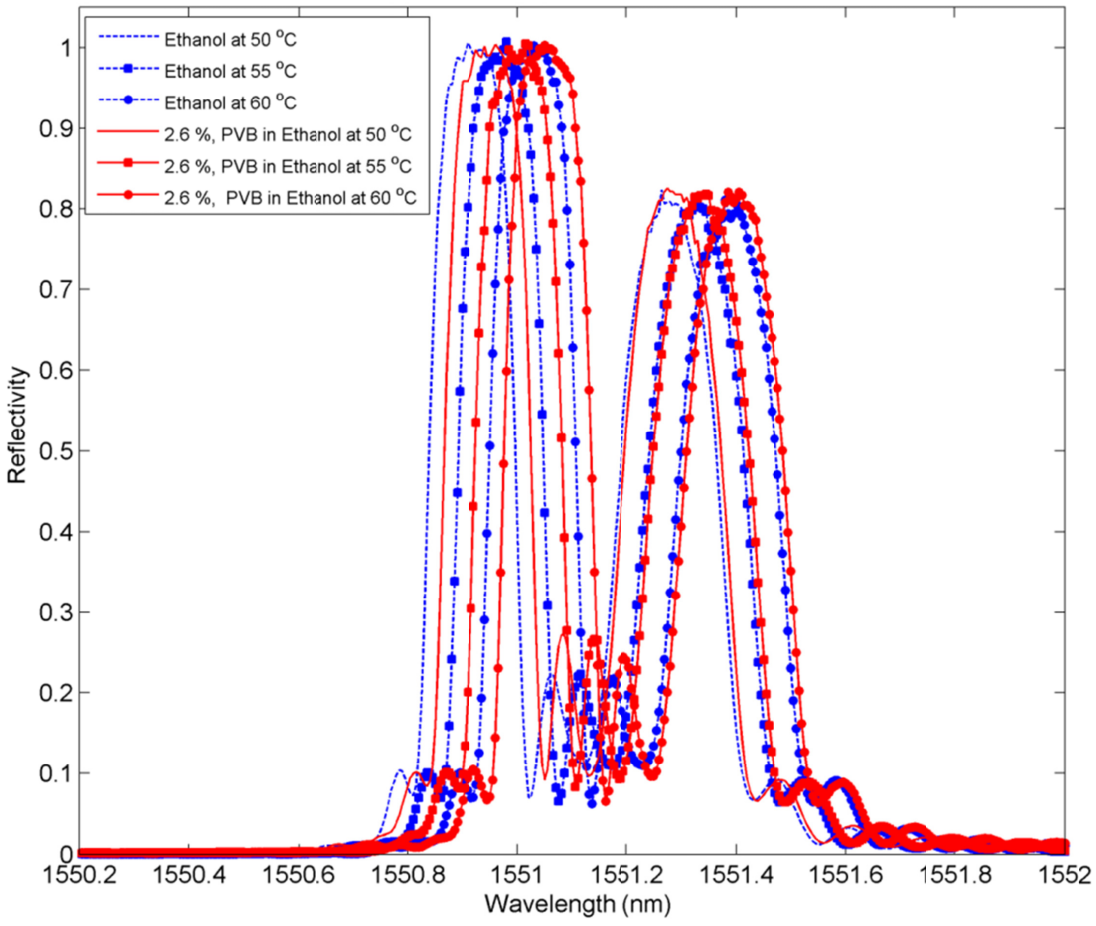

Figure 6-11: Reflection spectra of the micromachined FBG with dual resonance peaks at different temperatures in ethanol and 2.6% PVB solution in ethanol

Table 6-1 lists the average Bragg wavelengths spacing (Υ) from Figure 6-14 and the corresponding values of Δn_{eff} for the micromachined FBG in different liquid solutions at room temperature. Increasing the concentration, and hence, the index of refraction of the surrounding medium, causes Υ and Δn_{eff} to decrease accordingly. The Bragg wavelength spacing for a 2.6% solution of PVB in ethanol was 6.3% lower than the Bragg wavelength spacing for pure ethanol. In addition, Δn_{eff} changes from 3.360×10^{-4} in ethanol to 3.147×10^{-4} in a 2.6% solution of PVB in ethanol.

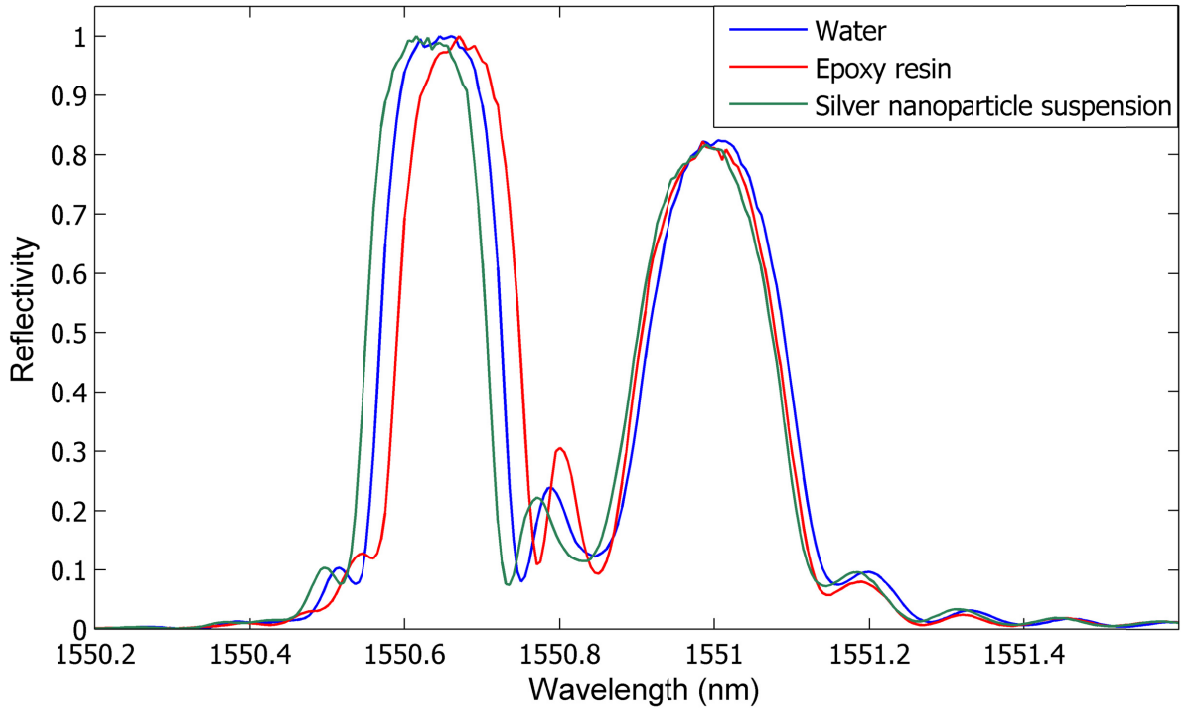

Figure 6-12: Reflection spectra of the micromachined FBG with dual resonance peaks placed in different liquids at room temperature

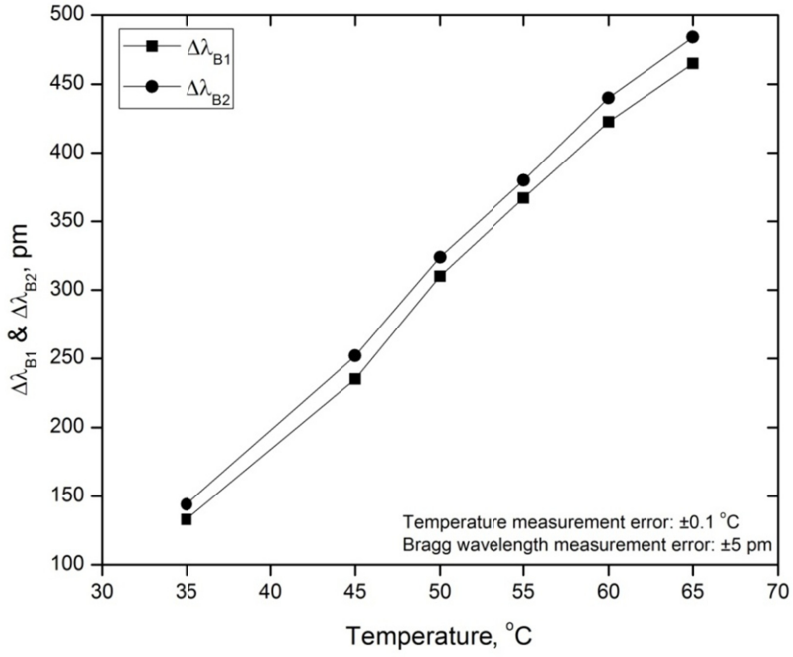

(a)

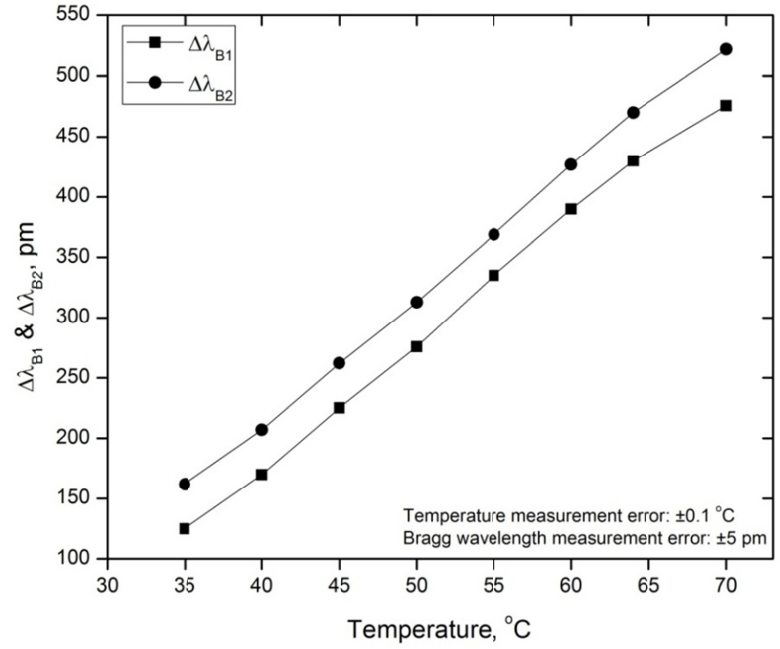

(b)

Figure 6-13: Bragg wavelength shifts ($\Delta\lambda_{B_1}$ and $\Delta\lambda_{B_2}$) in terms of temperature for micromachined FBG with dual resonance wavelengths placed in (a) 2.6% solution of PVB in ethanol and (b) ethanol

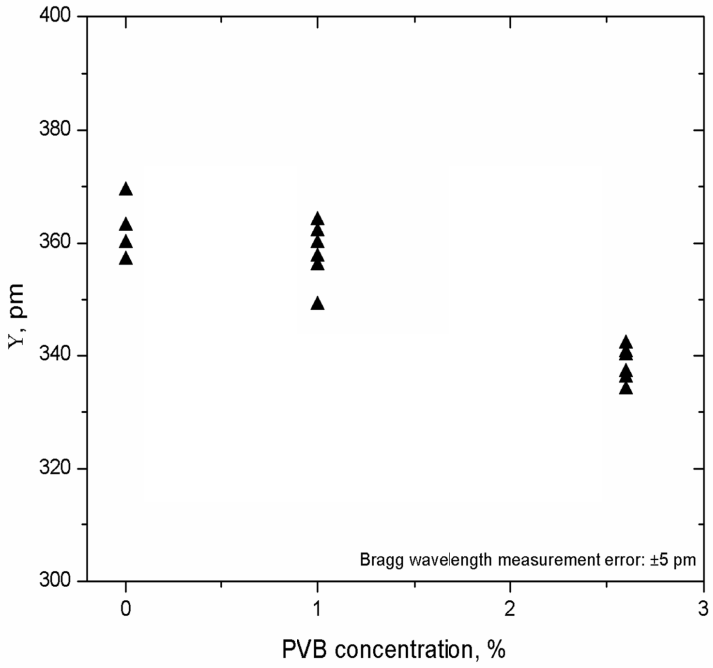

Figure 6-14: Bragg wavelength spacing (Υ) as a function of PVB concentration in ethanol

Table 6-1: Average Bragg wavelengths spacing (Υ) for different liquid concentrations in the micromachined FBG with dual resonance wavelengths at room temperature

Liquid Solution	Υ **(pm)**	Δn_{eff}
Ethanol	361.2	3.360×10^{-4}
1%, PVB in Ethanol	358.1	3.331×10^{-4}
2.6%, PVB in Ethanol	338.3	3.147×10^{-4}

It is clear in the experimental results that the sensitivity of the micromachined FBGs to the liquid concentration was increased by the fabrication of corrugated structures on the FBG cladding. This is attributed to the effects of the index of refraction of the surrounding liquid on the light propagation in the optical fiber. The effective mode index of refraction (n_{eff}) is affected by the indices of refraction of the surrounding media. When the corrugated structures are fabricated, the cladding effective thickness is decreased. As a result, the effects of the refractive index of the surrounding liquid become significant in the core-confined propagation modes of the optical fiber. According to (7.1), the Bragg condition is a function of n_{eff} and as a result, a Bragg wavelength shift occurs when a corrugated FBG is placed in a liquid with a different index of refraction. The effective parameter determining the index

of refraction in liquids is concentration which can be monitored by this type of sensors. In addition, according to the experimental results, the FBGs are sensitive to temperature which implies that, in contrast to the previous FBG sensors reported in the literature ([21, 122]), a single sensor of the type developed here can be used for the simultaneous measurement of temperature and concentration of liquids.

6.5 Comparison with the State-of-the-Art Technology

Compared with the available technologies for the measurement of the liquids concentration using FBGs, the developed method in this thesis has some advantages. Due to the selective nature of the laser micro-micromachining process, the geometrical features of the micro-grooves can be easily controlled. In addition, the sensor fabricated by this method has a better mechanical strength as opposed to the HF etched FBGs in which the diameter of the entire optical fiber is reduced. Only a single spectrum of light is needed to be analyzed for the simultaneous measurement of concentration and temperature. The speed of the fabrication process is another advantage of this method. The reported HF etching rates for optical fibers are 1.8 μm/min with 52% HF solution [17], 80 nm/min in buffered oxide etch (BOE), and 650 nm/min in 24% buffered HF solution [19].

In spite of the advantages, there are some limitations with this type of sensor that need improvement. The sensitivity of the sensor is smaller than that of previously reported HF etched FBGs. A nonlinear Bragg wavelength shift of 2.5 nm for the variation of the index of refraction from 1 to 1.378 have been reported for HF etched fibers with a reduced diameter of 6 μm [17]. It has been shown that the sensitivity of the FBG sensors to concentration depends on the cladding diameter [18, 19]. The sensitivity is also affected by the area of the micromachined surfaces. In the micromachined FBGs, only the micromachined grooves are the effective surfaces for the concentration measurement. The characteristics of the micromachined surface such as roughness can also affect the sensitivity of the micromachined FBGs. Surface roughness can also cause signal loss due to light scattering. The effects of surface roughness need to be further studied.

6.6 Summary

In this chapter, the experimental procedures for the development of a combined temperature-concentration FBG sensor were explored. Femtosecond laser micromachining using Ti:Sapphire laser was successfully incorporated for the inscription of micro-grooves and corrugated structures on as-fabricated FBGs. The performance of the developed sensors was investigated through experiments in liquid solutions of PVB in ethanol with various concentrations. The results showed that the FBG with laser-inscribed micro-grooves not only became sensitive to the concentration of the surrounding liquid, but also retained its sensitivity to temperature variations.

Chapter 7

Development of Metal-Embedded FBG Sensors

This chapter addresses embedded FBG sensors in metal parts for structural health monitoring. The fabrication procedures to embed FBGs along with numerical modeling and experimental results are discussed in this chapter.

7.1 Metal Embedded FBG Sensors

As mentioned in Chapter 2, the unique features of FBGs such as light weight, small size, long-term durability, long-range linearity, robustness to noise, and corrosion resistance encourage the development of methods and technologies thereafter to embed them inside metallic structures for in-situ load monitoring. For instance, the measurement of loads applied to machining tools, used for cutting, milling, and drilling, is essential for high precision manufacturing. In addition, tools failure diagnostics necessitate the real-time monitoring of applied thermal and structural loads during the machining process. In conventional surface-mounted sensors, such as strain gauges the measurements are limited to

peripheral surfaces. However, embedded sensors can monitor the loads at desired locations not accessible by surface-mounted sensors.

Although conventional sensors such as strain gauges can be used as embedded sensors, in case of embedding in metal parts, the requirement for insulation of such sensors adds more difficulties; whereas optical fiber sensors are electrically nonconductive and do not require any insulation.

7.2 Steps toward Embedding FBGs in Metallic Structures

Optical fibers are sensitive to high temperatures; high temperatures can degrade gratings and damage optical fibers permanently. The decay of gratings can start at a temperature of ~200 °C [2, 31]. Since most of the metal fabrication processes involve high temperatures, embedding optical fibers in metal parts is a challenging task. Some techniques have been proposed and developed to embed optical fibers in metallic structures.

Two techniques can be considered for embedding optical fibers. One is electrodeposition techniques such as electroplating and the other one is casting. Since optical fibers are not conductive, the pre-deposition of a thin layer of a conductive material on the optical fiber is required prior to the electrodeposition process. Conventional deposition techniques such as sputtering can be utilized for this purpose. Sputtering of Ti as a conductive interlayer on optical fibers has been reported in the literature [10]. Another recognized method is casting, in which a low temperature molten metal is casted around the optical fiber [57]. In this method, a low melting point material with good adhesion to silica can be melted and poured in a mold with a pre-placed optical fiber. The shortcoming of this method is the formation of large residual stresses after solidification. To diminish the effect of residual stresses on the optical response of the sensor, the optical fiber is held under tension during the casting process [123].

7.3 Embedded FBG Sensors in Smart Tools

In order to fabricate smart machining tools with embedded FBG sensors, the embedding processes described in the previous section can be followed by laser solid freeform fabrication (LSFF) process to deposit layers of tungsten carbide-cobalt (WC-Co). WC–Co is a hard material used in the production of cutting tools. Due to the existence of both tungsten

carbide (WC) and cobalt (Co), WC-Co has a combination of hardness and toughness together. The sample made by this fabrication protocol has a core of steel with embedded FBG sensors and a hard material on the surface used for machining. After the embedding process and deposition of WC-Co, the part is machined to the shape of tools.

The LSFF process at the University of Waterloo has been characterized for the deposition of WC-Co on steel [123, 124]. Two LSFF workstation setups were used for the deposition of WC-Co. One setup consists of a 1 kW pulse Nd:YAG laser system (LASAG, Thun, Switzerland) at a wavelength of 1064 nm, and the other one consists of a 1 kW CW Ytterbium fiber laser (IPG Photonics, Oxford, MA, USA) at an emission wavelength of 1070-1080 nm. In the LSFF workstation, argon gas is used as both shield and carrier gas.

In the LSFF process, the substrate is mounted on a CNC table to move it beneath the laser beam. The laser beam melts a thin layer of the substrate and creates a melting process zone. Metal powders are injected to the process zone through a nozzle connected to a powder feeder. After solidification, a thin layer of the secondary material forms on the substrate [124].

7.4 Embedding of FBGs Using Casting

7.4.1 Fabrication Procedures

The steps of the embedding process are shown in Figure 7-1. The optical fiber was placed in a block of steel (35×30×15 mm^3) with a machined channel with the size of 25×20×5 mm^3, and an alloy of tin-lead (Sn-Pb) with 65 wt% Sn was casted around the fiber. Sn-Pb alloy has a low melting point of 185 ^oC. To compensate for the effect of residual thermal stresses on the optical response of FBG, a constant tensile stress of 80 MPa was applied on the optical fiber during the embedding process. A FBG with a peak wavelength of ~1550 nm (Micron Optics, Inc., Atlanta, GA, USA) was used for the embedding process. The LSFF process was characterized for the deposition of WC-Co layers [123].

Table 7-1 summarizes the range of the optimized process parameters used in the experiments. Figure 7-2 shows a prototyped sample.

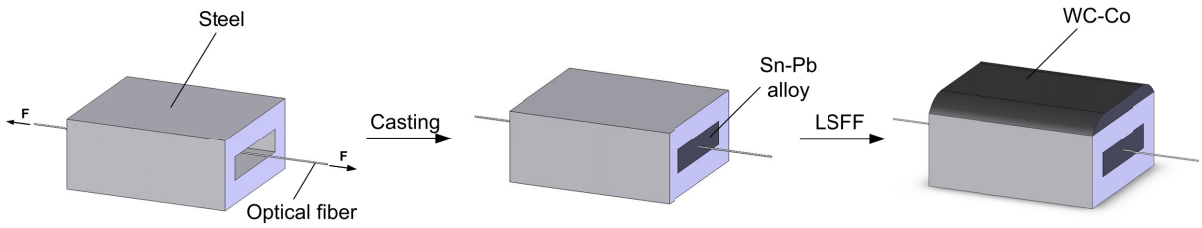

Figure 7-1: Steps toward embedding FBGs in a metal part using casting

Table 7-1: LSFF process parameters for the deposition of WC-Co using pulse Nd:YAG laser

Parameter	**Value**
Laser pulse energy (J)	2–5
Pulse frequency (Hz)	30–70
Pulse width (ms)	2–7
Laser scanning speed (mm/s)	2–5
Powder feed rate (g/min)	2–4
Laser spot diameter (mm)	1.5

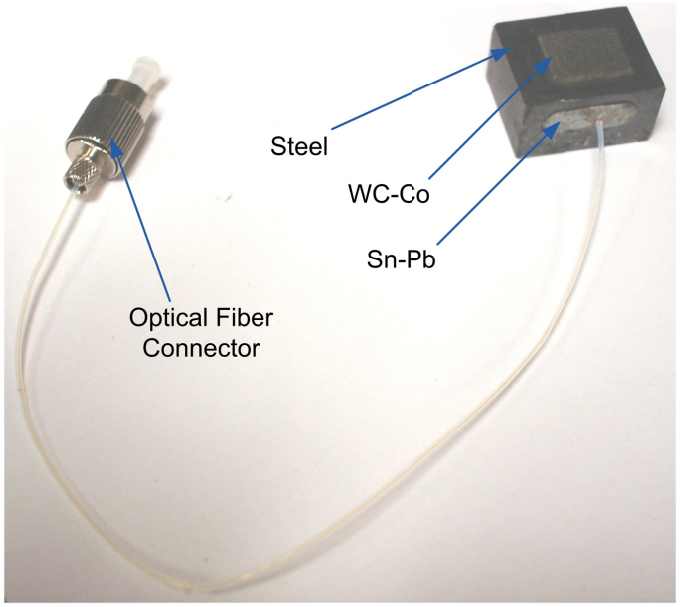

Figure 7-2: Prototyped sample with metal-embedded FBG using casting and the LSFF process

7.4.2 Microstructure Analysis

The cross section of the prototyped sample was examined using a scanning electron microscope (Jeol:JSM-6460, JEOL, Tokyo, Japan). Figure 7-3a shows the microstructure of the sample cross-section. The optical fiber surrounded by Sn–Pb alloy in a block of mild steel is labeled in this figure. Figure 7-3b shows a close-up view of the optical fiber and the surrounding material. This figure reveals that there is a good bonding between the surrounding layer and the optical fiber. As shown in the figure, cracks and porosity are not observed in the layers surrounding the optical fiber. In addition, the peripheral surface of the optical fiber was not damaged during the process, and the optical fiber retained its round shape after embedding.

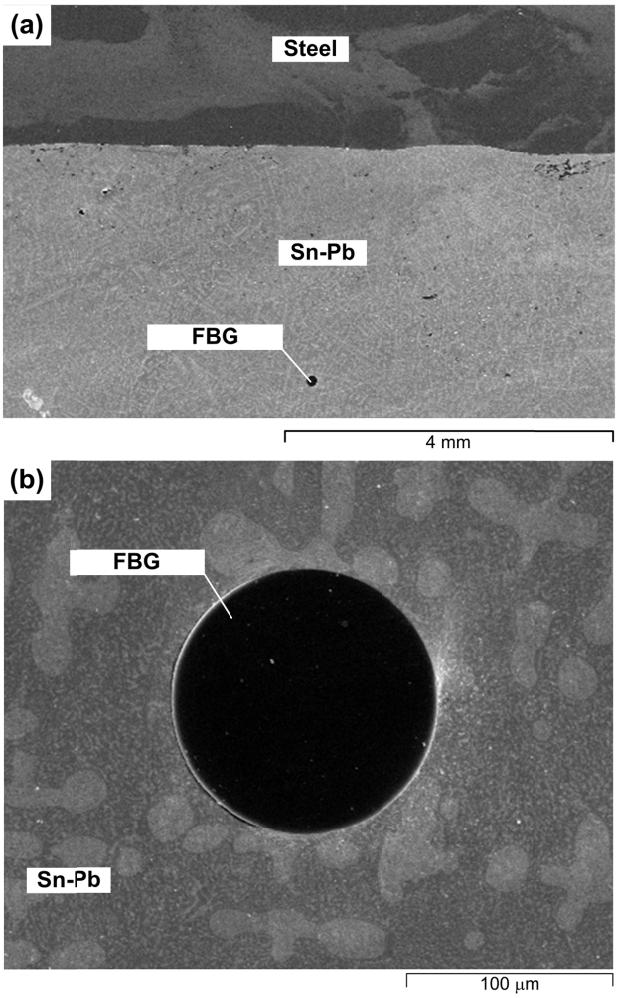

Figure 7-3: Cross section of the sample with embedded FBG manufactured by casting

7.4.3 Sensitivity Analysis

To investigate the sensitivity of the embedded FBG, the prototyped sample was loaded in a universal tensile test machine (Instron 4206, Instron, Norwood, MA, USA), as shown in Figure 7-4.

Figure 7-5a shows the reflection spectra of the sensor at different loads. As seen, there is a blue shift in the Bragg wavelength by increasing the load. During the test, the sample was mounted on a fixture in such a way that a compressive strain was applied on the embedded FBG. It is also observed that the bandwidth increases and the maximum reflectivity decreases with increasing the load. This is attributed to the Poisson's effect generating transverse strain components.

Figure 7-5b shows the Bragg wavelength shift ($\Delta\lambda_B$) as a function of the applied load. As illustrated, the shift in the Bragg wavelength as a function of the applied load has a linear trend with a sensitivity of 0.068 pm/N. The sensitivity of a bare FBG is 1.2 pm/με. This linear behavior results from the long range linear characteristic of FBG sensors and the linear structural properties of the metal part. The linear trend implies that there are no major cracks or delamination between the optical fiber and the surrounding metal layers.

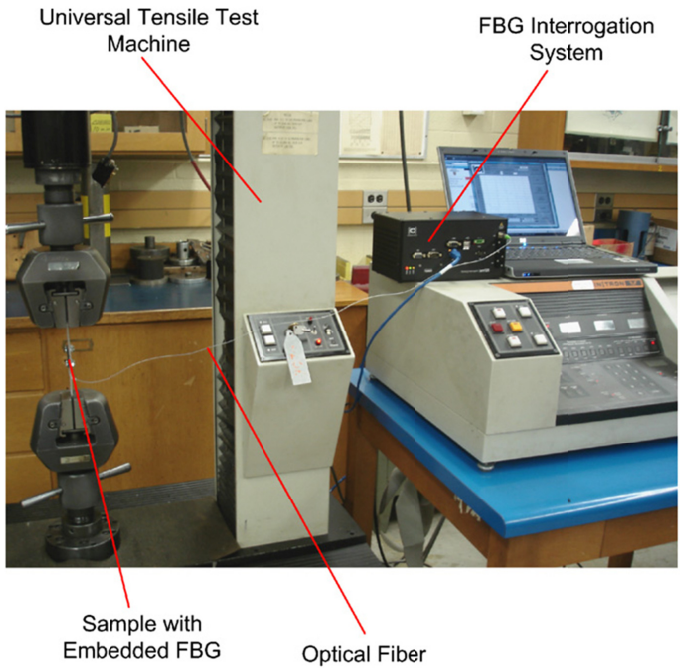

Figure 7-4: Setup of universal tensile test machine for loading the prototyped sample with embedded FBG sensors

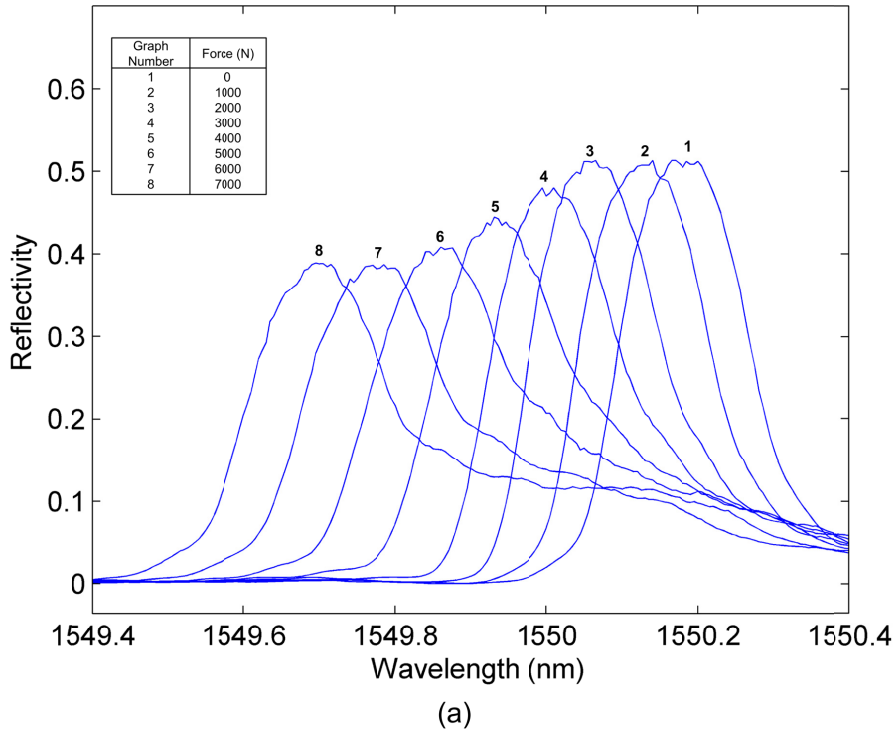

(a)

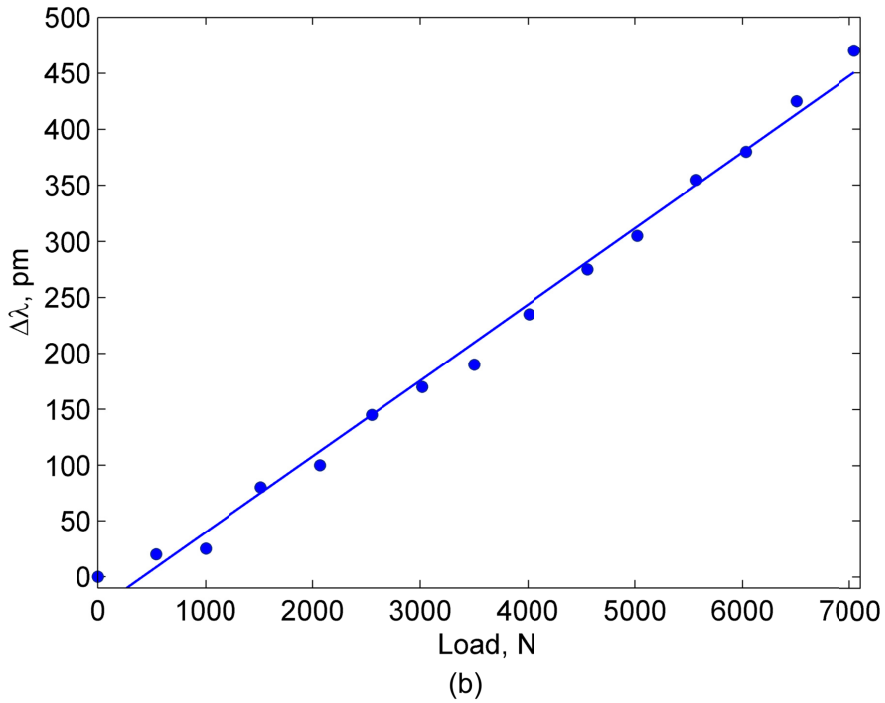

(b)

Figure 7-5: (a) The reflection spectra of metal-embedded FBG at different loads and (b) Bragg wavelength shift as a function of the applied load

7.5 Embedding of FBGs Using LAMM and Electroplating

7.5.1 Fabrication Procedures

An alternative embedding method implemented in this research consisted of thin film deposition by using LAMM and nickel electroplating. In this method, a silver thin film was deposited on the optical fiber as a conductive interlayer. It was followed by nickel electroplating in a steel part, as shown in Figure 7-6a. The LAMM process parameters for the deposition of the silver thin films on FBGs are listed in Table 7-2. The rational for using nickel is that its mechanical properties (Young's modulus and coefficient of thermal expansion) are close to those of steel, and it can be easily electroplated on steel. To fabricate smart tools with embedded FBG sensors, a layer of WC-Co was also deposited on the steel part using the LSFF process equipped with the CW Ytterbium fiber laser. The LSFF processing parameters are listed in Table 7-3. Figure 7-6b shows the schematic cross section of the sample with embedded FBG.

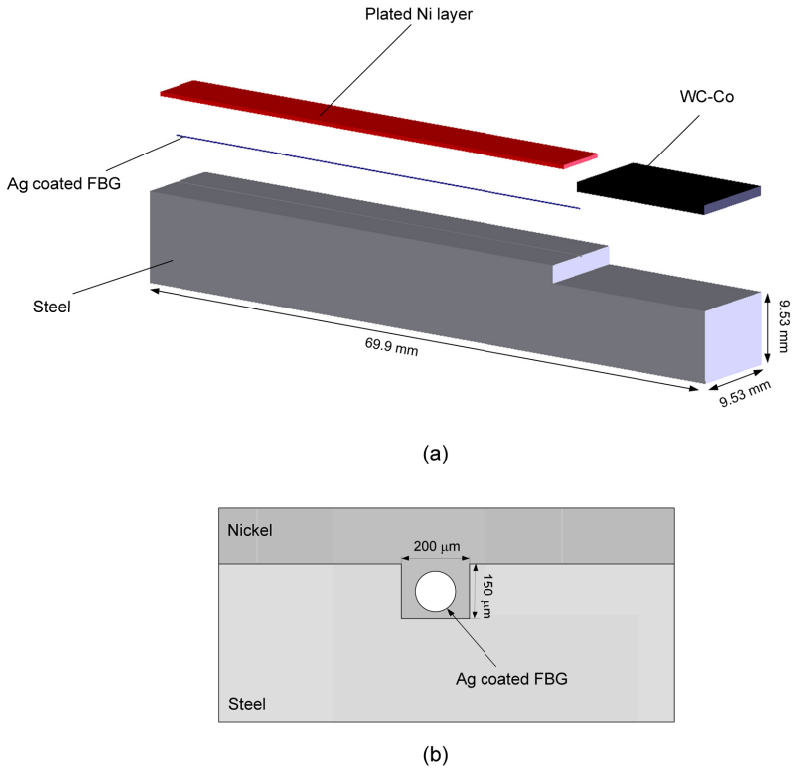

Figure 7-6: (a) Embedding process consisting of thin film deposition and electroplating and (b) schematic cross section of the sample with embedded FBG

A groove with a depth of 200 μm and a width of 150 μm was fabricated on a block of steel. The silver-coated optical fiber was placed in and aligned with the groove. Then, the sample was transferred to the Ni electroplating bath. A nickel sulfamate bath was used for the electrodeposition. Before plating, the recipient surfaces were polished, and the surfaces that did not need nickel plating were covered by Kapton tape. Prior to plating in the sulfamate bath, the sample was placed in steel activator bath, in which a current density of 0.215 mA/mm^2 with the reverse polarity was applied for 2 to 3 min. It was followed by a forward current density of 0.215 mA/mm^2 for 2 min. Then, the sample was rinsed with distilled water, dried, and placed in the nickel sulfamate bath. A current density of 0.215 mA/mm^2 was applied for about 14-16 hours, resulting in a plated nickel layer with a thickness of 230 μm. The chemical compositions of the electroplating baths are given in Table 7-4. A prototyped sample with embedded FBG is shown in Figure 7-7.

Table 7-2: LAMM process parameters for the deposition of on-fiber silver interlayer

Parameter	**Value**
Atomizer flow rate (cm^3/min)	740-750
Sheath gas flow rate (cm^3/min)	100
Virtual impactor gas flow rate (cm^3/min)	700
Deposition tip diameter (μm)	200
Deposition velocity (mm/s)	3
Laser power at the process zone (W)	3.3
Laser scanning speed (mm/s)	0.25
Laser spot size (μm)	200

Table 7-3: LSFF process parameters for the deposition of WC-Co using CW Ytterbium fiber laser

Parameter	**Value**
Laser power (W)	400
Laser scanning speed (mm/s)	6
Powder feed rate (g/min)	8
Laser spot diameter (mm)	1.5

Table 7-4: Chemical composition of sulfamate and steel activator baths for nickel electroplating

Sulfamate Bath	
Nickel Sulfamate, Ni $(SO_3NH_2)_2$	300-450 g/L
Nickel Chloride, $NiCl_2.6H_2O$	0-30 g/L
Boric Acid, H_3BO_3	30-45 g/L
Steel Activator Bath	
Nickel chloride hexahydrate	60 g/L
Hydrochloric acid	125 ml/L

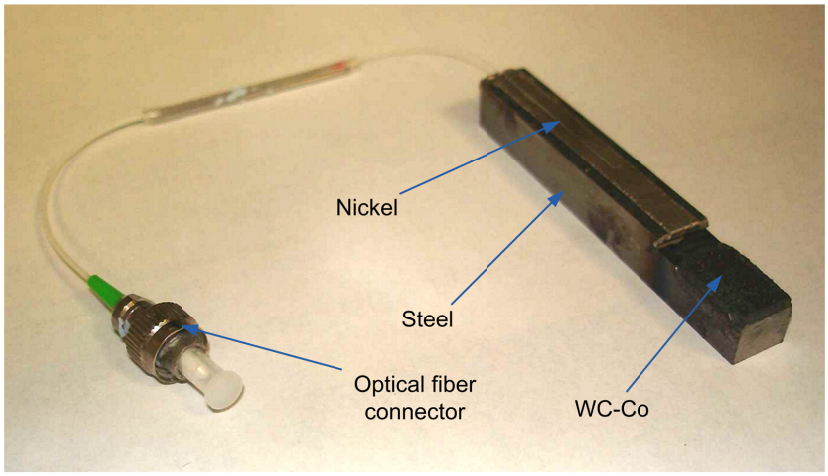

Figure 7-7: Prototyped sample with metal-embedded FBG using LAMM and electroplating

7.5.2 Microstructure Analysis

The microscopic images of the cross section of the sample with embedded FBG are shown in Figure 7-8. The optical fiber, electroplated nickel layer, and steel are labeled in the figure. A magnified image of the optical fiber, silver thin film with a thickness of 1.7-2.3 μm, and the electroplated nickel layer are also provided. According to the figure, there is a crack free interface between the optical fiber and silver layer as well as silver and the nickel layers. The black spots in figure are the residues of the polishing materials.

7.5.3 Opto-mechanical Modeling

The sensitivity of the embedded FBG sensor depends on the geometrical features and the mechanical properties of the metallic structures. In order to study the sensitivity of the

embedded FBG, a model has been developed, consisting of (1) a structural model to obtain the state of stress and strain distributions in the optical fiber and (2) an opto-mechanical model to obtain the spectral response of the embedded FBG.

To find the state of stress and strain in the embedded optical fiber, a coupled structural-thermal Finite Element (FE) model was developed in COMSOL Multiphysics. The cross section of the meshed model is shown in Figure 7-9. After the mesh independency analysis, the part was discretized with 18,670 mesh elements extruded from triangular mesh elements. As seen, finer mesh sizes were chosen at the location of the optical fiber and the electroplated nickel layer.

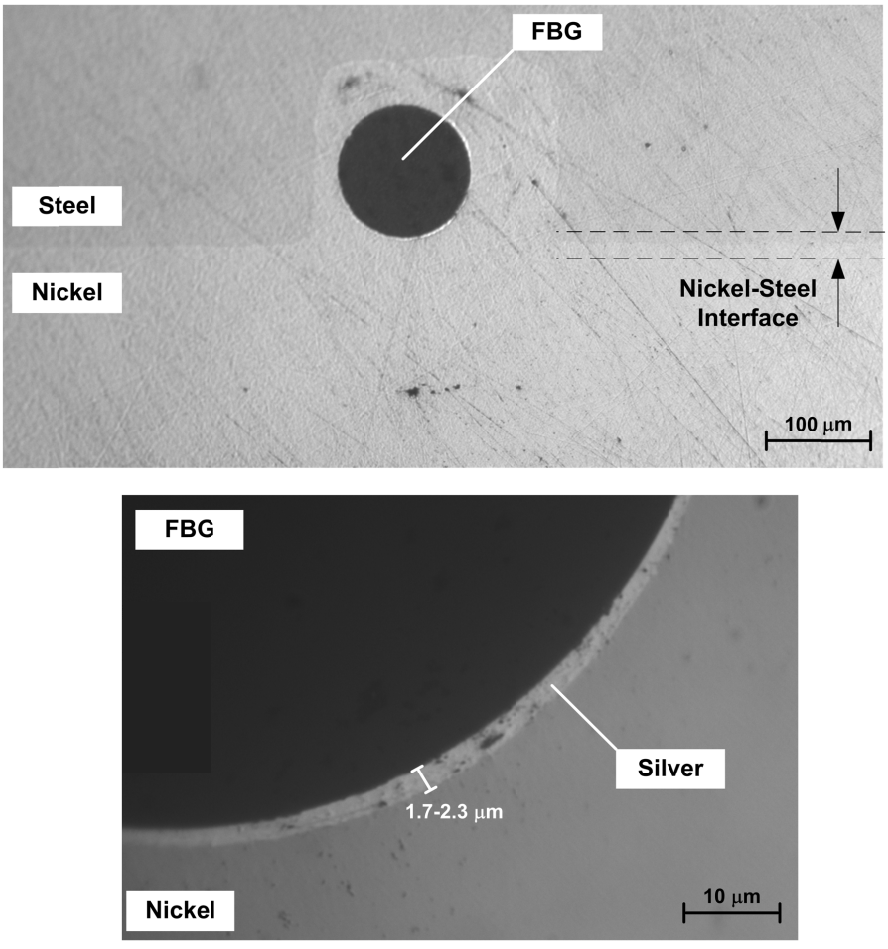

Figure 7-8: Cross section of the sample with embedded FBG manufactured by LAMM and nickel electroplating

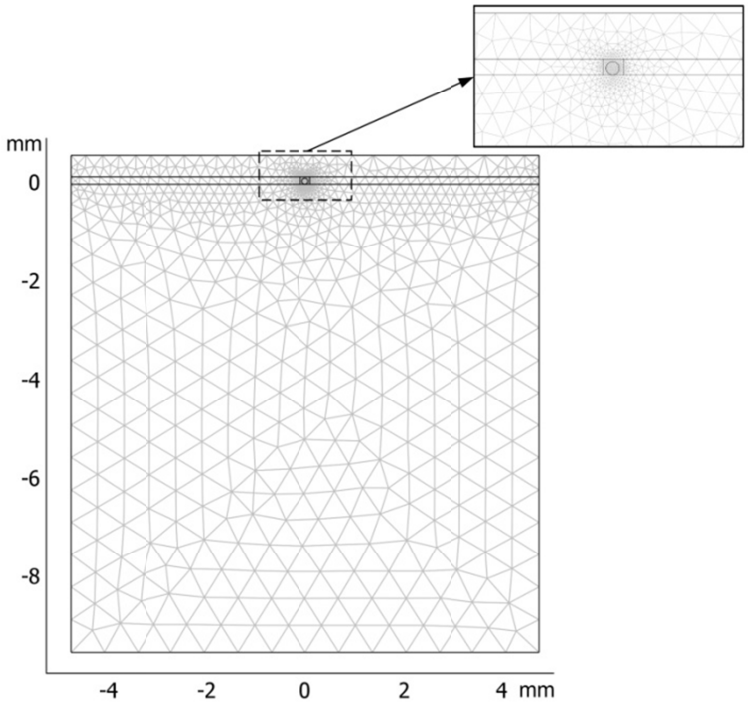

Figure 7-9: Cross section of meshed model for thermal-structural finite element analysis in COMSOL Multiphysics

In the FE analysis with COMSOL Multiphysics, the GMRES linear software with Algebraic Multigrid preconditioning and the quality of multigrid hierarchy of 5 were used.

The strain components obtained from structural analysis were used in the opto-mechanical model of FBGs to find the anisotropic indices of refraction and the modified effective mode index of refraction in the optical fiber, as described in Chapter 3. Accordingly, the shift of the Bragg wavelength is obtained from (3.16).

7.5.4 Sensitivity Analysis

The reflection spectra of the FBG before and after the embedding process are plotted in Figure 7-10. As seen, the two graphs are only slightly different implying that the magnitudes of residual stresses generated during the embedding process are very small. According to the figure, the FWHM of the Bragg peak is reduced from 0.321 nm to 0.272 nm. This is related to the compressive stress generated on the optical fiber during the electroplating process. The normalized bandwidth of Bragg gratings at the band edges is obtained from

$\Delta\lambda / \lambda = \nu_f \overline{\Delta n} / n_{eff}$ [3]. Compressive strain increases the index of refraction (according to (3.12)) which leads to the reduction of the bandwidth.

To investigate the performance of the embedded sensor, the prototyped sample was heated, and the reflection spectra of the FBG were obtained at different temperatures. Figure 7-11 gives the reflection spectra at different temperatures ranging from 32.2 °C to 121.7 °C, and the variations of the Bragg wavelength as a function of temperature are shown in Figure 7-12. The thermal process not only increases the FBG's temperature but also induces strain in the optical fiber, which concurrently affect the reflection spectrum of FBG. The maximum von Mises stress in the optical fiber corresponding to the temperature of 121.7 °C is obtained from the FE model and is equal to 30.5 MPa. According to Figure 7-12, the sensor preserves its linear behavior implying a good integrity between the layers which was also revealed in the microscopic images. The temperature sensitivity obtained from this graph is 25.8 pm/°C, which is around 2.58 times larger than that of a bare FBG (10 pm/°C). The value obtained from the model is 24 pm/°C showing a difference of 7.5%.

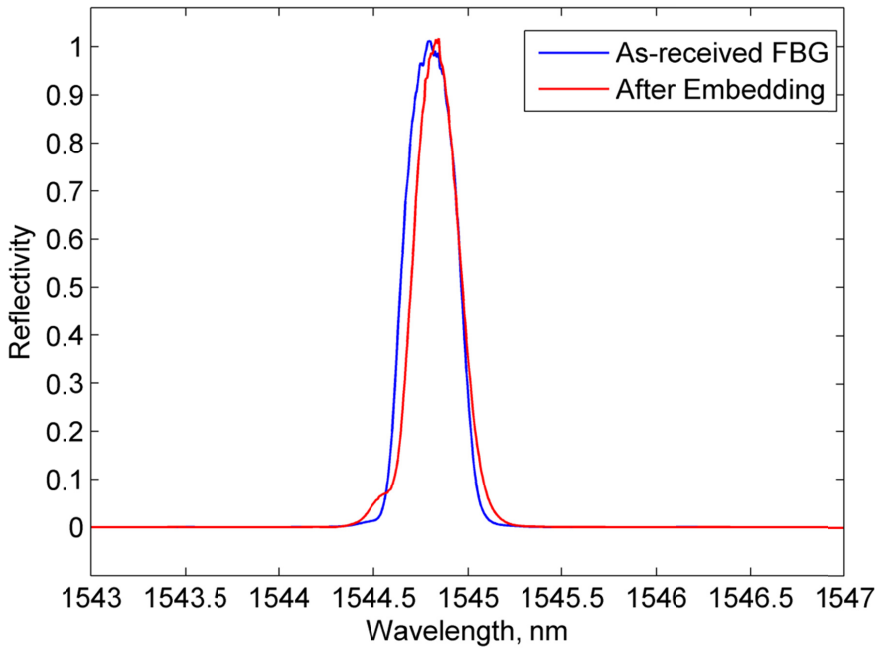

Figure 7-10: Reflection spectra of the FBG before and after embedding at room temperature

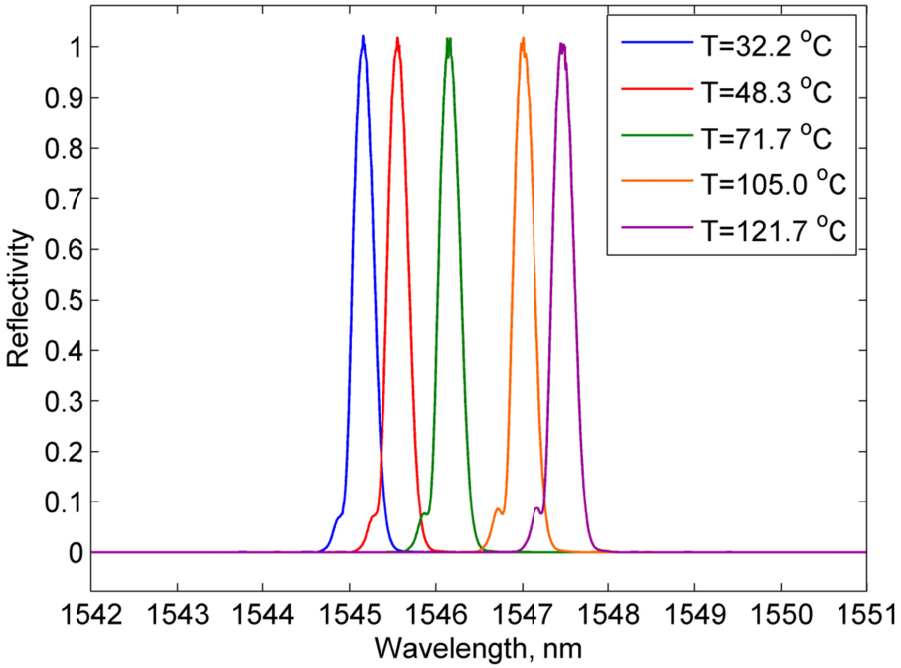

Figure 7-11: Reflection spectra of the embedded FBG at different temperatures ranging from 32.2 °C to 121.7 °C

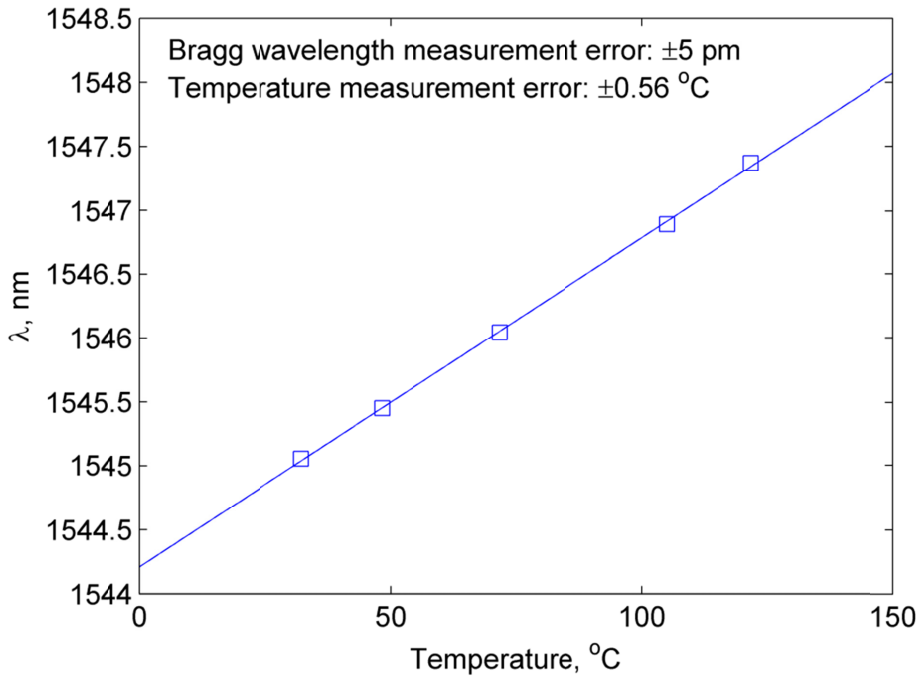

Figure 7-12: Bragg wavelength as a function of temperature for embedded FBG showing a sensitivity of 25.8 pm/°C

7.6 Summary

This chapter addressed the experimental procedures for embedding FBGs in metallic parts for structural health monitoring. Two approaches were explored for the embedding process: (1) casting and (2) thin film deposition followed by electroplating. Casting is a high temperature process causes residual stress in the optical fiber. Electroplating was implemented as a low temperature process and the results showed that residual stresses are minimal. To realize smart machining tools, the embedding processes were followed by the deposition of WC-Co, a hard material for machining tools, by using the LSFF process. The microstructural imaging of the prototyped samples proved good layers integrity without cracks, porosity, or delamination between layers. The performance of the prototyped samples was tested in structural loading and thermal cycling. The results showed that the FBG sensors retained their linear behavior after embedding. A model was also developed based on structural-thermal analysis of the parts with embedded FBG sensors and the opto-mechanical properties of optical fibers. It was shown that there is a good agreement between the model and the experimental results.

Chapter 8

Conclusions and Future Work

This thesis contributed to the field of optical fiber sensing by the design, modeling, and fabrication of FBG-based sensing devices. The developed sensing devices not only addressed the limitations associated with the applications of optical fiber sensors, but also moved forward the research front for the fabrication of optical fiber-based sensing devices. For this purpose, laser-based microfabrication processes including laser-assisted microdeposition of thin films and femtosecond laser micromachining were implemented. The main achievements of this thesis are as follows:

8.1 Superstructure FBG for Simultaneous Measurement of Strain and Temperature

Coupling of the effects of strain and temperature has been a long-lasting limitation in the field of optical fiber sensors. Development of methods and technologies to compensate the effect of temperature has been an active research topic. The use of multiple FBGs, combined FBG and Fabry Perot Cavity, and bi-material were the methods proposed for the compensation of the effect of temperature and/or multi-parameter measurement using FBGs. The superstructure approach that was proposed and implemented in this thesis added a new method for the simultaneous measurement of strain and temperature using a single FBG. Compared with the methods proposed in the literature, the superstructure FBG

provides an efficient and applicable solution not only for the compensation of the effect of temperature, but also for the simultaneous measurement of strain and temperature. The developed SFBG was based on periodic thin films with a thickness of 9 μm deposited on regular FBGs. It was shown that the reflectivities of the sidebands generated in the reflection spectrum of the SFBG are tunable with applied strain and temperature variations on the optical fiber. This property combined with the Bragg wavelength shift were used for the simultaneous measurement of strain and temperature in FBGs. The performance of the developed sensor was tested in a temperature range of 45 °C to 90 °C and an axial force as high as 1.75 N. Characteristic curves can be obtained for the SFBG to calibrate the response in terms of the measured values of strain and temperature.

8.2 Embedded FBG Sensors in Metal Structures for Health Monitoring

The unique features of optical fiber sensors, especially FBGs, encourage embedding of such sensors inside metal structures for in-situ load monitoring. The gratings inscribed in FBGs start to degrade at temperatures above 200 °C. As a result, any embedding process dealing with high temperatures cannot be used for this purpose. Low temperature casting was used in this thesis to embed FBGs in a steel structure. To do so, Sn-Pb alloy with a melting point of 185 °C was casted around an optical fiber. The casting process involves the solidification of the molten alloy which generates residual stress on the optical fiber. The residual stress can affect the optical response of the sensor. Another technique that was used for embedding FBGs in metal structures was electroplating. Since optical fibers are not conductive, a conductive interlayer is needed for the embedding process. As a result, FBGs were coated with a silver (LAMM) technology. Subsequently, nickel electroplating was used to embed FBGs in a steel part. The samples with embedded FBG sensors were loaded and the reflection spectra of the embedded FBGs were obtained. The result showed a linear trend in the response of the embedded FBGs. The linear response indicates the integrity of the layers and the absence of cracks and porosity. An opto-mechanical model was developed to predict the response of FBGs embedded in metal structures. The model was based on the photo-elastic and thermo-optic properties of FBGs. Microscopic imaging of the metal part and the embedded optical fiber exhibited mechanical integrity of layers that are free of cracks, porosity, and delamination.

8.3 FBG for Simultaneous Measurement of Concentration and Temperature in Liquids

FBGs on their original shape are not sensitive to the index of refraction of their surrounding medium, as the changes in the index of refraction of the medium do not affect the core-confined propagating mode and core-mode coupling. The reduction of the diameter of FBGs using HF etching has been the most common method for increasing the sensitivity of the sensor to the index of refection of liquids. The HF etched fibers suffer from the loss of mechanical strength due to the core diameter reduction. In addition, the developed sensors are not temperature compensated. In this thesis, femtosecond laser micromachining was implemented to inscribe micro-grooves on the cladding of regular FBGs. The selective nature of the laser micromachining process allows of the inscription of the micro-grooves at specific locations and with desired geometrical features on the optical fiber. It was shown that the micromachined FBGs became sensitive to the index of refraction while preserving their original sensitivity to temperature. As a result, a combined concentration temperature sensor was developed using on-fiber micro-groove inscription. The sensitivity of the developed sensor to the index of refraction is a function of the micro-grooves geometry (depth and width). Although, the sensitivity of the developed sensor cannot beat that of HF etched FBGs, this type of sensors has the capability of the simultaneous measurement of concentration and temperature of liquids. In addition, the mechanical strength loss due to the formation of the micro-grooves is smaller than that of etched fiber, as the diameter reduction is smaller and is not all the way along the optical fiber. The performance of the developed sensor for concentration and temperature measurements was investigated by placing the sensor in solutions of PVB in ethanol in the range of 0% to 4.8%. The reflection spectrum of the sensor contains two resonance peaks. The wavelength spacing of the peaks is a function of the concentration of the surrounding liquids. The experimental results showed that the wavelength spacing reduces with increasing the concentration.

To achieve the aforementioned contributions in the field of optical fiber sensors, the following tasks were performed during the course this PhD thesis:

1. **Opto-mechanical Modeling of Optical Fiber Sensors and the Sensing Devices Based on Optical Fiber Sensors**

   A model, based on the photo-elastic and thermo-optic properties of optical fibers, was developed to obtain the response of FBG sensors exposed to temperature variations and

structural loads. In the developed model, the state of strain in the optical fiber is mapped to the changes in the index of refraction. The results were used in light propagation equations to obtain the propagation constants, and the coupled-mode theory was utilized to obtain the spectral response. The model was also extended to predict the spectral response of superstructure fiber Bragg gratings with periodic on-fiber thin films.

2. Laser Direct Deposition of On-Fiber Metal Thin Films

In this thesis, a laser-based direct write method, called laser-assisted maskless microdeposition, was implemented for the selective deposition of on-fiber silver thin films with thicknesses of 1 to 9 μm and a minimum width of around 20 μm. The thin films were used for the development of the superstructure FBGs and also as the conductive interlayer in the electroplating process for embedding optical fibers in metal parts. The LAMM process was characterized to deposit silver thin films from a solution of silver nanoparticles on planar surfaces of silica and the non-planar surface of optical fibers. In the process characterization, the effects of the deposition process parameters on the geometrical features, microstructure, crystal structure, and mechanical properties of the thin films were investigated. The geometrical features of the deposited films were mainly dependent on the deposition process parameters: atomizer and sheath gas flow rates and the deposition velocity. It was found that the laser processing parameters including laser power and laser scanning velocity have significant effects on the mechanical and microstructural properties of the thin films. To investigate these effects, several tests, including optical profilometry, scanning electron microscopy, X-ray diffraction, and nanoindentation were performed.

3. Femtosecond Laser Micromachining of FBGs

The multi-parameter FBG sensor for the simultaneous measurement of temperature and concentration of liquids was fabricated by the inscription of micro-grooves on the outer surface of FBGs. The fabrication process was performed by using a Ti:Sapphire femtosecond pulse laser. For the micro-groove inscription, the femtosecond laser micromachining process was characterized to find the correlation between the geometry of micro-grooves and the laser processing parameters: laser pulse energy and laser scanning velocity. Micro-grooves with widths of 10 μm to 22 μm and depth of 32 μm were inscribed in the cladding of FBGs.

8.4 Future Work

To continue the research and extend the achievements of this thesis, the following research topics are recommended for future work:

1. **Development of Optical Fiber Biosensors for Multi-parameter Measurements in Biological Analytes**

In recent years, biophotonic sensors have opened new gates in biomedical research for the detection of analytes in biological agents. This new family of sensors has attracted the attention of researchers as the biomedical technology strives to meet the ever-increasing demands for accuracy, precision, repeatability, and low detection limits. Optical fiber biosensors can be incorporated in the detection of various biomolecules. Despite the widespread use of optical fibers for biomedical sensing, there is still an urgent need for biological sensors with multi-parameter sensing capabilities for multi-agent biological species. The use of optical fibers with multi-parameter sensing capabilities can reduce the size and the cost of sensing modules. In this way, multi-purpose portable measurement devices can be developed for both *in vitro* and *in vivo* applications. For instance, in cardiovascular surgery, the physical properties of blood can be monitored using these portable devices.

2. **Optical Fiber Biosensors for Multi-parameter Measurement in Cancerous Tissues**

The success of cancer chemotherapy highly depends on having accurate information about parameters such as the interstitial fluid pressure, level of oxygen, and PH in cancer tissues. These parameters directly affect the drug action, drug delivery, and the spread of metastasis. Optical fiber biosensors have the potential to open their way into research on cancer therapy to measure these parameters. Optical fiber sensor probes with multi-parameter sensing capability can be developed for the measurements in tumors. The use of an individual strand of optical fiber requires only a single spectrum to be captured and analyzed to obtain the values of parameters. As a result, a single optical fiber can replace multiple electrical and electromagnetic sensors requiring masses of wires and electrical insulation.

3. **Machining Tools with Embedded Optical Fiber Sensors for High-precision Manufacturing Processes**

Manufacturing industry dealing with the fabrication of optical devices such as lenses, mirrors, etc entails high precision during the fabrication process. The structural and thermal

loads generated during the fabrication process, can directly affect the precision of the final product. This necessitates the development of load monitoring techniques for the machining closed-loop control system. The applications of optical fiber sensors for structural health monitoring have been increasing rapidly during the past years. These sensors can be used for load monitoring in the machining tools. Their unique features encourage the use of embedded optical fibers in the metallic structure of machining tools.

4. Monitoring and/or Predicting Induced Residual Stresses in On-Fiber Thin Films Deposited by LAMM

The deposition of metal thin films by using LAMM induces residual stresses in the films and the optical fiber which affect the optical response of the sensor. For the systematic calibration of the developed sensors, research can be conducted to monitor and/or predict the residual stresses and obtain the correlation between the magnitude of the residual stresses and the fabrication process parameters.

5. Heterogeneous On-Fiber Thin Films: Modeling, Design and Fabrication

The development of thin films with heterogeneous material properties is recommended to enhance the sensing capabilities of optical fibers. For instance, tunable superstructure FBGs can be developed by the deposition of thin films with heterogeneous material properties. A model should be developed to design the geometrical features of the thin films, as well as to select the materials in terms of their mechanical properties. The heterogeneous thin films can be selectively deposited on optical fibers by using direct write technologies such as the LAMM process.

Appendix A

Closed-form Solution of Light Propagation in Isotropic Optical Fibers

The closed-form solution of the light propagation PDE in an isotropic optical fiber is found by the method of separation of variable. The solutions of electric field components in cylindrical coordinates are given in Table A-1 [37]. The cylindrical coordinates are shown in Figure A-1.

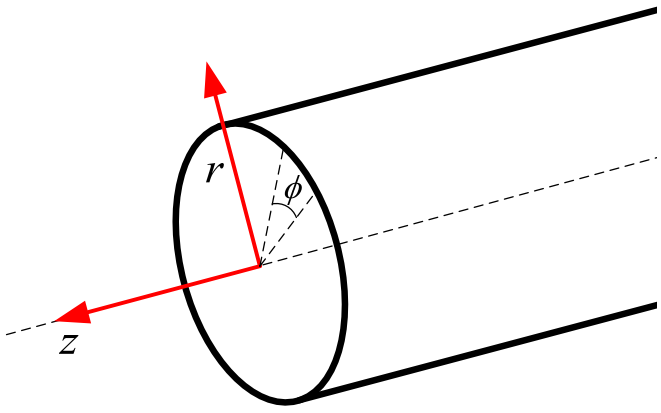

Figure A-1: Cylindrical coordinates in an optical fiber

Table A-1: Electric field components for a load free optical fiber

$r < r_{core}$	$E_z = AJ_q(ur \,/\, r_{core})\sin(q\phi)e^{-i\beta z}$ $E_r = [-A\frac{i\beta}{(u \,/\, r_{core})}J_q^{'}(ur \,/\, r_{core}) + B\frac{i\omega\mu}{(u \,/\, r_{core})^2}J_q(ur \,/\, r_{core})]\sin(q\phi)e^{-i\beta z}$ $E_\phi = [-A\frac{i\beta}{(u \,/\, r_{core})^2}\frac{q}{r}J_q(ur \,/\, r_{core}) + B\frac{i\omega\mu}{(u \,/\, r_{core})}J_q^{'}(ur \,/\, r_{core})]\cos(q\phi)e^{-i\beta z}$
$r > r_{core}$	$E_z = CK_q(wr \,/\, r_{core})\sin(q\phi)e^{-i\beta z}$ $E_r = [C\frac{i\beta}{(w \,/\, r_{core})}K_q^{'}(wr \,/\, r_{core}) - D\frac{i\omega\mu}{(w \,/\, r_{core})^2}\frac{q}{r}K_q(wr \,/\, r_{core})]\sin(q\phi)e^{-i\beta z}$ $E_\phi = [C\frac{i\beta}{(w \,/\, r_{core})^2}\frac{q}{r}K_q(wr \,/\, r_{core}) - D\frac{i\omega\mu}{(w \,/\, r_{core})}K_q^{'}(wr \,/\, r_{core})]\cos(q\phi)e^{-i\beta z}$

A, B, C, and D are constants, and J_q and K_q are ordinary and modified Bessel functions of the first kind, respectively. u and w are defined as

$$u = r_{core}\sqrt{n_{core}^2k^2 - \beta^2}$$
$$w = r_{core}\sqrt{\beta^2 - n_{clad}^2k^2} \tag{A.1}$$

The eigenvalue equations are obtained by applying the continuity condition to all tangential components of the electric and magnetic fields in the core-cladding interface [37]. By considering the weak guidance approximation ($n_{core} \approx n_{clad}$), which is the case in single-mode optical fibers, the eigenvalue equation is expressed as

$$\frac{J_q^{'}(u)}{uJ_q(u)} + \frac{K_q^{'}(w)}{wK_q(w)} = \pm q(\frac{1}{u^2} + \frac{1}{w^2}) \tag{A.2}$$

Equation (A.2) can be reformulated as

$$u\frac{J_0(u)}{J_1(u)} = -w\frac{K_0(w)}{K_1(w)} \qquad q = 0 \tag{A.3}$$

$$u\frac{J_q(u)}{J_{q+1}(u)} = -w\frac{K_q(w)}{K_{q+1}(w)} \qquad q \geq 1 \tag{A.4}$$

$$u\frac{J_q(u)}{J_{q-1}(u)} = w\frac{K_q(w)}{K_{q-1}(w)} \qquad q \geq 1 \tag{A.5}$$

In each equation for each value of q, there exists m solutions. Modes that are obtained by (A.3) are called transverse electric (TE_{0m}) and transverse magnetic (TM_{0m}). In the modes obtained from (A.4) and (A.5), none of the components become zero. As a result, they are called hybrid modes (EH_{qm} or HE_{qm}). By introducing the variable l, (A.3), (A.4) and (A.5) are expressed as [37]

$$u\frac{J_{l-1}(u)}{J_l(u)} = w\frac{K_{l-1}(w)}{K_l(w)} \qquad l = \begin{cases} 1 & TE_{0m}, TM_{0m} \\ q+1 & EH_{qm} \\ q-1 & HE_{qm} \end{cases} \tag{A.6}$$

In weakly guided optical fibers, a group of EH, HE, TE and TM modes superimposes and makes composite modes with the eigenvalue equation (A.6). These modes are called linearly polarized, and are denoted by LP_{lm}.

To study the characteristics of the light propagating in optical fibers, it is helpful to define two parameters called normalized frequency (V) and phase constant (b),

$$V = \left(u^2 + w^2\right)^{1/2} = r_{core}k(n_{core}^2 - n_{clad}^2) \tag{A.7}$$

$$b = 1 - \frac{u^2}{V^2} = \frac{\beta^2 - n_{clad}^2k^2}{n_{core}^2k^2 - n_{clad}^2k^2} \approx \frac{n_{eff} - n_{clad}}{n_{core} - n_{clad}} \tag{A.8}$$

where the approximation is based on the weak-guidance ($n_{core} \approx n_{clad}$) characteristic of single-mode optical fibers.

The normalized frequency is a constant number depending on the wavelength of the propagating light, fiber geometry, and the refractive indices of the core and the cladding. The phase constant as a function of the normalized frequency for different LP modes is plotted in Figure A-2. As shown, for all of the core guided modes in an optical fiber, b must be in the range $0 < b < 1$. According to this figure, the LP_{01} mode has the highest phase constant for all values of V. This mode is the most guided mode in single-mode optical fibers, and its cut-off frequency is zero [37].

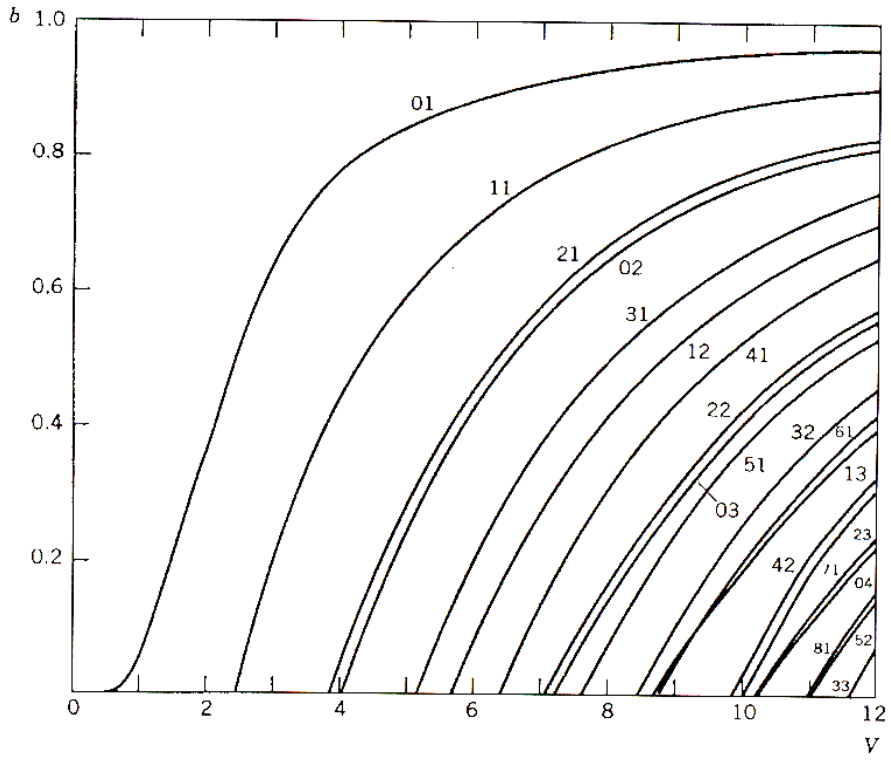

Figure A-2: Phase constant in terms of normalized frequency [37]

Appendix B

Finite Element Method to Obtain the Effective Mode Index of Refraction

Finite Element Analysis (FEA) can be used to solve the light propagation PDEs and obtain the effective mode index of refraction in optical fibers. In the FE analysis, the optical fiber is divided into longitudinal segments. The cross section of the optical fiber is discretized to elements at each segment (Figure B-1), and the light propagation PDEs are solved at each cross section.

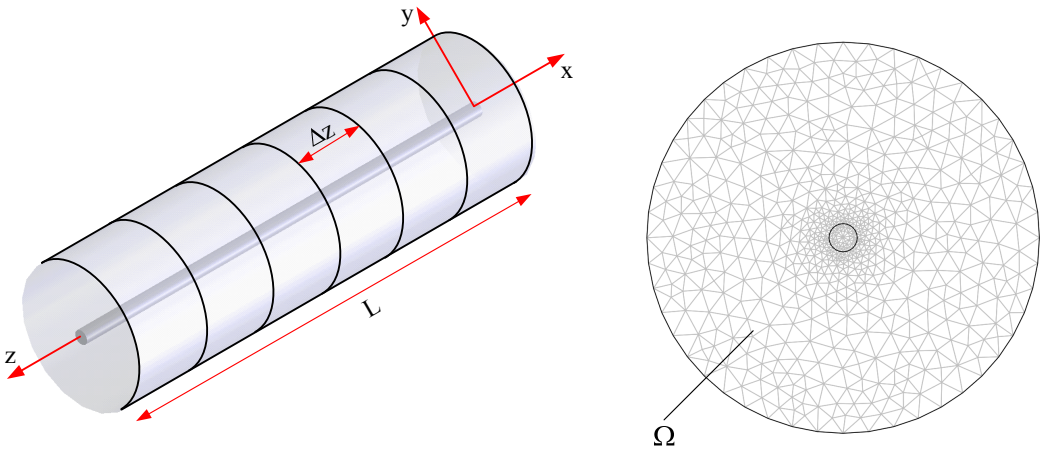

Figure B-1: Optical fiber divided into longitudinal segments and meshing of optical fiber cross section in COMSOL Multiphysics

The triangular element is shown in Figure B-2. By defining the element local coordinates ξ, η, and ζ, the transformation to Cartesian coordinates is [125]

$$\begin{bmatrix} 1 \\ x \\ y \end{bmatrix} = \begin{bmatrix} 1 & 1 & 1 \\ x_1 & x_2 & x_3 \\ y_1 & y_2 & y_3 \end{bmatrix} \begin{bmatrix} \xi \\ \eta \\ \zeta \end{bmatrix} \tag{B.1}$$

and the element shape function {N} is

$$\{N\} = [2\xi^2 - \xi \quad 2\eta^2 - \eta \quad 2\zeta^2 - \zeta \quad 4\xi\eta \quad 4\eta\zeta \quad 4\xi\zeta]^T \tag{B.2}$$

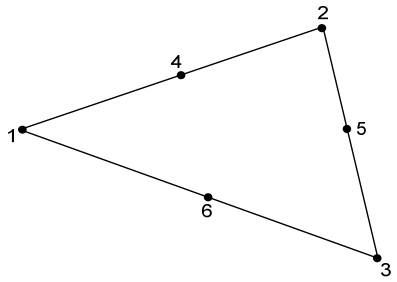

Figure B-2: Triangular quadratic element

The components of the electric field (E_x and E_y) are expressed as

$$\begin{aligned} E_x &= \sum_{i=1}^{6} E_{x_i} N_i \\ E_y &= \sum_{i=1}^{6} E_{y_i} N_i \end{aligned} \tag{B.3}$$

The Perpendicular Hybrid-Mode Wave physics was selected in COMSOL Multiphysics. The UMFPACK solver for mode analysis was chosen. This solver is a linear solver using the Gaussian elimination method.

To investigate the mesh independency and to find the optimum number of elements, several sample problems were solved with different numbers of elements. The variations of the eigenvalue (β) with increasing number of elements were studied. It was found that in

the solutions, where the number of meshes was higher than 1,280, the effect of the increasing mesh number on the final results was negligible.

B.1 FBG Subject to Non-uniform Strain Distribution

The spectral response of FBGs, subject to non-uniform strain fields, is presented in this section. It is assumed that the grating is placed in a linearly varying axial strain field, as denoted in Figure B-3. The simulation parameters are listed in Table B-1. The optical fiber is divided into longitudinal section and the distribution of the index of refraction is obtained for each segment. The light propagation PDEs are solved using COMSOL Multiphysics and MATLAB to obtain the effective mode index of refraction along the fiber ($n_{eff}(z)$). The effective mode index of refraction is shown in Figure B-2. As seen, the effective mode index of refraction decreases along the grating, which is attributed to the non-uniform strain distribution.

Table B-1: Simulation parameters

Parameter	**Value**
E_{silica}	73 GPa
L	6 mm
p_{11}	0.113
p_{12}	0.252
n_{core}	1.4457
n_{clad}	1.4378
$\overline{\Delta n}$	2.5×10^{-4}
ν_f	1

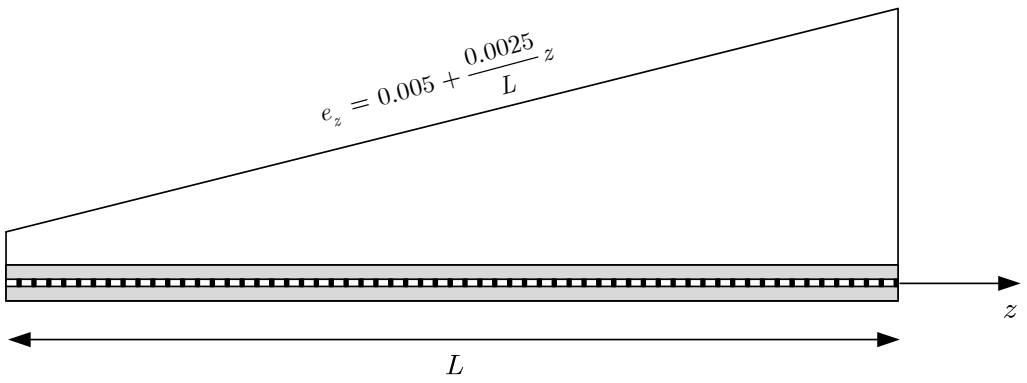

Figure B-3: FBG subject to linear non-uniform axial strain

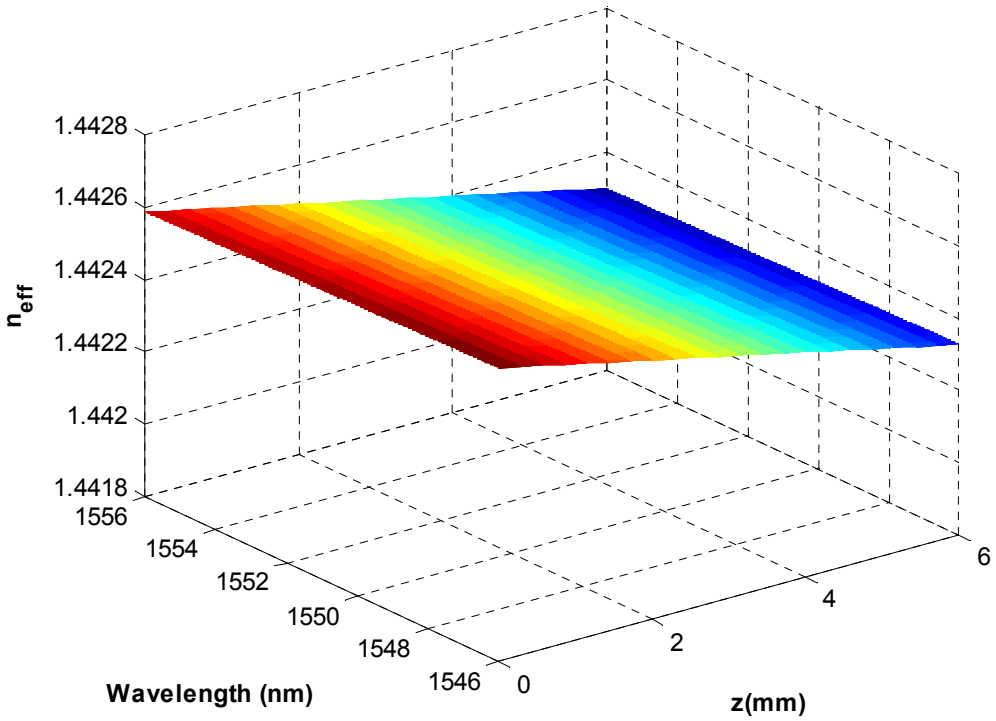

Figure B-4: Effective mode index of refraction along a FBG subject to linear non-uniform axial strain

Appendix C

Derivation of Coupled-Mode Theory for Optical Fiber Gratings

Coupled-mode theory is a useful tool for the quantitative analysis of the spectral response of fiber gratings. In this theory, the grating is modeled as a periodic perturbation in the dielectric tensor of the medium in which light is propagating. The perturbed dielectric tensor is written as

$$\varepsilon_p(x,y,z) = \varepsilon(x,y) + \Delta\varepsilon(x,y,z) \tag{C.1}$$

where $\varepsilon(x,y)$ is the unperturbed part of the dielectric tensor, and $\Delta\varepsilon(x,y,z)$ is the periodic perturbation in z direction. By considering the propagation of light in an unperturbed dielectric, the propagation of electric field ($\mathbf{E}(x,y,z)$) can be written as a linear combination of the normal modes,

$$\mathbf{E}(x,y,z) = \sum_l A_l \mathbf{E}_l(x,y) e^{i(\omega t - \beta_l z)} \tag{C.2}$$

where A_l's are constant coefficients, and $\mathbf{E}_l(x,y)$ is the l^{th} normal propagation mode in the unperturbed medium satisfying

$$\nabla_t^2 \mathbf{E}_l(x,y) + (k^2 - \beta^2)\mathbf{E}_l(x,y) = 0 \tag{C.3}$$

where

$$\nabla_t^2 = \frac{\partial^2}{\partial x^2} + \frac{\partial^2}{\partial y^2} \tag{C.4}$$

and

$$k = \left[\omega^2 \mu \varepsilon(x,y)\right]^{1/2} \tag{C.5}$$

The propagation of the electric field in the perturbed medium can also be expressed as a linear combination of unperturbed normal modes; however, the expansion coefficients are functions of z. This is derived from the method of variation of constants [96]. As a result, the electric field is written as

$$\mathbf{E}(x,y,z) = \sum_l A_l(z)\mathbf{E}_l(x,y)e^{i(\omega t - \beta_l z)} \tag{C.6}$$

By substituting (C.6) into the wave equation,

$$\nabla^2 \mathbf{E}(x,y,z) + \omega^2 \mu \big(\varepsilon(x,y) + \Delta\varepsilon(x,y)\big)\mathbf{E}(x,y,z) = 0 \tag{C.7}$$

Equation (C.7) is rewritten as

$$\left[\nabla_t^2 + \frac{\partial^2}{\partial z^2}\right]\mathbf{E}(x,y,z) + \omega^2 \mu(\varepsilon(x,y) + \Delta\varepsilon(x,y,z))\mathbf{E}(x,y,z) = 0 \tag{C.8}$$

and

$$\begin{aligned}&\sum_l A_l(z)\nabla_t^2 \mathbf{E}_l(x,y)e^{i(\omega t - \beta_l z)} + \sum_l \frac{\partial^2 A_l(z)e^{i(\omega t - \beta_l z)}}{\partial z^2}\mathbf{E}_l(x,y) + \\ &\omega^2 \mu\varepsilon(x,y)\sum_l A_l(z)\mathbf{E}_l(x,y)e^{i(\omega t - \beta_l z)} + \omega^2 \mu\Delta\varepsilon(x,y,z)\sum_l A_l(z)\mathbf{E}_l(x,y)e^{i(\omega t - \beta_l z)} = 0\end{aligned} \tag{C.9}$$

Then,

$$\sum_l A_l(z)\nabla_t^2\mathbf{E}_l(x,y)e^{i(\omega t-\beta_l z)}+\sum_l\left(\frac{\partial^2 A_l(z)}{\partial z^2}-2i\beta_l\frac{\partial A_l(z)}{\partial z}-\beta_l^2 A_l(z)\right)\mathbf{E}_l(x,y)e^{i(\omega t-\beta z)}+$$
$$\omega^2\mu\varepsilon(x,y)\sum_l A_l(z)\mathbf{E}_l(x,y)e^{i(\omega t-\beta_l z)}+\omega^2\mu\Delta\varepsilon(x,y,z)\sum_l A_l(z)\mathbf{E}_l(x,y)e^{i(\omega t-\beta_l z)}=0 \tag{C.10}$$

By substituting (C.3) in (C.10),

$$\sum_l\left(\frac{\partial^2 A_l(z)}{\partial z^2}-2i\beta_l\frac{\partial A_l(z)}{\partial z}\right)\mathbf{E}_l(x,y)e^{-i\beta_l z}+\omega^2\mu\Delta\varepsilon(x,y,z)\sum_l A_l(z)\mathbf{E}_l(x,y)e^{-i\beta_l z}=0 \tag{C.11}$$

By assuming weak perturbations, the variation of the amplitude $A_l(z)$ is small. It can be inferred that the second order term $\partial^2 A_l(z)/\partial z^2$ is much smaller than $2i\beta\partial A_l(z)/\partial z$. Therefore, (C.11) is simplified to

$$-2i\sum_l\beta_l\frac{\partial A_l(z)}{\partial z}\mathbf{E}_l(x,y)e^{-i\beta_l z}+\omega^2\mu\Delta\varepsilon(x,y,z)\sum_l A_l(z)\mathbf{E}_l(x,y)e^{-i\beta_l z}=0 \tag{C.12}$$

The Multiplication of (C.12) by $\mathbf{E}_m^*(x,y)$ and the integration over the xy plane lead to

$$\begin{aligned}&-2i\sum_l\beta_l\frac{\partial A_l(z)}{\partial z}e^{-i\beta_l z}\int_S\mathbf{E}_m^*(x,y)\cdot\mathbf{E}_l(x,y)dxdy+\\&\omega^2\mu\sum_l A_l(z)e^{-i\beta_l z}\int_S\mathbf{E}_m^*(x,y)\cdot\Delta\varepsilon(x,y,z)\mathbf{E}_l(x,y)dxdy=0\end{aligned} \tag{C.13}$$

By using the othogonality of propagation modes [96], (C.13) is expressed as

$$\frac{2\omega\mu}{|\beta_m|}\frac{dA_m(z)}{dz}e^{-i\beta_m z}-\frac{\omega^2\mu}{2i\beta_m}\sum_l A_l(z)e^{-i\beta_l z}\int_S\mathbf{E}_m^*(x,y).\Delta\varepsilon(x,y,z)\mathbf{E}_l(x,y)dxdy=0 \tag{C.14}$$

Equation (C.14) is rewritten as

$$\frac{dA_m(z)}{dz}=-i\frac{|\beta_m|}{\beta_m}\sum_l A_l(z)K_{ml}e^{i(\beta_m-\beta_l)z} \tag{C.15}$$

where K_{ml} is the coupling coefficient between the l^{th} and the m^{th} modes, defined by

$$K_{ml} = \frac{\omega}{4} \int_S \mathbf{E}_m^*(x,y) \Delta\varepsilon(x,y,z) \mathbf{E}_l(x,y) dxdy \tag{C.16}$$

Equation (C.15) is a set of coupled differential equations, describing the coupling among an infinite number of modes in the light propagation. By getting the conjugate transpose of (C.16),

$$K_{ml} = K_{ml}^* \tag{C.17}$$

Based on the direction of the propagating mode, the coupling can be co-directional, in which the modes propagate in the same direction, or contra-directional, in which the modes propagate in the opposite directions.

Appendix D

Design of Experiments to Identify the Effective Parameters in the LAMM Process

By using the Taguchi method, several sets of experiments were designed to study the effects of the process parameters on the geometrical features (width and thickness) of the deposited thin films.

D. 1 Deposition Width

The parameters deemed to be effective on the deposition width along with the selected levels and the degrees of freedom (DOF) are listed in Table D-1 The parameters and their levels are selected based on prior knowledge, whereas the degree of freedom of each factor was selected according to the chosen number of levels. In addition, the interactions between factors A and B (flow rates of atomizer gas and sheath gas) and between factors E and F (laser power and scanning velocity) are also investigated. Studying these interactions enables understanding of the levels of factors in which they are more effective. According to the total degree of freedom, which is eight, the L_{16} table is used to design the experiments [126].

In the experiments, the deposition width varies from 15.51 μm to 70.00 μm for various process parameters.

The results transferred to the analysis of variance (ANOVA) table to statistically study the results and obtain the F-test value of each experimental result. F-test is a statistical test to show the significance of the parameters. The F-test value is obtained based on a desired level of confidence (α) and the degrees of freedom of the parameters. The percentage of contribution can be used to show quantitatively the effects of the significant parameters [126].

By selecting the level of confidence of 90%, α is 0.1 and F_{α}=3.59. According to this selection, the most significant factors are A, C, and AB (interaction of A and B) in which the F-test value is larger than F_{α}.

The average widths for different factor levels are shown Figure D-1. These values are obtained by finding the average of the width data for the samples in which A, B,..., F are in level 1 or 2. A1, B1,..., F1 represent the experiments in which factors A, B,..., F are in level 1, and A2, B2,..., F2 are also defined in the same way. It is obvious that the changes in A and C have the most significant effects on the results; increasing the atomizer flow rate and/or reducing the deposition velocity results in wider depositions.

The effect of AB is shown in Figure D-2. It is obvious that the effect of factor A on the average width, which is the variations of the width due to the change in the level of A, depends on the level of factor B. When factor B is in level 1, the effect of A is larger than when it is in level 2. Since the effect of parameters E and F are not significant, their interaction is not effective.

Table D-1: Controlled parameters for the analysis of the films width

Factors	**Description**	**Level 1**	**Level 2**	**DOF**
A	Atomizer gas flow rate (cm^3/min)	7	12	1
B	Sheath gas flow rate (cm^3/min)	40	55	1
C	Deposition velocity (mm/s)	1	10	1
D	Number of layers	5	20	1
E	Laser scanning velocity (mm/s)	0.5	6	1
F	Laser power (W)	0.75	1.345	1
AB	Interaction of A and B	NA	NA	1
EF	Interaction of E and F	NA	NA	1
				Total DOF: 8

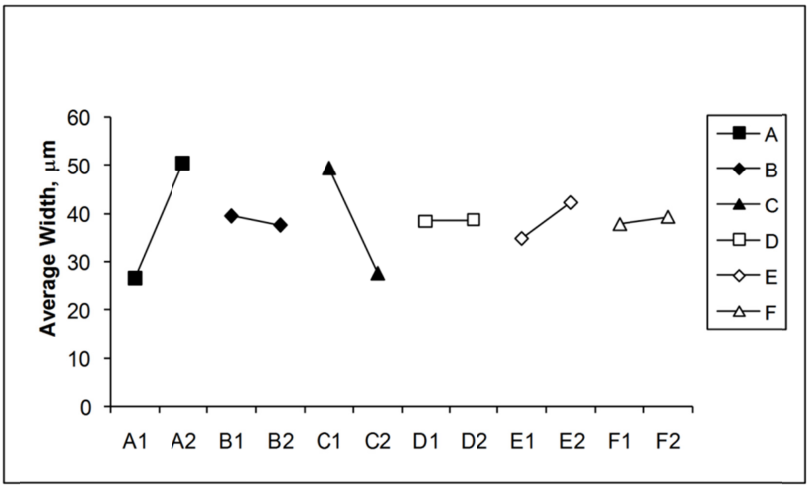

Figure D-1: Average width vs. the change of parameters levels

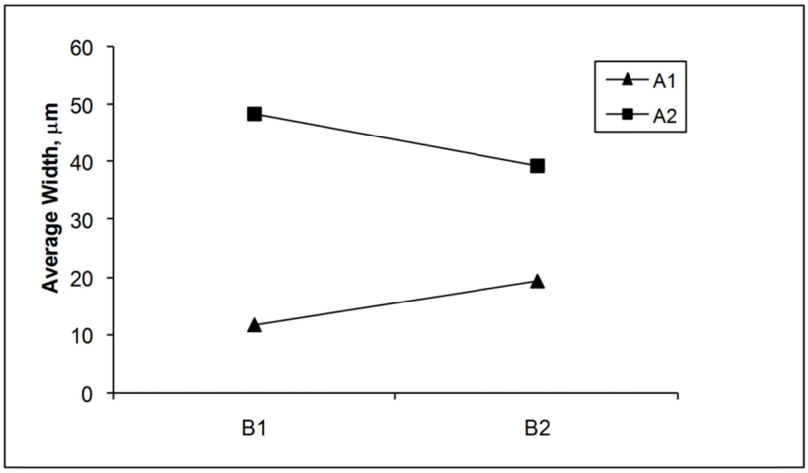

Figure D-2: Interaction of the factors A and B affecting the deposition width

Based on the DOE analysis, the most effective factors, in the order of significance, on the deposition width are

- Atomizer gas flow rate
- Deposition velocity
- Interaction of atomizer gas flow rate and sheath gas flow rate

By considering the interaction, it is concluded that the effect of the atomizer flow rate on the width of the deposited tracks depends on the sheath gas flow rate. In the

experiments, in which the sheath gas flow rate is low, the atomizer flow rate is more effective than the ones in which the sheath gas flow rate is high. Since the sheath and atomizer flows are mixed in the deposition head, increasing the sheath flow rate reduces the prominent role of the atomizer flow rate in the deposition width. This phenomenon was observed in the experiments by the formation of over-sprayed material and satellites on the sides of the deposition tracks at high sheath gas flow rates.

D.2 Deposition Thickness

A separate set of experiments was designed to study the effective parameters on the thickness of the depositions. The parameters supposed to be effective on the thickness are listed in Table D-2. The selection of the parameters and their levels were based on previous experience. According to the total degree of freedom, the L_8 table is used solution for the design of experiments. In the experiments, the thickness varies from 0.5 μm to 2.68 μm at different process parameters.

An ANOVA table was also constructed for this set of experiments. By considering the level of confidence of 90%, the most significant factors are the laser power (F) and the number of layers (D).

The average thickness results for different factor levels are shown in Figure D-3. According to this figure, it is evident that the change in D and F has the most significant effect on the results. Apparently, reducing the laser power and/or increasing the number of deposited layers result in thicker films. Although, the laser scanning velocity affects the thickness, its effect is less than that of the laser power and the number of layers.

The effect of FE is shown in Figure D-4. It is observed that the interaction of F and E is not significant in the final results; the individual effect of E or F is independent of the value of the other parameter.

Table D-2: Controlled parameters for the analysis of the thickness

Factors	**Description**	**Level 1**	**Level 2**	**DOF**
D	Number of layers	5	10	1
E	Laser scanning velocity (mm/s)	0.75	5.5	1
F	Laser power (W)	0.75	1.35	1
EF	Interaction EF	NA	NA	1
				Total DOF: 4

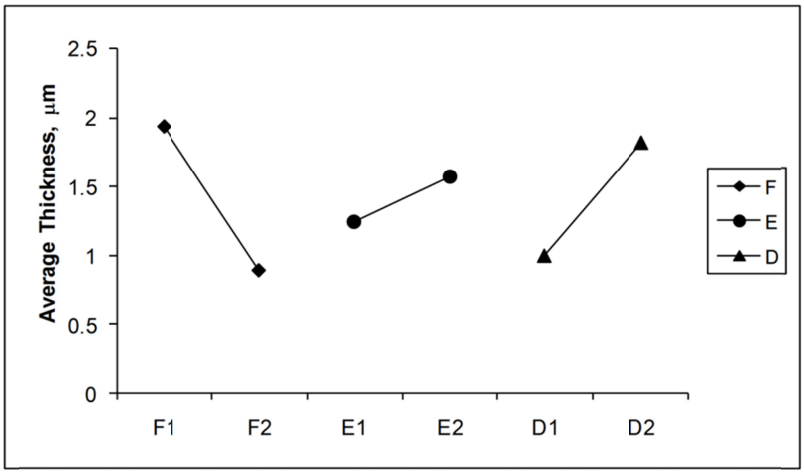

Figure D-3: Average thickness vs. the change of parameters levels

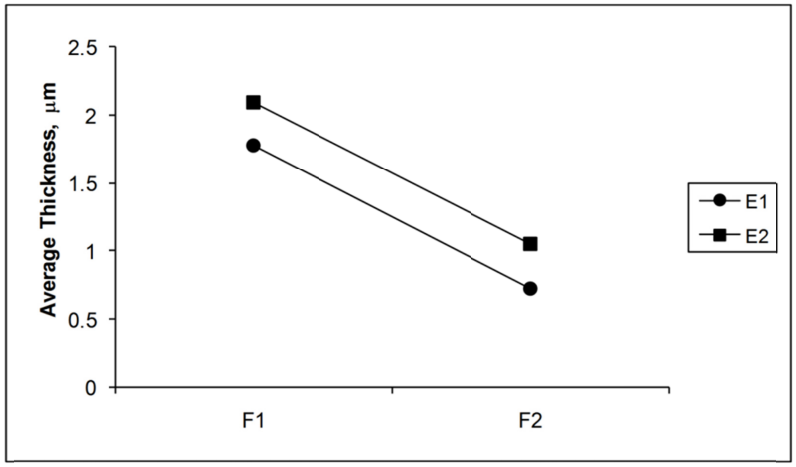

Figure D-4: Interaction of the factors E and F affecting the deposition thickness

Appendix E

MATLAB Codes for Solving Riccati Differential Equation for SFBGs

```
%Solution of Riccati Coupled-Mode ODEs for SFBG
%Developed by: Hamidreza Alemohammad

function R=runge_kutta4_FBG(a, b, N, alpha)

h = (b-a)/N;        %the step size
z(1) = a;
w(1) = alpha;       %the initial value

for i = 1:N
      k1 = h*f(z(i), w(i));
      k2 = h*f(z(i)+h/2, w(i)+(k1)/2);
      k3 = h*f(z(i)+h/2, w(i)+(k2)/2);
      k4 = h*f(z(i)+h, w(i)+k3);
      w(i+1) = w(i) + (k1 + 2*k2 + 2*k3 + k4)/6;
      z(i+1) = a + i*h;
end

R=[z',w'];

function dy = f(z, y)
global k sigma_h gamma_0 lambda fl1 e_com1 e_com2 dT F L alfa;

alfa=0.5e-6;
n_eff=1.44405;
% uniform grating
% del_n_eff=0.5e-4;
```

```
% nu_op=1.9;
% lambda_D=1549.015e-9;

% apodized Gaussian
lambda_D=1549.65e-9;
del_n_eff=0.1e-4*exp(-4*log(2)*z^2/(L/3)^2);
nu_op=25;
gamma_0=lambda_D/2/n_eff;
gamma_s=0*1e-7;

nu=0.17;
p11=0.113;
p12=0.252;
dn_dT=1.241e-5;
pe=n_eff^2/2*(p12-nu*(p11+p12));
de1_dz=0;
N_seg=7;
L1=1.5e-3;
L2=0.5e-3;
shift=0;

if z>=0
if (rem(abs(z),L/N_seg)>=L1/2+shift) &&
(rem(abs(z),L/N_seg)<=(L1/2+L2)+shift)%Small diameter
    e1=e_com1(1);
    e2=e_com1(2);
    e3=e_com1(3);
    n_eff_i=-n_eff^3/2*(p12*e2+p12*e1+p11*e3-2/n_eff^3*(dn_dT)*dT-
    (p11+2*p12)*alfa*dT)+n_eff;
    gamma=(gamma_0+gamma_s*z)*(1+e1);

else %Large diameter
    e1=e_com2(1);
    e2=e_com2(2);
    e3=e_com2(3);
    n_eff_i=-n_eff^3/2*(p12*e2+p12*e1+p11*e3-2/n_eff^3*(dn_dT)*dT-
    (p11+2*p12)*alfa*dT)+n_eff;
    gamma=(gamma_0+gamma_s*z)*(1+e1);
end
end
if z<0
if (rem(abs(z),L/N_seg)>=L1/2-shift) && (rem(abs(z),L/N_seg)<=(L1/2+L2)-
shift)%Small diameter
    e1=e_com1(1);
    e2=e_com1(2);
    e3=e_com1(3);
    n_eff_i=-n_eff^3/2*(p12*e2+p12*e1+p11*e3-2/n_eff^3*(dn_dT)*dT-
    (p11+2*p12)*alfa*dT)+n_eff;
    gamma=(gamma_0+gamma_s*z)*(1+e1);

else %Large diameter
      e1=e_com2(1);
      e2=e_com2(2);
```

```
      e3=e_com2(3);
      n_eff_i=-n_eff^3/2*(p12*e2+p12*e1+p11*e3-2/n_eff^3*(dn_dT)*dT-
      (p11+2*p12)*alfa*dT)+n_eff;
      gamma=(gamma_0+gamma_s*z)*(1+e1);
end
end

del_n_eff=del_n_eff*n_eff_i/n_eff;
n_eff=n_eff_i;
gamma=(gamma_0+gamma_s*z)*(1+e1);
dgamma_dz=gamma_s*(1+e1)+(gamma_0+gamma_s*z)*(de1_dz);
dgamma_dz=0;
phi_prime=2*pi*(-z/gamma^2*dgamma_dz+1/gamma-1/gamma_0)*0;
sigma_h=2*pi*n_eff*1/lambda-pi/gamma+2*pi*del_n_eff/lambda-0.5*phi_prime;
k=pi/lambda*nu_op*del_n_eff;
dy=(-i*k-2*i*sigma_h*y-i*k*y^2);

global lambda L fl1 e_com1 e_com2 dT fem0 F alfa;
alfa=0.55e-6;
L=0.014;
Ref_M_1=[];
Ref_M_2=[];
Ref_M=[];
lambda_M=[];
lambda_min=1548.5e-9;
lambda_max=1552e-9;
d_lambda=0.01*1e-9;
phase_M_1=[];
nu=0.16;
Ref_up_b=[];
T=[];
F_M=[];
lamb_max=[];

for F=0:0.1:0
for dT=0:10:75
      e0=0;
      %   thickness 15 Microns
      ezz=0.7532617110e-3*F+0.7094274902e-5*dT;
      err=-0.1459564732e-3*F+0.2269263208e-5*dT;

      %   thickness 9 microns
      %   ezz=0.5005585679e-5*dT+0.8654364913e-3*F;
      %   err=0.1769036815e-5*dT-0.1612325541e-3*F;

      %   thinkness 8 microns
      %   ezz=0.8282630358e-3*F+0.5757545074e-5*dT;
      %   err=-0.1573385087e-3*F+0.2069938674e-5*dT;
      %
      %   thickness 7 microns
      %   ezz=0.5248601220e-5*dT+0.8547878560e-3*F;
      %   err=0.1923052999e-5*dT-0.1606565650e-3*F;
```

```
      e_com2=[ezz;err;err]-e0;
      e_com1=[0.1086497746e-2*F+5.499999876*10^(-7)*dT;-0.1847046168e-
      3*F+5.499999822*10^(-7)*dT;-0.1847046168e-3*F+5.499999822*10^(-
      7)*dT];
      Ref_M_1=[];
      Ref_M_2=[];
      Ref_M=[];
      lambda_M=[];
      fl1=1;
for lambda=lambda_min:d_lambda:lambda_max;
      R=runge_kutta4_FBG(L/2,-L/2,400,0);
      z=R(:,1);
      ro=R(:,2);
      Ref_M_1=[Ref_M_1 abs(ro(length(ro)))^2];
      lambda_M=[lambda_M lambda];
end;
fl1=2;
for lambda=lambda_min:d_lambda:lambda_max;
      R=runge_kutta4_FBG(L/2,-L/2,400,0);
      z=R(:,1);
      ro=R(:,2);
      Ref_M_2=[Ref_M_2 abs(ro(length(ro)))^2];
end;
      Ref_M=(Ref_M_1+Ref_M_2)/2;
end

end
```

Bibliography

[1] Weisenbach, L., "Fiber optic sensors," BCC Research, Tech. Rep. IAS002D, 2008.

[2] Kashyap, R., *Fiber Bragg Gratings,* 1st ed. San Diego: Academic Press, 1999.

[3] Erdogan, T., "Fiber Grating Spectra," *Journal of Light Wave Technology,* vol. 15, no. 8, pp. 1277-1294, 1997.

[4] Kim, K. S., Ismail, Y. and Springer, G. S., "Measurement of strain and temperature with embedded intrinsic Fabry-Perot optical fiber sensors," *Journal of Composite Materials,* vol. 27, no. 17, pp. 1663-1677, 1993.

[5] Kim, K. S., Kollar, L. and Springer, G. S., "A model of embedded fiber optic Fabry-Perot temperature and strain sensors," *Journal of Composite Materials,* vol. 27, no. 17, pp. 1618-1662, 1993.

[6] Corning SMF-28 Optical Fiber, Product Information, 2002.

[7] Guemes, J. A. and Menendez, J. M., "Response of Bragg grating fiber-optic sensors when embedded in composite laminates," *Composites Science and Technology,* vol. 62, pp. 959-966, 2002.

[8] Lau, K. T., Chanb, C. C., Zhoua, L. M. and Jin, W., "Strain monitoring in composite-strengthened concrete structures using optical fibre sensors," *Composites, Part B-Engineering,* vol. 32, pp. 33-45, 2001.

[9] Kuang, K. S. C. and Cantwell, W. J., "Use of conventional optical fibers and fiber Bragg gratings for damage detection in advanced composite structures: A review," A*pplied Mechanics Reviews, vol. 56*, no. 5, pp. 493-513, 2003.

[10] Li, X. C., Golnas, A., and Prinz, F., "Shape deposition manufacturing of smart metallic structures with embedded sensors," *Proceedings of SPIE,* vol. 3986*,* 2000, pp. 160-171.

[11] Cheng, X., Datta, A., Choi, H., Zhang, X. and Li, X., "Study on Embedding and Integration of Microsensors into Metal Structures for Manufacturing Applications," *ASME Journal of Manufacturing Science and Engineering*, vol. 129, pp. 416-424, 2007.

[12] Zhang, X., Choi, H., Datta, A. and Li, X., "Design, fabrication and characterization of metal embedded thin film thermocouples with various film thicknesses and junction size," *Journal of Micromechanics and Microengineering*, vol. 16, pp. 900-905, 2006.

[13] Lupi, C., Felli, F., Ippoliti, L., Caponero, M. A., Ciotti, M., Nardelli, V. and Paolozzi, A., "Metal coating for enhancing the sensitivity of fibre Bragg grating sensors at cryogenic temperature," *Smart Materials and Structures,* vol. 14, pp. N71-N76, 2005.

[14] Sandlin, S., Kinnunen, T., Ramo, J. and Sillanpaa, M., "A simple method for metal re-coating of optical fibre Bragg gratings," *Surface and Coatings Technology*, vol. 201, pp. 3061-3065, 2006.

[15] Kong, C. Y. and Soar, R., "Methods for embedding optical fibers in an aluminum matrix by ultrasonic consolidation," *Applied Optics,* vol. 44, no. 30, pp. 6325-6333, 2005.

[16] Ling, H. Y., Lau, K. T., Cheng, L. and Jin, W., "Viability of using an embedded FBG sensor in a composite structure for dynamic strain measurement," *Measurement,* vol. 39, no. 4, pp. 328-334, 2006.

[17] Liang, W., Huang, Y., Xu, Y., Lee, R. K. and Yariv, A., "Highly sensitive fiber Bragg grating refractive index sensors," *Applied Physics Letters,* vol. 86, no. 15, 2005.

[18] Chryssis, A. N., Lee, S. M., Lee, S. B., Saini, S. S. and Dagenais, M., "High sensitivity evanescent field fiber Bragg grating sensor," *IEEE Photonics Technology Letters,* vol. 17, no. 6, pp. 1253-1255, 2005.

[19] Iadicicco, A., Cusano, A., Campopiano, S., Cutolo, A. and Giordano, M., "Thinned fiber Bragg gratings as refractive index sensors," *IEEE Sensors Journal,* vol. 5, no. 6, pp. 1288-1295, 2005.

[20] Pereira, D. A., Ao, O. F. and Santos, J. L., "Fiber Bragg grating sensing system for simultaneous measurement of salinity and temperature," *Optical Engineering,* vol. 43, no. 2, pp. 299-304, 2004.

[21] Huang, X., Chen, Z., Shao, L., Cen, K., Sheng, D., Chen, J. and Zhou, H., "Design and characteristics of refractive index sensor based on thinned and microstructure fiber Bragg grating," *Aplied Optics,* vol. 47, no. 4, pp. 504-511, February. 2008.

[22] Magne, S., Rougeault, S., Vilela, M. and Ferdinand, P., "State-of-strain evaluation with fiber Bragg grating rosettes: application to discrimination between strain and temperature effects in fiber sensors," *Applied Optics,* vol. 36, no. 36, pp. 9437-9447, 1997.

[23] Betz, D. C., Thursby, G., Culshaw, B. and Staszewski, W. J., "Advanced layout of a fiber bragg grating strain gauge rosette," *Journal of Lightwave Technology,* vol. 24, no. 2, pp. 1019-1026, 2006.

[24] Hsu, Y. S., Wang, L., Liu, W. F. and Chiang, Y. J., "Temperature compensation of optical fiber Bragg grating pressure sensor," *IEEE Photonics Technology Letters,* vol. 18, no. 7, pp. 874-876, 2006.

[25] Yoffe, G. W., Krug, P. A., Ouellette, K. F. and Thorncraft, D. A., "Passive temperature-compensating package for optical fiber gratings," *Applied Optics,* vol. 34, no. 30, pp. 6859-6861, 1995.

[26] James, S. W., Dockney, M. L. and Tatam, R. P., "Simultaneous independent temperature and strain measurement using in-fibre Bragg grating sensors," *Electronics Letters,* vol. 32, no. 12, pp. 1133-1134, 1996.

[27] Dong, X., Yang, X., Zhao, C. L., Ding, L., Shum, P. and Ngo, N. Q., "A novel temperature-insensitive fiber Bragg grating sensor for displacement measurement," *Smart Materials and Structures,* vol. 14, pp. N7-N10, 2005.

[28] Iwashima, T., Inoue, A., Shigematsu, M., Nishimura, M. and Hattori, Y., "Temperature compensation technique for fibre Bragg gratings using liquid crystalline polymer tubes," *Electronics Letters,* vol. 33, no. 5, pp. 417-419, 1997.

[29] Guan, B. O., Tam, H. Y., Tao, X. M. and Dong, X. Y., "Simultaneous strain and temperature measurement using a superstructure fiber Bragg grating," *IEEE Photonics Technology Letters,* vol. 12, no. 6, pp. 675-677, 2000.

[30] Lin, C., Liu, Y., Liu, W., Fu, M., Sheng, H., Bor, S. and Tien, C., "High-Sensitivity Simultaneous Pressure and Temperature Sensor Using a Superstructure Fiber Grating," *IEEE Sensors Journal,* vol. 6, no. 3, pp. 691-696, 2006.

[31] Shen, Y., He, J., Qiu, Y., Zhao, W., Chen, S., Sun, T. and Grattan, K. T. V., "Thermal decay characteristics of strong fiber Bragg gratings showing high-temperature sustainability," *Journal of Optical Society of America B,* vol. 24, no. 3, pp. 430-438, 2007.

[32] Bucaro, J. a. and Dardy, H. D., "High-temperature Brillouin scattering in fused quartz," *Applied Physics,* vol. 45, no. 12, pp. 5324-5329, 1974.

[33] Li, L., Geng, R., Zhao, L., Chen, G., Chen, G., Fang, Z. and Lam, C., "Response characteristics of thin-film-heated tunable fiber Bragg gratings," *IEEE Photonics Technology Letters,* vol. 15, no. 4, pp. 545-547, 2003.

[34] Steinvurzel, P., MacHarrie, R., Baldwin, K., Van Hise, C., Eggleton, B. and Rogers, J., "Optimization of distributed resistive metal film heaters in thermally tunable dispersion compensators for high-bit-rate communication systems," *Applied Optics,* vol. 44, no. 14, pp. 2782-2791, 2005.

[35] Fox, G., Muller, C., Setter, N., Costantini, D., Ky, N. and Limberger, H., "Wavelength tunable fiber Bragg grating devices based on sputter deposited resistive and piezoelectric

coatings," *Vacuum Science & Technology A: Vacuum Surfaces and Films,* vol. 15, no. 3, Part 2, pp. 1791-1795, 1997.

[36] Sutapun, B., Tabib-Azar, M. and Kazemi, A., "Pd-coated elastooptic fiber optic Bragg grating sensors for multiplexed hydrogen sensing," *Sensors and Actuators B-Chemical,* vol. 60, no. 1, pp. 27-34, 1999.

[37] Buck, J. A., *Fundamentals of Optical Fibers,* 2nd ed. Hoboken: Wiley, 2004.

[38] Othonos, A. and Kalli, K., *Fiber Bragg Gratings,* 1st ed. Boston: Artech House, 1999.

[39] James, S. W. and Tatam, R. P., "Optical fibre long-period grating sensors: characteristics and application," *Measurement Science and Technology,* vol. 14, pp. R49-R61, 2003.

[40] Mihailov, S. J., Smelser, C. W., Grobnic, D., Walker, R. B., Lu, P., Ding, H. and Unruh, J., "Bragg gratings written in all-SiO_2 and Ge-doped core fibers with 800-nm femtosecond radiation and a phase mask," *Journal of Lightwave Technology,* vol. 22, no. 1, pp. 94-100, 2004.

[41] Zhan, C., Lee, J., Yin, S., Ruffin, P. and Grant, J., "Photoenhanced polarization mode separated fiber Bragg gratings inscribed by femtosecond laser," *Journal of Applied Physics,* vol. 101, no. 5, 2007.

[42] Grobnic, D., Mihailov, S. J. and Smelser, C. W., "Localized High Birefringence Induced in SMF-28 Fiber by Femtosecond IR Laser Exposure of the Cladding," *Journal of Lightwave Technology,* vol. 25, no. 8, pp. 1996-2001, 2007.

[43] Martinez, A., Dubov, M., Khrushchev, I. and Bennion, I., "Direct writing of fibre Bragg gratings by femtosecond laser," *Electronics Letters,* vol. 40, no. 19, pp. 1170-1172, 2004.

[44] Bosia, F., Giaccari, P., Botsis, J., Facchini, M., Limberger, H. G. and Salathe, R. P., "Characterization of the response of fibre Bragg grating sensors subjected to a two-dimensional strain field," *Smart Materials and Structures,* vol. 12, pp. 925-934, 2003.

[45] Gafsi, R. and El-sherif, M. A., "Analysis of induced-birefringence effects on fiber Bragg gratings," *Optical Fiber Technology,* vol. 6, pp. 299-323, 2000.

[46] Wagreich, R. B., Atia, W. A., Singh, H. and Sirkis, J. S., "Effects of diametric load on fibre Bragg gratings fabricated in low birefringent fibre," *Electronics Letters,* vol. 32, no. 13, pp. 1223-1224, 1996.

[47] Lawrence, C. M., Nelson, D. V., Udd, E. and Bennett, T., "A fiber optic sensor for transverse strain measurement," *Experimental Mechanics,* vol. 39, no. 3, pp. 202-209, 1999.

[48] Silva-Lopez, M., Li, C., McPherson, W. N., Moore, A. J., Barton, J. S. and Jones, J. D. C., "Differential birefringence in Bragg gratings in multicore fiber under transverse stress," *Optics Letters,* vol. 29, no. 19, pp. 2225-2227, 2004.

[49] Xu, M. G., Dong, L., Reekie, L., Tucknott, J. A. and Cruz, J. L., "Temperature-independent strain sensor using a chirped Bragg grating in a tapered optical fibre," *Electronics Letters,* vol. 31, no. 10, pp. 823-824, 1995.

[50] Du, W. C., Tao, X. M. and Tam, H. Y., "Fiber Bragg grating cavity sensor for simultaneous measurement of strain and temperature," *IEEE Photonics Technology Letters,* vol. 11, no. 1, pp. 105-107, 1998.

[51] Yu, Y., Tam, H., Chung, W. and Demokan, M. S., "Fiber Bragg grating sensor for simulataneous measurement of displacement and temperature," *Optics Letters,* vol. 25, no. 16, pp. 1141-1143, 2000.

[52] Zhang, W., Dong, X., Zhao, Q., Kai, G. and Yuan, S., "FBG-type sensor for simulataneous measurement of force (or displacement) and temperature based on bilateral cantilever beam," *IEEE Photonics Technology Letters,* vol. 13, no. 12, pp. 1340-1342, 2001.

[53] Tanaka, N., Okabe, Y. and Takeda, N., "Temperature-compensated strain measurement using fiber Bragg grating sensors embedded in composite laminates," *Smart Materials and Structures,* vol. 12, pp. 940-946, 2003.

[54] Kuang, K. S. C., Kenny, R., Whelan, M. P., Cantwell, W. J. and Chalker, P. R., "Residual strain measurement and impact response of optical fibre Bragg grating sensors in fibre metal laminates," *Smart Materials and Structures,* vol. 10, pp. 338-346, 2001.

[55] Ling, H. Y., Lau, K. T., Cheng, L. and Chow, K. W., "Embedded fibre Bragg grating sensors for non-uniform strain sensing in composite structures," *Measurement Science and Technology,* vol. 16, pp. 2415-2424, 2005.

[56] Ling, H. Y., Lau, K. T., Cheng, L. and Jin, W., "Utilization of embedded optical fibre sensors for delamination characterization in composite laminates using a static strain method," *Smart Materials and Structures,* vol. 14, pp. 1377-1386, 2005.

[57] Seo, H. S., Paek, U. C., Oh, K. and Kurkjian, C. R., "Melt coating of tin on silica optical fiber," *Journal of Light Wave Technology,* vol. 16, no. 12, pp. 2355-2364, 1998.

[58] Lee, C. E., Gibler, W. N., Atkins, R. A., Alcoz, J. J. and Taylor, H. F., "Metal-embedded fiber-optic Fabry-Perot sensors," *Optics Letters,* vol. 16, no. 24, pp. 1990-1992, 1991.

[59] Lin, G. C., Wang, L., Yang, C. C., Shih, M. C. and Chuang, T. J., "Thermal Performance of Metal-Clad Fiber Bragg Grating Sensors," *IEEE Photonics Technology Letters,* vol. 10, no. 3, pp. 406-408, 1998.

[60] Li, X. C., Prinz, F. and Seim, J., "Thermal behavior of a metal embedded fiber Bragg grating sensor," *Smart Materials and Structures,* vol. 10, pp. 575-579, 2001.

[61] Tjin, S. C., Suresh, R. and Ngo, N. Q., "Fiber Bragg grating based shear-force sensor: modeling and testing," *Journal of Lightwave Technology,* vol. 22, no. 7, pp. 1728-1733, 2004.

[62] Peters, K., Pattis, P., Botsis, J. and Giaccari, P., "Experimental verification of response of embedded optical fiber Bragg grating seesors in non-homogeneous fields," *Optics and Lasers in Engineering,* vol. 33, pp. 107-119, 2000.

[63] Gupta, S., Mizunami, T., Yamao, T. and Shimomura, T., "Fiber Bragg grating cryogenic temperature sensors," *Applied Optics,* vol. 35, no. 25, pp. 5202-5205, 1996.

[64] Mizunami, T., Tadehata, H. and Kawashima, H., "High-sensitivity cryogenic fibre-Bragg-grating temperature sensors using Teflon substrates," *Measurement Science and Technology,* vol. 12, pp. 914-917, 2001.

[65] Prabhugoud, M. and Peters, K., "Efficient simulation of Bragg grating sensors for implementation to damage identification in composites," *Smart Materials and Structures,* vol. 12, pp. 914-924, 2003.

[66] Ahuja, A. K., Steinvurzel, P. E., Eggleton, B. J. and Rogers, J. A., "Tunable single phase-shifted and superstructure gratings using microfabricated on-fiber thin film heaters," *Optics Communications,* vol. 184, pp. 119-125, 2000.

[67] Eggleton, B. J., Rogers, J. A., Westbrook, P. S. and Strasser, T. A., "Electrically tunable power efficient dispersion compensating fiber Bragg grating," *IEEE Photonics Technology Letters,* vol. 11, no. 7, pp. 854-857, 1999.

[68] Rogers, J. A., Eggleton, B. J., Jackman, R. J., Kowach, G. R. and Strasser, T. A., "Dual on-fiber thin-film heaters for fiber grating with idependently adjustable chirp and wavelength," *Optics Letters,* vol. 24, no. 19, pp. 1328-1330, 1999.

[69] Huang, S., Ohn, M. M. and Measures, R. M., "Phase-based Bragg intragrating distributed strain sensor," *Applied Optics,* vol. 35, no. 7, pp. 1135-1142, 1996.

[70] Huang, S., Ohn, M. M., LeBlanc, M. and Measures, R. M., "Continuous arbitrary strain profile measurements with fiber Bragg gratings," *Smart Materials and Structures,* vol. 7, pp. 248-256, 1998.

[71] Skaar, J. and Risvik, K. M., "A genetic algorithm for the inverse problem in synthesis of fiber gratings," *Journal of Light Wave Technology,* vol. 16, no. 10, pp. 1928-1932, 1998.

[72] Cormier, G. and Boudreau, R., "Real-coded genetic algorithm for Bragg grating parameter synthesis," *Journal of the Optical Society of America,* vol. 18, no. 12, pp. 1771-1776, 2001.

[73] Azana, J., Muriel, M. A., Chen, L. R. and Smith, P. W. E., "Fiber Bragg grating period reconstruction using time-frequency signal analysis and application to distributed sensing," *Journal of Lightwave Technology,* vol. 19, no. 5, pp. 646-654, 2001.

[74] Casagrande, F., Crespi, P., Grassi, A. M., Lulli, A., Kenny, R. P. and Whelan, M. P., "From the reflected spectrum to the properties of a fiber Bragg grating: a genetic algorithm approach with application to distributed strain sensing," *Applied Optics,* vol. 41, no. 25, pp. 5238-5244, 2002.

[75] Gill, A., Peters, K. and Studer, M., "Genetic algorithm for the reconstruction of Bragg grating strain profiles," *Measurement Science and Technology,* vol. 15, pp. 1877-1884, 2004.

[76] Duty, C., Jean, D. and Lackey, W., "Laser chemical vapour deposition: materials, modelling, and process control," *International Materials Reviews,* vol. 46, no. 6, pp. 271-287, 2001.

[77] Bohandy, J., Kim, B. F. and Adrian, F. J., "Metal deposition form a supported metal-film using an excimer laser," *Applied Physics,* vol. 60, no. 4, pp. 1538-1539, 1986.

[78] Piqué, A., Auyeung, R., Stepnowski, J., Weir, D., Arnold, C., McGill, R. and Chrisey, D., "Laser processing of polymer thin films for chemical sensor applications," *Surface and Coatings Technology,* vol. 163, pp. 293-299, 2003.

[79] Bähnisch, R., Grosβ, W. and Menschig, A., "Single-shot, high repetition rate metallic pattern transfer," *Microelectronic Engineering,* vol. 50, no. 1-4, pp. 541-546, 2000.

[80] Modi, R., Wu, H. D., Auyeung, R. C. Y., Vollmers, J. E. S. and Chrisey, D. B., "Ferroelectric capacitors made by a laser forward transfer technique," *Integrated Ferroelectronics,* vol. 42, pp. 79-95, 2002.

[81] Landström, L., Klimstein, J., Schrems, G., Piglmayer, K. and Bäuerle, D., "Single-step patterning and the fabrication of contact masks by laser-induced forward transfer," *Applied Physics A-Materials Science & Processing,* vol. 78, no. 4, pp. 537-538, 2004.

[82] Yamada, H., Sano, T., Nakayama, T. and Miyamoto, I., "Optimization of laser-induced forward transfer process of metal thin films," *Applied Surface Science,* vol. 197, pp. 411-415, 2002.

[83] Zergioti, I., Papazoglou, D. G., Karaiskou, A., Vainos, N. A. and Fotakis, C., "Laser microprinting of InOx active optical structures and time resolved imaging of the transfer process," *Applied Surface Science,* vol. 197, pp. 868-872, 2002.

[84] Mathews, S. A., Auyeung, R. C. Y. and Piqué, A., "Use of Laser Direct-Write in Microelectronics Assembly," *Journal of Laser Micro/Nanoengineering,* vol. 2, no. 1, pp. 103-107, 2007.

[85] C. Y. Auyeung, M. W. Numberger, D. J. Wendland, A. Piqué, C. B. Arnold, A. R. Abbott and L. C. Schuette, "Laser fabrication of GPS conformal antennas," *Proceedings of SPIE,* vol. 5339*,* 2004, pp. 292-297.

[86] Blanchet, G. B., Loo, Y. L., Rogers, J. A., Gao, F. and Fincher, C. R., "Large area, high resolution, dry printing of conducting polymers for organic electronics," *Applied Physics Letters,* vol. 82, no. 3, pp. 463-465, 2003.

[87] S. Lamansky, T. R. Hoffend Jr, H. Le, V. Jones, M. B. Wolk and W. A. Tolbert, "Laser induced thermal imaging of vacuum-coated OLED materials," *Proceedings of SPIE,* vol. 5937*,* 2005, 593702.

[88] Bieri, N. R., Chung, J., Poulikakos, D. and Grigoropoulos, C. P., "Manufacturing of nanoscale thickness gold lines by laser curing of a discretely deposited nanoparticle suspension," *Superlattices and Microstructures,* vol. 35, no. 3-6, pp. 437-444, 2004.

[89] Cho, J. H., Lee, J., Xia, Y., Kim, B., He, Y., Renn, M. J., Lodge, T. P. and Daniel, "Printable ion-gel gate dielectrics for low-voltage polymer thin-film transistors on plastic," *Nature Materials,* vol. 7, no. 11, pp. 900-906, November. 2008.

[90] Khana, A., Rasmussen, N., Marinov, V. and Swenson, O. F., "Laser sintering of direct write silver nano-ink conductors for microelectronic applications," *Proceedings of SPIE,* vol. 6879, pp. 687910, 2008.

[91] Marinov, V. R., Atanasov, Y. A., Khan, A., Vaselaar, D., Halvorsen, A., Schulz, D. L. and Chrisey, D. B., "Direct-Write Vapor Sensors on FR4 Plastic Substrates," *IEEE Sensors Journal,* vol. 7, no. 6, pp. 937-944, 2007.

[92] Vaillancourt, J., Zhang, H., Vasinajindakaw, P., Xia, H., Lu, X., Han, X., Janzen, D. C., Shih, W. S., Jones, C. S., Stroder, M., Chen, M. Y., Subbaraman, H., Chen, R. T., Berger, U. and Renn, M., "All ink-jet-printed carbon nanotube thin-film transistor on a polyimide substrate with an ultrahigh operating frequency of over 5 GHz," *Applied Physics Letters,* vol. 93, no. 24, 2008.

[93] Alemohammad, H., Aminfar, O. and Toyserkani, E., "Morphology and microstructure analysis of nano-silver thin films deposited by laser-assisted maskless microdeposition," *Journal of Micromechanics and Microengineering,* vol. 18, no. 11, pp. 115015, 2008.

[94] Sears, J., Colvin, J. and Carter, M., "Fabricating Devices Using Nano-Particulates with Direct Write Technology," *Materials Science Forum,* vol. 534-536, no. 2, pp. 1385-1388, 2007.

[95] Nye, J. F., *Physical Properties of Crystals,* New York: Oxford University Press, 1985.

[96] Yariv, A. and Yeh, P., *Optical Waves in Crystals,* Hoboken: John Wiley & Sons, 2003.

[97] Mir, J. M., "Cavitation-induced capillary wave in ultrasonic atomization," *Journal of Acoustical Society of America,* vol. 67, pp. 201-205, 1980.

[98] Rajan, R. and Pandit, A. B., "Correlation to predict droplet size in ultrasonic atomisation," *Journal of Ultrasonics,* vol. 39, pp. 235-255, 2001.

[99] Nakaso, K., Shimada, M., Okuyama, K. and Deppert, K., "Evaluation of the change in the morphology of gold nanoparticles during sintering," *Journal of Aerosol Science,* vol. 33, no. 7, pp. 1061-1074, 2002.

[100] Auyeung, R. C. Y., Kim, H., Mathews, S. A. and Piqué, A., "Laser Direct-Write of Metallic Nanoparticle Inks," *JLMN-Journal of Laser Micro/Nanoengineering,* vol. 2, no. 21, pp. 21-25, 2007.

[101] Arcidiacono, S., Bieri, N. R., Poulikakos, D. and Grigoropoulos, C. P., "On the coalescence of gold nanoparticles," *International Journal of Multiphase Flow,* vol. 30, no. 7-8, pp. 979-994, 2004.

[102] Greer, J. and Street, R., "Thermal cure effects on electrical performance of nanoparticle silver inks," *Acta Materialia,* vol. 55, no. 18, pp. 6345-6349, 2007.

[103] Moon, K. S., Dong, H., Maric, R., Pothukuchi, S., Hunt, A., Li, Y. and Wong, C. P., "Thermal behavior of silver nanoparticles for low-temperature interconnect applications," *Electronic Materials,* vol. 34, no. 2, pp. 168-175, 2005.

[104] Oliver, W. C. and Pharr, G. M., "An improved technique for determining hardness and elastic modulus using load and displacement sensing indentation experiments," *Journal of Materials Research,* vol. 7, no. 6, pp. 1564-1583, 1992.

[105] Freud, L. B. and Suresh, S., *Thin Film Materials,* Cambridge: Cambridge University Press, 2003.pp. 545.

[106] Cao, Y., Allameh, S., Nankivil, D., Sethiaraj, S., Otiti, T. and Soboyejo, W., "Nanoindentation measurements of the mechanical properties of polycrystalline Au and Ag thin films on silicon substrates: Effects of grain size and film thickness," *Materials Science and Engineering A,* vol. 427, no. 1-2, pp. 232-240, 2006.

[107] Panin, A., Shugurov, A. and Oskomov, K., "Mechanical properties of thin Ag films on a silicon substrate studied using the nanoindentation technique," *Physics of the Solid State,* vol. 47, no. 11, pp. 2055-2059, 2005.

[108] Schaffer, C. B., Brodeur, A., García, J. F. and Mazur, E., "Micromachining bulk glass by use of femtosecond laser pulses with nanojoule energy," *Optics Letters,* vol. 26, no. 2, pp. 93-95, January. 2001.

[109] Schaffer, C. B., Brodeur, A. and Mazur, E., "Laser-induced breakdown and damage in bulk transparent materials induced by tightly focused femtosecond laser pulses," *Measurement Science and Technology,* vol. 12, no. 11, pp. 1784-1794, 2001.

[110] Liu, X., Du, D. and Mourou, G., "Laser ablation and micromachining with ultrashort laser pulses," *Journal of Quantum Electronics,* vol. 33, no. 10, pp. 1706-1716, 1997.

[111] Krüger, J. and Kautek, W., "Ultrashort laser interaction with dielectrics and polymers," *Advances in Polymer Science*, vol. 168, pp. 247-89, 2004.

[112] Grigoropoulos, C. P., *Transport in Laser Microfabrication,* 1st ed. New York: Cambridge university Press, 2009.

[113] Lenzner, M., Krüger, J., Sartania, S., Cheng, Z., Spielmann, C., Mourou, G., Kautek, W. and Krausz, F., "Femtosecond Optical Breakdown in Dielectrics," *Physical Review Letters,* vol. 80, no. 18, pp. 4076, May. 1998.

[114] Mao, S., Quere, F., Guizard, S., Mao, X., Russo, R., Petite, G. and Martin, P., "Dynamics of femtosecond laser interactions with dielectrics," *Applied Physics A-Materials Science & Processing,* vol. 79, no. 7, pp. 1695-1709, 2004.

[115] Poumellec, B., Sudrie, L., Franco, M., Prade, B. and Mysyrowicz, A., "Femtosecond laser irradiation stress induced in pure silica," *Optics Express,* vol. 11, no. 9, pp. 1070-1079, 2003.

[116] Gattass, R. R. and Mazur, E., "Femtosecond laser micromachining in transparent materials," *Nature Photonics,* vol. 2, no. 4, pp. 219-225, 2008.

[117] Chan, J. W., Huser, T., Risbud, S. and Krol, D. M., "Structural changes in fused silica after exposure to focused femtosecond laser pulses," *Optics Letters,* vol. 26, no. 21, pp. 1726-1728, 2001.

[118] Thomas, J., Wikszak, E., Clausnitzer, T., Fuchs, U., Zeitner, U., Nolte, S., Tunnermann and A., "Inscription of fiber Bragg gratings with femtosecond pulses using a phase mask scanning technique," *Applied Physics A,* vol. 86, no. 2, pp. 153-157, 2007.

[119] Wikszak, E., Thomas, J., Klingebiel, S., Ortaç, B., Limpert, J., Nolte, S. and Tünnermann, A., "Linearly polarized ytterbium fiber laser based on intracore femtosecond-written fiber Bragg gratings," *Optics Letters,* vol. 32, no. 18, pp. 2756-2758, 2007.

[120] Boresi, A. P., Schmidt, R. J. and Sidebottom, O. M., *Advanced Mechanics of Materials,* New York: John Wiley & Sons, 1993.

[121] Fertein, E., Przygodzki, C., Delbarre, H., Hidayat, A., Douay, M. and Niay, P., "Refractive-index changes of standard telecommunication fiber through exposure to femtosecond laser pulses at 810 cm," *Applied Optics,* vol. 40, no. 21, pp. 3506-3508, 2001.

[122] Kamikawachi, R., Abe, I., Paterno, A., Kalinowski, H., Muller, M., Pinto, J. and Fabris, J., "Determination of thermo-optic coefficient in liquids with fiber Bragg grating refractometer," *Optics Communications,* vol. 281, no. 4, pp. 621-625, 2008.

[123] Alemohammad, H., Toyserkani, E. and Paul, C. P., "Fabrication of smart cutting tools with embedded optical fiber sensors using combined laser solid freeform fabrication and moulding techniques," *Optics and Lasers in Engineering,* vol. 45, pp. 1010-1017, 2007.

[124] Paul, C. P., Alemohammad, H., Toyserkani, E., Khajepour, A. and Corbin, S., "Cladding of WC-12 Co on low carbon steel using pulsed Nd:YAG laser," *Materials Science and Engineering,* vol. 464, pp. 170-176, 2007.

[125] Koshiba, M., *Optical Waveguide Theory by Finite Element Method,* 1st ed. Springer, 1992.

[126] Taguchi, G., Konishi, S. and Wu, Y., *Taguchi Methods, Research and Development,* Dearborn: ASI Press, 1992.